

**Tuning of Magnetic and High Frequency Electromagnetic
Response of Transition Metal Oxide Based
Magnetic Nanostructures**

Thesis submitted for the award of the degree of

Doctor of Philosophy (Science)

in

Physics (Experimental)

By

Rupali Rakshit

Department of Physics
University of Calcutta

July, 2016

Dedicated to my beloved parents...

Acknowledgement

First of all I would like to convey my gratitude to my supervisor Prof. Kalyan Mandal for his immense help, inspiration, valuable discussions, and humble guidance. He always encouraged and motivated me to think and execute my research work independently in challenging areas. Without his wisdom, patience, and support, any of my research work would not get success. Thank you Sir for providing me opportunity to work in your laboratory and making my PhD life very much enjoyable.

I am grateful to S. N. Bose National Centre for Basic Sciences (SNBNCBS), Kolkata, and Department of Science and Technology (DST), India, for providing a beautiful campus, advanced instrumental facilities, wonderful research environment, and financial supports. I also wish to express my sincere gratitude to Prof. Masayoshi Tonouchi of Institute of Laser Engineering, Osaka University for his collaboration and for giving me an opportunity to work in his lab. I learned the electron beam lithography technique and terahertz time domain spectroscopy in his lab with Dr. Kazunori Serita. I must appreciate the enthusiasm, all time support of Dr. Serita during last three years of my research. The mutual co-operation of every member of this group and the supporting staffs was quite encouraging to me.

I would like to thank Dr. Dipankar Das from UGC DAE CSR, Kolkata for providing Superconducting quantum interference device facility. I am thankful to Dr. Pintu Sen of VECC, Kolkata for providing Physical property measurement set up facility. I am grateful to Mr. Md Azaharuddin Ahmed from CRNN, Kolkata and Ms. Anusree Das from UGC DAE CSR, Kolkata for performing AC susceptibility measurements and Mössbauer spectroscopy several times required for my research work.

I am also obliged to the ex-director of SNBNCBS, Prof. Arup Kumar Raychaudhuri for his great effort in increasing the experimental facility at the centre, which has proved to be a boon for our research work. I thank all those faculty members of our centre, especially Prof. Ranjan Chaudhuri whose encouragement and enthusiasm have helped to improve my research work. I thank all the staff members, the security men, the cleaner, the cook, and the gardener for their sincere cooperation which makes my centre beautiful. I would also like to thank all the technical staff members: Urmi Chakraborty, Dipankar Roy, Amit Chanda, Samik Roy Mouluk, Surajit Mukherjee, Joy Bandopadhyay, and Shakti Nath Das for their help in sample characterization.

I must acknowledge my seniors and labmates: Dr. Madhuri Mandal, Dr. Gobinda Gopal Khan, Dr. Arka Chaudhuri, Dr. Shyamsundar Ghosh, Dr. Rajasree Das, Dr. Debasish Sarkar, Dr. Ashutosh Kumar Singh, Dr. Monalisa Pal, Arup Ghosh, Mahebab Alam, Keshab Karmakar, Souvanik Talukdar, Indranil Chakraborty, Esmā Khatun, Anupam Gorai, Priya Maity, Shashank Gupta, Deblina Majumdar, Dipika Mandal, and Subrata Ghosh for providing me a homely and cheerful environment in lab. I thank them for their patience and helping attitude. I must thank specially to Monalisa, Mahebab, and Arup Da for being a great source of knowledge, expertise, and technical assistance. I am also thankful to all my friends: Aslam, Ambalika, Chandrima, Shirsendu, Joydeep, Arpita, Arpan, Hrishit, Anindita, Sudipto, Purnima, Manja, TJ, Pampi, Dhanalakshmi, Victor, Sutopa, Sankar, Anita, Suraka,

Debasmita, Anulekha, Suvodip, Ransell, Nirnay, Subarna Di, Biplab Da, Chauba Di, Debanjan Da, and Animesh Da for providing joyous company in several instances.

I am, especially, thankful to Monalisa and Urmi Di, my bestest buddies in S. N. Bose centre. Their constant encouragement and support helped me to accept the challenges of research and enrich my research work. They helped me to figure out my confusions, and shared various glorious as well as miserable moments over the almost last four years. They really supported me at every work as well as personal annoyance. No thanks would be enough for their love, support, tolerance, and forgiveness.

I am grateful to all of my school, college, and university teachers especially to Dr. Rita Das of Dum Dum Road Govt. Sponsored. High School For Girls (H.S.), Mrs. Tapashi Basu Kar of Holy Child Institute, Dr. Manisha Banerjee, Dr. Keya Bose, Dr. Manjusha Sinha Bera, Dr. Ajita Sen Gupta, Dr. Santa Bandopadhyay, Dr. Srirupa Das Gupta, and Dr. Ranta Koley of Bethune College, Dr. Salil Kumar Biswas, Dr. Sudipta Bandyopadhyay, Dr. Debnarayan Jana, Dr. Aritra Banerjee, and Dr. Biswajit Ray of Rajabazar Science College who motivated me to study physics and carry out research work.

I must name some of my very influential friend, philosopher, and guide who paved my life towards success and was a great source of strength: Mr. Pratik Tarafdar, Mr. Abir Sarkar, Mr. Abhishek Dey, Dr. Biswajit Guchhait, Dr. Anupam Giri, Dr. Satya Prakash Pati, and Dr. Bipul Das. Without their guidance, help, and support my dream of pursuing PhD would have never been realized. I also thank my school, college, university friends (Anindita, Debasmita, Dipanwita, Prabrisa, Paramita, Tanushree, Ziaul, Snehasish, Rabindranath, Manabendra, and Shreyasi) and some of my childhood friends (Debadrita, Suchandra, Sukannya, Ruchi, Sneha, and Shomi) for their colourful company.

Finally, I express my intense gratitude to my beloved parents (Mrs. Swapna Rakshit and Mr. Chinmoy Rakshit), for their sacrifice, moral support, inspiration, affection, love, and guidance. They are my best teachers. I thank my elder sisters (Mrs. Barnali Basu, Mrs. Sonali Modak), and elder brothers (Mr. Jyotirmoy Rakshit, Mr. Abhijit Basu, Mr. Rungshit Modak) for their cheerful company and strong support in all difficult moments of my life. They always ignore my irresponsible and uninvolved behaviour and boost me to work hard with dedication. My sweet niece Sanjana Basu also deserves mention for adding vital colours to my life. I am blessed to have enjoyable company of my aunts (Ashima Masi, Archana Masi, Manju Pisi, Arati Pisi, Mantu Pisi, Mejho Mami, Sejho Mami, and Sila Mami), uncles (Mejho Mama, Muni Mama, Saikat Mama, Anjan Meso, Amolesh Meso, Prasanta Pisa, and Sankar Pisa) and cousins, specially Bapi Da, Mini Di, Babu Da, Bappa Da, Papai, Tupai, Rumi Di, Buri Di, Pinka Da, Rimi, Soumi, and Babu for being extremely supportive.

Rupali Rakshit
Rupali Rakshit

Publications

1. **R. Rakshit**; M. Mandal; M. Pal; K. Mandal,
“Tuning of magnetic properties of CoFe₂O₄ nanoparticles through charge transfer effect”
Applied Physics Letters, **2014**, *104*, 092412.
2. **R. Rakshit**; M. Pal; M. Mandal; K. Mandal,
“Charge transfer mediated magnetic response of cobalt ferrite nanoparticles”
Materials Letters, **2015**, *151*, 64.
3. **R. Rakshit**; D. Sarkar; M. Pal; K. Serita; M. Tonouchi; K. Mandal,
“Acoustic vibration induced high electromagnetic responses of Fe₃O₄ nano-hollow spheres in THz regime”
Journal of Physics D: Applied Physics, **2015**, *48*, 245301.
4. **R. Rakshit**; M. Pal; A. Chaudhuri; M. Mandal; K. Mandal,
“Facile synthesis of CoFe₂O₄ nano-hollow spheres for efficient bilirubin adsorption”
APL Materials, **2015**, *3*, 110701.
5. **R. Rakshit**; M. Pal; K. Mandal,
“Terahertz conductivity study of magnetite nanostructures”
AIP Conference Proceedings, **2015**, *1665*, 050007.
6. **R. Rakshit**; M. Pal; K. Serita; A. Chaudhuri; M. Tonouchi; K. Mandal,
“Evaluation of SiO₂@CoFe₂O₄ nano-hollow spheres through THz pulses”
AIP Conference Proceedings, **2016**, *1728*, 020084.
7. M. Pal; **R. Rakshit**; K. Mandal,
“Surface modification of MnFe₂O₄ nanoparticles to impart intrinsic multiple fluorescence and novel photocatalytic properties”
ACS Applied Materials and Interfaces, **2014**, *6*, 4903.

-
8. M. Pal; R. Rakshit; K. Mandal,
“Facile functionalization of Fe₂O₃ nanoparticles to induce inherent photoluminescence and excellent photocatalytic activity”
Applied Physics Letters, **2014**, *104*, 233110.
 9. M. Pal; A. K. Singh, R. Rakshit; K. Mandal,
“Surface chemistry modulated introduction of multifunctionality within Co₃O₄ nanocubes”
RSC Advances, **2015**, *5*, 16311.
 10. M. Pal; A. Kundu, R. Rakshit; K. Mandal,
“Ligand induced evolution of intrinsic fluorescence and catalytic activity from cobalt ferrite nanoparticles”
ChemPhysChem, **2015**, *16*, 1627.
 11. M. Pal; R. Rakshit; M. Mandal, K. Mandal,
“Surface modification of α -Fe₂O₃ nanoparticles to develop as intrinsic photoluminescent probe and unprecedented photocatalyst”
Magnetics, IEEE Transactions on, **2014**, *50*, 1.
 12. D. Sarkar; A. Ghosh; R. Rakshit; K. Mandal,
“Magnetic properties of Fe₃O₄ nano-hollow spheres”
Journal of Magnetism and Magnetic Materials, **2015**, 393,192.
 13. M. Pal; R. Rakshit; A. K. Singh; ; K. Mandal,
“Ultra high supercapacitance for ultrasmall Co₃O₄ nanocubes”
Energy, **2016**, *103*, 481.
 14. R. Rakshit; K. Serita; M.Tonouchi; K. Mandal,
“THz conductivity of semi-metallic CoFe₂O₄ nanostructures through thermally activated Polaron”
Manuscript under review.

-
15. ***R. Rakshit***; M. Pal; K. Serita; M. Tonouchi; K. Mandal,
“Facile solvothermal synthesis of MnFe₂O₄ nano-hollow spheres for evaluation through THz Pulses.”
Manuscript under review.
16. ***R. Rakshit***; E. Khatun; M. Pal; S. Talukdar; K. Mandal,
“Effect of functional group of dye on adsorption of CoFe₂O₄ nano-hollow spheres.”
Manuscript under review.

Contents

	Page
Acronyms	I
Table of Symbols	II-III
Chapter 1: Introduction	
Detail Literature Review & Outline of Thesis	1-55
1.1. Nanomaterials	1-2
1.2. Transition Metal Oxide Based Magnetic Nanomaterials	3-6
1.3. Crystal Structure	6-7
1.3.1. Normal Spinel Ferrite	7
1.3.2. Mixed Spinel Ferrite	7
1.3.3. Inverse Spinel Ferrite	7
1.4. Surface Modification of Nanomaterials	7-10
1.4.1. Ligand Field Theory	8-9
1.4.2. Spectrochemical Series	9
1.4.3. Ligand-Metal & Metal-Ligand Charge Transfer	9-10
1.5. Magnetic Properties of Nanomaterials	10-16
1.5.1. Magnetic Anisotropy	11-13
1.5.1.1. Magnetocrystalline Anisotropy	12
1.5.1.2. Shape Anisotropy	13
1.5.2. Surface Anisotropy	13
1.5.3. Magnetic Domain Theory	13-15

1.5.4. Saturation Magnetization	15
1.5.5. Hysteresis	15-16
1.6. Terahertz Electromagnetic Interaction with Nanomaterials	16-33
1.6.1. Terahertz Wave in Matter	16-27
1.6.1.1. The Wave Equation	17-20
1.6.1.2. Transfer Functions: Fresnel Equation	20-24
1.6.1.3. Extraction of Material Parameters	24-27
1.6.2. Terahertz Radiation & Elementary Excitation	27-30
1.6.3. Terahertz Shielding & Mechanism	30-33
1.6.3.1. Reflection	31
1.6.3.2. Multiple Reflections	31-32
1.6.3.3. Absorption	32
1.6.3.4. Transmission	32-33
1.7. Terahertz Conductivity of Nanomaterials	33-39
1.7.1. Terahertz Conductivity of Matters	34-35
1.7.2. Terahertz Conductivity Models	35-39
1.7.2.1. Drude Model	36
1.7.2.2. Drude-Lorentz Model	36-37
1.7.2.3. Drude-Smith Model	37-38
1.7.2.4. Hopping Model	39
1.8. Adsorption Activity of Nanomaterials	40-43
1.8.1. Kinetics of Adsorption	41-42
1.8.2. Equilibrium Modelling	42-43

1.9. Motivation & Objective of Thesis	43-46
1.10. Organization of Thesis	46-47
Bibliography	48-55
Chapter 2: Experimental Details	
2. Material Synthesis & Characterization	56-88
2.1. Preamble	56
2.2. Synthesis of Nanoparticles	56-57
2.2.1. Top-Down Approach	57
2.2.2. Bottom-Up Approach	57
2.3. Formation of Nanoparticles in Wet Chemical Methods	58-60
2.4. Wet Chemical Synthesis of Nanostructures	60-65
2.4.1. Micelle Assisted Co-precipitation Method	61-62
2.4.2. Solvothermal Method	62-64
2.4.3. Stöber Method	64-65
2.5. Phase & Morphology Characterization Techniques	66-77
2.5.1. X-Ray Diffractometer	66-67
2.5.2. Electron Microscopes	67-71
2.5.2.1. Scanning Electron Microscope	67-69
2.5.2.2. Transmission Electron Microscope	69-71
2.5.3. Atomic & Magnetic Force Microscope	71-72
2.5.4. Mössbauer Spectroscopy	73-77
2.5.4.1. Mössbauer Parameters	75-77
2.5.4.1.1. Isomer Shift	75-76

2.5.4.1.2. Quadrupole Splitting	76
2.5.4.1.3. Magnetic Hyperfine Splitting	76-77
2.6. Thermo-Analytical Characterization Methods	77-78
2.6.1. Differential Thermal Device	77-78
2.7. Optical Characterization Techniques	78-83
2.7.1. UV-Visible Absorption Spectroscopy	78-79
2.7.2. Fourier Transformed Infrared Spectroscopy	79-80
2.7.3. Terahertz-Time Domain Spectroscopy	80-83
2.8. Magnetic Characterization Techniques	83-86
2.8.1. Vibrating Sample Magnetometer	83-84
2.8.2. Superconducting Quantum Interference Device	84-85
Bibliography	86-87

Chapter 3: Synthesis of Ionic Surfactant Coordinated CoFe₂O₄ Nanoparticles For Magnetic Characterization

3. Tuning of Magnetic Response of CoFe₂O₄ Nanoparticles Through Ionic Surfactants	88- 99
3.1. Preamble	88-90
3.2. Experimental Section	90-91
3.2.1. Material Used	90
3.2.2. Synthesis of Surfactant Coordinated CoFe ₂ O ₄ Nanoparticles	90-91
3.3. Result & Discussions	91-96
3.4. Conclusion	96-97

Bibliography 98-99

Chapter 4: Synthesis of Non-ionic Surfactant Coordinated CoFe_2O_4 Nanoparticles For Magnetic Characterization

4. Tuning of Magnetic Response of CoFe_2O_4 Nanoparticles Through Non-ionic Surfactants 100- 108

4.1. Preamble 100-101

4.2. Experimental Section 101-102

4.2.1. Material Used 101

4.2.2. Synthesis of Surfactant Coordinated CoFe_2O_4 Nanoparticles 101-102

4.3. Result & Discussions 102-106

4.4. Conclusion 106-107

Bibliography 108

Chapter 5: Morphology & Size Dependent Magnetic Responses of MFe_2O_4 (M= Fe, Co, & Mn) & SiO_2 Coated MFe_2O_4 Nanostructures

5. Morphology & Size Dependent Magnetic Response of MFe_2O_4 (M= Fe, Co, & Mn) & SiO_2 Coated MFe_2O_4 Nanomaterials 109-133

5.1. Preamble 109-110

5.2. Experimental Section 110-114

5.2.1. Material Used 110

5.2.2. Synthesis of MFe_2O_4 (M= Fe, Co, & Mn) Nanoparticles & Nano hollow spheres 111-113

5.2.3. Synthesis of SiO ₂ coated MFe ₂ O ₄ (M= Fe, Co, & Mn) Nanoparticles & Nano hollow spheres	114
5.3. Result & Discussions	114-131
5.4. Conclusion	131
Bibliography	132-133
Chapter 6: High Frequency Electromagnetic Responses of MFe₂O₄ (M= Fe & Co) Nanostructures in Terahertz Region	
6. Morphology & Size Dependent Electromagnetic Response of MFe₂O₄ (M=Fe & Co) Nanostructures in Terahertz Region	134-166
6.1. Preamble	134-135
6.2. Experimental Section	136
6.2.1. Material Used	136
6.2.2. Synthesis of MFe ₂ O ₄ (M= Fe, Co, & Mn) Nanoparticles & Nano hollow spheres	136
6.3. Result & Discussions	136-152
6.4. Conclusion	152
Bibliography	153-155
Appendix	156-166
Chapter 7: Biomedical Application of CoFe₂O₄ & SiO₂ Coated CoFe₂O₄ Nano hollow spheres Through Bilirubin Adsorption	
7. Excellent Bilirubin Adsorption of CoFe₂O₄ & SiO₂ Coated CoFe₂O₄ Nanoparticles & Nano hollow spheres	167-179

7.1. Preamble	167-168
7.2. Experimental Section	168-169
7.2.1. Synthesis of CoFe_2O_4 & SiO_2 coated CoFe_2O_4 Nanoparticles & Nano hollow spheres	168-169
7.2.2. Adsorption Study	169
7.3. Result & Discussions	169-175
7.4. Conclusion	175-176
Bibliography	177-178

Chapter 8: Environmental Application of CoFe_2O_4 Nano hollow spheres Through Dye Adsorption

8. Effect of Functional Group of Dye on Adsorption Property of CoFe_2O_4 Nano hollow spheres	179-188
8.1. Preamble	179-180
8.2. Experimental Section	180-181
8.2.1. Synthesis of CoFe_2O_4 Nano hollow spheres	180
8.2.2. Adsorption Study	180-181
8.3. Result & Discussions	181-186
8.4. Conclusion	187
Bibliography	188

Chapter 9: Conclusion & Scope for Future Work

9.1. Epilogue	189-190
9.2. Scope for Future Work	190-191

Acronyms

NSs: Nanostructures

NMs: Nanomaterials

NPs: Nanoparticles

NHSs: Nano hollow spheres

SD: Single domain

MD: Multi-domain

PSD: Pseudo-domain

SPM: Superparamagnetic

LFT: Ligand field theory

LMCT: Ligand-metal charge transfer

MLCT: Metal-ligand charge transfer

CFSE: Crystal field splitting energy

XRD: X-ray diffraction

FESEM: Field emission scanning electron microscope

TEM: Transmission electron microscope

HRTEM: High resolution transmission electron microscope

EDX: Energy dispersive X-ray

SAED: Selected area electron diffraction

AFM: Atomic force microscopy

MFM: Magnetic force microscopy

DTA: Differential thermal analysis

EM: Electromagnetic

THz: Terahertz

THz-TDS: THz-time domain spectroscopy

PCA: Photoconductive antenna

PPLN: Periodically poled LiNbO₃

DC: Direct current

AC: Alternating current

VSM: Vibrating sample magnetometer

SQUID: Superconducting quantum interference device

Table of Symbols

M_s : Saturation magnetization
M_r : Remanence
H_c : Coercivity
χ : Susceptibility
t_N : Néel relaxation time
t_B : Brown relaxation time
T_B : Blocking temperature
T_c : Curie temperature
E_A : Magnetocrystalline anisotropy energy
K : Magnetocrystalline anisotropy constants
D : Diameter
V : Volume
L : Length
A : Area
V : Voltage
I : Current
l : Mean free path
eV: Electron volt
k_B : Boltzmann constant
T : Temperature
I : Intensity of light
A : Absorbance
E : Electric field
B : Magnetic field
Φ_0 : Flux
F : Force
H : Magnetic field strength
D : Electric displacement
P : Polarization
M : Magnetization

ρ_f : Free charge density

J_f : Free current density

ϵ : Electric permittivity

ϵ_0 : Free space permittivity

ϵ : Molar extinction coefficient

μ : Magnetic permeability

μ_0 : Free space permeability

σ : Electric conductivity

\tilde{n} : Refractive index

n : Ordinary refractive index

κ : Extinction co-efficient

v : Velocity

c : Velocity of light in free space

k : Wave vector

ω : Angular frequency

λ : Wavelength

\tilde{r} : Amplitude reflection coefficient

\tilde{t} : Amplitude transmission coefficient

α_{abs} : Absorption co-efficient

m : Mass

m^* : Effective mass

q : Charge

C : Concentration

q : Amount of adsorbate adsorbed per unit mass of adsorbent

τ : Scattering time

f : Volume fill fraction

g : Geometrical factor

\tilde{t} : Transmission co-efficient

\tilde{r} : Reflection co-efficient

Chapter 1 | Introduction

This introductory chapter consists of the detailed literature review of various works that motivated to work in this specific field. In addition, it contains a brief outline of the entire work, and the theoretical aspects that helps to explain the findings.

1.1. Nanomaterials

Nanomaterials (NMs) are of great excitement to the researchers due to evolution of new phenomena and significant improvement of various properties as compared to their bulk counterpart. NMs are usually defined to have at least one dimension within the range of 1-100 nm (1 nm = 10^{-9} m). Due to large surface area to volume ratio and quantum confinement, NMs interact with each other, surrounding substances, light, electric, and magnetic field in different way. A graphical presentation of the variation of percentage of surface atoms with diameter of the particles in the nanometer size regime is shown in Figure 1.1 (a). Since the atoms at surfaces have fewer neighbors in NMs, they are co-ordinatively unsaturated which lead to decrease in their stabilization in contrast to the atoms present at bulk. The density of states ($D(E)$) of electrons in the material also changes from a continuous function ($D(E) \propto E^{1/2}$) to discontinuous delta function as it moves from bulk to nanoscale as shown in Figure 1.1 (b). It leads to constrain the movement of electrons within an infinite potential well of extremely small particles as well as affects the macroscopic properties of the NMs, giving rise to a wide variety of new phenomena. It is obvious that when the size of NMs becomes comparable to or less than certain characteristics length scales such as carrier mean free path, superconducting coherence length, magnetic domain wall width, spin diffusion length etc, there arises some novel properties¹ which are absent in their bulk counterparts.

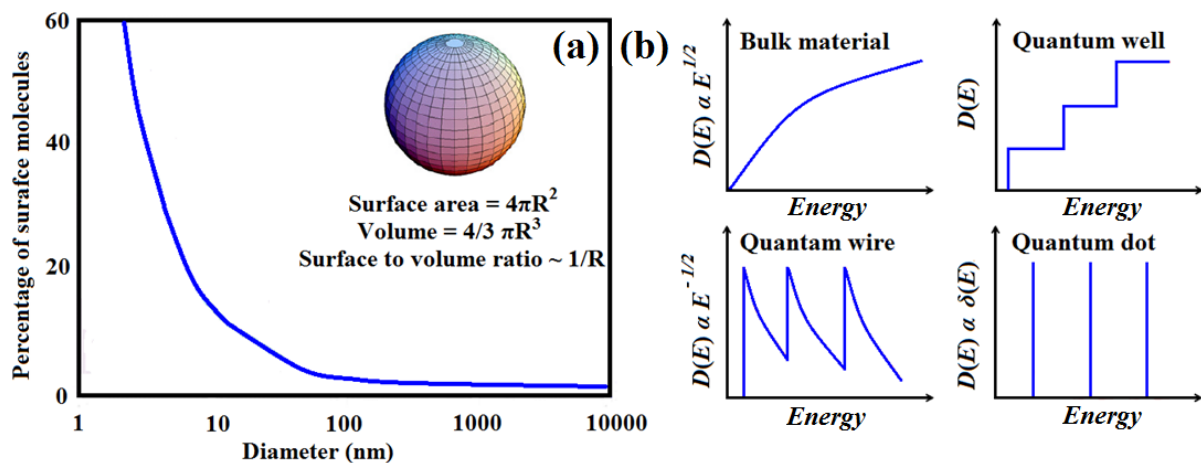


Figure 1.1. (a) A graphical presentation showing the variation of percentage of surface atoms with diameter of nanoparticles. (b) Change in density of states of electron in NMs with reducing size: starting from bulk to quantum well to quantum wire to quantum dot.

Chemical reactivity, optical property, electronic excitation, conductivity etc. of metal or semiconductors nanoparticles (NPs) are found to be influenced significantly by their size. It has been observed that with reduction of size, the metals show non-metallic band gaps and thus showing electronic absorption spectra.² The clusters of non-magnetic bulk materials are also found to exhibit magnetic ordering at nano level which leads to giant magnetoresistance, enhanced coercivity (H_c), remanence (M_r), and many other properties of magnetic materials.³ Cox and his co-workers found that bare rhodium clusters display non-zero magnetic moment for less than 60 atoms in it, which is an indication of either ferromagnetic or ferrimagnetic ordering even though the bulk rhodium is Pauli paramagnet at all temperature.⁴

The novel properties of NMs can also be tailored by manipulating the self-assembly and self-organizing techniques of their nanoscale building blocks.¹ It has been found that NMs having building blocks with same composition but different morphology like sphere, cube, disc, rod, wire, tube, film, etc exhibit different properties.^{5,6} Among all the nanostructures (NSs), in last few years, researchers are very much interested in fabricating nano hollow spheres (NHSs) because of its hollow interior which enhances its effective surface area. These hollow structures have several applications such as in catalysis, controlled delivery, light fillers, artificial cells, low dielectric constant materials, radar absorbing materials, photonic crystals, high density magnetic storage, spintronics device etc.⁷⁻¹² Large void space of NHSs can be used to encapsulate drugs, cosmetics, and DNA and also for their controlled release. In addition, they have low density due to hollow interior and large effective surface area which help to expand the array of imaging markers that are very suitable for revelation of cancer at an early stage.¹³ Till now, NMs have been synthesized with large chemical diversity, consisting metals,¹⁴ metal oxides,¹⁵ semiconductors,^{16,17} polymers,¹⁸ and carbonaceous materials.^{19,20} Having novel optical, magnetic, thermal, electrochemical, electrical properties, these NMs have become promising candidate to solve challenges in the field of medicine,^{21,22} energy storage,^{23,24} catalysis,²⁵⁻²⁷ sensing,²⁸ and information technology.²⁹

1.2. Transition Metal Oxide Based Magnetic Nanomaterials

Unique properties of magnetic NMs such as magnetocrystalline anisotropy, magnetostriction, saturation magnetization (M_s), relaxation times (Neel relaxation time, t_N , Brown relaxation time, t_B), and blocking temperature (T_B) as shown in Figure 1.2 raise the interest of the researchers towards this field. In addition, the magnetic NMs are found to possess a number of unusual properties– giant magnetoresistance, abnormally high magnetocaloric effect, and so on. 3d transition metal oxide based magnetic NMs such as magnetite (Fe_3O_4), manganese ferrite (MnFe_2O_4), cobalt ferrite (CoFe_2O_4) have attracted tremendous attention in contrast to 4f transition metal based magnetic alloys such as Nd-B-Fe and Sm-Co due to their low cost, easy synthesis procedures, high chemical and mechanical stability, non-toxicity, and high Curie temperature (T_c). A long term research finds immense applications of those ferrite NMs in different biomedical and technological fields such as biosensor, bio-separation, molecular imaging, hyperthermia, catalysis, information storage, electromagnetic (EM) interference shielding due to their superior magnetic, optical, electronic, catalytic, and EM properties.³⁰⁻³⁶ In biosensing, bio-separation, molecular imaging, NPs with higher M_s are preferred because they provide higher sensitivity and efficiency whereas in information storage, NPs with higher H_c are required. The necessity of precise magnetic property required for specific application leads to the concept of tuning the magnetic properties of NMs.

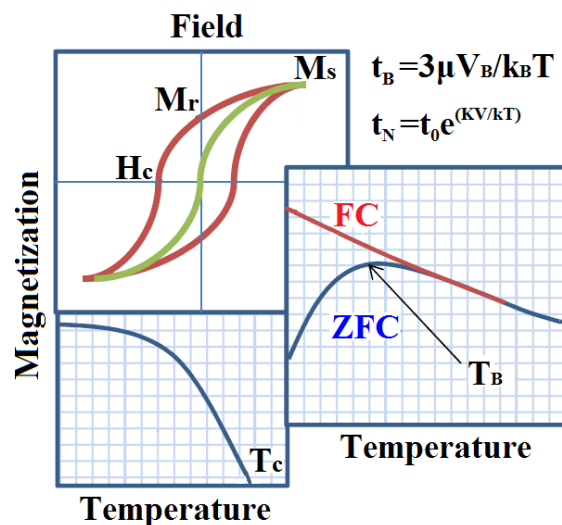


Figure 1.2. The properties of magnetic NMs.

The magnetic properties of NMs are determined by many factors, the key of these includes the chemical composition, type, and the degree of defectiveness of crystal lattice, particle size, shape, morphology, interaction of the particle with the surrounding matrix and the neighbouring particles. Dependence of M_s and H_c on the size of the magnetic NMs is shown in Figure 1.3 (a) and (b). It is found that M_s varies proportionally with size until it reaches a threshold size beyond which it is constant and is close to the bulk value whereas H_c changes in a different way. For larger crystals, H_c increases with decreasing particle size and below a critical diameter (D_c), the particles become single domain (SD). At this critical state, H_c reaches its maximum value. Further decrease in size of NPs reduces H_c and the particles reach a superparamagnetic (SPM) state where H_c is zero. Therefore, a long term efforts have been concentrated in enhancing the magnetic properties of NMs which have diameter above and below D_c .

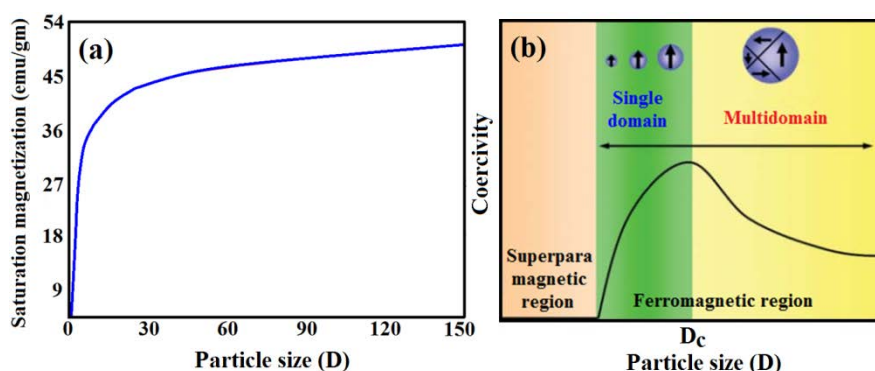


Figure 1.3. Variation in (a) M_s , and (b) H_c of magnetic NMs with size.

Co and his co-workers have shown enhanced M_s (~ 81 emu/gm) of sulfur doped coral-like CoFe_2O_4 NPs with average sizes of about 90-100 nm.³⁷ Skoropata et al.³⁸ have shown that CoO coated $\gamma\text{-Fe}_2\text{O}_3$ core-shell NPs of average size of 7.9 nm exhibit higher H_c (~ 0.298 T) in contrast to its bare configuration with H_c of the order of 0.03 T. They explained that enhanced H_c originates due to migration of shell ions, e.g., Co^{2+} , into the octahedral site vacancies of surface layers of $\gamma\text{-Fe}_2\text{O}_3$ core. Pal and his co-workers³⁹ have been able to prepare micelle coated CoFe_2O_4 NPs of diameter 16 nm which show enhanced H_c in contrast to its bare configuration. Therefore, a thorough research has been concentrated on the size, morphology, core-shelling, and functionalization dependent physical, chemical, and magnetic properties of

different magnetic NSs including nanorods, nanowires, nanotubes, tiles, blocks, flowers so as to enhance their magnetic properties.

In addition, magnetic property is also found to play a crucial role in determining the EM absorption properties of NMs. 3d-transition metal oxide based magnetic NMs for example; Fe_3O_4 is a well known shielding material due to their very high permeability which provides large number of magnetic dipoles for absorbing EM waves. For absorption to occur, a shielding material should possess electric and/or magnetic dipoles to interact with EM field. The dipoles present in the shield destroy the electric field of EM waves by converting it into heat. Since electric dipoles essentially originate from the electronic, ionic, and intrinsic electric dipole polarization of the material on which the crystal structure, size, and geometrical morphology have an extensive impact,⁴⁰ the permittivity of the ferrite NSs can be enhanced by tailoring their physical properties. Along with all these criteria, a good shielding material should also possess high surface to volume ratio and high surface resistivity for better absorption loss.

Tong and his co-workers⁴¹ have investigated the morphology dependent static magnetic and microwave EM characteristics of Fe_3O_4 NMs. They have shown that compared to Fe_3O_4 nanospheres and urchins, enhanced M_s and H_c were observed in case of Fe_3O_4 sponge, composed of ordered nanofibers which lead to enhanced microwave absorption. Li et al.⁴² have shown excellent microwave absorption of porous flower like structure of Fe_3O_4 NSs. Du et al.⁴³ have investigated shell thickness dependent microwave absorption of core-shell $\text{Fe}_3\text{O}_4@\text{C}$ NSs. They have found that the coating of Fe_3O_4 microspheres with carbon shells will not only increase the complex permittivity but also improve characteristic impedance, leading to multiple relaxation processes in these composites, thus greatly improve their microwave absorption. Very interestingly, they have been able to find a critical thickness of carbon shells which leads to an unusual dielectric behaviour, endowing a strong reflection loss in the high frequency range. Li and his co-workers also found that Fe_3O_4 NSs densely coated with Ni-B alloy exhibit better absorption performance

than pure Fe_3O_4 in the range of 2–18 GHz with more powerful absorbing capability and a wider EM wave absorbing frequency band.⁴⁴

1.3. Crystal Structure

3d transition metal oxide based magnetic NMs, spinel ferrites are a class of compounds of general formula MFe_2O_4 (M= Mn, Co, Fe, and so on). The spinel structure belongs to space group $\text{Fd}\bar{3}\text{m}$. The cubic unit cell is formed by 56 atoms, 32 oxygen anions distributed in a cubic close packed structure, and 24 cations occupying 8 of the 64 available tetrahedral sites (A sites) and 16 of the 32 available octahedral sites (B sites) as shown in Figure 1.4.⁴⁵ The structural formula for a generic spinel compound MFe_2O_4 can be written as⁴⁶



where the amounts in brackets represent the average occupancy of A sites and B sites and i is the inversion parameter. Depending on cation distribution, a spinel can be normal, inverse, and mixed. In a normal spinel structure, 8 bivalent cations are all located in tetrahedral sites and 16 trivalent cations are all located in octahedral sites, while, in an inverse spinel structure, 8 bivalent cations occupy 8 octahedral sites and 16 trivalent cations are distributed between 8 tetrahedral and 8 octahedral sites.⁴⁷ For a normal spinel, $i=0$, and for an inverted spinel, $i=1$. If the bivalent cations are present on both tetrahedral and octahedral sites, the spinel is mixed and $0 < i < 1$.

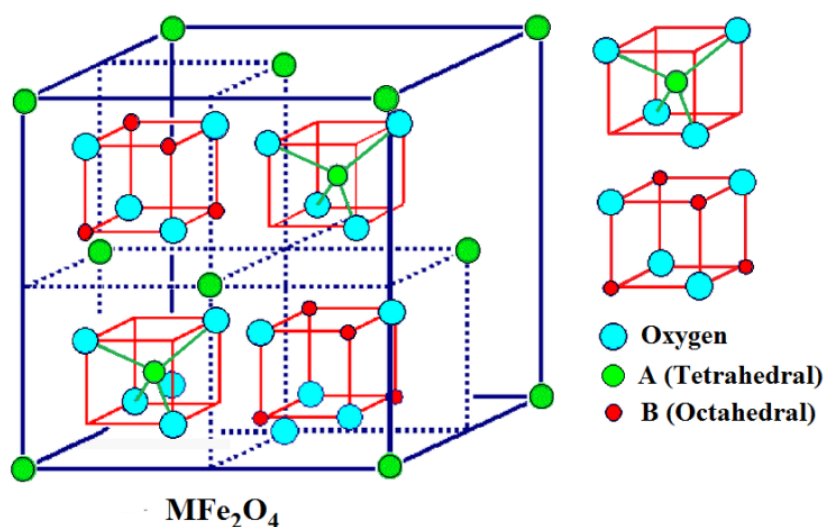


Figure 1.4. Crystal structure of MFe_2O_4 . (© chemwiki.ucdavis.edu)

1.3.1. Normal Spinel Ferrite

Normal spinel structure, where all M^{2+} occupy A sites and the structural formula of such ferrite is $M^{2+}[Fe_2^{3+}]O_4^{2-}$. This type of distribution takes place in zinc ferrites $Zn^{2+}[Fe^{2+}Fe^{3+}]O_4^{2-}$. This type spinel ferrite is schematically illustrated in Figure 1.5 (a).

1.3.2. Mixed Spinel Ferrite

Mixed spinel structure, when cations M^{2+} and Fe^{3+} occupy both A and B positions and the structural formula of this ferrite is $M_{(1-i)}^{2+}Fe_i^{3+}[M_i^{2+}Fe_{(2-i)}^{3+}]O_4^{2-}$, where i is the degree of inversion. $MnFe_2O_4$ represent this type of structure and has an inversion degree of $i=0.2$ and its structural formula therefore is $Mn_{0.8}^{2+}Fe_{0.2}^{3+}[Mn_{0.2}^{2+}Fe_{1.8}^{3+}]O_4^{2-}$.⁴⁸ This spinel ferrite is schematically illustrated in Figure 1.5 (b).

1.3.3. Inverse Spinel Ferrite

Inverse spinel structure, where all M^{2+} are in B-positions and Fe^{3+} are equally distributed between A and B-sites: the structural formula of these ferrites are $Fe^{3+}[M^{2+}Fe^{3+}]O_4^{2-}$. Fe_3O_4 , $CoFe_2O_4$, and $NiFe_2O_4$ have inversed spinel structure.⁴⁸ In the inversed ferrites, one half of Fe^{3+} is placed in A-sites and another half in B-sites. Their magnetic moments are mutually compensated and the resulting moment is due to the magnetic moments of M^{2+} in the B-positions. This type spinel ferrite is schematically illustrated in Figure 1.5 (c).

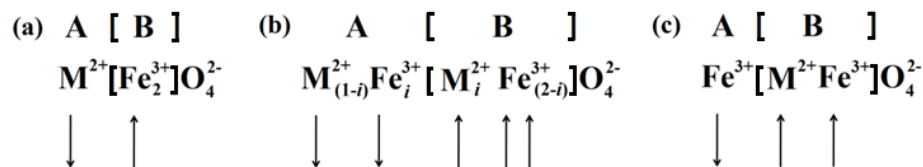


Figure 1.5. Cations distribution in (a) normal, (b) mixed, (c) inverse spinel ferrites.

1.4. Surface Functionalization of Nanomaterials

Surface functionalization of NMs is necessary to tune their optical, magnetic, catalytic and electrochemical properties to suit different applications in the field of nanotechnology. It is carried out for various purposes, firstly synthesis of NSs,

generally, involves surfactant molecules which have head as well as tail groups that bind to the NP surface to stabilize the nuclei and prevent aggregation through repulsive force, as well as control the growth of NPs in terms of rate, final size or geometric shape. Secondly, NPs can be functionalized with suitable ligands so that, they can be dispersed in either aqueous or organic solvent due to hydrophilic or hydrophobic behavior, respectively.⁴⁹ Polar ligand molecules (citric, tartaric, glucose, etc) provide solubility in polar or aqueous solvents.⁵⁰ Moreover, NPs functionalized by special groups (e.g. -OH, -COOH, -NH₂, -SH) are suitable for attachment of different bioactive molecules for their various biomedical applications. In addition, some inorganic materials such as silica, Au, metal oxides etc also help in binding various biological ligands to the NP surface.

1.4.1. Ligand Field Theory

The surface of the NPs contains numerous uncompensated coordination spheres due to broken bonds. Metal ions residing within those uncompensated coordination spheres form complexes with the ligands upon functionalization, resulting completely new optical, magnetic, catalytic properties.⁵¹ Figure 1.6 (a) shows the orientation of metal *d*-orbitals in octahedral and tetrahedral coordination. Ligand field theory (LFT) resulted from combination of the principles laid out in molecular orbital theory and crystal field theory, describes the loss of degeneracy of metal *d*-orbitals in transition metal complexes.

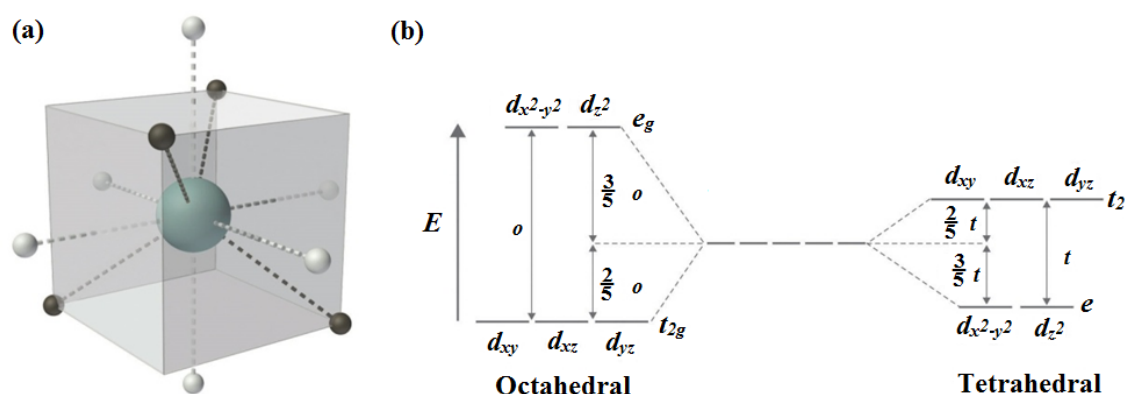


Figure 1.6. (a) White and black spheres indicate orientation of metal *d*-orbitals in octahedral and tetrahedral coordination spheres, respectively, (b) Energy splitting of *d*-orbitals in octahedral and tetrahedral field.

Metal d -orbitals split in the following fashion as shown in the Figure 1.6 (b). In octahedral field, ligands approach from the direction of axes resulting in destabilization of the orbitals along the axes ($d_{x^2-y^2}$ and d_z^2), and stabilization of the orbitals lying in between the axes (d_{xy} , d_{yz} , d_{xz}). In case of tetrahedral field, d_{xy} , d_{yz} , d_{xz} orbitals are nearer to the direction of approach of the ligands than the $d_{x^2-y^2}$ and d_z^2 orbitals, so the inverse arrangement is observed.⁵²

1.4.2. Spectrochemical Series

The splitting of d -orbitals (Δ =crystal field splitting energy, CFSE) primarily depends on type of ligands, metal ions (CFSE increases down the group) and charge over metal ions (CFSE increases with increasing oxidation number). A spectrochemical series is a list of ligands arranged on the basis of ligand strength and a list of metal ions based on oxidation number, group, and its nature as shown in Figure 1.7.⁵²

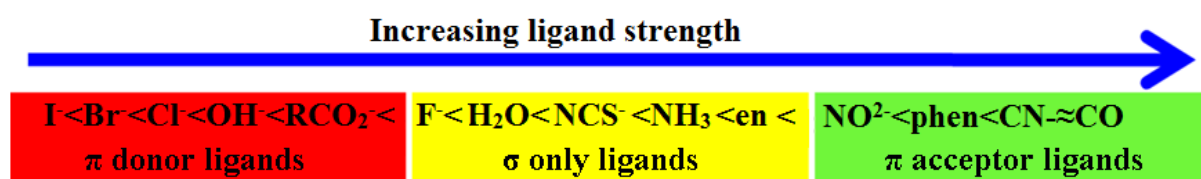


Figure 1.7. Spectrochemical series of various ligands in the increasing order of ligand strength.

π donor ligands having occupied p orbitals tend to donate π electrons to the metal ions along with the σ bonding electrons, exhibiting stronger metal-ligand interactions and an effective decrease of CFSE. π acceptor ligands having vacant π^* with comparable energy to metal d -orbitals, can undergo π back bonding, resulting in increase of CFSE. The metal ions can also be arranged in order of increasing CFSE, as $Mn^{2+} < Ni^{2+} < Co^{2+} < Fe^{2+} < V^{2+} < Fe^{3+} < Cr^{3+} < V^{3+} < Co^{3+}$.

1.4.3. Ligand-Metal & Metal-Ligand Charge Transfer

Ligands possess σ , σ^* , π , π^* , and nonbonding molecular orbitals. If the ligand molecular orbitals are full, charge transfer may occur from the ligand molecular orbitals to the empty or partially filled metal d -orbitals. The absorptions that arise

from this process are called ligand-metal charge transfer (LMCT) transitions as shown in Figure 1.8. LMCT transitions result in intense bands.⁵²

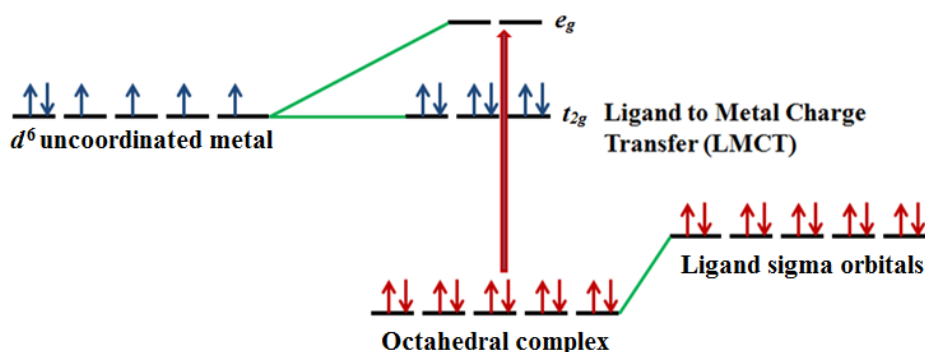


Figure 1.8. LMCT involving an octahedral d^6 complex.

If the metal is in a low oxidation state (electron rich) and the ligand possesses low lying empty orbitals (e.g., CO or CN^- having π^* orbitals), then a metal-ligand charge transfer (MLCT) transition may occur. MLCT transitions are common for coordination compounds having π -acceptor ligands. Upon absorption of light, electrons in the metal orbitals are excited to the ligand π^* orbitals. Figure 1.9 illustrates the metal to ligand charge transfer in a d^5 octahedral complex. MLCT transitions result in intense bands.⁵²

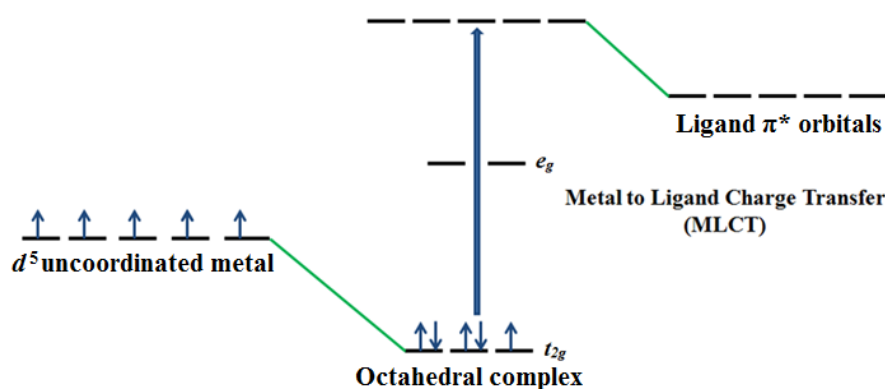


Figure 1.9. MLCT involving an octahedral d^5 complex.

1.5. Magnetic Properties of Nanomaterials

In cubic spinel structure, ions on octahedral sites interact directly with each other and their spins are aligned in parallel direction. They also interact with those on tetrahedral sites but in this case, they interact through the oxygen ions and the spins are aligned in antiparallel direction through super exchange interaction. In inverse spinel ferrites, MFe_2O_4 (where M^{2+} = divalent ions of Fe, Co, Ni), the Fe^{3+}

ions on tetrahedral sites are aligned antiparallel to those on octahedral sites, so that there is no net magnetization from these ions. M^{2+} ions having unpaired electrons, tend to align their spins parallel with those of Fe^{3+} ions on adjacent octahedral sites, and hence with those of other M^{2+} ions. This produces a resultant ferromagnetic interaction for those ferrites where M^{2+} ions have unpaired electrons.

Two key issues dominate the magnetic properties of NMs are finite size and surface effects which give rise to various special features. Magnetic domains have dimensions within the range of 10-1000 nm which is comparable to the size of nanocrystals. So if the crystal size approaches to the SD dimension upon scaling down the particle size of ferromagnetic material, all the spins get aligned to each other, so the demagnetization becomes difficult. When the particle size becomes smaller than the SD dimension, then the force aligning the spins becomes so weak that it cannot overcome thermal randomization in absence of any external magnetic field. This phenomenon is called superparamagnetism. Generally, the surface anisotropy in NMs is found to be one order of magnitude higher than the bulk value which is due to larger fraction of superficial ions in smaller particles.⁵³ These surface spins are disordered because they reside within an uncompensated coordination sphere due to broken bonds, vacancies, and also due to bond formation with capping organic molecule.⁵⁴ Thus, the surface anisotropy makes the surface layer magnetically harder than the core region of NMs. In addition to surface anisotropy, there exists magnetic anisotropy which is discussed below.

1.5.1. Magnetic Anisotropy

Magnetic anisotropy is the dependence of magnetic energy on the relative orientation of magnetization direction with the crystal axis. The associated energy is called anisotropy energy. In a material, the magnetic anisotropy may arise due to the symmetry of crystalline lattice or due to specific shape of that particular piece of material. In absence of any external magnetic field, there is an energetically favorable direction for spontaneous magnetization, called easy axis of that particular material that can be determined by various magnetic anisotropy energies as given below.

1.5.1.1. Magnetocrystalline Anisotropy

Magnetocrystalline anisotropy is the most prominent contribution to the magnetic anisotropy which arises due to the symmetry axis of local atomic structure. It arises because of spin-orbit coupling which is the exchange interaction via spin-spin coupling between neighboring spins. This strong spin-orbit coupling keeps the neighboring spins to be parallel or anti-parallel to each other. However, the associated energy is isotropic and therefore the coupling cannot contribute to the crystal anisotropy. Magnitude of magnetocrystalline anisotropy depends on the ratio of crystal field energy and spin orbit coupling.⁵⁵ There are two models to describe the magnetic anisotropy; (a) Néel model which says that the magnetic anisotropy arises due to pair interactions between two essentially magnetic ions⁵⁶ and (b) Single-ion or crystal field model which describes crystal field interactions with atoms that are not essentially magnetic.⁵⁷ As the magnetocrystalline energy is associated with the relative orientation of the total magnetization with respect to magnetic easy axis of the crystal, i.e. θ , the magnetocrystalline anisotropy energy can be expressed as,

$$E_A = V(K_0 + K_1 \sin^2 \theta + K_2 \sin^4 \theta) \quad (1.2)$$

where, K_n ($n = 0, 1, 2 \dots$) are the magnetocrystalline anisotropy constants. K_0 is θ independent, arbitrary and thus an irrelevant parameter.

In cubic crystals, like Fe_3O_4 , the magnetocrystalline anisotropy is given by a series expansion in terms of the angles between magnetization direction and cube axes. However, it is sufficient to retain only the first two terms in the series expansion where each of the two terms contains an empirical constants associated with them known as first and second order anisotropy constants (K_1 and K_2 , respectively). In case of hexagonal crystals like $\alpha\text{-Fe}_2\text{O}_3$, magnetization generally lies along the c-axis, which is the direction of anisotropy axis, leading to its antiferromagnetic behavior at lower temperature. Upon significant thermal excitation, these spins can tilt slightly along the basal plane rendering ferromagnetic behavior of the material.

1.5.1.2. Shape Anisotropy

In case of polycrystalline material with no preferred direction of its grains, has no overall crystalline anisotropy. If the material is perfectly spherical in shape, then the external applied field will magnetize it in every possible direction in same extent. However, if the material is not spherical but having a preferred growth direction, then it is easy to magnetize it along the long axis than along the short one. This type of crystalline anisotropy is known as shape anisotropy. In this case, demagnetization field comes into play which actually determines the actual field inside a specimen. For shape anisotropy, $K_1 = \mu_0(1-3D_m)M_s^2/4$, where D_m is the demagnetization factor which is 0 for long cylinders, 1/3 for spheres and 1 for plates.⁵⁸

1.5.2. Surface Anisotropy

Surface anisotropy was first introduced by Néel⁵⁶ in case of materials having complicated structures and morphologies such as monolayer transition metal films, multi-layers, rough surfaces, and especially in smaller particles. Generally, surface anisotropy in NPs is found to be one order of magnitude higher than the bulk value which is due to larger fraction of superficial ions in smaller particles.^{59,60} This surface spins are disordered because they reside within an uncompensated coordination sphere due to broken bonds, vacancies, and also due to bond formation with some organic molecule.⁵⁹ Thus, the surface anisotropy makes the surface layer magnetically harder than the core region of a fine NPs. For a spherical particle the effective anisotropy energy (K_{eff}) can be written as, $K_{eff} = K_b + (6/D)K_s$, where K_b and K_s are the bulk and surface anisotropy energy density, respectively, and D is the diameter of the particle.

1.5.3. Magnetic Domain Theory

Domains constitute the fundamental concept of magnetism in ferromagnetic or ferrimagnetic materials. Each magnetic material consists of small regions, called magnetic domains (having size 1-100's μm) that have uniform magnetization; i.e. the moments in individual domains are aligned in the same direction. These domains

are separated by the domain walls where magnetization must change direction from that in one domain to that in the other one. These domain walls have finite width that is determined by exchange and magnetocrystalline energy. The magnetic behavior can be subdivided into four ranges depending on the grain size.⁶¹

Large sized particles contain multi-domain (MD) configuration. With increasing size, they behave as bulk material. Domain wall nucleation and motion are the main mechanism behind the magnetization reversal of these MD particles. To change the direction of magnetization of a MD grain, the domain wall has to be translated which is an energetically easy process and can be accomplished in relatively low fields. Thus MD grains are magnetically soft with low value of coercivity and remanence. With decrease of grain size, a critical size is reached where the grain cannot accommodate a wall. Below this critical size, the grain contains a SD. An SD grain is uniformly magnetized to its M_s and magnetically hard as characterized by high H_c and M_r because the only way to change the direction of magnetization of a SD grain is to rotate the magnetization which is an energetically difficult process. Thus, SD grains are magnetically hard and have high coercivity and remanence. The distinction between SD and MD is straightforward. However, small MD grains exhibit a mixture of SD-like (high remanence) and MD-like (low coercivity) behavior which are called pseudo-domain (PSD). With further decrease of grain size within SD regime, another critical threshold is reached, below which H_c and M_r becomes zero. In this condition, the grain becomes SPM even when the temperature is below T_c or Néel temperature. In SPM particles, the magnetic relaxation process can be represented by Néel- Arrhenius equation,^{59,62} given as

$$f = f_0 \exp\left(-\frac{KV}{k_B T}\right) \quad (1.3)$$

where, f_0 is the Larmor frequency lying in the range of 10^9 - 10^{12} sec⁻¹, K is the anisotropy constant, V is the particle volume, k_B is Boltzmann constant and T is the absolute temperature. As the size of SPM particles are too small, therefore a small anisotropy energy ($E_A=KV$) allows the magnetization to fluctuate randomly between two energetically favorable ground states (up and down states) upon small thermal

agitation; i.e. they behave paramagnetically, however their magnetization is much higher than the typical paramagnets. Hence the term superparamagnetism, which denotes a much higher susceptibility value as compared to a simple paramagnet. For this type of particles, total magnetic moment at $T > 0$ K and in absence of any magnetic field will average to zero.

1.5.4. Saturation Magnetization

M_s is the maximum possible magnetization of a magnetic material under a large external field. Assuming each atom has the same magnetic moment; M_s is dependent on the magnitude of atomic moment and also density of atoms. M_s of NMs is found to be affected significantly by the size and their synthesis procedure as there is a large fraction of superficial ions in NMs. As it is moved from bulk to nanoscale, M_s decreases which may be due to different reasons. According to Gangopadhyay et al.⁶³ the M_s reduction is due to formation of a disordered nonmagnetic shell layer over the magnetically aligned core in NMs. According to other models this reduction in M_s was due to surface spin canting. Similar argument was given by Parker et al.⁶⁴ where it has been suggested that the spin canting occurs in the whole sample due to quantum size effects. Moreover, for a bulk material where the temperature dependence of M_s is found to follow Bloch's $T^{3/2}$ law, the NPs show a deviation from this $T^{3/2}$ behavior.

1.5.5. Hysteresis

Magnetic hysteresis loop which is a plot of variation of magnetization under applied magnetic field is the most common way to represent the bulk properties of a magnetic material. This hysteresis behavior, i.e. the inability to trace back the same magnetization curve is related to the presence of domains within the material. When these domains are magnetized in one direction, it needs some energy to turn them back again. This property of magnetic materials is very useful for magnetic storage application. Magnetic anisotropy yields easy magnetization directions corresponding to local energy minima and energy barriers that separate the easy directions in a SD particle. On an atomic scale, the barriers are easily overcome by

thermal fluctuations, but on nanoscale or macroscopic length scales excitations are usually too weak to overcome the barriers. This is observed as magnetic hysteresis. The most useful information that one can get from the hysteresis loop is the maximum energy product which is the product of maximum field (H_{\max}) and maximum magnetization (M_{\max}). This is a measure of maximum amount of work that can be performed by magnetic material. H_c is the field that is required to reduce M_r to zero. It is a measure of how strongly a magnetic material can oppose an external magnetic field. M_r is the magnetization of a magnetic material when the field is reduced to zero after its complete magnetization. For SD non-interacting particles, Stoner and Wohlfarth theoretically determined that H_c is related to M_s and K , according to the relation, $H_c=2K/M_s$. It has been found that the order of magnitude of K for NPs is higher than their corresponding bulk values which can be attributed to the exchange interaction at the core-shell interface and/or the magnetoelastic energies caused by stress/pinning induced by the lattice mismatch at the coated surface.^{59,60}

1.6. Terahertz Electromagnetic Interaction with Nanomaterials

EM industries rely heavily upon high performance materials that are designed to support, direct, and absorb EM fields. This can only be achieved with the knowledge of intrinsic dielectric and magnetic properties of the materials involved: typically their complex dielectric permittivity and magnetic permeability, but also related parameters such as anisotropy, susceptibility and H_c of the material.

1.6.1. Terahertz Wave in Matter

Classical EM theory provides a general description of terahertz (THz) waves which propagate in and interact microscopically with the uniform medium. The macroscopic form of Maxwell's equation for describing THz wave is given by,

$$\nabla \cdot \mathbf{D} = \rho_f \quad (1.4)$$

$$\nabla \cdot \mathbf{B} = 0 \quad (1.5)$$

$$\nabla \times \mathbf{E} = -\frac{\partial \mathbf{B}}{\partial t} \quad (1.6)$$

$$\nabla \times \mathbf{B} = \mathbf{J}_f + \frac{\partial \mathbf{D}}{\partial t} \quad (1.7)$$

where \mathbf{E} , \mathbf{B} , \mathbf{D} , ρ_f , and \mathbf{J}_f are the electric field, magnetic field, electric displacement, free charge density, and free current density respectively. The macroscopic field \mathbf{D} and magnetic field strength (\mathbf{H}) are related to the fundamental fields \mathbf{E} and \mathbf{B} as

$$\mathbf{D} = \epsilon_0 \mathbf{E} + \mathbf{P} = \epsilon \mathbf{E} \quad (1.8)$$

$$\mathbf{H} = \frac{1}{\mu_0} \mathbf{B} - \mathbf{M} = \frac{1}{\mu} \mathbf{B} \quad (1.9)$$

where ϵ_0 and μ_0 are the permittivity and permeability of free space. The polarization (\mathbf{P}) and magnetization (\mathbf{M}) contain the information about the macroscopic scale EM properties of the matter. ϵ and μ denote the electric permittivity and magnetic permeability, are valid only if the media is isotropic and linear.

1.6.1.1. The Wave Equation

The coupled electric and magnetic fields in Maxwell's equation can be disentangled by taking curl of Equation 1.6 and 1.7 and using linear relations of Equation 1.8 and 1.9.

$$\nabla \times \nabla \times \mathbf{E} + \mu \epsilon \frac{\partial^2 \mathbf{E}}{\partial t^2} = -\mu \frac{\partial \mathbf{J}_f}{\partial t} \quad (1.10)$$

$$\nabla \times \nabla \times \mathbf{H} + \mu \epsilon \frac{\partial^2 \mathbf{H}}{\partial t^2} = \nabla \times \mathbf{J}_f \quad (1.11)$$

We can rewrite the wave equation into the form as

$$\nabla^2 \mathbf{E} - \mu \epsilon \frac{\partial^2 \mathbf{E}}{\partial t^2} = \mu \frac{\partial \mathbf{J}_f}{\partial t} + \frac{1}{\epsilon} \nabla \rho_f \quad (1.12)$$

$$\nabla^2 \mathbf{H} - \mu \epsilon \frac{\partial^2 \mathbf{H}}{\partial t^2} = -\nabla \times \mathbf{J}_f \quad (1.13)$$

Assuming \mathbf{J}_f is linear with \mathbf{E} ,

$$\mathbf{J}_f = \sigma \mathbf{E} \quad (1.14)$$

where σ is the electric conductivity, and neglecting charge density fluctuation, i.e. $\nabla \rho_f = 0$, we can simplify the wave equation for \mathbf{E} as,

$$\nabla^2 \mathbf{E} = \mu \sigma \frac{\partial \mathbf{E}}{\partial t} + \mu \varepsilon \frac{\partial^2 \mathbf{E}}{\partial t^2} \quad (1.15)$$

Here σ and ε are real and independent. The wave equation for \mathbf{H} takes an identical form. These time varying fields are closely intertwined by Maxwell's equation: if one is known, the other is fully determined. The coupled entity of the two fields is called an EM wave.

If the material is a dielectric or an insulator, the wave equation takes the universal form:

$$\nabla^2 \mathbf{E} = \mu \varepsilon \frac{\partial^2 \mathbf{E}}{\partial t^2} = \frac{1}{v^2} \frac{\partial^2 \mathbf{E}}{\partial t^2} \quad (1.16)$$

which signifies that EM wave propagates in homogeneous media at a speed

$$v = \frac{1}{\sqrt{\mu \varepsilon}} = \frac{c}{\tilde{n}} \quad (1.17)$$

where $c (=1/\sqrt{\mu_0 \varepsilon_0})$ is the speed of light in the free space. ε_0 and μ_0 denote the electric permittivity and magnetic permeability in free space and $\tilde{n} (= \sqrt{\varepsilon/\varepsilon_0})$ is the refractive index, assuming $\mu = \mu_0$.

General solutions of the wave equation are linearly-polarized monochromatic plane waves:

$$\mathbf{E}(r,t) = \mathbf{E}_0 e^{i(k \cdot r - \omega t)} \text{ and } \mathbf{H}(r,t) = \mathbf{H}_0 e^{i(k \cdot r - \omega t)} \quad (1.18)$$

where \mathbf{k} is the wave vector and ω is the angular frequency. From Maxwell's equations, we can draw the relations between \mathbf{E} and \mathbf{H} associated with \mathbf{k} and ω . Substituting plane waves into $\nabla \cdot \mathbf{E} = 0$ and $\nabla \cdot \mathbf{B} = 0$, we obtain

$$\mathbf{k} \cdot \mathbf{E} = 0 \text{ and } \mathbf{k} \cdot \mathbf{H} = 0 \quad (1.19)$$

This means that \mathbf{E} and \mathbf{H} are both perpendicular to the wave vector, that is, the EM wave is transverse. The curl equations give the relation

$$\mathbf{k} \times \mathbf{E} = \omega \mu \mathbf{H} \quad (1.20)$$

Inserting Equation 1.18 into Equation 1.16, we obtain the dispersion relation

$$k^2 = \epsilon \mu \omega^2 \quad (1.21)$$

As ϵ and μ quantify the EM properties of the material, the dispersion relation governs how the wave propagates into the medium. For non-magnetic medium, the wave vector k is related to the wavelength λ by the relation

$$k = \frac{2\pi}{\lambda} = \tilde{n} \frac{\omega}{c} \quad (1.22)$$

The energy flux of the EM wave is the time-averaged Poynting vector,

$$\langle \mathbf{S} \rangle = \frac{1}{2} \mathbf{E} \times \mathbf{H}^* = \frac{1}{2} v \epsilon |E_0|^2 \mathbf{e}_k \quad (1.23)$$

where $\mathbf{e}_k (= \mathbf{k}/k)$ is a unit vector in the direction of wave propagation. The magnitude of the energy flux,

$$I = \langle \mathbf{S} \rangle = \frac{1}{2} v \epsilon |E_0|^2 \quad (1.24)$$

is the radiation intensity, which is the measurement quantity of typical light detectors. A commonly used unit of light intensity is W/cm^2 .

In a conducting medium, general solution of the wave Equation 1.15, also takes the form of the plane wave in Equation 1.18. Even Equation 1.19 and 1.20 are still valid. Wave propagation in a conductor is, however, quite different from that in

the dielectric medium. If the medium has a very high conductivity such that $\sigma \gg \omega\epsilon$, the wave equation leads to the dispersion relation,

$$k^2 \approx i\sigma\mu\omega \quad (1.25)$$

Evidently the amplitude of the wave vector is complex in number,

$$k = k_r + ik_i \approx \sqrt{\frac{\omega\mu\sigma}{2}}(1 + i) \quad (1.26)$$

This means that when an EM wave is incident on a conductor, the field decays exponentially with an attenuation length δ , which is called penetration depth or the skin depth:

$$\delta = \sqrt{\frac{2}{\omega\mu\sigma}} \quad (1.27)$$

Typical metals behave like an ideal conductor for THz waves. For example, the skin depth of copper is $\delta \approx 0.07 \mu\text{m}$ for the frequency $\gamma (= \omega/2\pi) = 1 \text{ THz}$, which is almost negligible when compared to the free space wavelength, $300 \mu\text{m}$.

1.6.1.2. Transfer Functions: Fresnel Equation

The Fresnel equations determine reflection and transmission of light incident on an interface of two media with different refractive indices. They basically relate the amplitudes, phases, and polarizations of the transmitted and reflected waves that emerge when light enters an interface between two transparent media with different indices of refraction, to the corresponding parameters of the incident waves. A detailed derivation of the Fresnel equations is based on Snell's law and the boundary relations for the electric and magnetic fields at an interface between two media with different EM properties.

To derive the Fresnel equations, consider two optical media separated by an interface, as shown in Figure 1.10. A plane optical wave is propagating toward the interface with wave vector k_i oriented at angle θ_i with respect to the interface normal. The electric field amplitude of the wave is given by E_i .

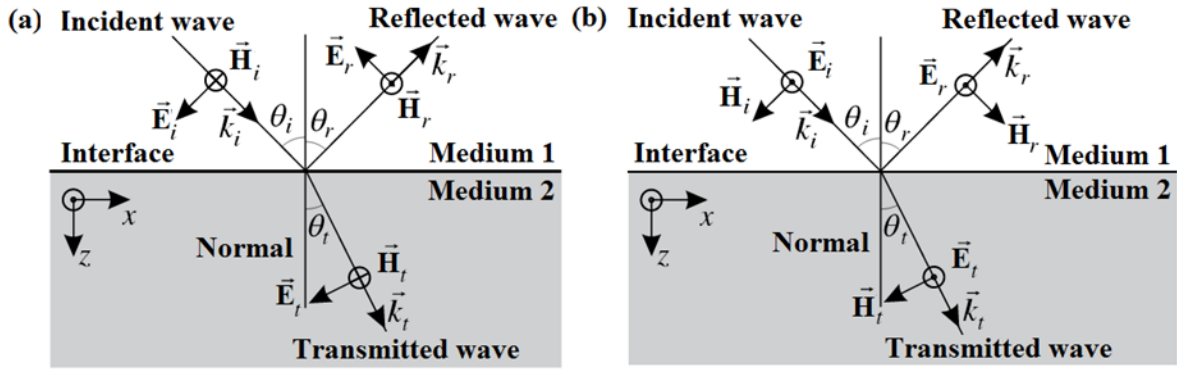


Figure 1.10. Field vectors of the incident, transmitted, and reflected waves in case (a) the electric field vectors lie within the plane of incidence (P-polarization), (b) the electric field vectors are perpendicular to the plane of incidence (S-polarization).

On incidence at the interface, this wave will be partially transmitted and partially reflected. The transmitted wave will propagate at angle θ_t which is determined by Snell's law:

$$\frac{\sin\theta_i}{\sin\theta_t} = \frac{\tilde{n}_2}{\tilde{n}_1} \quad (1.28)$$

where \tilde{n}_1 and \tilde{n}_2 are the refractive indices of the two media. The angle θ_r of the reflected wave is equal to θ_i according to the law of reflection. We denote the amplitudes of these two waves as E_t and E_r , respectively. Our goal is to determine these amplitudes.

Because EM wave is transverse, the field incident onto the interface can be decomposed into two polarization components, one P-polarized, i.e., with the electric field vector inside the plane of incidence, and the other one S-polarized, i.e., orthogonal to that plane. The derivation of Fresnel equations for these two cases will be carried out separately.

We begin by concentrating on the case when the incident wave is P-polarized (Figure 1.10 (a)). Due to symmetry, the transmitted and reflected waves will have the same polarization. Because the E , H , and k vectors must form a right handed triad for each of the waves, the directions of all field vectors are uniquely defined up to a sign convention, which is chosen as illustrated in Figure 1.10 (a). The boundary condition for the electric field then becomes:

$$E_i \cos \theta_i + E_r \cos \theta_i = E_t \cos \theta_t \quad (1.29)$$

For the magnetic field, which is collinear in all three waves, this condition takes the form:

$$H_i - H_r = H_t \quad (1.30)$$

To solve these equations, we need to incorporate the relation between the electric and magnetic field amplitudes for each wave. We know from Maxwell equations that these amplitudes in any plane EM wave must satisfy

$$H = \sqrt{\frac{\varepsilon}{\mu}} E \quad (1.31)$$

where ε and μ are the electric permittivity and magnetic permeability, respectively, of the material in which the wave propagates. Since the index of refraction of a material is given by $\tilde{n} = c\sqrt{\mu\varepsilon}$, we have:

$$H_{i,r} = \frac{\tilde{n}_1 E_i}{\mu_1 c} \text{ and } H_t = \frac{\tilde{n}_2 E_t}{\mu_2 c} \quad (1.32)$$

and thus, from Equation (1.30),

$$\frac{\tilde{n}_1 (E_i - E_r)}{\mu_1} = \frac{\tilde{n}_2 E_t}{\mu_2} \quad (1.33)$$

Combining Equations 1.29 and 1.33, we arrive at the Fresnel equations for the P-polarized wave:

$$\tilde{r}_p = \frac{\left(\frac{\tilde{n}_1}{\mu_1}\right) \cos \theta_t - \left(\frac{\tilde{n}_2}{\mu_2}\right) \cos \theta_i}{\left(\frac{\tilde{n}_1}{\mu_1}\right) \cos \theta_t + \left(\frac{\tilde{n}_2}{\mu_2}\right) \cos \theta_i} \quad (1.34)$$

$$\tilde{t}_p = \frac{2 \left(\frac{\tilde{n}_1}{\mu_1}\right) \cos \theta_i}{\left(\frac{\tilde{n}_1}{\mu_1}\right) \cos \theta_t + \left(\frac{\tilde{n}_2}{\mu_2}\right) \cos \theta_i} \quad (1.35)$$

where we defined the amplitude reflection and transmission coefficients:

$$\tilde{r} = \frac{E_r}{E_i} \text{ and } \tilde{t} = \frac{E_t}{E_i} \quad (1.36)$$

In the case of S-polarization (Figure 1.10 (b)), in much the same way, we write the boundary conditions as

$$E_i + E_r = E_t \quad (1.37)$$

$$-H_i \cos \theta_i + H_r \cos \theta_i = -H_t \cos \theta_t \quad (1.38)$$

from which we derive the second pair of Fresnel equations:

$$\tilde{r}_s = \frac{\left(\frac{\tilde{n}_1}{\mu_1}\right) \cos \theta_i - \left(\frac{\tilde{n}_2}{\mu_2}\right) \cos \theta_t}{\left(\frac{\tilde{n}_1}{\mu_1}\right) \cos \theta_i + \left(\frac{\tilde{n}_2}{\mu_2}\right) \cos \theta_t} \quad (1.39)$$

$$\tilde{t}_s = \frac{2 \left(\frac{\tilde{n}_1}{\mu_1}\right) \cos \theta_i}{\left(\frac{\tilde{n}_1}{\mu_1}\right) \cos \theta_i + \left(\frac{\tilde{n}_2}{\mu_2}\right) \cos \theta_t} \quad (1.40)$$

Equations 1.34 and 1.35 as well as Equations 1.39 and 1.40 present Fresnel equations in their general form, which are also valid for materials with negative indices of refraction (also known as metamaterials or left-handed materials). Most of the dielectrics are essentially non-magnetic ($\mu_1 = \mu_2 \approx \mu_0$). For nearly normal incidence, θ_i and θ_t tend to zero. Then the Equations 1.34, 1.35, 1.39, and 1.40 become,

$$\tilde{r}_{p,s} = \frac{\tilde{n}_1 - \tilde{n}_2}{\tilde{n}_1 + \tilde{n}_2} \quad (1.41)$$

$$\tilde{t}_{p,s} = \frac{2\tilde{n}_1}{\tilde{n}_1 + \tilde{n}_2} \quad (1.42)$$

For most practical purposes, the reflection and transmission coefficients for the intensity are of interest rather than field amplitudes. For a wave of amplitude E propagating in a non-magnetic medium with the refractive index \tilde{n} , we have:

$$I = 2 \tilde{n} c \epsilon_0 |E|^2 \quad (1.43)$$

Because the incident and reflected waves propagate in the same medium, we can write for the intensity reflection coefficient:

$$R = \frac{|E_r|^2}{|E_i|^2} = |\tilde{r}|^2 \quad (1.44)$$

$$T=1-R = T = \frac{\tilde{n}_2 \cos \theta_t}{\tilde{n}_1 \cos \theta_i} \frac{|E_t|^2}{|E_i|^2} = \frac{\tilde{n}_2 \cos \theta_t}{\tilde{n}_1 \cos \theta_i} |\tilde{t}|^2 \quad (1.45)$$

Note that, in contrast to the reflection coefficient, the intensity of transmissivity is not simply the square of the amplitude transmissivity, as two additional factors must be taken into account. First, one must account for the refractive index of the propagation medium, which enters the expression for the intensity (Equation 1.43). Second, the intensity is calculated per unit of the wave front area, and the wave fronts of the incident and transmitted wave are tilted with respect to the interface at different angles θ_i and θ_t , respectively.

1.6.1.3. Extraction of Material Parameters

The spectroscopy in reflection or transmission geometry is a commonly used technique to measure the optical constants of materials. The coherent detection scheme in THz-time domain spectroscopy (THz-TDS) measuring both the amplitude and phase of the EM fields warrants simultaneous determination of real and imaginary part of refractive index (\tilde{n}), dielectric constant (ε), and conductivity (σ). Unlike common optical spectroscopy which only measures the intensity of light at specific frequencies, the THz-TDS technique directly measures the THz wave's temporal electric field. Fourier transformations of this time-domain data gives the information of amplitude and phase of the THz wave pulse. The ratio of the Fourier transforms of the data recorded with and without the sample yields the complex transmission coefficient (\tilde{t}) of the sample in the frequency domain, therefore providing the real and imaginary parts of dielectric constant. This allows precise measurements of refractive index and absorption coefficient (α_{abs}) of samples.

Based on the Fresnel's equations, the functions of transmission coefficient \tilde{t}_{as} , \tilde{t}_{sa} , and reflection coefficient \tilde{r}_{sa} can be expressed as:

$$\tilde{t}_{as} = \frac{2\tilde{n}_a}{\tilde{n}_s + \tilde{n}_a} \quad (1.46)$$

$$\tilde{t}_{sa} = \frac{2\tilde{n}_s}{\tilde{n}_s + \tilde{n}_a} \quad (1.47)$$

$$\tilde{r}_{as} = \frac{\tilde{n}_s - \tilde{n}_a}{\tilde{n}_s + \tilde{n}_a} \quad (1.48)$$

where s =sample and a =air.

If the pulse transmitted the sample includes m echoes, the ratio of their Fourier transforms can be given by the complex refractive index of the sample $\tilde{n}(\omega)$ (or written as \tilde{n} , we usually assume \tilde{n} of air is 1):

$$\tilde{t}_m = \frac{E_{sam}(\omega)}{E_{ref}(\omega)} = \tilde{t}_{as} \tilde{t}_{sa} \exp\left[-i \frac{(\tilde{n}-1)\omega d}{c}\right] \left[1 + \sum_{l=1}^m r_{sa}^{2l} \exp\left(-i \frac{2l\tilde{n}\omega d}{c}\right)\right] \quad (1.49)$$

$$= \frac{4\tilde{n}}{(\tilde{n}+1)^2} \exp\left[-i \frac{(\tilde{n}-1)\omega d}{c}\right] \left[1 + \sum_{l=1}^m \left(\frac{\tilde{n}-1}{\tilde{n}+1}\right)^{2l} \exp\left(-i \frac{2l\tilde{n}\omega d}{c}\right)\right] \quad (1.50)$$

$$= \sqrt{T(\omega, \varphi)} \exp(-i\varphi(\omega)) \quad (1.51)$$

$T(\omega, \varphi)$ and $\varphi(\omega)$ are the experimentally obtained power transmittance and relative phase shift respectively, and d is the thickness of samples.

In case of optically thick samples, we can separate the echoes and just use the first echo, so the Fabry-Perot effect can be ignored. Therefore, the transmission coefficient can be expressed as:

$$\tilde{t}_m = \frac{E_{sam}(\omega)}{E_{ref}(\omega)} = \tilde{t}_{as} \tilde{t}_{sa} \exp\left[-i \frac{(\tilde{n}-1)\omega d}{c}\right] \quad (1.52)$$

$$= \frac{4\tilde{n}}{(\tilde{n}+1)^2} \exp\left[-i\frac{(\tilde{n}-1)\omega d}{c}\right] \quad (1.53)$$

$$= \sqrt{T(\omega, \varphi)} \exp(-i\varphi(\omega)) \quad (1.54)$$

$$= \rho(\omega) \exp(-i\varphi(\omega)) \quad (1.55)$$

where $\rho(\omega)$ and $\varphi(\omega)$ are the amplitude and phase shift of the ratio between the sample and reference THz pulses, respectively and they can be obtained experimentally. Considering κ and n for the general case, we can obtain:

$$\tilde{t}_m \approx \frac{4n}{(n+1)^2} \exp\left(-\frac{\kappa\omega d}{c}\right) \exp\left[-i\frac{(n-1)\omega d}{c}\right] \quad (1.56)$$

Then we can obtain,

$$\rho(\omega) = \frac{4n}{(n+1)^2} \exp\left(-\frac{\kappa\omega d}{c}\right) \quad (1.57)$$

$$\varphi(\omega) = \exp\left[-i\frac{(n-1)\omega d}{c}\right] \quad (1.58)$$

Therefore, the complex refractive index $\tilde{n} = n + i\kappa$,

$$n = \frac{\varphi(\omega)c}{\omega d} + 1 \quad (1.59)$$

$$\kappa = -\frac{c}{\omega d} \ln \frac{\rho(\omega)(n+1)^2}{4n} \quad (1.60)$$

$$= \frac{c}{\omega d} \ln \frac{4n}{\rho(\omega)(n+1)^2} \quad (1.61)$$

The complex refractive index $\tilde{n}(\omega)$ is like a density to an EM wave. It quantifies the speed of an EM wave through the material. Wave travels slower through a material with higher refractive index.

$$\tilde{n} = n + i\kappa = \pm \sqrt{\varepsilon(\omega)} \quad (1.62)$$

where n is the ordinary refractive index and κ is the extinction co-efficient. Therefore, the conversion between dielectric function and refractive index is given by the equations

$$n+i\kappa = \sqrt{\varepsilon'(\omega)+i\varepsilon''(\omega)} \quad (1.63)$$

$$\varepsilon'(\omega) = n^2(\omega) - \kappa^2(\omega) \quad (1.64)$$

$$\varepsilon''(\omega) = 2n(\omega)\kappa(\omega) \quad (1.65)$$

Again the complex conductivity ($\sigma = \sigma'(\omega) + i\sigma''(\omega)$) is related to complex permittivity by the relation

$$\varepsilon = \varepsilon'(\omega) + i\varepsilon''(\omega) = \varepsilon_\infty - i \frac{\sigma}{\omega \varepsilon_0} \quad (1.66)$$

$$\sigma'(\omega) = \omega \varepsilon_0 \varepsilon''(\omega) \quad (1.67)$$

$$\sigma''(\omega) = \omega \varepsilon_0 (\varepsilon_\infty - \varepsilon') \quad (1.68)$$

The $\alpha_{abs}(\omega)$, the absorption co-efficient is given by

$$\alpha_{abs}(\omega) = \frac{2\omega\kappa(\omega)}{c} \quad (1.69)$$

where $\kappa(\omega)$ is the imaginary part of the complex refractive index, ω , the frequency of the incident THz radiation, and c is the velocity of light in free space.

1.6.2. Terahertz Radiation and Elementary Excitation

The quantum energy of THz photons is in the range of 0.0001 to 0.001 eV. Interaction of THz waves with matter involves low energy excitations corresponding to THz frequencies. Some elementary excitations of cardinal interest including Rydberg transition in atoms,⁶⁵⁻⁶⁷ transitions among impurity states in semiconductors,⁶⁸ intra-band transitions in semiconductor NSs,^{69,70} many body interaction in strongly correlated electron system,⁷¹ phonon modes in organic and inorganic crystals,⁷² rotation-vibration transitions in molecule,⁷³ and collective large amplitude motion in biological molecules.⁷⁴

A crystalline solid has ions arranged in a periodic structure on the microscopic level. The ions, however, are not completely static: a closer look may find that each ion wiggles in the vicinity of its lattice site, while the average positions retain the periodic arrangement. A collective oscillation of the ions with well defined frequency and wavelength is called a normal mode of lattice vibration, and its quantization is called a phonon. The phonon resonances are our great interest because, in general, the normal mode frequencies fall into the THz region. Not all normal modes, however, interact with EM radiation. Only the long wavelength optical modes in ionic crystals can be involved in such interactions.

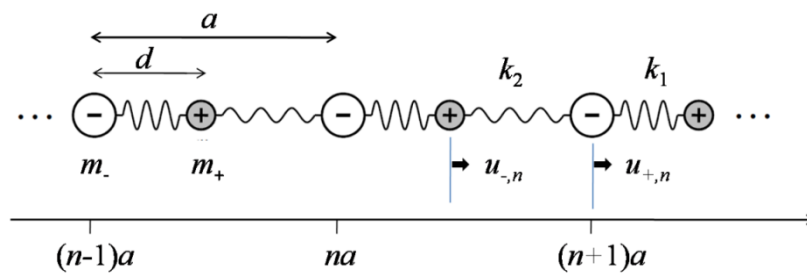


Figure 1.11. Harmonic model for a one dimensional lattice with two ions in a unit cell. a : lattice constant, m_{\pm} : masses of the ions, $u_{\pm,n}$: displacements of the ions from equilibrium positions at n^{th} unit cell, $k_{1,2}$: spring constants.

A one dimensional lattice with two species of ions has been considered to describe the normal modes, and how they interact with external EM waves has been discussed. Figure 1.11 illustrates the harmonic model for a one dimensional ionic crystal. It is convenient to assume that (i) the number of unit cells in the system, N , is large, yet finite, and (ii) the displacements of the ions satisfy the periodic boundary condition, $u_1 = u_N$. The equations of motion at the n^{th} unit cell are written as

$$\begin{aligned} m_+ \ddot{u}_{+,n} &= -k_1(u_{+,n} - u_{-,n}) - k_2(u_{+,n} - u_{-,n-1}) \\ m_- \ddot{u}_{-,n} &= -k_1(u_{-,n} - u_{+,n}) - k_2(u_{-,n} - u_{+,n+1}) \end{aligned} \quad (1.70)$$

where m_{\pm} are the masses of the ions, and $u_{\pm,n}$ are the displacements of the ions from equilibrium positions at n^{th} unit cell. A normal mode solution with angular frequency ω and wave vector k has the form

$$u_{+,n} = u_+ e^{i(kna - \omega t)}$$

$$u_{-,n} = u_- e^{i(kna - \omega t)} \quad (1.71)$$

Inserting Equation 1.71 into Equation 1.70, we obtain two coupled equations,

$$\begin{aligned} \left[m_+ \omega^2 - (k_1 + k_2) \right] u_+ + \left[k_1 + k_2 e^{-ika} \right] u_- &= 0 \\ \left[k_1 + k_2 e^{ika} \right] u_+ + \left[m_- \omega^2 - (k_1 + k_2) \right] u_- &= 0 \end{aligned} \quad (1.72)$$

The solution of these equations leads to the dispersion relation,

$$\omega^2 = \frac{k_1 + k_2}{2\mu_r} \left[1 \pm \sqrt{1 - \frac{8\mu_r k_1 k_2}{\mu_c (k_1 + k_2)^2} (1 - \cos ka)} \right] \quad (1.73)$$

with the reduced mass, $\mu_r = m_+ m_- / (m_+ + m_-)$, and the total mass, $\mu_c = m_+ + m_-$. The dispersion relation is defined in a reciprocal unit cell, $-\pi/a < k < \pi/a$ as shown in Figure 1.12. The two curves are referred to as the optical branch and the acoustic branch.

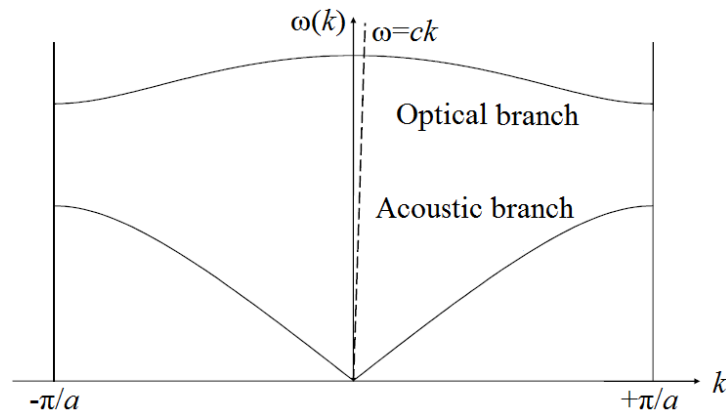


Figure 1.12. Dispersion relation for a one dimensional ionic crystal. The upper and lower curves are optical and acoustic branches, respectively.

Analyzing the dynamics of lattice vibrations in the long wavelength limit helps us to understand how normal modes interact with external EM fields and here the branch names come from. In the limit of $k \ll \pi/a$, the dispersion relation is approximated as

$$\omega \cong \sqrt{\frac{k_1 + k_2}{\mu_r}} : \text{Optical branch} \quad (1.74)$$

$$\omega \cong \sqrt{\frac{k_1 k_2}{\mu_c (k_1 + k_2)}} ka : \text{Acoustic branch} \quad (1.75)$$

The frequency of an optical mode depends on reduced mass, but not total mass; the opposite is true for acoustic mode. This is because optical modes are associated with relative motions between two ions, while acoustic modes are associated with center of mass motions as shown in Figure 1.13.

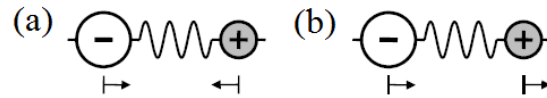


Figure 1.13. (a) Optical and (b) acoustic modes are associated with relative and center of mass motions of the ions, respectively.

1.6.3. Terahertz Shielding and Mechanism

Due to rapid enhancement of wireless communication, digital systems, and fast processors, a considerable attention has been focused on EM interference (EMI) shielding. EMI can be defined as the degradation in the performance of an electronic system caused by other external EM disturbances.⁷⁵⁻⁷⁸ Moreover, EM radiation affects the network of veins in high risk organs in human body such as eye, due to heat build up by the EM field.⁷⁹ Therefore, shielding of EM radiation is essential in order to avoid these hazards in human body as well as to protect sensitive circuits from undesired EM radiation.

The EM wave consists of electric and magnetic fields which are oscillating phase perpendicular to each other and also perpendicular to the direction of energy propagation. These electric and magnetic fields can be arrested by means of reflection or absorption. Many research works have been carried out on shielding material starting from metals to conductive fabrics, and composites with required shielding and mechanical properties. In general, the low frequency signals can be arrested by means of reflection whereas high frequency signals should be arrested by means of absorption which needs much attention. Much research has been conducted to develop high

frequency EM absorbers by means of coating fillers with magnetic materials or incorporation of magnetic materials in polymer matrix.

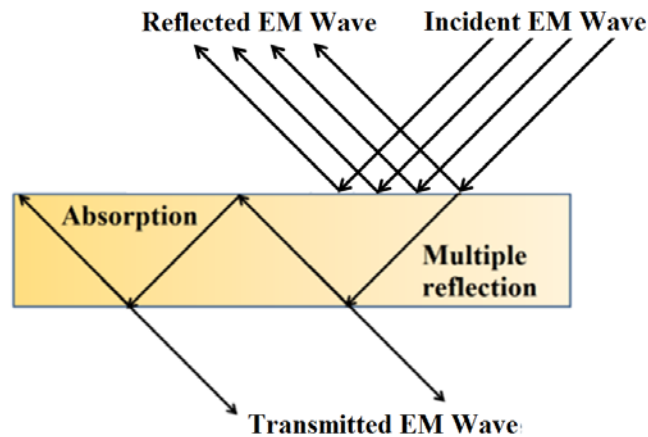


Figure 1.14. Shielding mechanism of a homogenous material.

When the EM waves impinge on surface of an object, it undergoes four different mechanisms, namely reflection, multiple reflection, absorption, and transmission. In order to arrest EM wave, it should be either reflected (multiple reflection) or absorbed by the shielding materials. Figure 1.14 shows the mechanism of EM shielding which depends on the nature of wave and material characteristics.

1.6.3.1. Reflection

The reflection of EM waves takes place when the shielding material is made of highly conductive materials. If the shield has limited conductivity, some signal may penetrate through it. When it reaches the opposite face of the shield, it encounters another boundary (Figure 1.14) and gets reflected back into the shield. The reflection of EM waves by the shield is decided by the frequency of incident wave, conductivity, and magnetic permeability of the material.⁸⁰ The reflection loss is a function of the ratio σ/μ_r , where σ , is the electrical conductivity and μ_r , is the relative magnetic permeability.

1.6.3.2. Multiple Reflections

Multiple reflections of EM waves occur due to various surfaces or phases present inside the shielding material. Materials with large specific surface (internal surface) like foamed materials and composite with filler show internal

reflections of EM waves.⁸¹ The loss due to multiple reflections can be neglected when the distance between the reflecting surfaces or interfaces is large compared to the skin depth.

1.6.3.3. Absorption

For absorption of EM waves to occur, a shield should contain electric and/or magnetic dipoles to interact with the EM field. Material with high dielectric constant (BaTiO_3) provides electric dipoles and the material with high magnetic permeability (Fe_3O_4) provides magnetic dipoles for absorbing EM waves.⁸² Electric dipoles present in the shield destroy the electric field of EM waves by converting it as heat.⁸³ Along with all these criteria, a good shielding material should also possess better absorption loss (insertion loss), lower volume, and surface resistivity. The absorption loss is a function of the product $\sigma\mu_r$, where σ , is the electrical conductivity and μ_r , is the relative magnetic permeability.

1.6.3.4. Transmission

When EM waves pass through the shielding material without any attenuation, then high transmission of EM waves is observed. The non-conductive materials like glass, polyester, and polypropylene show less or zero transmission loss to the EM waves.

In general, the shielding enclosures are used to protect the inner electronic device from EM radiation and mechanical damage. It is usually made of conductive materials such as metals and conductive composites, which has complex shapes with various apertures and slots for cable passage, air ventilation etc. Designing of an enclosure depends on the properties of material, geometric size and thickness, position and number of apertures, electronic characteristics of inner device etc. Metal based enclosures like Mu-metal was initially used as EM shielding material. Nevertheless it has some limitations like metal oxidation, fabrication of complex shapes etc. which restrict their usage as shielding

materials. In order to overcome this problem, many core-shell structured nanocomposites containing Fe_3O_4 cores (e.g., $\text{Fe}_3\text{O}_4/\text{C}$,⁸⁴ $\text{Fe}_3\text{O}_4/\text{ZnO}$,⁸⁵ $\text{Fe}_3\text{O}_4/\text{SnO}_2$,⁸⁶ or $\text{Fe}_3\text{O}_4/\text{TiO}_2$ ^{87,88}) show the microwave absorption performance better than the pure core or shell materials. Very recently, Wang et al. have reported an atomic layer deposition strategy to coat carbon nano coils with magnetic Fe_3O_4 or Ni for the synthesis of coaxial multi-layer NSs, which exhibit remarkably improved microwave absorption properties compared to pristine carbon nano coils.⁸⁹ Moreover, Liu et al.⁹⁰ have shown an excellent microwave absorption properties of yolk-shell microspheres with magnetic iron oxide cores and hierarchical copper silicate shells. In considering the unique properties of hollow NSs such as low density, large surface area, and synergistic effects, hollow structures of magnetic Fe_3O_4 may have the potential to satisfy the increasing demand of light weight, thin thickness, wide absorption bandwidth, and strong absorption characteristics for innovative EMI shielding systems.

1.7. Terahertz Conductivity of Nanomaterials

The effect of size on the conductivity of NMs is very intricate as it depends on various independent mechanisms. These mechanisms can be summarized into following categories; surface scattering including grain boundary effect, quantized electronic conduction, coulomb charging and tunnelling, increase of band gap and change of microstructure.⁹¹ In addition, improvement in crystal perfection, such as fewer defects, dislocations, and impurities would also affect the electrical conductivity of the NSs. Electron collisions with phonons are the source of thermal or phonon contribution, which increases with temperature. However, impurity atoms, defects such as vacancies, and grain boundaries locally destroy the periodic electric potential of the lattice and effectively cause electron scattering. Smaller nanocomposites have lots of grain boundaries, which behave as potential barrier for free flow of charge carriers, electrons, and holes which cause reduction of conductivity in smaller particles.^{92,93} Surface scattering of electrons also reduces the conductivity as seen in nanowires and thin films. When the dimension of thin films or nanowires becomes comparable or smaller than the electron mean free path, the

motion of electrons will be interrupted through elastic or inelastic collisions with the surface. In elastic collisions, the electrons reflect in the same way and do not lose its energy or momentum. As a result, the conductivity remains same as in the bulk, i.e. there is no size effect. However, in case of inelastic collisions, the electron trajectory or scattering angle after collision is random. The scattered electrons lose velocity parallel to the conduction direction and the electrical resistivity decreases. So, there will be a size effect on electrical conductivity.⁹¹ However, in case of semiconductor nanowires it has been found that the crystallinity plays an important role on their conducting property. For example, in case of defect free Si nanowires having four atoms per unit cell, generally three conductance channels are observed.⁹⁴ Whereas, in the case of defect induced Si nanowires, the number of such conductance channels varies causing significant variation in their conductance behavior. Doping also changes the conductivity. For example, annealing of ZnO nanorods in H₂ atmosphere introduces n-type carriers into it that changes their I-V characteristics.⁹⁵

1.7.1. Terahertz Conductivity of Matters

Apart from monitoring the kinetic energy, experimental studies of EM response over a broad energy range allow one to examine all essential energy scales in solids associated with both elementary excitations and collective modes. Complementary to this, the time domain measurements allow one to directly investigate the dynamical properties of a correlated matter. For these reasons, optical studies have immensely advanced the physics of some of the most fascinating many-body phenomena in correlated electron systems. In condensed matter physics, many elementary and collective low energy excitations occur in the THz range, such as phonons, magnons, plasmons, energy band gap transition of superconductors, excitonic transition of semiconductor etc. Moreover, majority of dynamical phenomena in solids such as scattering, tunnelling, and recombination occur on characteristic times scales of picoseconds, i.e., in the THz frequency range. Therefore, THz-TDS can be helpful in understanding electron dynamics over nanometer length scales, in particular, in NMs. The interaction of THz radiation with matter provides a

vital low energy probe of the electronic nature of a system close to its equilibrium state.

Historically, it has been challenging to generate and detect light in the far-infrared (or THz) range, roughly defined as 0.1–10 THz (or 0.4–40 meV), owing to the presence of background sources of incoherent light (room temperature is 25 meV, or 6 THz). The last two decades have seen a surge in interest in the generation, detection, and spectroscopic applications of THz radiation owing to rapid developments in both continuous wave systems and pulsed sources based on THz-TDS. Time-resolved techniques also offer novel experimental paradigms, such as tracking the dynamic photoconductivity of a material on picosecond to nanosecond timescales. The combination of dramatic improvements in experimental technique and its applicability to materials of contemporary interest is making the THz range an increasingly vital part of EM spectrum. Nemec et al.⁹⁶ reviewed THz-TDS studies of polymer-fullerene heterojunctions and dye-sensitized NPs. The dynamics of charges in superconductors and other correlated electron systems using THz-TDS and visible ultrafast spectroscopy has been reviewed by Averitt et al.⁹⁷ and Basov.⁹⁸

1.7.2. Terahertz Conductivity Models

In this section, various models of THz conductivity are outlined. As soon as a conductivity spectrum of a material is obtained, a general approach is to fit them into some model so as to obtain some important parameters like carrier density, scattering time, carrier mobility etc. The THz conductivity of homogeneous media has been discussed in order to elucidate the underlying physics of charge transport. The Drude model has been explored and also investigated the limits of its applicability, before discussing phenomenological expressions for conductivity of NMs at THz frequencies. A discussion of how to model THz conductivity of inhomogeneous materials, such as blends of two or more constituents, is described through quantum hopping models.

1.7.2.1. Drude Model

The simplest model of frequency dependent conductivity of metals and semiconductors is provided by Drude model, in which an electron and hole plasma is treated as a non-interacting gas. Carriers undergo collisions that randomize their momentum with a rate $\Gamma = 1/\tau$ that is assumed to be independent of energy. The Drude model assumes that the displacement (x) of carrier (with effective mass m^* and charge q) from its equilibrium position is given by:

$$\frac{d^2x}{dt^2} + \Gamma \frac{dx}{dt} = \frac{qE}{m^*} \quad (1.76)$$

Under a constant applied field, carriers drift with velocity $qE\tau/m^*$. If the incident electric field oscillates at angular frequency ω , i.e. is of the form $E = E_0 e^{-i\omega t}$, then the displacement can be assumed to have the same form $x = x_0 e^{-i\omega t}$. Substitution for x and E in Equation 1.76 readily yields x_0 . The dielectric function ϵ can be determined from the definition of the polarization $P = X\epsilon_0 E = Nqx$, and the conductivity is then

$$\sigma(\omega) = \frac{Nq^2}{m^*} \frac{\tau}{1 - i\omega\tau} \quad (1.77)$$

which has a peak in σ' at zero frequency and a maximum in σ'' at $\omega = 1/\tau$. While the Drude conductivity is adequate to model the intra-band conductivity of some metals and semiconductors, it often fails as the electron scattering rate is in fact energy dependent, and bands are parabolic only close to extrema. A further constraint is that the material is uniform over the length scale that electrons explore during their motion.

1.7.2.2. Drude-Lorentz Model

The Drude-Lorentz model offers a straightforward extension to the Drude model. Here, the motion of electrons under a restoring force and an external EM wave is described by the equation of motion of a damped, driven simple harmonic oscillator.⁹⁹ The restoring force can be provided electrostatically, for instance by a

surface depletion or accumulation field, as is often found close to the interfaces of semiconductors. The Drude-Lorentz model has therefore been applied to model the THz conductivity of semiconductor NMs. Equation 1.76 is altered by the addition of the term $\omega_0^2 x$ to the left-hand side, where ω_0 is the angular frequency of the oscillatory response. A larger restoring force requires a greater value of ω_0 . The conductivity in this model is

$$\sigma(\omega) = \frac{Ne^2}{m^*} \frac{\tau}{1 - i\omega\tau_D \left(1 - \frac{\omega_0^2}{\omega^2}\right)} \quad (1.78)$$

For particular geometries ω_0 can be linked to the plasma frequency $\omega_p = (Ne^2/m^*\epsilon_\infty\epsilon_0)^{1/2}$ by $\omega_0^2 = g\omega_p^2$. Under the assumption that charges are located on the surface of a small spherical particle the geometrical factor $g=1/3$,⁹⁹ while for cylindrical wires $g=0$ when the electric field is axial and the wave vector k is radial, $g=1/2$ when E and k are radial, and $g=1/3$ for radial E and axial k .^{100,101}

1.7.2.3. Drude-Smith Model

As established in Section 1.7.2.1, when an electron or hole's displacement under E becomes comparable to the dimension L of the material (in the direction of E) then the conductive response of the medium will differ significantly from that of the bulk material. A criterion for this to occur is that the electron or hole mean free path l should be greater than L , i.e. $l = v\tau > L$, where the carrier velocity is often equated with the thermal velocity $v = \sqrt{3k_B T / m^*}$. For room temperature, the electrons close to the Γ -valley minimum of GaAs with $v \sim 5 \times 10^5 \text{ ms}^{-1}$ and $\tau \sim 100 \text{ fs}$, yield $L < 50 \text{ nm}$. Similarly, for silicon ($m^* = 0.26m_e$, $v \sim 2 \times 10^5 \text{ ms}^{-1}$ and $\tau \sim 100 \text{ fs}$) the estimate is $L < 20 \text{ nm}$. In materials satisfying this dimensional constraint scattering from the interface may therefore be expected to play an important role. This argument, however, neglects three important considerations. Firstly, the carrier velocity v should not be equated to the thermal velocity, rather it is the Fermi velocity v_F - only electrons within $k_B T$ of the Fermi surface can scatter from an occupied to an

unoccupied state. For materials photoexcited well above band gap, the mean carrier velocity will be a function of time, since the carriers will cool. Secondly, THz electric field can give electrons significant kinetic energy when E is too high. Finally, at $L < 50$ nm quantum confinement effects can also become significant: for instance in a GaAs quantum well with infinite barriers. The spacing between the lowest two electron sub-bands is 1 THz when $L = 63$ nm. This conductivity models that include the role of interface will therefore be applicable when the average electron displacement approaches the sample's dimensions, but when quantum confinement is not yet significant.

An extension to Drude model aimed at modelling the conductivity of carriers undergoing restricted motion is that proposed by Smith,¹⁰² in which a carrier retains a part of its initial velocity upon scattering. The collisions are assumed to be randomly distributed in time, and the fraction (c_n) of a carrier's initial velocity retained after n scattering events allows Drude model to be generalized to

$$\begin{aligned}\sigma(\omega) &= \frac{Nq^2}{m^*} \frac{\tau}{1-i\omega\tau} \left[1 + \sum_{n=1}^{\infty} \frac{c_n}{(1-i\omega\tau)^n} \right] \\ &= \sigma_D(\omega) \left[1 + \sum_{n=1}^{\infty} \frac{c_n}{(1-i\omega\tau)^n} \right]\end{aligned}\quad (1.79)$$

Here, the term $\sigma_D(\omega)$ is the Drude conductivity. For elastic collisions, the parameter c_n is the expectation value of $\langle \cos n\theta \rangle$, for scattering angle θ . If the carrier's momentum is randomized then $c_n = 0$, while if it is completely backscattered then $c_n = -1$. Commonly, the infinite series in Equation 1.79 is truncated at $n = 1$, which corresponds to the assumption that the carrier retains a part of its initial momentum during the first scattering event, but in every subsequent scattering events the velocity is randomized. Deviations from the Drude behavior of free carriers within or near the THz range is quite dramatic in nanostructured materials, such as metals,¹⁰³⁻¹⁰⁵ semiconductors,^{99,106-107} and oxides.^{108,111} In a wide class of NMs stated above, the Drude-Smith model has been used to interpret the complex conductivity in the THz frequency range.

1.7.2.4. Hopping Model

An alternative approach to model the THz conductivity of composite materials is to treat charge transport as consisting of an intra-particle and an interparticle component. In arrays of closely spaced semiconductor nanocrystals, there is a finite probability that electrons will tunnel quantum mechanically from one grain to another, thereby contributing to the conductivity. This model was developed by Dyre^{114,115} to account for the thermally activated conductivity of disordered solids, and has been applied to the optical conductivity of metallic polymers¹¹⁶ and recently to the THz conductivity of semiconductor NPs.¹¹⁷ The conductivity resulting from quantum tunnelling can be written within the hopping model¹¹⁴ as

$$\sigma_h(\omega) = \frac{-\sigma_t i \omega \tau_t}{\ln(1 - i \omega \tau_t)} \quad (1.80)$$

where the expression for DC tunnelling conductivity $\sigma_t(\omega) = \frac{N_t e^2 R}{6k_B T \tau_t}$ depends on the spacing R between the NPs, the temperature T , the tunnelling density N_t and the tunnelling time τ_t . The intra-particle conductivity $\sigma_p(\omega)$ was assumed to be described by Drude model, and the effective conductivity of the composite σ^* was obtained by assuming the two channels combine in series according to

$$\frac{1}{\sigma^*(\omega)} = \frac{f}{\sigma_p} + \frac{(1-f)}{\sigma_h} \quad (1.81)$$

Here, f is the volume fill fraction of particles. The real part of the hopping conductivity increases with frequency, as electrons gain more energy and become increasingly likely to tunnel through the barrier region between particles. In combination with the Drude model (peak in σ' at low frequency), this creates a resonant line shape.

1.8. Adsorption Activity of Nanomaterials

NMs are generally valued for their strength, highly active sites, and low mass. Therefore, to meet the industrial as well as biomedical demands, NMs can be utilized for waste water and extracorporeal treatments (hemodialysis, hemoperfusion) respectively. Dyes are major water pollutants. The excessive exposure of dye causes skin irritation, respiratory problems, and for some dyes, increases cancer risk in humans.¹¹⁸ In addition, the presence of dyes in waste water also contributes to high chemical oxidation demand and causes foul odor.¹¹⁹ Thus, it is of utmost importance to remove dyes from waste water effectively to ensure safe discharge of treated liquid effluent into watercourses. Typically, dye waste water is treated using coagulation–flocculation,¹²⁰ aerobic or anaerobic treatment,¹²¹ electrochemical treatment,¹²² membrane filtration,¹²³ and adsorption methods.¹²⁴ Adsorption is the most popular of these methods, due to its effectiveness and simplicity. Dye manufacturing factories commonly use commercial activated carbon for dye removal due to its high porosity and large surface area (500–2000 m²/g).¹²⁵ Activated carbon is also used for hemoperfusion and hemodialysis techniques. Shinke et. al.¹²⁶ have reported the adsorption of 90% of bilirubin in presence of carbon NMs within 60 min. However, commercial activated carbon is relatively expensive because of high production cost in addition to separation inconvenience.¹²⁷ The regeneration of activated carbon requires high pressure which contributes to high operation cost of this treatment.¹²⁸ This high cost and separation inconvenience have motivated the search for alternative adsorbents that are both economical and efficient for removal.

In this regard, magnetic NSs, especially ferrite NSs are found to be the best for waste water treatment and biomedical applications due to their fast magnetic separation after adsorption in addition to their high surface area, chemical stability, biocompatibility, and low cost of synthesis. Zhou et. al.¹²⁹ have reported effective adsorption of different dyes and drugs on carboxylic hyperbranched polyglycerol functionalized iron oxide-silica magnetic NPs. Haik group and Afkhami group

reported the adsorption of acridine orange and congo red by γ -Fe₂O₃ magnetic NPs, respectively.^{130,131}

1.8.1. Kinetics of Adsorption

In order to examine the controlling mechanism of adsorption such as mass transfer, physisorption, and chemisorption; different kinetic models such as intraparticle diffusion (mass transfer) model, pseudo 1st order (physisorption), and pseudo 2nd order (chemisorption) models are applied to test the obtained experimental data for different adsorbent concentration. The amount of dye on adsorbent is calculated from the following equation:

$$q_e = \frac{(C_0 - C_e)V}{m} \quad (1.82)$$

where q_e (mg/g) is the amount of dye adsorbed at equilibrium, C_0 and C_e (mg/L) are the liquid phase concentrations of dye at initial and equilibrium points respectively. V is the volume of the solution and m is the mass of dry adsorbent used.

Intraparticle diffusion model based on the theory proposed by Weber and Morris¹³² is tested to identify the diffusion mechanism. Adsorption is a multistep process involving the transport of solute molecules from the aqueous phase to the surface of solid particulates followed by diffusion into the interior of pores. According to this theory, the rate expression for Intraparticle diffusion model is,

$$q_t = k_i t_{1/2} + C \quad (1.83)$$

where k_i (mg/g h^{1/2}), the intraparticle diffusion rate constant, is obtained from the slope of the straight line of q_t vs. $t_{1/2}$.

The pseudo 1st order rate expression of Lagergren¹³³ is:

$$\log(q_{e_1} - q_t) = \log q_{e_1} - \frac{k_1}{2.303} t \quad (1.84)$$

where q_e and q_t (mg/g) are the amounts of dye adsorbed at equilibrium and at time t (h), respectively and k_1 (h^{-1}) is the adsorption rate constant. A straight line of $\log(q_{e_1} - q_t)$ would suggest the applicability of this kinetic model.

The pseudo 2nd order¹³⁴ equation based on equilibrium adsorption data is expressed as:

$$\frac{t}{q_t} = \frac{1}{k_2 q_e^2} + \frac{1}{q_e} t \quad (1.85)$$

where k_2 (g/mg h) is the rate constant for the pseudo 2nd order adsorption kinetics.

1.8.2. Equilibrium Modelling

The analysis of equilibrium sorption data by fitting them into different isotherm models is an important step for the description of how adsorbate will interact with an adsorbent.¹³⁵ The Langmuir equation is valid for monolayer adsorption on a surface with a finite number of identical sites and is expressed as:¹³⁶

$$\frac{C_e}{q_e} = \frac{1}{k_L q_m} + \frac{C_e}{q_m} \quad (1.86)$$

where C_e (mg/L) is the initial concentration of adsorbate and q_e (mg/g) is the amount of adsorbate adsorbed per unit mass of adsorbent at equilibrium. q_m is the maximum amount of the dye per unit mass of adsorbent to form a complete monolayer on the surface at high C_e (mg/L) and k_L (L/mg) is a constant related to the affinity of the binding sites.

The empirical Freundlich isotherm¹³⁷ based on adsorption on a heterogeneous surface is given by the following equation:

$$\log q_e = \log k_F + \frac{1}{n} \log C_e \quad (1.87)$$

where k_F (mg/g (L/mg)^{1/n}) and n are Freundlich constants with n giving an indication of how favorable is the adsorption process. k_F is the adsorption capacity of the adsorbent which can be defined as the adsorption or distribution coefficient. It

represents the quantity of dye adsorbed onto adsorbent for a unit equilibrium concentration. The slope of $1/n$ ranging between 0 and 1 is a measure of adsorption intensity or surface heterogeneity, becoming more heterogeneous as its value gets closer to zero.¹³⁸ Value for $1/n$ below one indicates a normal Langmuir isotherm while $1/n$ above one is an indicator for cooperative adsorption.¹³⁹

Dubinin–Radushkevich (D-R) isotherm¹⁴⁰ is generally applied to express the adsorption mechanism with a Gaussian energy distribution onto a heterogeneous surface. D-R isotherm¹⁶ is represented by the following equation:

$$\ln q_e = \ln Q_0 - K_{DR} \varepsilon^2 \quad (1.88)$$

where K_{DR} ($\text{mol}^2 \text{kJ}^{-2}$) is a constant related to mean adsorption energy and ε is the Polanyi potential, which can be calculated from equation:

$$\varepsilon = RT \ln \left(1 + \frac{1}{C_t} \right) \quad (1.89)$$

The slope of the plot of $\ln(q_e)$ versus ε^2 gives K_{DR} ($\text{mol}^2 \text{kJ}^{-2}$), and the intercept yields the sorption capacity, Q_0 (mg g^{-1}). T is the absolute temperature in Kelvin, and R is the universal gas constant ($8.314 \text{ J mol}^{-1} \text{ K}^{-1}$).

1.9. Motivation and Objective of Thesis

Till now, Nd-Fe-B and Sm-Co based alloys are found to be the best magnetic materials due to their very high H_c and M_r . However, they are very expensive due to the presence of rare earth elements. In addition to that, they are very corrosive also. So, if by any means, we can enhance the magnetic property of ferrite NMs, then we can solve those problems. Moreover, ferrites possess very high T_c ¹⁴¹ in contrast to Nd-Fe-B, Sm-Co based alloys, leading to their applicability in high temperature also.

A long term research unfolds that ferrite NMs have tremendous applications in biomedical as well as technological fields such as information storage, magnetic sensors, bio-separation, and drug delivery due to their remarkable chemical and mechanical stability, high magnetocrystalline anisotropy and magnetostriction,

moderate M_s , low thermal conductivity, high electrical resistance, excellent corrosion resistance, high T_c , and low cost of synthesis.¹⁴²⁻¹⁴⁴ In some application NPs with higher M_s is required, say for example bio-sensing, bio-separation, molecular imaging¹⁴⁵⁻¹⁴⁷ and in other, NP with higher H_c is required as in case of information storage devices.¹⁴⁸ Moreover, NMs with higher relaxation time (t_B , t_N) as well as higher H_c are required for its application in hyperthermia¹⁴⁹ and for the drug delivery; SPM NPs with lower T_B is required so that it does not agglomerate at body temperature.¹⁵⁰ Therefore, tuning of magnetic properties of ferrite NMs is very essential for their utilization in specific biological or technological applications.

Being different from their bulk counterparts, there exists many influencing parameters which can change the magnetic properties of NMs significantly. Song et al.¹⁵¹ have reported that keeping the volume of NP same, spherical NP shows greater H_c than the cubic NP whereas M_s and M_r remain almost same. The size of the NPs also plays an important role in controlling the H_c and M_s of the NMs. It is found that there exists a critical diameter (D_c), above and below which H_c decreases significantly. Therefore, a long-term endeavour has been concentrated to enhance the magnetic properties of the NPs without going to D_c and it is found that functionalization³⁹ and core-shelling³⁸ can also enhance the H_c significantly in addition to the size and morphology of the NMs.

Since enhanced magnetic properties of NMs play an important role in enhancing their EM absorption property, the EM responses of transition metal oxide magnetic NSs have also been investigated. In general, the properties which help in absorbing EM radiation are high magnetization, high electric polarization, low conductivity, and high surface area. Interestingly, ferrite NSs possess all these properties because of which it is used as a shielding material in microwave as well as radio frequency region.⁴¹ However, the study of ferrite NMs with varying sizes and morphology in the THz frequency region is still absent from the literature.

Basically, 1 THz corresponds to 4.13 meV, a very low magnitude of energy which is not able to excite the electron from valance band to conduction band. It is found that many elementary and low energy excitations occur in the THz range,

such as phonons, magnons, plasmon etc.¹⁵² Moreover, majority of dynamical phenomena in solids such as scattering, tunnelling, and recombination occur on characteristic times scale of picoseconds, i.e., in the THz frequency range. Therefore, the THz wave can be utilized for studying the conduction dynamics of the electron.

In order to obtain some basic parameter like scattering time, carrier density, a general approach is to fit the conductivity spectra into some models like Drude model or Drude-Smith model. Drude treats the electrons as non-interacting classical gas which leads to mean free path in nanometer scale range. Therefore, in NMs, it is obvious that the electron gets back scattered from the grain boundary before it could finish its mean free path. Smith incorporates the back scattering parameter into Drude model and till now, most of the researchers utilize this model for many systems. However, it is not correct to use this model in case of bad conductor where there is no free electron. In ferrites, polaron is the fundamental carrier for electrical transportation and their hopping is the main mechanism for conduction.¹⁵³

In an attempt to solve the problem of environmental pollution due to improper management of industrial water, the industrial dye effluents need to be effectively treated before being discharged into the environment. Due to large specific surface area, chemical stability, facile separation, and low cost of synthesis, ferrite NMs have attracted tremendous attention of the current researchers in this regards. Moreover, the biocompatibility of ferrite NSs can be utilized in removing the biologically harmful dye, bilirubin which is responsible for jaundice, hyperbilirubinemia, and neurotoxicity. The conventional treatments for hyperbilirubinemia include exchange blood transfusion which consists of passage of patient's blood through a column with absorptive materials. Therefore, excellent adsorption activity of ferrite NMs can replace the commercially available activated carbon and resin which are generally used for this purpose.

The key focus of this thesis, is

- We have synthesized transition metal oxide (Fe_3O_4 , CoFe_2O_4 , and MnFe_2O_4) based magnetic NSs (NPs and NHSs) by different chemical synthesis procedures.
- We have enhanced as well as tuned the H_c of the 3d-transition metal oxide based magnetic NSs.
- We have studied their EM responses in high frequency THz region since they are highly magnetic as well as highly resistive in nature; also show no eddy current and no corrosion in contrast to the metal.
- We have developed a theoretical model to describe the conductivity of ferrite NSs since polaron plays key role in determining their electrical transport property instead of electron.
- We have carried out some practical biomedical and environmental applications utilizing ferrite NSs.

1.10. Organization of Thesis

The entire thesis has been divided into eight different chapters. A brief sketch of the chapters is given below.

Chapter 1 gives a brief introduction about transition metal based different magnetic NSs, their crystal structure, magnetic, EM, electrical conduction, and adsorption properties. Here we have also discussed the necessity of surface functionalization of NMs, types, procedures, and consequences of surface modification on different properties of NMs, particularly the enhancement of magnetic properties in the light of LFT. Moreover, the motivation of thesis work and the outline of work done are also included.

Chapter 2 provides the synthesis procedures of different NSs, and various characterization techniques including instrumental details and experimental methods.

Chapter 3 describes the synthesis of functionalized CoFe_2O_4 NPs through co-precipitation route with different ionic surfactants in order to study their magnetic responses depending on nature of head and chain-length of tail group of surfactant. Meticulous investigation through VSM along with theoretical support from literature unfold that LMCT transition from the surfactant to the energy level of metal ions of NPs plays key role in controlling the magnetic properties of functionalized CoFe_2O_4 NPs.

Chapter 4 demonstrates the effect of nature and the number of donor head group as well as chain-length of tail group of surfactant on the magnetic response of surfactant coordinated CoFe_2O_4 NPs. Detailed study reveals that the ligand that induces smallest CFSE results in strongest ferrimagnetic activation of the functionalized CoFe_2O_4 NPs. Moreover, H_c is found to increase with increasing chain-length of the surface binding ligand.

Chapter 5 exhibits synthesis and detailed morphology, size, and non-magnetic SiO_2 coating effect on the magnetic responses of as-synthesized different MFe_2O_4 (M= Fe, Co, and Mn) NSs such as NPs and NHSs of different diameter.

Chapter 6 demonstrates the morphology, size dependent EM responses of as-synthesized MFe_2O_4 (M= Fe, and Co) NSs in the THz frequency limit in detail. Further, a model has been developed confirming the polaronic transport property in semi-metallic NMs.

Chapter 7 shows an unprecedented bilirubin adsorption efficiency of CoFe_2O_4 and SiO_2 coated CoFe_2O_4 NSs, specifically NPs and NHSs in contrast to the commercially available activated carbon and resin which are generally used for hemoperfusion and hemodialysis.

Chapter 8 demonstrates an unprecedented dye adsorption capability of CoFe_2O_4 NHSs and the influence of different functional group of dye on their adsorption rate.

Chapter 9 concludes the thesis with an idea about the scope for future work in this direction.

Bibliography

- [1] Martín, J. I.; Nogués, J.; Liu, K.; Vicent, J. L.; Schuller, I. K., Ordered magnetic nanostructures: fabrication and properties. *Journal of Magnetism and Magnetic Materials* 2003, **256**, 449.
- [2] Bose, S.; Banerjee, R.; Genc, A.; Raychaudhuri, P.; Fraser, H. L.; Ayyub, P., Size induced metal-insulator transition in nanostructured niobium thin films: intra-granular and inter-granular contributions. *Journal of Physics: Condensed Matter* 2006, **18**, 4553.
- [3] Cox, A. J.; Loudereback, J. G.; Bloomfield, L. A., Experimental observation of magnetism in rhodium clusters. *Physical Review Letters* 1993, **71**, 923.
- [4] Cox, A. J.; Loudereback, J. G.; Apsel, S. E.; Bloomfield, L. A., Magnetism in 4d-transition metal clusters. *Physical Review B* 1994, **49**, 12295.
- [5] Rabani, E.; Reichman, D. R.; Geissler, P. L.; Brus, L. E., Drying-mediated self-assembly of nanoparticles. *Nature (London)* 2003, **426**, 271.
- [6] Sun, S., Recent Advances in Chemical Synthesis, Self-Assembly, and Applications of FePt Nanoparticles. *Advance Materials* 2006, **18**, 393.
- [7] Cao, S. W.; Zhu, Y. J.; Ma, M. Y.; Li, L. J.; Zhang, L. J., Hierarchically nanostructured magnetic hollow spheres of Fe₃O₄ and γ -Fe₂O₃: preparation and potential application in drug delivery. *Journal of Physical Chemistry C* 2008, **112**, 1851.
- [8] Hyeon, T.; Lee, S. S.; Park, J.; Chung, Y.; Na, H. B., Synthesis of highly crystalline and monodisperse maghemite nanocrystallites without a size-selection process. *Journal of American Chemical Society* 2001, **123**, 12798.
- [9] Woo, K.; Lee, H. J.; Ahn, J.; Park, Y. S., Sol-gel mediated synthesis of Fe₂O₃ nanorods. *Advance Materials* 2003, **15**, 1761.
- [10] Wang, Y.; Teng, X.; Wang, J.; Yang, H., Solvent-free atom transfer radical polymerization in the synthesis of Fe₂O₃@polystyrene core-shell nanoparticles. *Nano Letters* 2003, **3**, 789.
- [11] Caruso, F.; Spasova, M.; Susa, A.; Giersig, M.; Caruso, R. A., Magnetic nanocomposite particle and hollow spheres constructed by a sequential layering approach. *Chemistry of Material* 2001, **13**, 109.
- [12] Kim, D. K.; Zhang, Y.; Kehr, J.; Klason, T.; Bjelke, B.; Muhammed, M. J., Characterization and MRI study of surfactant-coated superparamagnetic nanoparticles administered into the Rat Brain. *Journal of Magnetism and Magnetic Materials* 2001, **225**, 256.
- [13] Guan, N.; Wang, Y.; Sun, D.; Xu, J., A simple one-pot synthesis of single-crystalline magnetite hollow spheres from a single iron precursor. *Nanotechnology* 2009, **20**, 105603.
- [14] Lopez-Sanchez, J. A.; Dimitratos, N.; Hammond, C.; Brett, G. L.; Kesavan, L.; White, S.; Miedziak, P.; Tiruvalam, R.; Jenkins, R. L.; Carley, A. F.; Knight, D.; Kiely, C. J.; Hutchings, G. J., Facile Removal of stabilizer-ligands from supported gold nanoparticles. *Nature Chemistry* 2011, **3**, 551.
- [15] Brollo, M. E. F.; López-Ruiz, R.; Muraca, D.; Figueroa, S. J. A.; Pirota, K. R.; Knobel, M., Compact Ag@Fe₃O₄ core-shell nanoparticles by means of single-step thermal decomposition reaction. *Scientific Reports* 2014, **4**, 6839.
- [16] Alamo, J. A. del, Nanometre-scale electronics with III-V compound semiconductors. *Nature* 2011, **479**, 317.
- [17] Erwin, S. C.; Zu, L.; Haftel, M. I.; Efros, A. L.; Kennedy, T. A.; Norris, D. J., Doping semiconductor nanocrystals. *Nature* 2005, **436**, 91.
- [18] Cheng, C. J.; Tietjen, G. T.; Saucier-Sawyer, J. K.; Saltzman, W. M., A holistic approach to targeting disease with polymeric nanoparticles. *Nature Reviews Drug Discovery* 2015, **14**, 239.

- [19] Ren, W.; Cheng, H.-M., The global growth of graphene. *Nature Nanotechnology* 2014, **9**, 726.
- [20] Novoselov, K. S.; Falko, V. I.; Colombo, L.; Gellert, P. R.; Schwab, M. G.; Kim, K., A Roadmap for graphene. *Nature* 2012, **490**, 192.
- [21] Juliano, R., Nanomedicine: Is the wave cresting? *Nature Reviews Drug Discovery* 2013, **12**, 171.
- [22] Veiseh, O.; Tang, B. C.; Whitehead, K. A.; Anderson, D. G.; Langer, R., Managing diabetes with nanomedicine: challenges and opportunities. *Nature Reviews Drug Discovery* 2015, **14**, 45.
- [23] Larcher, D.; Tarascon, J. M., Towards greener and more sustainable batteries for electrical energy storage. *Nature Chemistry* 2015, **7**, 19.
- [24] Arico, A. S.; Bruce, P.; Scrosati, B.; Tarascon, J.-M.; van Schalkwijk, W., Nanostructured materials for advanced energy conversion and storage devices. *Nature Materials* 2005, **4**, 366.
- [25] Hashmi, A. S. K.; Hutchings, G. J., Gold catalysis. *Angewandte Chemie International Edition* 2006, **45**, 7896.
- [26] Grunwaldt, J.-D.; Kiener, C.; Wögerbauer, C.; Baiker, A., Preparation of supported gold catalysts for low-temperature CO oxidation via "size-controlled" gold colloids. *Journal of Catalysis* 1999, **181**, 223.
- [27] Garadkar, K. M.; Ghule, L. A.; Sapnar, K. B.; Dhole, S. D., A facile synthesis of ZnWO₄ nanoparticles by microwave assisted technique and its application in photocatalysis. *Materials Research Bulletin* 2013, **48**, 1105.
- [28] Zhang, W.; Li, X.; Zou, R.; Wu, H.; Shi, H.; Yu, S.; Liu, Y., Multifunctional glucose biosensors from Fe₃O₄ nanoparticles modified chitosan/graphene nanocomposites. *Scientific Reports* 2015, **5**, 11129.
- [29] Corr, S. A., Metal oxide nanoparticles. In nanoscience: Volume 1: Nanostructures through chemistry. *The Royal Society of Chemistry* 2013, **1**, 180.
- [30] Zhao, Z.; Zhou, Z.; Bao, J.; Wang, Z.; Hu, J.; Chi, X.; Ni, K.; Wang, R.; Chen, X.; Chen, Z.; Gao, J., Octapod iron oxide nanoparticles as high-performance T₂ contrast agents for magnetic resonance imaging. *Nature Communication* 2013, **4**, 2266.
- [31] Li, C.; Han, X.; Cheng, F.; Hu, Y.; Chen, C.; Chen, J., Phase and composition controllable synthesis of cobalt manganese spinel nanoparticles towards efficient oxygen electrocatalysis. *Nature Communication* 2015, **6**, 1.
- [32] Xiao, J.; Tian, X. M.; Yang, C.; Liu, P.; Luo, N. Q.; Liang, Y.; Li, H. B.; Chen, D. H.; Wang, C. X.; Li, L.; Yang, G. W., Ultrahigh relaxivity and safe probes of manganese oxide nanoparticles for in vivo imaging. *Scientific Reports* 2013, **3**, 3424.
- [33] Zhang, M.; de Respinis, M.; Frei, H., Time-resolved observations of water oxidation intermediates on a cobalt oxide nanoparticle catalyst. *Nature Chemistry* 2014, **6**, 362.
- [34] Hankare, P. P.; Pandav, R. S.; Patil, R. P.; Vader, V. T.; Garadkar, K. M., Synthesis, structural and magnetic properties of copper substituted nickel manganite. *Journal of Alloys Compound* 2012, **544**, 197.
- [35] Blanco-Andujar, C.; Ortega, D.; Southern, P.; Pankhurst, Q. A.; Thanh, N. T. K., High performance multi-core iron oxide nanoparticles for magnetic hyperthermia: microwave synthesis, and the role of core-to-core interactions. *Nanoscale* 2015, **7**, 1768.
- [36] Kim, D. K.; Amin, M. S.; Elborai, S.; Lee, S-H; Koseoglu, Y.; Zahn, M.; Muhammed, M., Energy absorption of superparamagnetic iron oxide nanoparticles by microwave irradiation. *Journal of Applied Physics* 2005, **97**, 10J510.
- [37] Cao, D.; Wang, X.; Pan, L.; Li, H.; Jing, P.; Wang, J.; Liu, Q., Nonmetal sulfur-doped coral-like cobalt ferrite nanoparticles with enhanced magnetic properties. *Journal of Material Chemistry C* 2016, **4**, 951.

- [38] Skoropata, E.; Desautels, R. D.; Chi, C.-C.; Ouyang, H.; Freeland, J. W.; Lierop, J. van, Magnetism of iron oxide based core-shell nanoparticles from interface mixing with enhanced spin-orbit coupling. *Physical Review B* 2014, **89**, 024410.
- [39] Pal, D.; Mandal, M.; Chaudhuri, A.; Das, B.; Sarkar, D.; Mandal, K., Micelles induced high coercivity in single domain cobalt-ferrite nanoparticles. *Journal of Applied Physics* 2010, **108**, 124317.
- [40] Zhuo, R. F.; Feng, H. T.; Chen, J. T.; Yan, D.; Feng, J. J.; Li, H. J.; Geng, B. S.; Cheng, S.; Xu, X. Y.; Yan, P. X., Multistep synthesis, growth mechanism, optical, and microwave absorption properties of ZnO dendritic nanostructures. *Journal of Physical Chemistry C* 2008, **112**, 11767.
- [41] Tong, G.; Wu, W.; Qiao, R.; Yuan, J.; Guan, J.; Qian, H., Morphology dependence of static magnetic and microwave electromagnetic characteristics of polymorphic Fe₃O₄ nanomaterials. *Journal of Materials Research* 2011, **26**, 1639.
- [42] Li, X.; Zhang, B.; Ju, C.; Han, X.; Du, Y.; Xu, P., Morphology controlled synthesis and electromagnetic properties of porous Fe₃O₄ nanostructures from iron alkoxide precursors. *Journal of Physical Chemistry C* 2011, **115**, 12350.
- [43] Du, Y.; Liu, W.; Qiang, R.; Wang, Y.; Han, X.; Ma, J.; Xu, P., Shell thickness-dependent microwave absorption of core-shell Fe₃O₄@C composites. *ACS Applied Materials and Interfaces* 2014, **6**, 12997.
- [44] Li, X.; Han, X.; Tan, Y.; Xu, P., Preparation and microwave absorption properties of Ni-B alloy-coated Fe₃O₄ particles. *Journal of Alloys and Compounds* 2008, **464** 352.
- [45] Verwey, J. W.; Heilmann, E. L., Physical properties and cation arrangement of oxides with spinel structures I. cation arrangement in spinels. *Journal of Chemical Physics* 1947, **15**, 4.
- [46] Sickafus, K. E.; Wills, J. M.; Grimes, N. W., Structure of spinel. *Journal of American Ceramics Society* 1999, **82**, 3279.
- [47] Harris, V. G.; Koon, N. C.; Williams, C. M.; Zhang, Q.; Abe, M.; Kirkland, J. P., Cation distribution in NiZn-ferrite films via extended X-ray absorption fine structure. *Applied Physics Letters* 1996, **68**, 2082.
- [48] Daliya, S. M.; Juang, R. S., An overview of the structure and magnetism of spinel ferrite nanoparticles and their synthesis in microemulsions. *Chemical Engineering Journal* 2007, **129**, 51.
- [49] Uyeda, H. T.; Medintz, I. L.; Jaiswal, J. K.; Simon, S. M.; Mattoussi, H., Synthesis of compact multidentate ligands to prepare stable hydrophilic quantum dot fluorophores. *Journal of American Chemical Society* 2005, **127**, 3870.
- [50] Giri, A.; Goswami, N.; Bootharaju, M. S.; Xavier, P. L.; John, R.; Thanh, N. T. K.; Pradeep, T.; Ghosh, B.; Raychaudhuri, A. K.; Pal, S. K., Emergence of multicolor photoluminescence in La_{0.67}Sr_{0.33}MnO₃ nanoparticles. *Journal of Physical Chemistry C* 2012, **116**, 25623.
- [51] Vestal, C. R.; Zhang, Z. J., Effects of Surface coordination chemistry on the magnetic properties of MnFe₂O₄ spinel ferrite nanoparticles. *Journal of American Chemical Society* 2003, **125**, 9828.
- [52] Huheey, J. E.; Keiter, E. A.; Keiter, R. L.; Medhi, O. K., Inorganic chemistry: principles of structure and reactivity (Pearson Education, South Asia, 2006).
- [53] Shao, H.; Huang, Y.; Lee, H.; Suh, Y. J.; Kim, C. O., Effect of PVP on the morphology of cobalt nanoparticles prepared by thermal decomposition of cobalt acetate. *Current Applied Physics* 2006, **6**, e195.
- [54] Wen-yao, H.; Guo.-cai, X., Characterization of nano-Ag/PVP composites synthesized via ultra-violet irradiation. *Journal of coal Science and Engineering* 2010, **16**, 188.
- [55] Bethe, H., Splitting of terms in crystals. *Annalen der Physik* 1929, **3**, 133.

- [56] Neel, L., Anisotropie magnétique superficielle et surstructures d'orientation. *Journal of Physics Radium* 1954, **15**, 225.
- [57] Skomski, R.; Coey, J. M. D., Permanent magnetism (Institute of Physics, Bristol, 1999)
- [58] Osborn, J. A., Demagnetizing factors of the general ellipsoid. *Physical Review* 1945, **67**, 351.
- [59] Sarkar, D.; Mandal, M., Static and dynamic magnetic characterization of DNA-templated chain-like magnetite nanoparticles. *Journal of Physical Chemistry C* 2012, **116**, 3227.
- [60] Batlle, X.; Labarta, A., Finite-size effects in fine particles: magnetic and transport properties. *Journal of Physics D: Applied Physics* 2002, **35**, R15.
- [61] Cullity, B. D., Introduction to magnetic materials (Addison-Wesley, Reading, Massachusetts, 1972).
- [62] Neel, L., Théorie du traînage magnétique des ferromagnétiques en grains fins avec application aux terres cuites. *Annales de Géophysique* 1949, **5**, 99.
- [63] Gangopadhyay, S.; Hadjipanayis, G. C.; Dale, B.; Sorensen, C. M.; Klabunde, V. Papaefthymiou, K. J.; Kostikas, A.; Magnetic properties of ultrafine iron particles. *Physical Review B* 1992, **45**, 9778.
- [64] Parker, F. T.; Berkowitz, A. E., Field response of surface spins on Co-adsorbed γ -Fe₂O₃. *Physical Review B* 1991, **44**, 7437.
- [65] Tielking, N. E.; Jones, R. R., Coherent population transfer among Rydberg states by subpicosecond, half-cycle pulses. *Physical Review A* 1995, **52**, 1371.
- [66] Ahn, J.; Weinacht, T. C.; Bucksbaum, P. H., Quantum information storage and retrieval in rydberg wave packets. *Science* 2000, **287**, 463.
- [67] Ahn, J.; Hutchinson, D. N.; Rangan, C.; Bucksbaum, P. H., Quantum phase retrieval of a rydberg wave packet using a half-cycle pulse. *Physical Review Letters* 2001, **86**, 1179.
- [68] Cole, B. E.; Williams, J. B.; King, B. T.; Sherwin, M. S.; Stanley, C. R., Coherent manipulation of semiconductor quantum bits with terahertz radiation. *Nature* 2001, **410**, 60.
- [69] Nordstrom, K. B.; Johnsen, K.; Allen, S. J.; Jauho, A.-P.; Birnir, B.; Kono, J.; Noda, T.; Akiyama, H.; Sakaki, H., Excitonic dynamical Franz-Keldysh effect. *Physical Review Letters* 1998, **81**, 457.
- [70] Carter, S. G.; Birkedal, V.; Wang, C. S.; Coldren, L. A.; Maslov, A. V.; Citrin, D. S.; Sherwin, M. S., Quantum coherence in an optical modulator. *Science* 2005, **310**, 651.
- [71] Kida, N.; Murakami, H.; Tonouchi, M., in Terahertz optoelectronics, edited by K. Sakai (Springer-Verlag, Berlin, 2005), Chap. 6, pp. 275–334.
- [72] Schall, M.; Walther, M.; Jepsen, P. Uhd, Fundamental and second-order phonon processes in CdTe and ZnTe. *Physical Review B* 2001, **64**, 094301.
- [73] Harde, H.; Keiding, S.; Grischkowsky, D., THz commensurate echoes: Periodic rephasing of molecular transitions in free-induction decay. *Physical Review Letters* 1991, **66**, 1834.
- [74] Globus, T.; Woolard, D.; Khromova, T.; Crowe, T.; Bykhovskaia, M.; Gelmont, B.; Hesler, J.; Samuels, A., THz-spectroscopy of biological molecules. *Journal of Biological Physics* 2003, **29**, 89.
- [75] Ghasemi, A.; Morisako, A.; Structural and electromagnetic characteristics of substituted strontium hexaferrite nanoparticles. *Journal of Magnetism and Magnetic Materials* 2008, **320**, 1167.
- [76] Du, L., Du, Y., Li, Y.; Wang, J.; Wang, C.; Wang, X.; Xu, P.; Han, X., Surfactant-assisted solvothermal synthesis of Ba(CoTi)_xFe_{12-2x}O₁₉ nanoparticles and enhancement in microwave absorption properties of polyaniline. *Journal of Physical Chemistry C* 2010, **114**, 19600.
- [77] Wang, Z. H.; Han, Z.; Geng, D. Y.; Zhang, Z. D., Synthesis, characterization and microwave absorption of carbon coated Sn nanorods. *Chemical Physics Letters* 2010, **489**, 187.

- [78] Stojanovic, G.; Damjanovic, M.; Desnica, V.; Zivanov, L.; Raghavendra, R.; Bellew, P.; Mcloughlin, N., High performance zig-zag and meander inductors embedded in ferrite material. *Journal of Magnetism and Magnetic Materials* 2006, **297**, 76.
- [79] Lai, K.; Sun, R. J.; Chen, M. Y.; Wu, H.; Zha, A. X., Electromagnetic shielding effectiveness of fabrics with metallized polyester filaments. *Textile Research Journals* 2007, **77**, 242.
- [80] Roh, J. S.; Chi, Y. S.; Kang, T. J.; Nam, S. W., Electromagnetic shielding effectiveness of multifunctional metal composite fabrics. *Textile Research Journal* 2008, **78**, 825.
- [81] Brzeziński, S.; Rybicki, T.; Karbownik, I.; Malinowska, G.; Rybicki, E.; Szugajew, L.; Lao, M.; Śledzińska, K., Textile Multi-layer systems for protection against electromagnetic radiation. *Fibres and Textiles in Eastern Europe* 2009, **17**, 66.
- [82] Chung, D. D. L., Materials for electromagnetic interference shielding. *Journal of Materials Engineering and Performance* 2000, **9**, 350.
- [83] Motojima, S.; Noda, Y.; Hoshida, S.; Hishikawa, Y., Electromagnetic wave absorption property of carbon microcoils in 12–110 GHz region. *Journal of Applied Physics* 2003, **94**, 2325.
- [84] Chen, Y. J.; Xiao, G.; Wang, T. S.; Ouyang, Q. Y.; Qi, L. H.; Ma, Y.; Gao, P.; Zhu, C. L.; Cao, M. S.; Jin, H. B., Porous Fe₃O₄/Carbon Core/Shell nanorods: synthesis and electromagnetic properties. *Journal of Physical Chemistry C* 2011, **115**, 13603.
- [85] Chen, Y. J.; Zhang, F.; Zhao, G. G.; Fang, X. Y.; Jin, H. B.; Gao, P.; Zhu, C. L.; Cao, M. S.; Xiao, G., Direct incorporation of magnetic constituents within ordered mesoporous carbon-silica nanocomposites for highly efficient electromagnetic wave absorbers. *Journal of Physical Chemistry C* 2010, **114**, 9239.
- [86] Chen, Y. J.; Gao, P.; Wang, R. X.; Zhu, C. L.; Wang, L. J.; Cao, M. S.; Jin, H. B., Porous Fe₃O₄/SnO₂ core/shell nanorods: synthesis and electromagnetic properties. *Journal of Physical Chemistry C* 2009, **113**, 10061.
- [87] Zhu, C. L.; Zhang, M. L.; Qiao, Y. J.; Xiao, G.; Zhang, F.; Chen, Y. J., Fe₃O₄/TiO₂ Core/Shell nanotubes: synthesis and magnetic and electromagnetic wave absorption characteristics. *Journal of Physical Chemistry C* 2010, **114**, 16229.
- [88] Liu, J. W.; Che, R. C.; Chen, H. J.; Zhang, F.; Xia, F.; Wu, Q. S.; Wang, M., Microwave absorption enhancement of multifunctional composite microspheres with spinel Fe₃O₄ cores and anatase TiO₂ shells. *Small* 2012, **8**, 1214.
- [89] Wang, G. Z.; Gao, Z.; Tang, S. W.; Chen, C. Q.; Duan, F. F.; Zhao, S. C.; Lin, S. W.; Feng, Y. H.; Zhou, L.; Qin, Y., Microwave absorption properties of carbon nanocoils coated with highly controlled magnetic materials by atomic layer deposition. *ACS Nano* 2012, **6**, 11009.
- [90] Liu, J.; Cheng, J.; Che, R.; Xu, J.; Liu, M.; Liu, Z., Synthesis and microwave absorption properties of yolk-shell microspheres with magnetic iron oxide cores and hierarchical copper silicate shells. *ACS Applied Materials and Interfaces* 2013, **5**, 2503.
- [91] Cao, G., Nanostructures and nanomaterials: Synthesis, properties, and applications (Imperial College Press, United Kingdom, 2004)
- [92] Muthuselvan, I. P.; Bhowmik, R. N., Connectivity between electrical conduction and thermally activated grain size evolution in Ho-doped CoFe₂O₄ ferrite. *Journal of Physics D: Applied Physics* 2010, **43**, 465002.
- [93] Ponpandian, N.; Narayanasamy, A., Influence of grain size and structural changes on the electrical properties of nanocrystalline zinc ferrite. *Journal of Applied Physics* 2002, **92**, 2770.
- [94] Zhao, J.; Buia, C.; Han, J.; Lu, J. P., Quantum transport properties of ultrathin silver nanowires. *Nanotechnology* 2003, **14**, 501.

- [95] Heo, Y. W.; Norton, D. P.; Tien, L. C.; Kwon, Y.; Kang, B. S.; Ren, F.; Pearton, S. J.; LaRoche, J. R., ZnO nanowire growth and devices. *Materials Science and Engineering : R* 2004, **47**, 1.
- [96] Nemeč, H.; Kuzel, P.; Sundstrom, V., Charge transport in nanostructured materials for solar energy conversion studied by time-resolved terahertz spectroscopy. *Journal of Photochemistry and Photobiology A: Chemistry* 2010, **215**, 123.
- [97] Averitt, R. D.; Taylor, A. J., Ultrafast optical and far-infrared quasiparticle dynamics in correlated electron material. *Journal of Physics: Condensed Matter* 2002, **14**, R1357.
- [98] Basov, D. N.; Averitt, R. D.; Marel, D. van der; Dressel, M.; Haule, K., Electrodynamics of correlated electron materials. *Reviews of Modern Physics* 2011, **83**, 471.
- [99] Nienhuys, H. K.; Sundstrom, V., Influence of plasmons on terahertz conductivity measurements. *Applied Physics Letters* 2005, **87**, 012101.
- [100] Parkinson, P.; Lloyd-Hughes, J.; Gao, Q.; Tan, H. H.; Jagadish, C.; Johnston, M. B.; Herz, L. M., Transient terahertz conductivity of GaAs nanowires. *Nano Letters* 2007, **7**, 2162.
- [101] Pitarke, J. M.; Silkin, V. M.; Chulkov, E. V.; Echenique, P. M., Theory of surface plasmons and surface-plasmon polaritons. *Reports on Progress in Physics* 2007, **70**, 1.
- [102] Smith, N.V., Classical generalization of the Drude formula for the optical conductivity. *Physical Review B* 2001, **64**, 155106.
- [103] Thoman, A.; Kern, A.; Helm, H.; Walther, M., Nanostructured gold films as broadband terahertz antireflection coatings. *Physical Review B* 2008, **77**, 195405.
- [104] Lovrinčić, R.; Pucci, A., Infrared optical properties of chromium nanoscale films with a phase transition. *Physical Review B* 2009, **80**, 205404.
- [105] Takano, K.; Shibuya, K.; Akiyama, K.; Nagashima, T.; Miyamaru, F.; Hangyo, M., A metal-to-insulator transition in cut-wire-grid metamaterials in the terahertz region. *Journal of Applied Physics* 2010, **107**, 024907.
- [106] Cooke, D. G.; MacDonald, A. N.; Hryciw, A.; Wang, J.; Li, Q.; Meldrum, A.; Hegmann, F. A., Transient terahertz conductivity in photoexcited silicon nanocrystal films. *Physical Review B* 2006, **73**, 193311.
- [107] Fekete, L.; Kuzel, P.; Nemeč, H.; Kadlec, F.; Dejneka, A.; Stuchlick, J.; Fejfar, A., Ultrafast carrier dynamics in microcrystalline silicon probed by time-resolved terahertz spectroscopy. *Physical Review B* 2009, **79**, 115306.
- [108] Mendoza-Galvan, A.; Gonzalez-Hernandez, J., Drude-like behavior of Ge: Sb: Te alloys in the infrared. *Journal of Applied Physics* 2000, **87**, 760.
- [109] Ahn, H.; Ku, Y.-P.; Wang, Y.-C.; Chuang, C.-H., Terahertz spectroscopic study of vertically-aligned InN nanorods. *Applied Physics Letters* 2007, **91**, 163105.
- [110] Nemeč, H.; Kuzel, P.; Sundstrom, V., Far-infrared response of free charge carriers localized in semiconductor nanoparticles. *Physical Review B* 2009, **79**, 115309.
- [111] Shportko, K.; Kremers, S.; Woda, M.; Lencer, D.; Robertson, J.; Wuttig, M., Resonant bonding in crystalline phase-change materials. *Nature Materials* 2008, **7**, 653.
- [112] Turner, G. M.; Beard, M. C.; Schmittenmaer, C. A., Carrier localization and cooling in dye-sensitized nanocrystalline titanium dioxide. *Journal of Physical Chemistry B* 2002, **106**, 11716.
- [113] Qazilbash, M. M.; Brehm, M.; Chae, B. G.; Ho, P. C.; Andreev, G. O.; Kim, B. J.; Yun, S. J.; Balatsky, A. V.; Maple, M. B.; Kleilmann, F.; Kim, H. T.; Basov, D. N., Mott transition in VO₂ revealed by infrared spectroscopy and nano-imaging. *Science* 2007, **318**, 1750.
- [114] Dyre, J. C., The random free-energy barrier model for ac conduction in disordered solids. *Journal of Applied Physics* 1988, **64**, 2456.
- [115] Dyre, J. C., Universal low-temperature ac conductivity of macroscopically disordered nonmetals. *Physical Review B* 1993, **48**, 12511.
- [116] Shimakawa, K.; Naito, H.; Kasap, S.O., The origin of anomalous optical conductivity in metallic polymers: A unified model. *Philosophical Magazine Letters* 2009, **89**, 673.

- [117] Shimakawa, K.; Itoh, T.; Naito, H.; Kasap, S. O., The origin of non-Drude terahertz conductivity in nanomaterials. *Applied Physics Letters* 2012, **100**, 132102.
- [118] Rai, H. S.; Bhattacharyya, M. S.; Singh, J.; Bansal, T. K.; Vats, P.; Banerjee, U. C., Removal of dyes from the effluent of textile and dyestuff manufacturing industry: a review of emerging techniques with reference to biological treatment. *Critical Reviews in Environmental Science and Technology* 2005, **35**, 219.
- [119] Midha, V.; Dey, A., Biological treatment of tannery waste water for sulfide removal journal of international. *Chemical Science* 2009, **6**, 472.
- [120] García-Montaño, J.; Domènech, X.; García-Hortal, J. A.; Torrades, F.; Peral, J., The testing of several biological and chemical coupled treatments for Cibacron Red FN-R azo dye removal. *Journal of Hazardous Materials* 2008, **154**, 484.
- [121] Koupaie, E. H.; Moghaddam, M. R. A.; Hashemi, S. H., Post-treatment of an aerobically degraded azo dye acid red 18 using aerobic moving bed bio-film process: enhanced removal of aromatic amines. *Journal of Hazardous Materials* 2011, **195**, 147.
- [122] Körbahti, B. K.; Artut, K.; Geçgel, C.; Özer, A., Electrochemical decolorization of textile dyes and removal of metal ions from textile dye and metal ion binary mixtures. *Chemical Engineering Journal* 2011, **173**, 677.
- [123] Alventosa-deLara, E.; Barredo-Damas, S.; Alcaina-Miranda, M. I.; Iborra-Clar, M. I., Ultrafiltration technology with a ceramic membrane for reactive dye removal: optimization of membrane performance. *Journal of Hazardous Materials* 2012, **209-210**, 492.
- [124] Zhang, G.; Yi, L.; Deng, H.; Sun, P., Dyes adsorption using a synthetic carboxymethyl cellulose-acrylic acid adsorbent. *Journal of Environmental Science* 2014, **26**, 1203.
- [125] Carrott, P. J. M.; Carrott, M. M. L. R.; Roberts, R. A., Physical adsorption of gases by microporous carbons. *Colloids and Surfaces* 1991, **58**, 385.
- [126] Shinke, K.; Ando, K.; Koyama, T.; Takai, T.; Nakaji, S.; Ogino, T., Properties of various carbon nanomaterial surfaces in bilirubin adsorption. *Colloids and Surfaces B: Biointerfaces* 2010, **77**, 18.
- [127] Abdullah, A. Z.; Salamatinia, B.; Kamaruddin, A. H., Application of response surface methodology for the optimization of NaOH treatment on oil palm frond towards improvement in the sorption of heavy metals. *Desalination* 2009, **244**, 227.
- [128] Marsh, H.; Rodríguez-Reinoso, F., Activated carbon (Elsevier Science Ltd, Oxford, 2006).
- [129] Zhou, L.; Gao, C.; Xu, W., Magnetic dendritic materials for highly efficient adsorption of dyes and drugs. *ACS Applied Materials and Interfaces* 2010, **2**, 1483.
- [130] Qadri, S.; Ganoe, A.; Haik, Y., Removal and recovery of acridine orange from solutions by use of magnetic nanoparticles. *Journal of Hazardous Materials* 2009, **169**, 318.
- [131] Afkhami, A.; Moosavi, R., Adsorptive removal of congo red, a carcinogenic textile dye, from aqueous solutions by maghemite nanoparticles. *Journal of Hazardous Materials* 2010, **174**, 398.
- [132] Weber, W. J.; Morriss, J. C., Kinetics of adsorption on carbon from solution. *Journal of the Sanitary Engineering Division. by. American Society of Civil Engineers* 1963, **89**, 31.
- [133] Lagergren, S., About the theory of so-called adsorption of soluble substance. *Kungliga Svenska Vetenskapsakademiens Handlingar* 1898, **24**, 1.
- [134] Ho, Y.S.; McKay, G., Sorption of dye from aqueous solution by peat. *Chemical Engineering Journal* 1998, **70**, 115.
- [135] El-Guendi, M., Homogeneous surface diffusion model of basic dyestuffs onto natural clay in batch adsorbers. *Adsorption Science and Technology* 1991, **8**, 217.
- [136] Langmuir, I., Adsorption of gases on plain surfaces of glass mica platinum. *Journal of American Chemical Society* 1918, **40**, 136.
- [137] Freundlich, H.M.F., Über die adsorption in losungen. *Journal of Physical Chemistry* 1906, **57**, 385.

- [138] Haghseresht, F.; Lu, G., Adsorption characteristics of phenolic compounds onto coal-reject-derived adsorbents. *Energy Fuels* 1998, **12**, 1100.
- [139] Fytianos, K.; Voudrias, E.; Kokkalis, E., Sorption-desorption behavior of 2,4-dichlorophenol by marine sediments. *Chemosphere* 2000, **40**, 3.
- [140] Dada, A. O.; Olalekan, A. P.; Olatunya, A. M.; Dada, O.; Langmuir, Freundlich, Temkin and Dubinin-Radushkevich isotherms studies of equilibrium sorption of Zn^{2+} unto phosphoric acid modified rice husk. *IOSR Journal of Applied Chemistry* 2012, **3**, 38.
- [141] Franco Jr., A.; e Silva, F. C., High temperature magnetic properties of cobalt ferrite nanoparticles. *Applied Physics Letters* 2010, **96**, 172505.
- [142] Liu, C.; Zou, B.; Rondinone, A. J.; Zhang, Z. J., Chemical control of superparamagnetic properties of magnesium and cobalt spinel ferrite nanoparticles through atomic level magnetic couplings. *Journal of American Chemical Society* 2000, **122**, 6263.
- [143] Chikazumi, S., Physics of magnetism (Wiley, New York, 1969).
- [144] Mohaideen, K. K.; Joy, P. A., High magnetostriction and coupling coefficient for sintered cobalt ferrite derived from superparamagnetic nanoparticles. *Applied Physics Letters* 2012, **101**, 072405.
- [145] Haun, J. B.; Yoon, T.-J.; Lee, H.; Weissleder, R., Magnetic nanoparticle biosensors. *Wiley Interdisciplinary Reviews: Nanomedicine and Nanobiotechnology* 2010, **2**, 291.
- [146] Kyeong, S.; Jeong, C.; Kang, H.; Cho, H. -J.; Park, S.-J.; Yang, J.-K.; Kim, S.; Kim, H.-M.; Jun, B.-H.; Lee, Y.-S., Double-layer magnetic nanoparticle embedded silica particles for efficient bio-separation. *Public Library of Science One* 2015, **10**, e0143727.
- [147] Lee, J.-H.; Huh, Y.-M.; Jun, Y.-W.; Seo, J.-W.; Jang, J.-T.; Song, H.-T.; Kim, S.; Cho, E.-J.; Yoon, H.-G.; Suh, J.-S.; Cheon, J., Artificially engineered magnetic nanoparticles for ultra-sensitive molecular imaging. *Nature Medicine* 2007, **13**, 95.
- [148] Reiss, G.; Hütten, A., Magnetic nanoparticles: applications beyond data storage. *Nature Materials* 2005, **4**, 725.
- [149] Bañobre-López, M.; Teijeiro, A.; Rivas, J., Magnetic nanoparticle-based hyperthermia for cancer treatment. *Reports of Practical Oncology and Radiotherapy* 2013, **18**, 397.
- [150] Granitzer, P.; Rumpf, K.; Gonzalez, R.; Coffey, J.; Reissner, M., Magnetic properties of superparamagnetic nanoparticles loaded into silicon nanotubes. *Nanoscale Research Letters* 2014, **9**, 413.
- [151] Song, Q.; Zhang, Z. J., Shape control and associated magnetic properties of spinel cobalt ferrite nanocrystals. *Journal of American Chemical Society* 2004, **126**, 6164.
- [152] Tonouchi, M., Cutting-edge terahertz technology. *Nature Photonics* 2007, **1**, 97.
- [153] Tannhauser, D. S., Conductivity in iron oxides. *Journal of Physics and Chemistry of Solids* 1962, **23**, 25.

Chapter 2 | Experimental Details

The chapter describes different synthesis techniques of 3d transition metal oxide based magnetic nanostructures along with their surface coating with SiO₂. Various techniques to characterize their physical, optical, and magnetic properties are also presented herein.

2. Material Synthesis and Characterization Techniques

2.1. Preamble

In this chapter, a brief overview of different experimental procedures such as chemical co-precipitation, solvothermal methods used to synthesize various 3d transition metal oxide based magnetic nanostructures (NSs) along with their SiO₂ coating through Stöber process are described. In addition, the characterization techniques which are employed to investigate their physical, optical, magnetic, and electromagnetic (EM) properties are also presented here.

The phase and morphology of as-synthesized NSs are studied using X-ray Diffraction (XRD), Field Emission Scanning Electron Microscope (FESEM), Transmission Electron Microscope (TEM), High Resolution Transmission Electron Microscope (HRTEM), Energy Dispersive X-ray (EDX) Analysis, Selected Area Electron Diffraction (SAED). The surface and magnetic properties of magnetic nanomaterials (NMs) are characterized by Atomic Force Microscopy (AFM) and Magnetic Force Microscopy (MFM). The oxidation state, spin state, valance state, and co-ordination of an atom in as-synthesized NSs are investigated utilizing Mössbauer Spectroscopy. The phase transition of the sample was studied by the Differential Thermal Analysis (DTA). Spectroscopic analyses are carried out through UV-Visible (UV-Vis) and Fourier Transformed Infrared (FTIR) Spectrometer whereas the high frequency EM responses of the NSs in terahertz (THz) frequency region are characterized through THz-Time Domain Spectroscopy (THz-TDS). The magnetic characterizations are carried out employing Vibrating Sample Magnetometer (VSM) and Superconducting Quantum Interference Device (SQUID).

2.2. Synthesis of Nanoparticles

There are various techniques for the fabrication of different nanostructured materials and all of them can be categorized into two simple groups, (1) top-down (i.e. bulk to nano) and (2) bottom-up (i.e. atom to nano) approaches.

2.2.1. Top-Down Approach

Top-down approach refers to the successive cutting of a bulk material to get nano sized particle. Attrition or milling is a typical top-down method in making nanoparticles (NPs). The biggest problem with milling is the imperfection of surface structure and significant crystallographic defect which in turn lead to extra challenges in the device design and fabrication. However, this approach leads to the bulk production of NMs. Various types of lithographic techniques (such as photo-, ion beam-, electron- or X-ray- lithography) are also examples of top-down approaches which can overcome all the shortcomings of milling, however are still limited by the resolution of the tools, restricting the smallest size of the NSs. In today's life, lithography techniques have been greatly used for the miniaturization of electronic components, such as computer chips, MEMS (micro-electromechanical systems) in consumer products like computer hard drives, and CD and DVD players. High cost of the device and clean room environment, special arrangement to reduce the tremendous heat dissipation for smaller geometry, and wastage of materials limit their uses only to the commercial fields. A brief discussion on photolithography that is applied to prepare the sample holder used in THz-TDS measurement is presented in Section 2.7.3.

2.2.2. Bottom-Up Approach

Bottom up approach refers to the building up of a material from the bottom: atom by atom, molecule by molecule or cluster by cluster. The ability to assemble nanoscale functional building blocks is useful and modular way for scientists to design valuable materials with specific physical and chemical properties.¹ Wet chemical synthesis, self-assembly, molecular fabrication, and electrodeposition are all examples of bottom-up techniques. It is easier and more economical and allows forming NSs of smaller geometry than lithography. However, there are some challenges in fabricating complex, robust nanostructured materials using bottom-up approaches. An overview of different bottom-up approaches for the synthesis of various 3d transition metal oxide magnetic NSs is described in Section 2.4 in detail.

2.3. Formation of Nanoparticles in Wet Chemical Methods

In wet chemical synthesis, homogeneous nucleation occurs when nuclei forms uniformly throughout the parent phase, called supersaturation. This condition can be achieved by rational control of reaction conditions such as solvent, capping agents, temperature etc. The process of homogeneous nuclei formation can be considered thermodynamically by looking at the total free energy (ΔG) of a NP defined as the sum of the surface free energy and the bulk free energy. The overall free energy change (ΔG) associated with the homogeneous nucleation process is the total change in free energy between a small solid particle of a solute and the solute in solution. The excess surface free energy, ΔG_s , is the excess surface energy between the NPs and the corresponding bulk material. Excess volume free energy, ΔG_v , is the excess free energy between a very large particle and the solute in the solution. Dependence of ΔG_s and ΔG_v on particle size with radius (r) can be observed from Equation 2.1 and also depicted in the Figure 2.1.²

$$\Delta G = \Delta G_s + \Delta G_v = 4\pi r^2 \gamma + \frac{4}{3}\pi r^3 \Delta G_v \quad (2.1)$$

where, ΔG_v is the free energy change per unit volume and γ is the interfacial tension between the growing NP surface and the supersaturated solution.

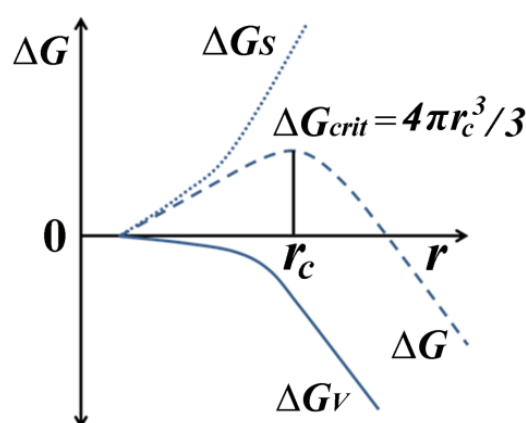


Figure 2.1. Free energy diagram for nucleation process explaining the existence of a “critical nucleus”. (© S. Kumar and T. Nann, *Small* **2**, 316 (2006))

As ΔG_s is always positive and ΔG_v is always negative, it is possible to find a ΔG for a stable nucleus having an optimum size (critical radius, r_c) by differentiating

ΔG with respect to r and setting it to zero, which gives a critical free energy as shown in Equation 2.2. The critical radius is defined in Equation 2.3. It is evident from Figure 2.1, that the total excess free energy, ΔG , passes through a maximum, ΔG_{Crit} , corresponding to the critical nucleus size, r_c ,

$$\left. \frac{d(\Delta G)}{dr} \right|_{r=r_c} = 8\pi r_c \gamma + 4\pi r_c^2 \Delta G_v = 0 \quad (2.2)$$

$$\Rightarrow r_c = -\frac{2\gamma}{\Delta G_v} \quad (2.3)$$

From Equations 2.1 and 2.3, we can obtain the critical value of ΔG as

$$\Delta G|_{r=r_c} = \Delta G_{Crit} = \frac{16\pi\gamma^3}{3(\Delta G_v)^2} = \frac{4\pi\gamma r_c^2}{3} \quad (2.4)$$

i.e. the minimum energy barrier that a nucleation process must overcome is ΔG_{Crit} , which corresponds to the minimum size of a stable spherical nucleus (r_c). This critical radius corresponds to the minimum size at which a particle can survive in solution without being redissolved.

Crystal structure, size, and morphology of the growing particles mainly depend on the system and the reaction parameters. The growth of NPs is dependent on two mechanisms: the surface reaction and the monomer's diffusion to the surface. Different theories have been proposed to explain the nucleation and growth mechanism of various reactions.³ Such as, in the LaMer mechanism, the process of nucleation and growth are divided into three portions. Firstly, a rapid increase in the concentration of free monomers in solution, secondly, the monomer undergoes "burst nucleation" which significantly reduces the concentration of free monomers in solution. The rate of nucleation is described as "effectively infinite" and after this point, nucleation almost stops due to low concentration of monomers and in third stage, the growth occurs under the control of diffusion of monomers through solution. Ostwald and digestive ripening mechanism say that, growth is caused by the change in solubility of NPs which is dependent on their size. According to

Ostwald ripening, due to high solubility and surface energy of smaller particles within solution, they redissolve and in turn allow the larger particles to grow even more. Digestive ripening, described by Lee et al., is effectively the inverse of Ostwald ripening, where smaller particles grow at expense of the larger ones by surface energy controlled process.⁴ The Finke-Watzky two step mechanism is a process of nucleation and growth where both steps happen simultaneously.⁵ The first is a slow continuous nucleation as shown in Equation 2.5 and the second is the autocatalytic surface growth which is not diffusion controlled, as shown in Equation 2.6.



Shape of the crystallites occurs either in order to minimize the surface energy of the particles or because of the kinetics of growth. If kinetics dominates, the shape is then determined by the rate at which different crystal faces grow. In thermal equilibrium, the crystal shape is determined by minimization of surface energy.² An overview of chemical co-precipitation and solvothermal process for the synthesis of 3d transition metal oxide magnetic NPs is presented in detail in Section 2.4.

2.4. Wet Chemical Synthesis of Nanostructures

Wet chemical method refers to a particular group of methods where generally nano- or ultra- dispersed inorganic materials have been produced in aqueous or non-aqueous solutions. It is different from conventional solid state procedure in respect to that it can only be done in liquid phase and more importantly it can produce much smaller, monodispersed grains or crystallites usually at lower temperature and have shorter duration of phase formation. It is mainly a “bottom-up” method to synthesize NPs basically by chemical reduction of metal salts, electrochemical trails or through controlled decomposition of different metastable organo-metallic compounds.

2.4.1. Micelle Assisted Co-precipitation Method

A micelle is an aggregate of surfactant molecules which consist of hydrophilic “head” and hydrophobic “tail” regions (as shown in Figure 2.2 (a)) dispersed in a liquid colloid. A typical micelle in aqueous solution forms an aggregate with the hydrophilic "head" regions in contact with surrounding solvent, sequestering the hydrophobic single tail regions in the micelle centre as shown in Figure 2.2 (b). The micellar reagent acts more like a physical boundary to hold the NPs than acting as surface capping agent that are used very popularly to synthesize NPs. When the surfactant concentration exceeds the critical micelle concentration (CMC) in water, micelles are formed as aggregates of surfactant molecules. Above the CMC, the physical state of the surfactant molecules changes radically, and additional surfactant exists as aggregates or micelles. As the surfactant concentration increases further, micelles can be deformed and can change into different shapes, which make it possible to synthesize different shapes of NPs. The micelle helps in synthesizing the NPs by confining the chemical reaction, nucleation, and growth processes within its small hollow space.

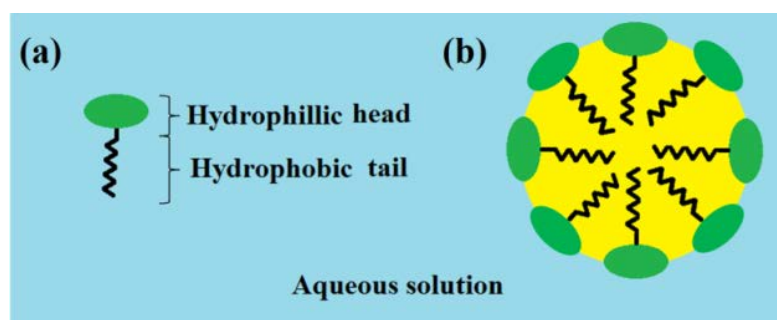


Figure 2.2. Schematic diagrams of (a) surfactant, (b) micelle dispersed in aqueous solution. (© C. Burda, X. Chen, R. Narayanan and M.A. El-Sayed, Chem. Rev. **105**, 1025 (2005))

Micelle assisted co-precipitation is carried out by dissolving one or more salts containing the constituent elements with proper ratio in aqueous solvent in presence of suitable micelle in a burette, followed by its drop by drop addition into the aqueous solution of co-precipitating agent heated to a temperature at about the boiling point of its solvent, in a three neck flask with the burette placed over it. After the completion of reaction of 1 h, the reaction medium is cooled to room temperature and the precipitation is collected and washed several times to eliminate impurities

followed by drying. This method is employed extensively in material science and industry to synthesize complex oxides with high crystallinity, compositional homogeneity, and better stoichiometry. The experimental setup used in our laboratory for fabrication of various oxide NPs is shown in Figure 2.3.

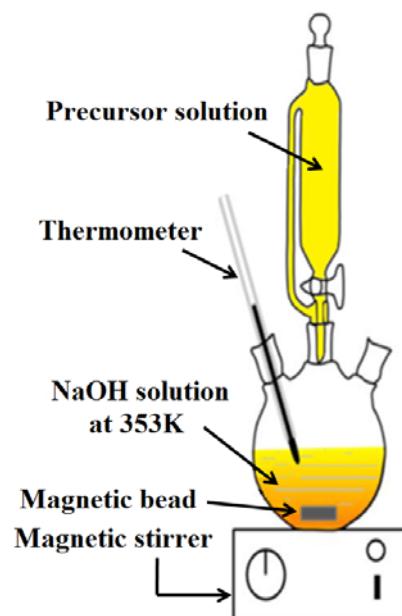


Figure 2.3. Schematic diagram of chemical co-precipitation technique.

The micelle assisted wet chemical technique has been utilized to synthesize the functionalized CoFe_2O_4 NPs which will be elaborately described in *Chapter 3* and *Chapter 4* of the thesis. In short, it involves a drop wise addition of the aqueous solution of metal ion salts (Iron(III) chloride, $\text{FeCl}_3, 6\text{H}_2\text{O}$ and Cobalt (II) chloride, $\text{CoCl}_2, 6\text{H}_2\text{O}$) with proper molar ratio (Co: Fe in 1:2) and micelle into the aqueous solution of co-precipitating agent, NaOH which is heated to temperature of about 80°C for 1 h.

2.4.2. Solvothermal Method

Solvothermal technique is a method for fabrication of NSs of various metals, semiconductors, ceramics, and also polymers from aqueous or non-aqueous medium by controlling temperature, pressure, capping agent, chemical composition, and duration of reaction. This process involves different polar (like, water, ethanol etc) or non-polar solvents (like Benzene, Ethylene Glycol, Ethylene di-amine etc) under high pressure and temperature (generally above the boiling point of solvent) to

facilitate the interaction of different precursor molecules during the synthesis procedure.

Solvothermal chemistry involves the use of a sealed reaction vessel and a temperature which is above the boiling point of the solvent. It helps to develop an autogeneous pressure.⁶ The pressure within the sealed reaction container is not only found to increase dramatically with temperature, but also depend on other experimental factors, such as the percentage fill of the vessel, any dissolved salts, and capping agents. This method is called hydrothermal route when the solvent is water. A number of fundamental properties of solvents are greatly affected by pressure and temperature. For example, the viscosity of water decreases with increasing temperature, such as at 500 °C and 10 bar, the viscosity of water is only 10% of its magnitude under ambient conditions.⁷ Thus, it is evident that the mobility of dissolved ions and molecules is higher under solvothermal conditions than at ambient pressure and temperature. Similarly, the dielectric constants of solvents are considerably reduced above the critical pressure and temperature; this can have major implications on the solubility of solid reagents under reaction conditions.⁶ In this technique, precursors are dissolved in the solvent by magnetic stirring or sonication, the homogeneous mixture is transferred into teflon lined stainless steel autoclave chamber, as shown in Figure 2.4.

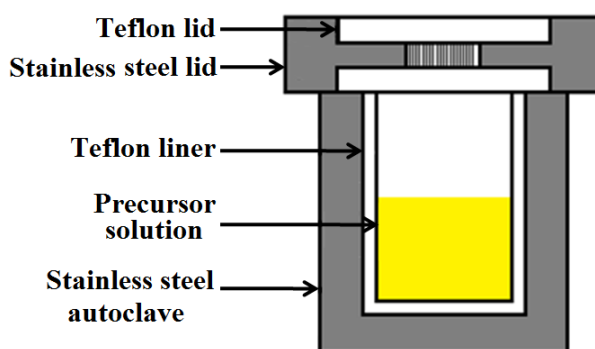


Figure 2.4. Schematic diagram of an autoclave and a teflon chamber used in solvothermal synthesis. (© R. I. Walton, Chem. Soc. Rev. 31, 230 (2002))

The precursor solution is poured in the chamber in such a way that 70% of it should be filled. The autoclave is then sealed and heated to a certain temperature in an oven. This method can be used to prepare various types of NSs such as particles,

wires, rods, hollow spheres, spindles etc. The advantageous aspects of the solvothermal synthesis route, in particular the formation of homogeneous sample of complex mixed metal solids, the isolation of metastable phases not seen at high temperature, and the control of crystal form, make the method particularly attractive for future study. Dissolution and crystallization mechanism of solvothermal method are greatly influenced by different thermodynamic and crystallographic effects behind the formation of various fascinating NSs such as oriented attachment of phases, selective adsorption of solvent or ligand molecules, molecular template mechanism etc.

The MFe_2O_4 ($M=Fe, Co, \text{ and } Mn$) NPs and nano hollow spheres (NHSs) are synthesized by template free solvothermal route which involves high temperature ($\sim 200^\circ C$) heating of metal ion salts (only Iron(III) chloride, $FeCl_3, 6H_2O$ in case of Fe_3O_4 and addition of Cobalt (II) chloride, $CoCl_2, 6H_2O$ /Manganese (II) chloride, $MnCl_2, 6H_2O$ in case of $CoFe_2O_4$, and $MnFe_2O_4$ NSs respectively) in a polar solvent, ethanol and non-polar solvent, ethylene glycol, for 12 h in case of Fe_3O_4 and $CoFe_2O_4$ and 24 h in case of $MnFe_2O_4$ NHSs, in presence of capping agents, oleylamine ($CH_3(CH_2)_7CH=CH(CH_2)_7NH_2$) in a teflon lined stainless steel autoclave. A brief discussion of the synthesis and growth mechanism of NHSs has been described in *Chapter 5* of the thesis.

2.4.3. Stöber Method

Stöber method is a process for the fabrication of monodispersed silica (SiO_2) particles. The process involves the hydrolysis and condensation of tetraethyl orthosilicate under alkaline conditions in ethanol. In general, it is used to coat different magnetic NMs. Most of the applications of magnetic NSs require a coating with a non-magnetic and biocompatible ligand since the magnetic NSs possess an immense tendency to get agglomerated very easily and SiO_2 coated magnetic NPs are found to get more easily dispersed in liquid media by screening the magnetic dipolar attraction among the magnetic NPs. The SiO_2 coating also protects the NPs from leaching in an acidic environment. The existence of abundant silanol groups on

the silica layer of magnetic NSs helps to attach various functional groups and most importantly, it can provide a chemically inert surface for magnetic NPs in biological systems^{8,9} which can be very useful in biomedical applications such as cell labeling¹⁰ and cell separation,¹¹ targeted drug delivery,^{12,13} and magnetic ferrofluids hyperthermia.^{14,15} Moreover, SiO₂ coating of magnetic NPs provides immense importance in the applications EM shielding due to its high dielectric property as well as diamagnetism.

In this technique, tetraethyl orthosilicate is added to an excess of water containing a low molar mass alcohol such as ethanol and containing ammonia and the resulting solution is stirred for 12 h. The reaction takes place through hydrolysis of silyl ether to a silanol followed by condensation. Ammonia is used as a catalyst in this reaction. With the increase or decrease of the concentration of ammonia, the rate of hydrolysis and condensation increases and decreases respectively. The reaction mechanism of Stöber process is shown in the Figure 2.5.

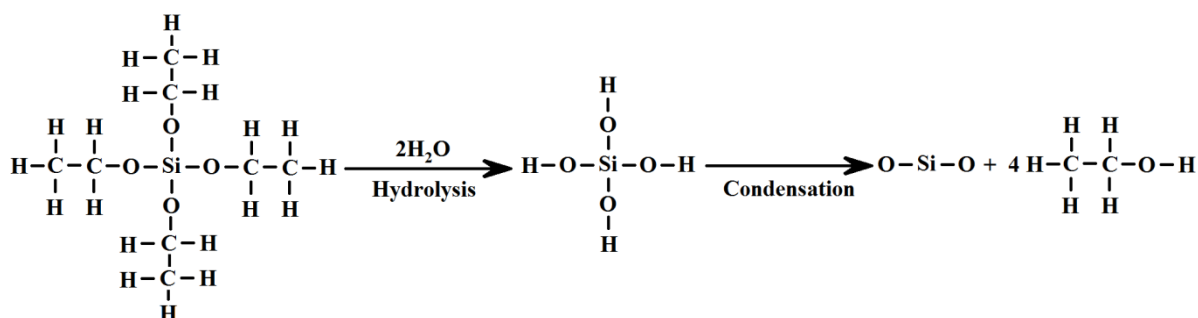


Figure 2.5. The reaction mechanism of SiO₂ synthesis through hydrolysis and condensation of tetraethyl orthosilicate.

Depending on type of silicate ester used, type of alcohol used, and volume ratios, the resulting SiO₂ particles are found to have diameters between 50 and 2000 nm.¹⁶ Herein, SiO₂ coated MFe₂O₄ (M=Fe, Co, and Mn) NPs and NHSs are synthesized using the similar strategy of Stöber which involves room temperature stirring of water, alcohol, ammonia, and tetraethyl orthosilicate in the presence of as-prepared MFe₂O₄ (M= Co, Fe, and Mn) NSs for 12 h in a beaker as described in Chapter 7 of thesis.

2.5. Phase and Morphology Characterization Techniques

2.5.1. X-Ray Diffractometer (XRD)

XRD is used to probe the crystal structure of micro and NSs, thin films, and bulk samples in a non-destructive way. In this method of determining molecular and atomic structure of a crystalline material, atomic planes of the material diffract incident X-rays in different specific directions depending on their orientations. By measuring the angle and intensity of the diffracted beams, a three dimensional idea of the density of electrons within the specified crystal can be obtained. From this density of electrons, mean position of the atoms in the crystal can be determined as shown in Figure 2.6.

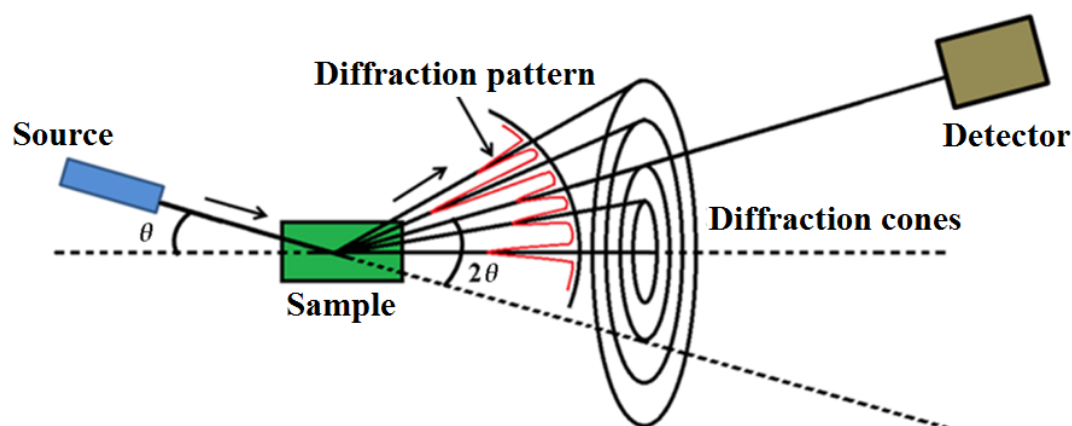


Figure 2.6. Schematic diagram of XRD.

In XRD instrument, a monochromatic beam of X-rays falls on a crystalline sample as shown in Figure 2.7. Those X-rays are scattered elastically by the electrons within the crystal planes. Then, the scattered waves interfere constructively in few specific directions that can be determined by Bragg's law given as Equation 2.7:

$$2d\sin\theta = n\lambda \quad (2.7)$$

where, d is the crystal plane spacing, θ is the diffraction angle, n is an integer, and λ is the wavelength of incident light. The angle and the intensity of the diffracted beams are processed and recorded electronically using a detector, resulting in intensity vs. 2θ plot for a specific sample.

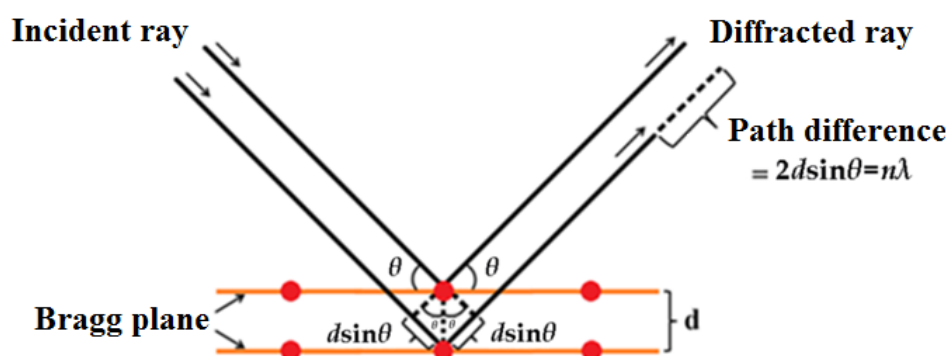


Figure 2.7. Schematic diagram of diffraction of X-rays by a crystal.

The grain size (D) of the sample can be calculated by observing the width of the diffraction peaks and using the relation as given by Debye-Scherrer Equation 2.8:

$$D = \frac{0.9\lambda}{\beta \cos\theta} \quad (2.8)$$

where, β is the full width at the half maximum of the diffraction peak at a diffraction angle of 2θ . XRD patterns of our samples were obtained by applying a scanning rate of $0.02^\circ \text{ s}^{-1}$ in the 2θ range from 20° to 80° by Rigaku miniflex II diffractometer equipped with Cu K_α ($\lambda \sim 1.54 \text{ \AA}$) radiation (at 40 mA and 40 kV).

2.5.2. Electron Microscopes

An electron microscope is a type of microscope that uses a beam of highly energetic electrons to illuminate a specimen and produces its magnified image. We have used two types of electron microscopes to analyze as-synthesized samples as described below.

2.5.2.1. Scanning Electron Microscope (SEM)

In SEM, a tiny electron beam, formed either thermionically or field emission,¹⁷ is focused onto the sample. Simultaneous to scanning the beam across a selected rectangular area of sample, generated signals are recorded and thereby an image is formed pixel by pixel as shown in Figure 2.8.

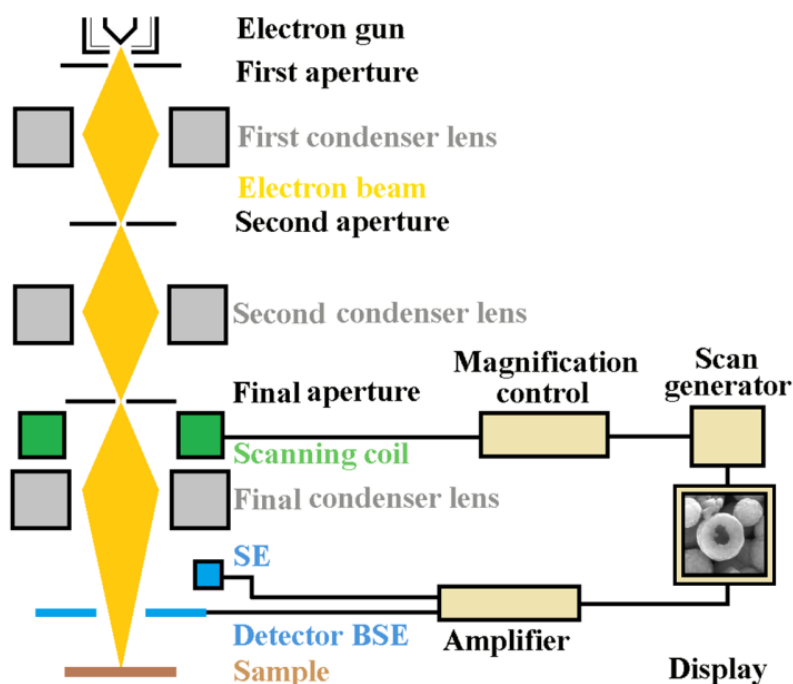


Figure 2.8. Schematic diagram of SEM. The display shows the image of CoFe_2O_4 NHSs.

Valuable information about morphology, surface topology, and composition can be obtained. It works within the voltage ranging from 2 to 50 kV. The interactions which are responsible for a multitude of signal types are back scattered electrons (BSEs), secondary electrons (SEs), X-rays, Auger electrons, and cathodoluminescence as shown in Figure 2.9. Inelastic events occur when an incident beam electrons interact with the electric field of sample's electrons, resulting transfer of energy leading to potential expulsion of an electron from that atom as a SEs. The energy SEs, by definition is less than 50 eV. If the vacancy due to formation of SE is filled from a higher level orbital, the X-ray characteristic of that energy transition is produced. Elastic events occur when a beam electron interacts with the electric field of the nucleus of a specimen atom, resulting change of direction of electrons without altering energy of the electron significantly ($< 1\text{eV}$). Among the elastically scattered electrons which are deflected backward are called BSEs. BSEs have energy in between 50 eV to the energy of incident beam. Generally, the image displayed by a SEM is a mapping of varying intensity of the signal produced by SEs into image in a position corresponding to the exact position of the beam on the specimen. Whereas the characteristic X-rays are used for elemental analysis, this method is known as

EDX. Morphology of our samples was tested by FESEM (FEI QUANTA FEG-250) operating at 5-10 keV.

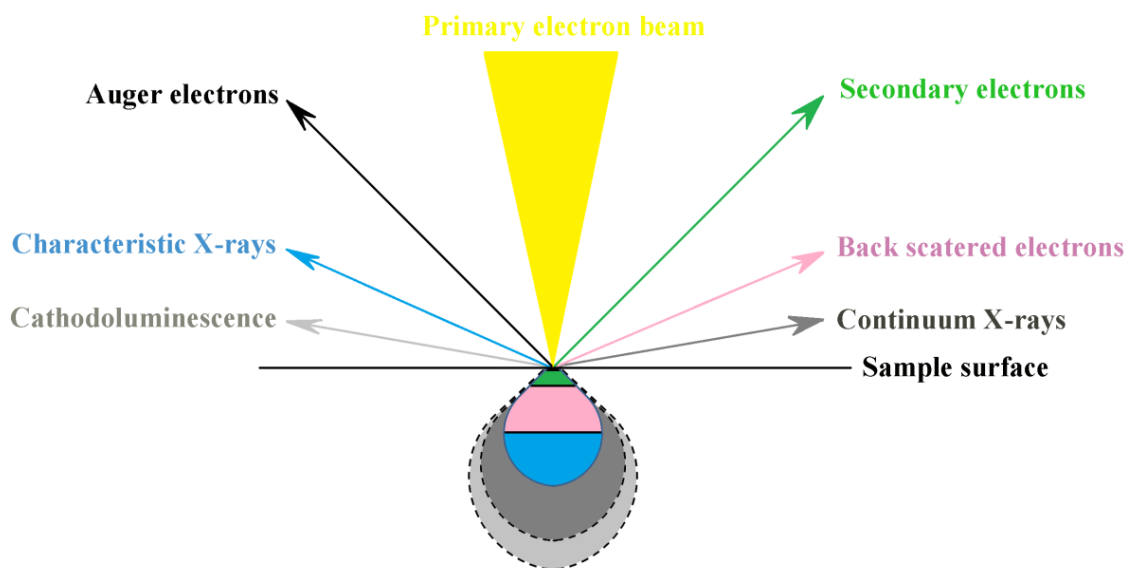


Figure 2.9. The typical spatial resolution of different signals: SEs, BSEs, X-rays, Auger electron, and cathodoluminescence in SEM.

2.5.2.2. Transmission Electron Microscope (TEM)

TEM uses mainly two different types of interactions between the electron beam and specimen to construct an image; such as unscattered electrons (transmitted beam) and elastically scattered electrons (diffracted beam). Schematic diagram of a TEM is shown in Figure 2.10. In this process, incident electrons are transmitted through the thin specimen without causing any interaction within the specimen. The transmission of unscattered electrons is inversely proportional to the specimen thickness. Areas of the specimen that are thicker will have fewer transmitted unscattered electrons and so will appear darker; conversely the thinner areas will have more transmitted and thus will appear lighter. This mode of operation to create contrast in image is known as bright field imaging mode.

Another important mode of TEM imaging is electron diffraction. In case of crystalline sample, the electron beam undergoes Bragg scattering in accordance with the Bragg's law as given by Equation 2.7. All incident electrons have the same energy (thus wavelength) and enter the specimen perpendicularly to its surface.

Now, the electrons that are scattered by the same set of parallel planes can be collated using magnetic lenses to form a pattern of spots; each spot corresponding to a specific atomic spacing (or crystalline plane). This pattern can then yield information about the orientation, atomic arrangements, and phases present in the area being examined.

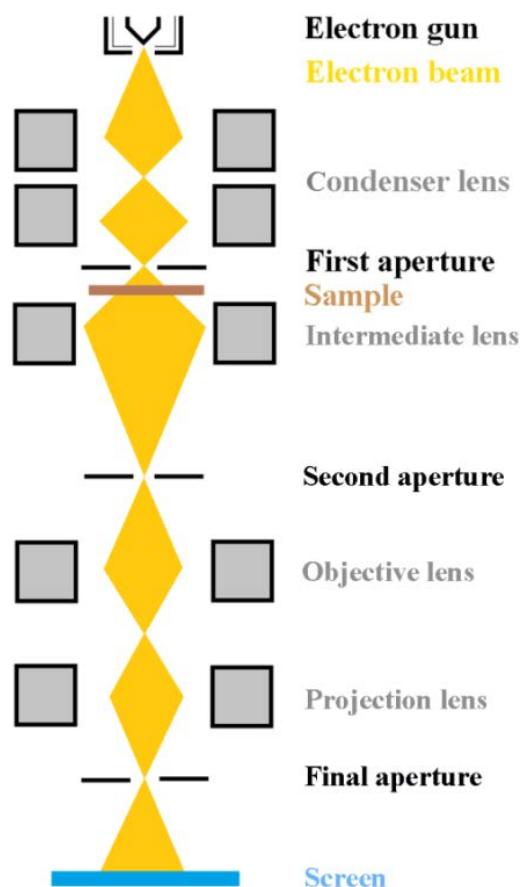


Figure 2.10. Schematic diagram of TEM.

In case of HRTEM mode, we can achieve a resolution around 0.2 nm which is very efficient in observing the lattice fringes of the specimen under observation. As the electron beam is transmitted through the thin section, a variety of beam specimen interactions occur that yield transmitted electrons, elastically and inelastically scattered (energy loss) electrons, SEs, BSEs, Auger electrons, and X-ray photons. TEM based elemental analysis techniques use X-ray photons in EDX and inelastically scattered electrons or the “energy loss” electrons in electron energy loss spectroscopy (EELS), and energy filtered TEM (EFTEM).

For TEM study, we prepared samples by drop casting the NSs in ethanol, water, or hexane on 300-mesh carbon coated copper grid and dried overnight in air. Particle size was calculated from TEM micrographs and elemental analysis was carried out from EDX spectrum recorded by a FEI Tecnai TF-20 field-emission high resolution TEM operating at 200 keV.

2.5.3. Atomic and Magnetic Force Microscope (AFM & MFM)

AFM is a high resolution imaging technique in which the forces due to individual atom are exploited. The AFM consists of a silicon or silicon nitride cantilever with a sharp tip which is used to scan the specimen surface. The radius of curvature of the tip is typically of the order of nanometer. As soon as the tip is brought into the proximity of sample surface, the force between the tip and the sample leads to a deflection of the cantilever according to Hooke's law.¹⁸ The forces that are measured in AFM include mechanical contact force, Van der Waals force, capillary force, chemical bonding, electrostatic force, magnetic force, Casimir force, solvation force etc.

In case of AFM, the force between the probe and the specimen surface can be measured in two different modes. In contact mode, the tip is directly in contact with the surface and the interaction force is dominated by Van der Waals interaction. The other mode is the tapping mode, a non-contact mode. Here, the probe is oscillated by a mechanical oscillator. The interaction between the tip and the surface changes the cantilever oscillation amplitude or phase relative to the drive signal.

Unlike AFM in which the atomic or electrostatic forces are measured, the MFM technique uses the magnetic force of the sample to generate the images of magnetic domains within the specimen as shown in Figure 2.11 (a). The MFM is another mode of AFM in which the AFM tip is coated with a thin layer of magnetic film, such as Ni or Co with high coercivity so that the tip's magnetic state does not change during imaging. Many kinds of magnetic interactions are measured by MFM, including magnetic dipole-dipole interaction.

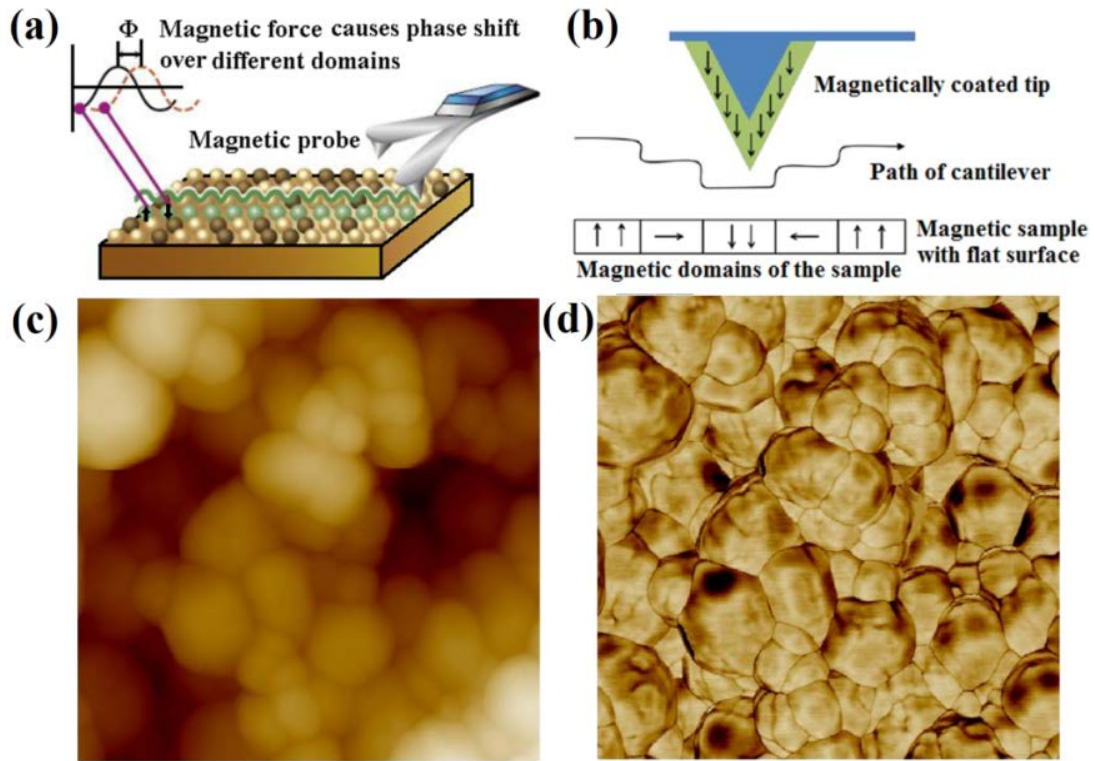


Figure 2.11. Schematic diagram of (a) MFM using silicon probe, (b) MFM tip scan over a flat magnetic surface. (c) AFM and (d) MFM micrographs of Fe_3O_4 NHSs of 160 nm diameter.

During MFM measurements, the magnetic force between the sample and the tip can be expressed as

$$F = \mu_0(m \cdot \nabla)H \quad (2.9)$$

where, m is the magnetic moment of the tip approximated as a point dipole, H is the magnetic stray field from the sample surface and μ_0 is the free space permeability.

The stray magnetic field from the sample can affect the magnetic state of the tip, and vice versa. Thus, interpretation of MFM measurement is not straightforward. Figure 2.11 (b) shows schematic diagram of the magnetic tip movement over a magnetic sample. The stray field of MFM tip magnetizes the sample surface locally along its own direction of magnetization. Figure 2.11 (c) and (d) show typical AFM and MFM micrographs, respectively, of Fe_3O_4 NHSs having average diameter of 160 nm. In MFM micrographs, the bright and dark spots may correspond to the local magnetic stray field of the sample either in the upward or in the downward direction with respect to sample's horizontal surface.

2.5.4. Mössbauer Spectroscopy

Mössbauer spectroscopy is a spectroscopic technique based on the Mössbauer effect. It probes the tiny changes of an atomic nuclear energy levels in response to its environment. Typically, three types of nuclear interactions may be observed: isomeric shift, also known as a chemical shift; quadrupole splitting; and magnetic or hyperfine splitting, also known as the Zeeman Effect. In the study of solid, Mössbauer spectroscopy reveals the interaction of gamma (γ) ray (10^4 - 10^5 eV) with atomic nuclei, more specifically, the emission of a γ ray from the excited state of a nucleus and the resonant absorption of γ ray by the ground state of an identical nucleus that loses no energy to recoil. The energy level diagram and absorption of different γ rays of ^{57}Co , the relevant Mössbauer source, are shown in Figure 2.12. ^{57}Co has a half life of 270 days. Primarily, it decays to the 136.3 keV level of ^{57}Fe that is an excited state. It may return to the ground state in two possible ways. The γ ray can return directly to the ground state by emitting γ photon of energy 136.3 keV. This process occurs almost 9%. Otherwise, it de-excites to 14.4 keV state before returning to ground state. Of this 14.4 keV transitions, approximately 11% results in the emission of γ rays, which is abundant enough for Mössbauer experiments to be performed.

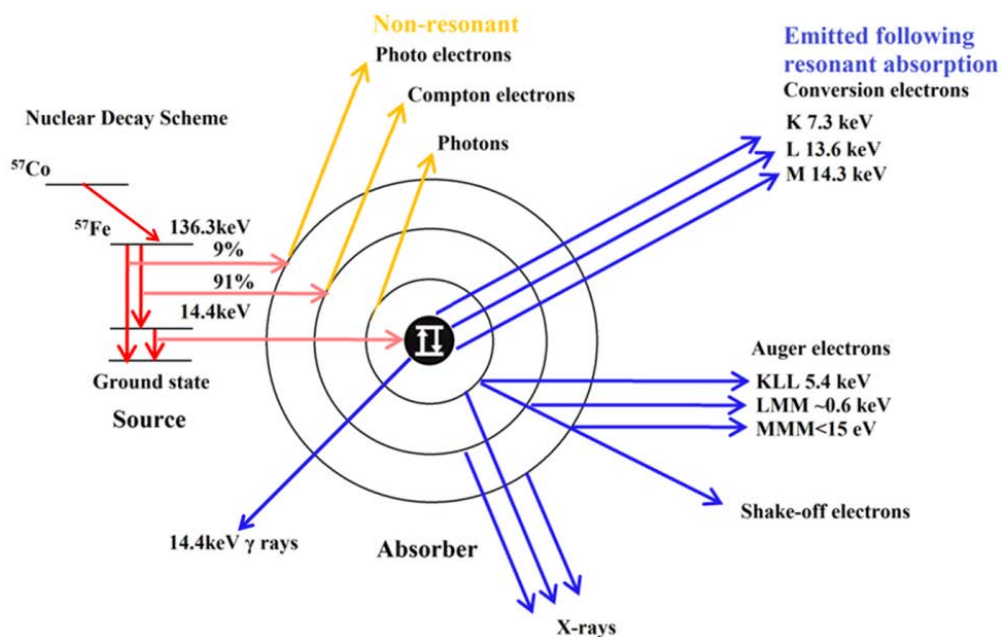


Figure 2.12. The various back scattering processes for ^{57}Fe following the resonant absorption of an incident gamma ray.

The two main obstacles in the path of achieving nuclear resonant emission and absorption are the recoil energy shift and the thermal Doppler shift. They can be overcome and thereby Mössbauer effect can be achieved if the γ ray emitting atoms are bound in a solid matrix. To obtain a large fraction of recoil free emission, the Mössbauer nuclide must be embedded in a crystal or metallic matrix such that the solid matrix as a whole takes up momentum recoil on emission and absorption of a γ ray. Figure 2.13 shows the simplest scheme of Mössbauer spectroscopy set-up. In Mössbauer spectroscopy, γ ray from a radioactive source, such as ^{57}Co are passed through a collimator and then it interacts with the sample. The decrease in the intensity of the γ ray is detected. The detector counts the number of γ photons that pass through the sample.

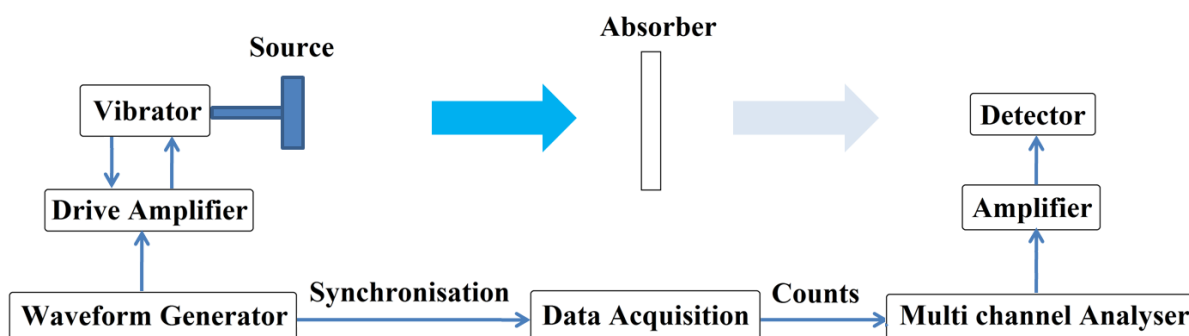


Figure 2.13. Block diagram representing the scheme of Mössbauer spectroscopy set-up.

In order to obtain a spectrum, a range of transmission energies is created by adding a slight Doppler velocity to the source. The source is oscillating, modifying the γ ray emission so that γ ray with multiple energies can be obtained. The resultant spectrum is a graph of transmission verses Doppler velocity.

The acquisition of Mössbauer spectrum from this added Doppler shift is shown in Figure 2.14. The absorber interacts with γ photons with energies that vary with the amount of Doppler shift. Therefore, the final curve produced (at the bottom of Figure 2.14) is the proportion of the change in the amount of overlap between the source and the absorber.

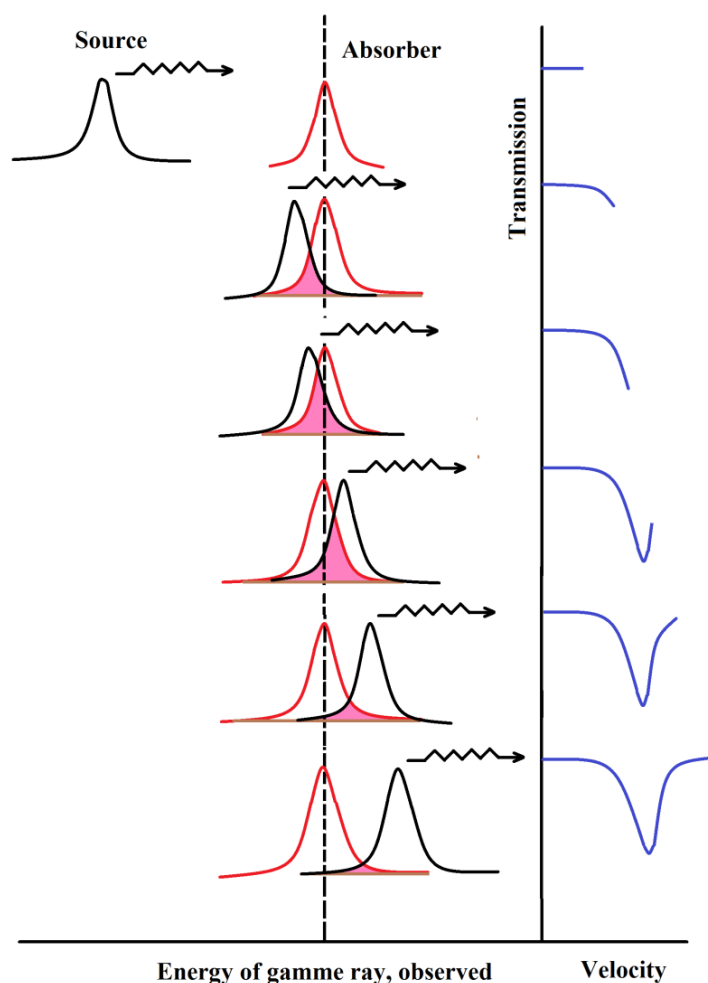


Figure 2.14. Schematic diagrams of the acquisition of Mössbauer spectrum. The source is moved by a Doppler velocity, creating an overlap of the source and absorber energy distributions. When there is no overlap, the Mössbauer spectrum shows 100% transmission (0% absorption). As more overlap is created by the Doppler velocity, fewer γ rays get through to the detector, creating a drop in absorption that forms the peak in the spectrum.

2.5.4.1. Mössbauer Parameters

2.5.4.1.1. Isomer Shift

The isomer shift arises due to non-zero volume of nucleus and the electron charge density due to s-electrons within it leading to an electric monopole or Coulomb interaction, which shifts the nuclear energy levels as shown in Figure 2.15. In a Mössbauer spectrum, isomer shift is observed when the Doppler velocity modifies γ energy of the source to account the difference between source and the absorber energy levels. Because of the dynamics of the electronic environment,

isomer shift is sensitive to the differences in oxidation states, spin state, valance state, and co-ordination.

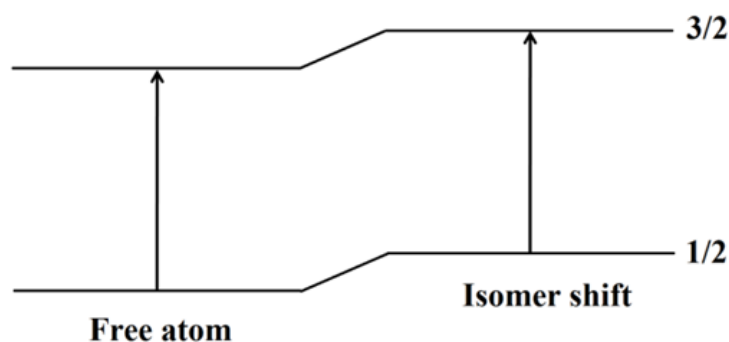


Figure 2.15. Isomer shift of the nuclear states of ^{57}Fe .

2.5.4.1.2. Quadrupole Splitting

A nucleus that has a spin quantum number $I > 1/2$, has a non-spherical charge distribution and said to have a quadrupole moment. An asymmetric charge distribution around the nucleus causes an asymmetric electric field at the nucleus, characterized by a tensor, quantity called electric field gradient. The electric quadrupole interaction between these two quantities gives rise to splitting in the nuclear energy levels that is known as quadrupole splitting. Quadrupole splitting is sensitive to the coordination and oxidation states of the atom because any change in the electronic shape changes the electric field gradient.

2.5.4.1.3. Magnetic Hyperfine Splitting

The magnetic hyperfine splitting is caused by the dipole interaction between the nuclear spin magnetic moment and the magnetic field i.e. Zeeman splitting. The effective magnetic field experienced by the nucleus is a combination of the fields of atom itself from the lattice through crystal field effects and the external applied fields. The magnetic field splits the nuclear level of spins I into $(2I+1)$ equispaced non-degenerate sub-states. The splitting is governed by the selection rule $\Delta m_I = 0, \pm 1$, where m_I is the magnetic quantum number.^{19,20} The right part of the Figure 2.16 shows the hyper splitting for a $3/2$ to $1/2$ transition.

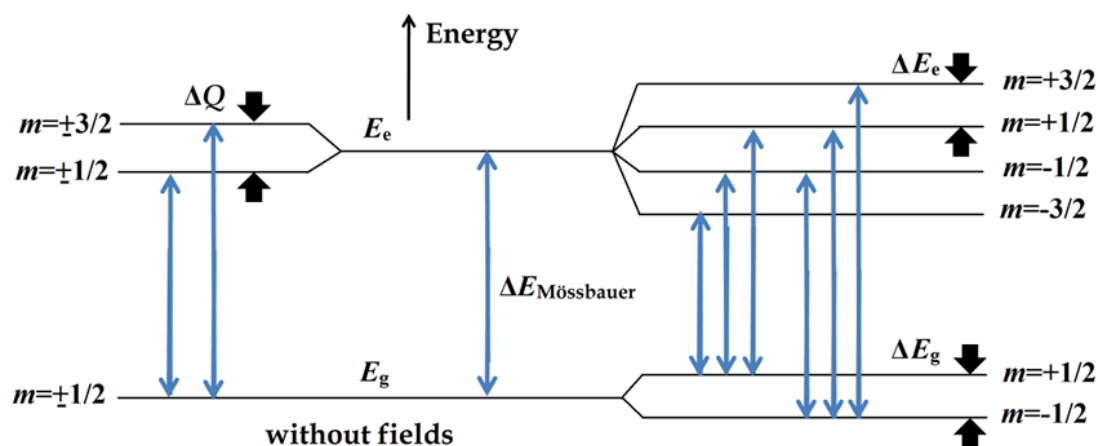


Figure 2.16. Quadrupole splitting (left) and magnetic hyperfine splitting (right) of the nucleus states of ^{57}Fe nucleus.

A commercially available 25 m ^{57}Co in Rh matrix is used as a source for study as described in *Chapter 5* of thesis. The system was calibrated with high purity iron foil of thickness 12 μm . A least square fitting program LGFIT2 was used to fit the experimental data.²¹

2.6. Thermo-Analytical Characterization Technique

2.6.1. Differential Thermal Device

Differential thermal device measures the difference in temperature between a sample and a thermally inert reference as the temperature is raised. The plot of differential thermal analysis (DTA) provides the information on exothermic and endothermic reactions taking place in the sample. The technique is routinely applied in a wide range of studies such as identification, quantitative composition analysis, phase diagrams, hydration-dehydration, thermal stability, phase transitions, and melting points.²² A DTA consists of a sample holder comprising thermocouples, sample containers and a ceramic or metallic block, a furnace, a temperature programmer, and a recording system as shown in Figure 2.17. The key feature is the existence of two thermocouples connected to a voltmeter. One thermocouple is placed in an inert material such as Al_2O_3 , while the other is placed in a sample under study. As the temperature is increased, there will be a brief deflection of the voltmeter if the sample is undergoing a phase transition. This occurs because the

input of heat will raise the temperature of the inert substance, but be incorporated as latent heat in the material changing phase.

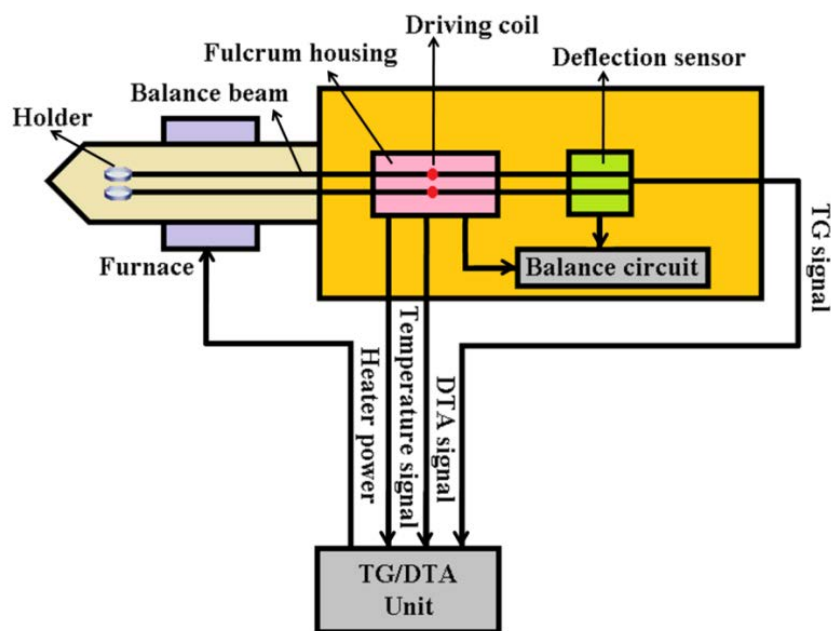


Figure 2.17. Schematic diagram of differential thermal device.

2.7. Optical Characterization Techniques

2.7.1. UV-Visible (UV-Vis) Absorption Spectroscopy

Upon absorption of energy, in visible and adjacent (near-UV and near-infrared (IR)) region of EM spectrum the molecules undergo electronic transition from ground state to another excited state. This technique is often used to measure the concentration of an absorbing species in solution using Beer-Lambert law as given below.

$$A = \log_{10}(I_0/I) = \epsilon.C.l \quad (2.10)$$

where, A is the absorbance of sample, I_0 is the intensity of incident light at a given wavelength, I is that for the transmitted light, l is the path length of light covered through the sample, C is the concentration of the absorbing species, and ϵ is the molar absorptivity or molar extinction coefficient that is characteristics of a particular absorber and constant at a particular wavelength.

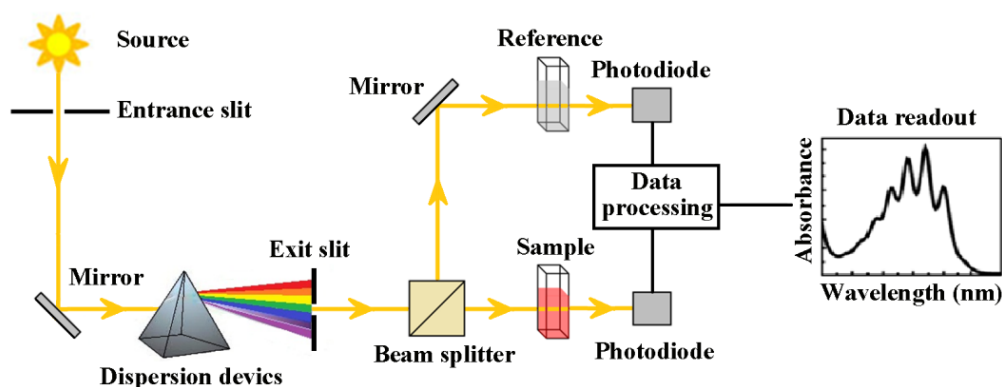


Figure 2.18. Schematic diagram of a UV-Vis spectrometer.

The schematic diagram of the UV-Vis spectrometer is demonstrated in Figure 2.18. UV-Vis absorbance spectra of our samples were obtained from a Shimadzu Model UV-2600 spectrophotometer using a quartz cuvette of 1 cm path length.

2.7.2. Fourier Transformed Infrared (FTIR) Spectroscopy

FTIR, a powerful tool to identify the functional groups and chemical bonds within a molecule, is called molecular fingerprint. When the frequency of a polar vibrational mode of a bond matches with the incident IR frequency, then due to absorbance of IR, FTIR signal is obtained. Additionally, the peaks get shifted or broadened due to interaction of functional groups with solvent molecules or NPs surface. Figure 2.19 shows schematic diagram of FTIR instrument.

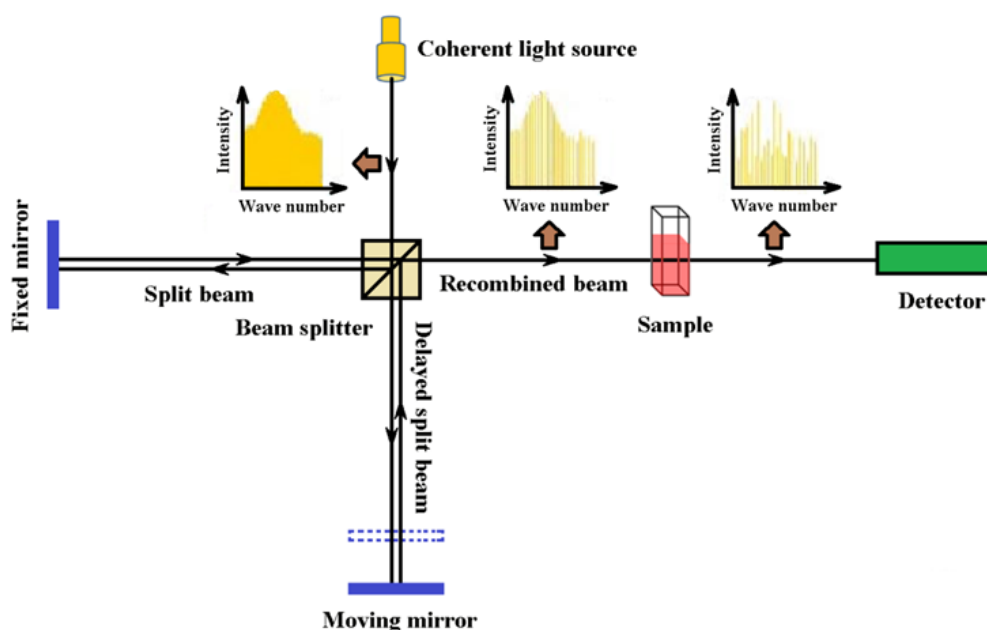


Figure 2.19. Schematic diagram of FTIR spectrometer.

As shown in the diagram, there are mainly two components in IR spectroscopy instrument, source and detector. The most common source of IR spectrometer is Nernst glower which consists of a rod of a sintered mixture of the oxides of Zirconium, Ytterbium, and Erbium. The rod is electrically heated upto 1773 K to produce IR radiations. Sodium chloride or other alkali metal halides are the best material to form cell container as they are transparent in IR region. The collimated IR beam is partially reflected by and transmitted through the beam splitter (a half silvered mirror) and moves to the stationary and moving mirrors, respectively. The transmitted beam from the moving mirror and reflected beam from the fixed mirror may interfere constructively or destructively at the back side of the beam splitter depending on the wavelength of the light and the optical path difference introduced by the moving mirror. This resulting signal is called interferogram. At last, Fourier transformation of this interferogram is performed to have a frequency spectrum (plot of intensity at each frequency). A JASCO FTIR-6300 spectrometer is used to carry out the FTIR studies. For the FTIR measurements, powdered samples were mixed with KBr powder and pelletized. The background correction was made using a reference pure KBr pellet before every measurement.

2.7.3. Terahertz-Time Domain Spectroscopy (THz-TDS)

Figure 2.20 shows a schematic drawing of scanning laser THz near-field imaging system. In this system, a 1.56 μm femtosecond fiber laser (TOPTICA FFS.SYS.HP: maximum power 350 mW, pulse width 110 fs) operating at 80 MHz repetition rate is used for the generation of single-cycle THz pulses.

Initially, the laser beam is divided into pump and trigger beams using a beam splitter. The pump beam is modulated by means of an acousto-optic modulator (AOM) and scanned over the 2D THz emitter plate with a galvanometer.²³ For the THz emitter, a GaAs crystal is employed and it is known as one of the appropriate THz generation sources for 1.56 μm wavelength laser excitation.²⁴

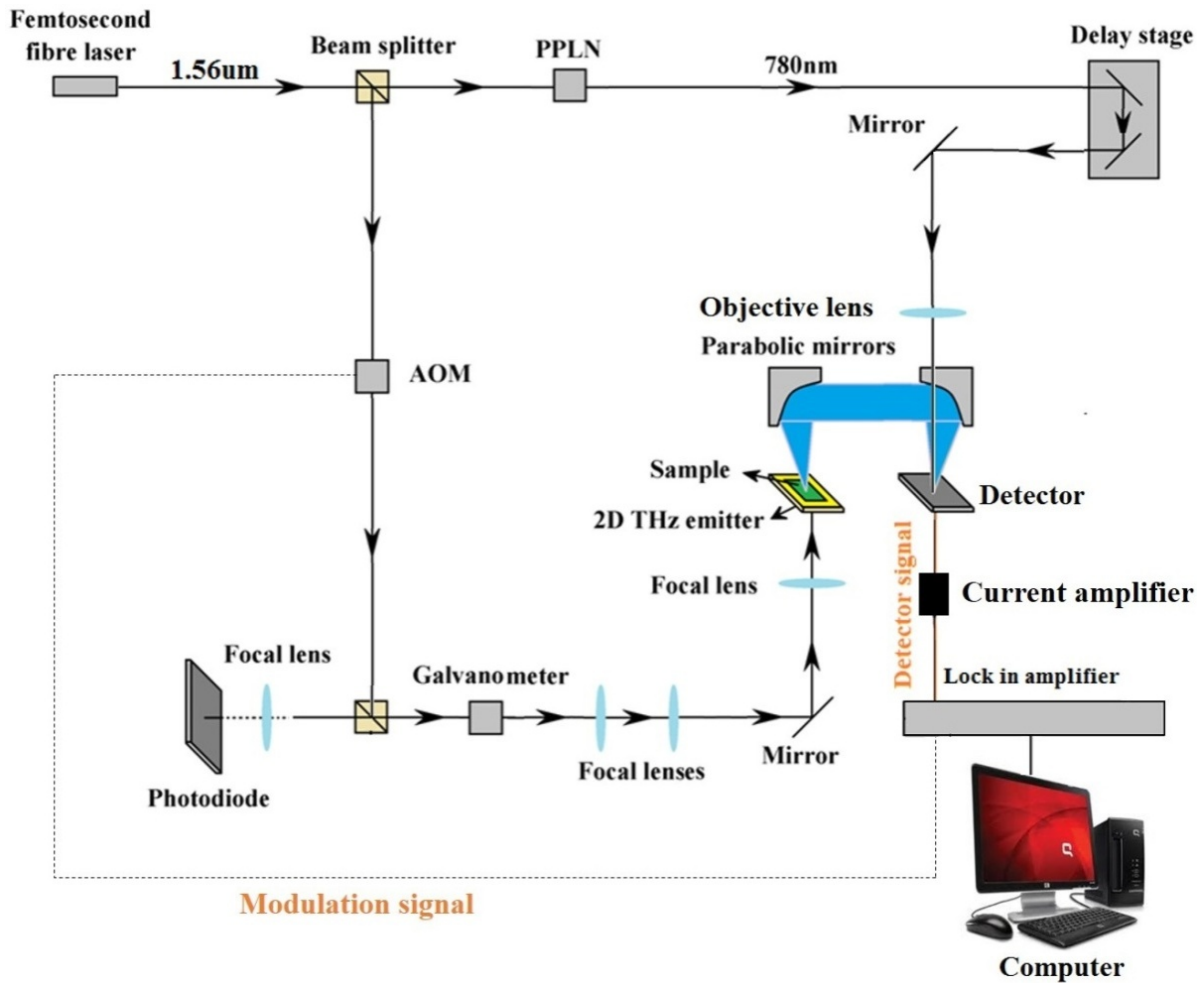


Figure 2.20. Schematic diagram of THz-time domain spectrometer.

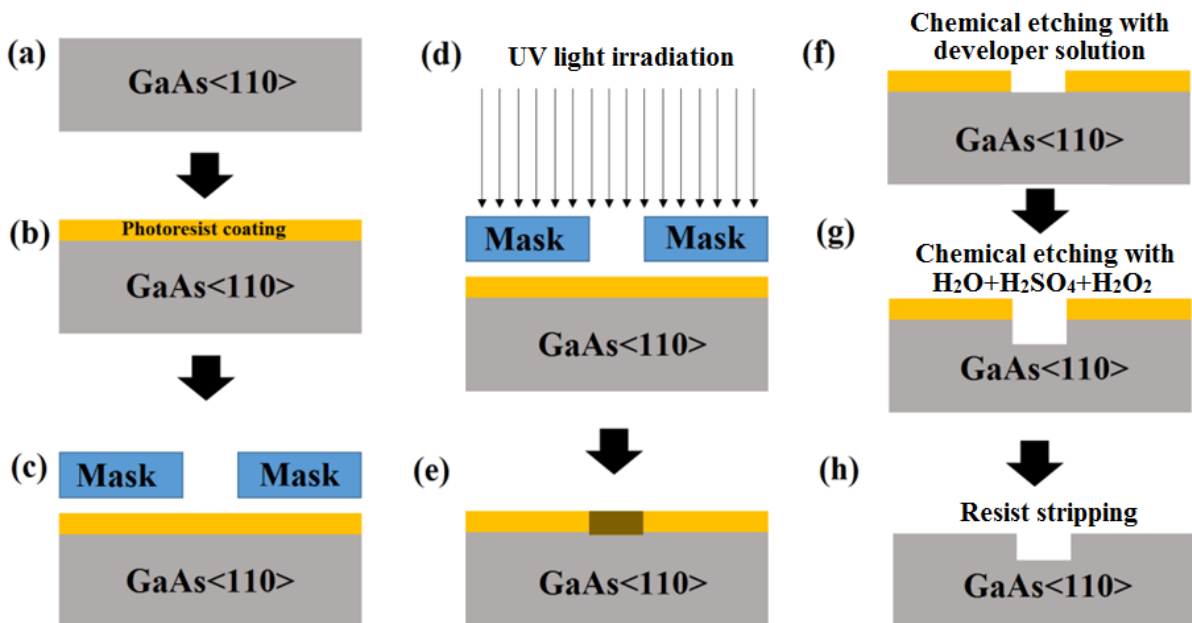


Figure 2.21. Schematic diagram of the scoop formation in GaAs crystal surface through photolithography.

A micro-dimensional scoop ($500\mu\text{m} \times 500\mu\text{m} \times 40\mu\text{m}$) is fabricated on the surface of GaAs substrate using photolithography. The general sequence of formation of micro-dimensional scoop is as follows: substrate preparation, photoresist spin coat, bake, exposure, development, scooping, and resist stripping as shown in Figure 2.21. Initially, the GaAs substrate preparation is carried out to improve the adhesion of the photo-resist material to the substrate. This is accomplished by cleaning the substrate with acetone, ethanol, and water respectively each for 4 min to remove contamination (Figure 2.21 (a)). Thereafter, a thin, uniform coating of photo-resist (S1818G) at a specific, well controlled thickness is carried out by spin coating the GaAs wafer with 1000 rpm for 3 sec and then with 4000 rpm for 40 sec (Figure 2.21 (b)). After coating, the resulting resist film will contain between 20–40% of solvent which has been removed through drying at $100\text{ }^{\circ}\text{C}$ for 1 min. The mask is then aligned with the photo-resist GaAs wafer (Figure 2.21 (c)) and it is exposed through the pattern of the mask with a high intensity UV light of power 350 Watt for 3.7 sec (Figure 2.21 (d)). The mask contains a large number of transparent square holes of length $500\text{ }\mu\text{m}$ and breadth $500\text{ }\mu\text{m}$, leading to the formation of photo reacted region of same dimension (Figure 2.21 (e)) in GaAs crystal. After that, a chemical etching has been carried out by using developer solution for 1 min in order to remove the photo-resist which is exposed to UV light as shown in Figure 2.21 (f) and then it is washed in water and dried. Next, a solution of $\text{H}_2\text{O}:\text{H}_2\text{SO}_4:\text{H}_2\text{O}_2$ has been prepared in 1:3:1 ratio followed by heating to $43\text{ }^{\circ}\text{C}$ and then the GaAs crystal is put within that solution for 13 min 20 sec in order to create a scoop of depth $40\text{ }\mu\text{m}$ as shown in Figure 2.21 (g). Finally, acetone is used to remove rest of the photo-resist (Figure 2.21 (h)) and a micro-dimensional scoop of length $500\text{ }\mu\text{m}$, breadth $500\text{ }\mu\text{m}$, and height $40\text{ }\mu\text{m}$ in the GaAs crystal surface is obtained within which the nanostructured samples are placed manually. This GaAs crystal is used as a THz emitter. The THz beams that are locally generated at the pump beam irradiation spot on GaAs crystal transmit through the sample which is set directly on the emitter as shown in Figure 2.22. Therefore, the spot size of the THz source approximately corresponds to the pump beam irradiation spot.

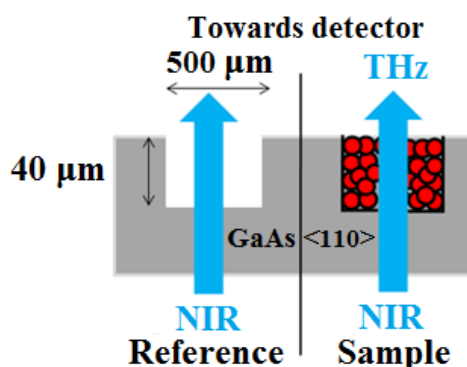


Figure 2.22. Schematic diagram of the sample with holder used in THz-TDS measurement.

The transmitted THz field amplitudes are focused onto a detector by using a pair of parabolic mirrors. For a detector, a bow-tie shaped photoconductive antenna (PCA) that is fabricated on a low temperature grown GaAs (LT-GaAs) is used. On the other hand, the trigger beams are converted to 780 nm by a periodically poled LiNbO₃ (PPLN) crystal, and then irradiated to the PCA. Therefore, we can observe a THz transmission image of the sample by monitoring the amplitude of the THz pulses. In addition, reflected laser beam from the emitter is detected by a photodiode, so we can observe a laser reflection image of emitter surface or a sample and compare it with the THz images at the same time. By scanning the localized THz point light sources two dimensionally, and also by setting the sample in vicinity of such light sources, the sample interacts with the THz waves and allows us to observe THz transmission images at a spatial resolution of sub-wavelength order.

2.8. Magnetic Characterization Techniques

2.8.1. Vibrating Sample Magnetometer (VSM)

In a VSM, the sample is placed in a direct current (DC) magnetic field (H) and vibrated sinusoidally so that the resulting variation of magnetic flux (B) can induce a voltage in pickup coils. According to Faraday's law of EM induction, the voltage induced (V) in a pickup coil of N turns with a cross-sectional area of A is given by Equation 2.11

$$V = -NA \frac{dB}{dt} \quad (2.11)$$

where, $B = \mu_0 H$ (here μ_0 is a constant called the vacuum permeability)

Now, if a sample having magnetization M is placed in the pickup coil, the total magnetic induction B can be written as

$$B = \mu_0(H + M) \quad (2.12)$$

Therefore, the change in flux due to sample insertion is $\Delta B = \mu_0 M$. Hence, the Equation 2.11, can be rewritten as,

$$V dt = -\mu_0 N A M \quad (2.13)$$

The intensity of the signal is proportional to the magnetic moment of the sample and the frequency is the same as that of the sinusoidal motion. The schematic diagram of the sample holder and detection mechanism of a VSM is shown in Figure 2.23. Magnetic study of our sample was performed in a Lake Shore VSM equipped with an electromagnet, capable of generating field of up to 1.6 T at 300 K.

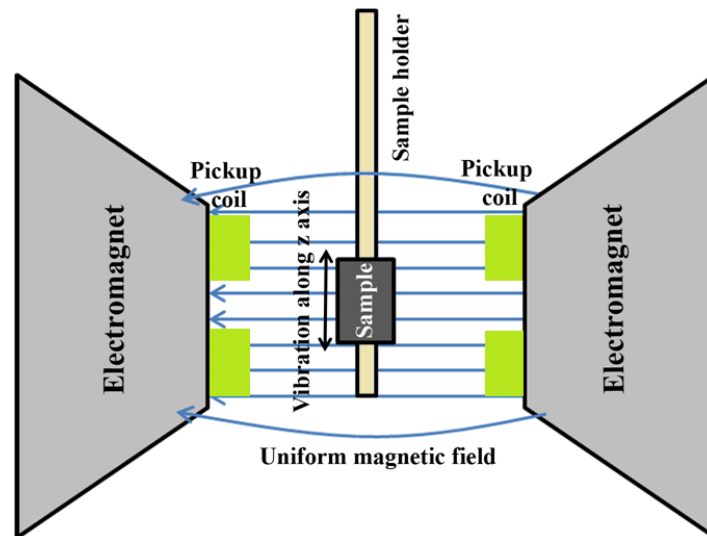


Figure 2.23. Schematic diagram of VSM.

2.8.2. Superconducting Quantum Interference Device (SQUID)

SQUID is the most sensitive and effective device that has been designed till now to detect incredibly small magnetic field and moment. It consists of two

superconductors separated by a thin insulating layer to form two parallel Josephson junctions, as shown in the Figure 2.24.

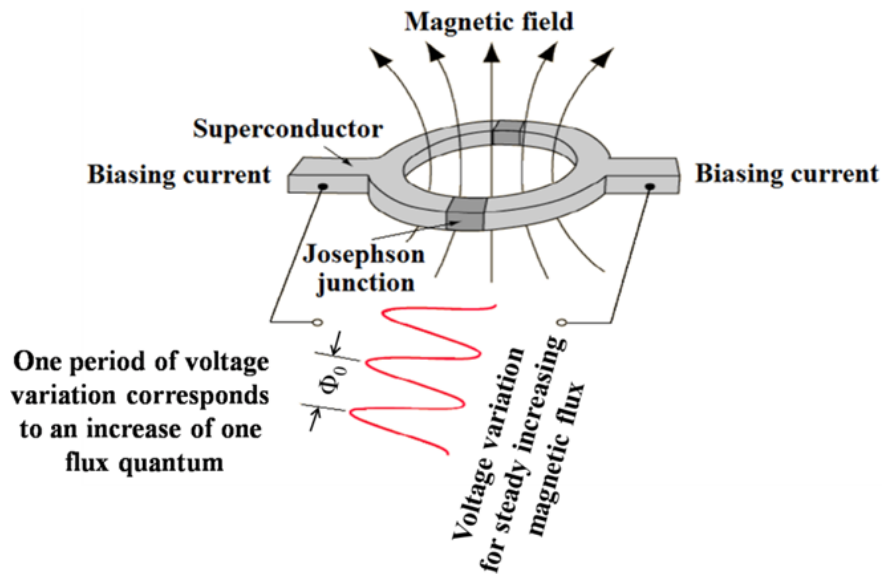


Figure 2.24. Schematic diagram of SQUID.

The insulating layer is thin enough such that the Cooper pairs can easily tunnel through the insulating junction. In the absence of any external magnetic field, the biasing current 'I' splits into two branches equally. As superconductor excludes magnetic flux through it, so, if a small external magnetic field is applied to the superconducting loop, a screening current, 'I_s', will generate to cancel the externally applied field. The induced current is in the same direction as 'I' in one of the branches of the superconducting loop, and is opposite to 'I' in the other branch. As soon as the current in either branch exceeds the critical current (I_c) of the Josephson junction, a voltage appears across the junction. Now consider the external flux is further increased until it exceeds $\Phi_0/2$, half the magnetic flux quantum. Since the flux enclosed by the superconducting loop must be an integral number of flux quanta, instead of screening the flux the SQUID now energetically prefers to increase it to Φ_0 . The screening current now flows in the opposite direction. Thus the screening current changes direction every time the flux increases by half integer multiples of Φ_0 . The SQUID detects the change in this current to deduce the magnetic moment of the sample.²⁵

Bibliography

- [1] Min, Y.; Kwak, J.; Soon, A.; Jeong, U., Nonstoichiometric nucleation and growth of multicomponent nanocrystals in solution. *Accounts of Chemical Research* 2014, **47**, 2887.
- [2] Kumar, S.; Nann, T., Shape control of II–VI semiconductor nanomaterials. *Small* 2006, **2**, 316.
- [3] Thanh, N. T. K.; Maclean, N.; Mahiddine, S., Mechanisms of nucleation and growth of nanoparticles in solution. *Chemical Reviews* 2014, **114**, 7610.
- [4] Lee, W.-r.; Kim, M. G.; Choi, J.-r.; Park, J.-I.; Ko, S. J.; Oh, S. J.; Cheon, J., Redox–transmetalation process as a generalized synthetic strategy for core–shell magnetic nanoparticles. *Journal of the American Chemical Society* 2005, **127**, 16090.
- [5] Watzky, M. A.; Finke, R. G., Nanocluster size-control and “magic number” investigations. Experimental tests of the “living-metal polymer” concept and of mechanism-based size-control predictions leading to the syntheses of iridium(0) nanoclusters centering about four sequential magic numbers. *Chemistry of Materials* 1997, **9**, 3083.
- [6] Walton, R. I., Subcritical solvothermal synthesis of condensed inorganic materials. *Chemical Society Reviews* 2002, **31**, 230.
- [7] Rabenau, A., The role of hydrothermal synthesis in preparative chemistry. *Angewandte Chemie International Edition in English* 1985, **24**, 1026.
- [8] Deng, Y. H.; Wang, C. C.; Hu, J. H.; Yang, W. L.; Fu, S. K., Investigation of formation of silica-coated magnetite nanoparticles via sol-gel approach. *Colloids and Surfaces A: Physicochemical and Engineering Aspects* 2005, **262**, 87.
- [9] Mazaleyrat, F.; Ammar, M.; LoBue, M.; Bonnet, J. P.; Audebert, P.; Wang, G. Y.; Champion, Y.; Hÿtch, M.; Snoeck, E., Silica coated nanoparticles: synthesis, magnetic properties and spin structure. *Journal of Alloys and Compounds* 2009, **483**, 473.
- [10] Farrell, E.; Wielopolski, P.; Pavljasevic, P.; Kops, N.; Weinans, H.; Bernsen, M. R.; Osch, G. J. V. M. van, Cell labelling with superparamagnetic iron oxide has no effect on chondrocyte behaviour. *Osteoarthritis and Cartilage* 2009, **17**, 961.
- [11] Ahn, J.; Chung, W. J.; Pinnau, I.; Guiver, M. D., Polysulfone/silica nanoparticle mixed-matrix membranes for gas separation. *Journal of Membrane Science* 2008, **314**, 123.
- [12] Emerich, D. F.; Thanos, C. G., The pinpoint promise of nanoparticle-based drug delivery and molecular diagnosis. *Biomolecular Engineering* 2006, **23**, 171.
- [13] Kearney, A. S., Prodrugs and targeted drug delivery. *Advanced Drug Delivery Reviews* 1996, **19**, 225.
- [14] Hergt, R.; Dutz, S., Magnetic Particle Hyperthermia – Biophysical Limitations of a Visionary Tumour Therapy. *Journal of Magnetism and Magnetic Materials* 2007, **311**, 187.
- [15] Hergt, R.; Hiergeist, R.; Hilger, I.; Kaiser, W. A.; Lapatnikov, Y.; Margel, S.; Richter, U., Maghemite nanoparticles with very high AC-losses for application in RF-magnetic hyperthermia. *Journal of Magnetism and Magnetic Materials* 2004, **270**, 345.
- [16] Bogush, G. H.; Tracy, M. A.; Zukoski IV, C. F., Preparation of monodisperse silica particles: control of size and mass fraction, *Journal of Non-Crystalline Solids* 1988, **104**, 95.
- [17] Groves, T. R.; Pfeiffer, H. C.; Newman, T. H.; Hohn, F. J., EL3 System for quarter-micron electron beam lithography. *Journal of Vacuum Science and Technology B* 1988, **6**, 2028.
- [18] Cappella, B.; Dietler, G.; Force-distance curves by atomic force microscopy. *Surface Science Reports* 1999, **34**, 1.
- [19] Dickson, D.P.E.; Berry, F.J., Mössbauer spectroscopy (Cambridge University Press, UK, 2015).
- [20] Bancroft, G.M., Mössbauer spectroscopy an introduction for inorganic chemists and geochemists (McGraw-Hill Book Company, UK, 1973).

- [21] E. V. Meerwall, A least-squares spectral curve fitting routine for strongly overlapping lorentzians or gaussians. *Computer Physics Communications* 1975, **9**, 117.
- [22] Speyer, R.F., Thermal analysis of materials (Marcel Dekker, Inc., New York, 1994).
- [23] Serita, K.; Mizuno, S. ; Murakami, H.; Kawayama, I. ; Takahashi, Y.; Yoshimura, M.; Mori, Y.; Darmo, J.; Tonouchi, M., Scanning laser terahertz near-field imaging System. *Optics Express* 2012, **20**, 12959.
- [24] Nagai, M.; Tanaka, K.; Ohtake, H.; Bessho, T.; Sugiura, T.; Hirosumi, T.; Yoshida, M., Generation and detection of terahertz radiation by electro-optical process in GaAs using 1.56 μ m fiber laser pulses. *Applied Physics Letters* 2004, **85**, 3974.
- [25] Cheng, C. W.; Sie, E. J.; Liu, B.; Huan, C. H. A.; Sum, T. C.; Sun, H. D.; Fan, H. J., Surface plasmon enhanced band edge luminescence of ZnO nanorods by capping Au nanoparticles. *Applied Physics Letters* 2010, **96**, 071107.

Chapter 3

Synthesis of Ionic Surfactant Coordinated CoFe_2O_4 Nanoparticles For Magnetic Characterization

In this chapter we have demonstrated the synthesis of CoFe_2O_4 nanoparticles through chemical co-precipitation route with different ionic surfactants in order to study their magnetic property depending on nature of head and chain-length of tail group of the surfactant.

3. Tuning of Magnetic Response of CoFe_2O_4 Nanoparticles Through Ionic Surfactants

3.1. Preamble

3d transition metal oxide based highly coercive nanomaterials (NMs) are the proper substituent over the currently used alloy-based materials like Nd-Fe-B, Sm-Co, because of its low cost, remarkable chemical and mechanical stability, high magnetocrystalline anisotropy and magnetostriction, moderate saturation magnetization, better coupling coefficient, low thermal conductivity, high electrical resistance, and excellent corrosion resistance.¹⁻³ Among them, inverse spinel type ferrimagnetic CoFe_2O_4 nanoparticles (NPs) have attracted enormous concern due to its potential applications in diverse fields ranging from magnetic data storage, catalysis to drug delivery.⁴⁻⁹ Most of the application of CoFe_2O_4 NPs are strongly influenced by its coercivity which depends mainly on the size of the particle. For larger crystals, the coercivity increases with decreasing particle size and below a critical diameter, the particles become single domain. At this critical state, coercivity reaches its maximum value. Further decrease in size of NPs reduces the coercivity and the particles reach to a superparamagnetic state.¹⁰ Thus, if the demagnetization occurs by perfect coherent rotation of the domain magnetization, as in the case of magnetically isolated single domain particles of a few tens of nanometers, the coercivity will be very high of the order of kOe.¹¹ Hence, for a NP larger than its critical diameter, the coercivity becomes far below to this level. Therefore, long-term endeavors have been concentrated on the synthesis techniques for the enhancement of coercivity of CoFe_2O_4 NPs without going to the single domain configuration.

Various synthetic techniques have been explored to increase the coercivity of as-synthesized nanocrystalline CoFe_2O_4 , such as mechanical milling,¹² oil-in-water microemulsion,¹³ and surface treatment.^{14,15} Liu et al.¹² have explained the reason behind the development of high coercivity (~ 5.1 kOe) of mechanically milled CoFe_2O_4 NPs of 110 nm on the basis of high density of defects and high level of strain developed during the milling. Pillai and Shah have explicated the evolution of

high coercivity (~ 1.4 kOe) of the CoFe_2O_4 magnetic NPs of 50 nm in terms of magnetocrystalline anisotropy imparted by cobalt to the oxide during microemulsion process. Further, it is observed that functional surface modification of CoFe_2O_4 NPs with crystallite size ~ 20 nm has induced a very large coercivity of the order of 9.1 kOe.¹⁵ They explained that the covalent bonding of oleic acid to NP surface might enhance the surface spin disorder, strain, anisotropy, and subsequently increase the coercivity of surfactant coordinated CoFe_2O_4 NPs. It is well recognized that surfactant-assisted surface modification technique provides a huge enhancement in coercivity of magnetic NPs against other synthesis techniques. Therefore, innumerable surface modifications have been performed for achieving the maximum possible coercivity of NPs by varying many surface binding ligands.¹⁶ However, studies regarding the tuning of magnetic properties with the variation of surface coordination environment of monodispersed nanocrystals are scarce in the extant articles. Hence, it would be of fundamental research interest to ascertain the cause of the subtle differences in magnetic response of functionalized NPs with the variation of surface coordinating ligands.

In this chapter, we have reported the quantum origin of enhanced coercivity accompanied with reduced magnetization of the functionalized CoFe_2O_4 NPs with reference to bare one as well as the fine tuning of their magnetic response through a systematic variation of nature of the surface binding ligand. For the purpose, we have synthesized a series of nearly monodispersed CoFe_2O_4 NPs through surfactant-assisted wet chemical method in which nature of the surface binding ligands is chosen by selectively varying both the head and tail part of it. To compare the effect of head group in the magnetic response of functionalized NPs, we have selected π -acceptor and π -donor ligands. Moreover, different chain-length of surfactants having same surface binding head group helps to identify the magnetic responses solely evoked by its chain-length. We have demonstrated an elucidative correlation between the nature of surface binding ligand and magnetic properties of functionalized NPs in terms of NP-ligand interaction which modifies the splitting of d -orbital energy levels. Moreover, increase in coercivity with increasing chain-length

of the surface binding ligand of functionalized CoFe_2O_4 NPs has been explained in the context of additive nature of Vander Waal's interaction.

3.2. Experimental Section

3.2.1. Material Used

The precursor salts, Cobalt Chloride ($\text{CoCl}_2 \cdot 6\text{H}_2\text{O}$), Ferric Chloride ($\text{FeCl}_3 \cdot 6\text{H}_2\text{O}$), and a series of surfactants namely, (1) Tetradecyltrimethyl ammonium bromide (TTAB) ($\text{C}_{17}\text{H}_{38}\text{NBr}$), (2) Cetyltrimethyl ammonium bromide (CTAB) ($\text{C}_{19}\text{H}_{42}\text{NBr}$), (3) Sodium Dodecyl Sulfate (SDS) ($\text{C}_{12}\text{H}_{25}\text{NaSO}_4$), and (4) Dioctyl sodium sulfosuccinate (AOT) ($\text{C}_{20}\text{H}_{37}\text{NaO}_7\text{S}$) are obtained from Sigma-Aldrich. Sodium hydroxide (NaOH) is purchased from Merck. All the reagents are of analytical grade and used without further purification. Double distilled, de-ionized water is used as a solvent.

3.2.2. Synthesis of Surfactant Coordinated CoFe_2O_4 Nanoparticles

We have synthesized CoFe_2O_4 NPs by surfactant-assisted wet chemical route with controllable size distribution by using four different surfactants, namely, (1) TTAB, (2) CTAB, (3) SDS, and (4) AOT as shown in Figure 3.1. TTAB and CTAB belong to π -acceptor ligand group $[\text{N}^+(\text{CH}_3)_3]$ with a minor difference in chain-length (TTAB < CTAB), whereas SDS and AOT belong to π -donor ligand $[\text{SO}_4^-]$ group in which chain-length of SDS is less than that of AOT.

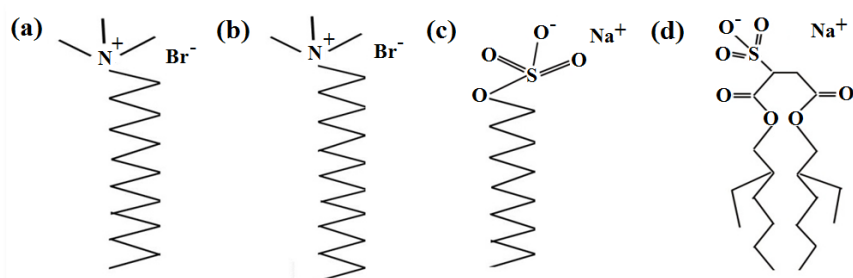


Figure 3.1. Schematic diagrams of surfactants (a) TTAB, (b) CTAB, (c) SDS, (d) AOT used in the synthesis of CoFe_2O_4 NPs. The surfactants TTAB, CTAB contain π -acceptor $[\text{N}^+(\text{CH}_3)_3]$ ligand group whereas SDS, AOT contain π -donor $[\text{SO}_4^-]$ ligand group.

Initially, the aqueous solutions of 0.2M CoCl₂, 6H₂O, 0.4M FeCl₃, 6H₂O, 4M NaOH, and a series of surfactants were prepared individually. The mixture of salt solutions along with different micelle (as described in *Chapter 2*) is stirred constantly for 15 min and heated to a constant temperature of 45 °C in a thermostat. It is then added drop by drop to the pre-heated NaOH solution at 80 °C, taken in three-neck flask, keeping the flow rate, stirring speed, temperature constant. Initially, the mixture is turned into reddish brown and after 1 h of constant stirring at 80 °C, a black solution is obtained. Finally, the precipitation is collected by centrifugation, washed several times by distilled water, and dried at room temperature. Since reaction temperature, pressure, reagent concentration, stirring speed, and reactant addition rate influence the size of the particle, they are maintained in a similar manner in all the cases and a thorough control of these reaction parameters allows us to narrow down the size distribution (60–69 nm) with dispersion less than 10%.

3.3. Result and Discussions

We have synthesized surfactant coordinated CoFe₂O₄ NPs following a wet chemical method (as described in *Chapter 2* in detail). The XRD patterns of all the samples as shown in Figure 3.2 (a) confirm their single phase inverse spinel face centred cubic structure (JCPDS Card No. 22-1086). From the broadening of Bragg reflection peaks, the average grain size of the particles is evaluated to be 23±4 nm using Scherrer's equation for all the cases. TEM study was performed to characterize the size and morphology of the as-prepared and functionalized NPs as shown in Figure 3.2 (b) and (d) respectively. They reveal that all the particles were spherical in shape and fairly monodispersed with particle diameter in the range of 60–70 nm. The size distribution graphs, as shown in Figure 3.2 (c) and (e) demonstrate that the average size of the particles was of the order of 66 nm for both the cases.

The FTIR spectroscopic analysis of functionalized CoFe₂O₄ NPs with reference to its corresponding ligand was carried out in order to study the interaction of surfactant molecules with the NP surface. The surfactant SDS, as shown in Figure 3.2 (f) exhibits four characteristic bands (in the range of 900–1600 cm⁻¹) in which 993,

1219, and 1278 cm^{-1} are associated with the vibrational modes of sulfate group and 1472 cm^{-1} corresponds to the scissoring of methylene group. However, the suppression/broadening of FTIR peaks of functionalized CoFe_2O_4 NPs in comparison to the surfactant imply a potent surface modification of magnetic NPs. These comparative studies help to identify the strong coordination of both head and tail group of surfactant to NP surface.

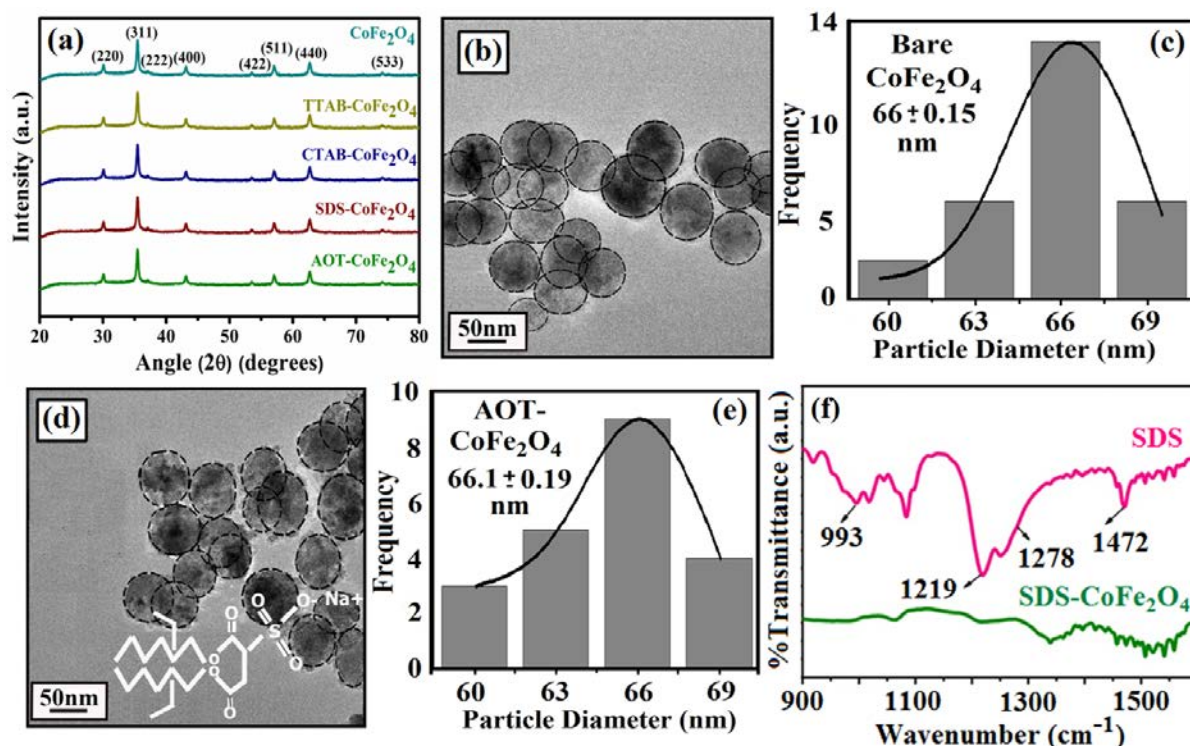


Figure 3.2. (a) Powder X-ray diffractograms of bare and functionalized CoFe_2O_4 NPs. All diffraction peaks in the figure are perfectly indexed in the literature to the face centred cubic inverse spinel structure of CoFe_2O_4 NPs. (b) TEM image, (c) Size distribution graph of as-prepared CoFe_2O_4 NPs. (d) TEM image, (e) Size distribution graph of AOT functionalized CoFe_2O_4 NPs. (f) FTIR spectra of SDS- CoFe_2O_4 NPs along with SDS alone.

In order to study the effect of surface modification on the magnetic response of both bare and ligand functionalized CoFe_2O_4 NPs, we have performed room temperature field dependent magnetization (M-H) measurement. Herein, the surface functionalization of CoFe_2O_4 NPs has so been performed that the effect of both head and tail group of surfactant on the magnetic behaviour of NPs can be identified individually. Figure 3.3 (a)-(d) shows room temperature magnetic hysteresis loops of both bare and modified CoFe_2O_4 NPs, whereas Table 3.1 lists the changes in coercivity and saturation magnetization of functionalized CoFe_2O_4 NPs with reference to the bare NPs and helps to demonstrate distinctly the differences in

obtained results for all the cases. The experimental error on repeated measurements is estimated to be 2.1% and 1.8% for coercivity and saturation magnetization, respectively. The error due to the slight difference ($\sim 1-2$ nm) in the peak of the particle size distributions of all functionalized NPs is very small (a fraction of one Gauss) with respect to the obtained data which is of the order of kG.¹⁷ Taking all these errors under consideration, Table 3.1 suggests that the surface modification of CoFe_2O_4 NPs with surfactant has a notable impact on the ferrimagnetic properties of CoFe_2O_4 NPs at room temperature.

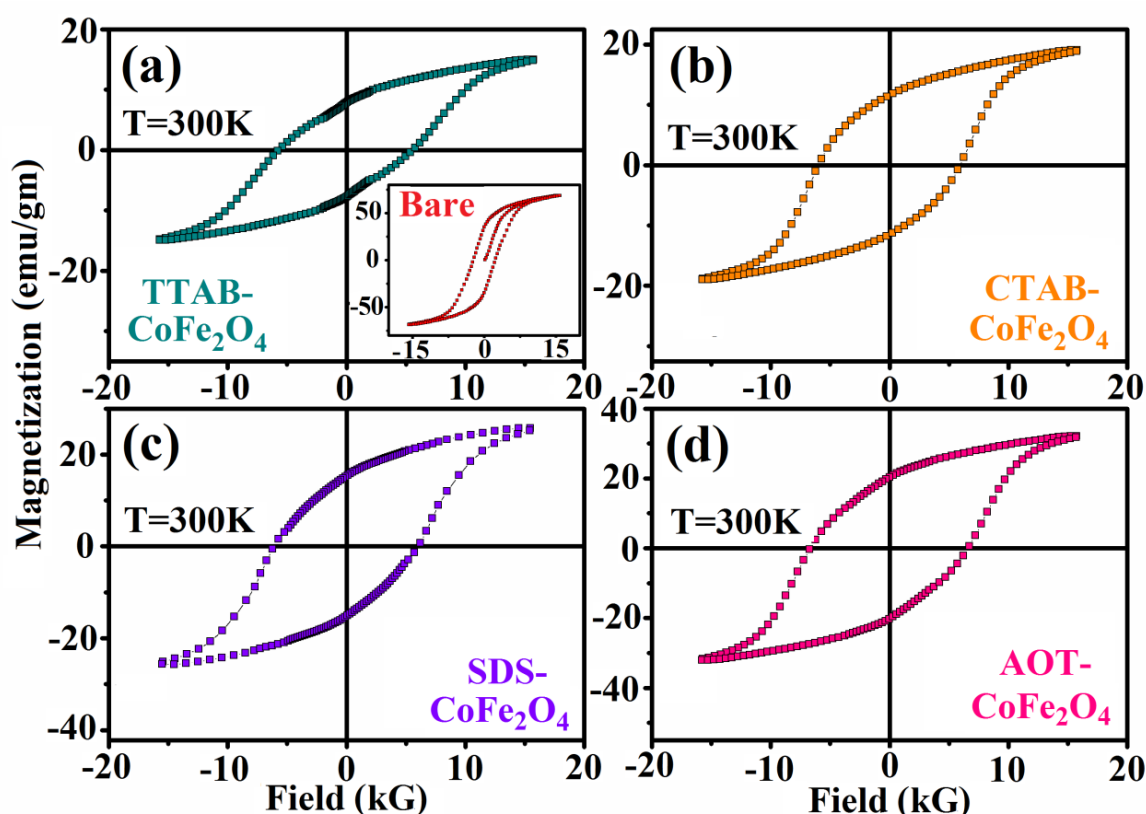


Figure 3.3. Field dependent magnetization of (a) TTAB- CoFe_2O_4 , (b) CTAB- CoFe_2O_4 , (c) SDS- CoFe_2O_4 , and (d) AOT- CoFe_2O_4 NPs at room temperature. The inset of (a) shows the same for bare CoFe_2O_4 .

Table 3.1. List of percentage changes in coercivity (H_c), saturation magnetization (M_s), and magnetocrystalline anisotropy energy (E_A) of bare and functionalized CoFe_2O_4 NPs.

Name	H_c (kOe)	M_s (emu/g)	E_A (J/kg)	% H_c increase	% M_s decrease
Bare CoFe_2O_4	2.29	69.08	4.62		
TTAB- CoFe_2O_4	5.64	15.03	10.2	59.40	78.24
CTAB- CoFe_2O_4	5.95	18.99	13.07	61.51	72.51
SDS- CoFe_2O_4	6.07	25.77	17.83	62.27	62.69
AOT- CoFe_2O_4	6.66	32.20	23.9	65.61	53.39

The coordination of surfactant molecules to the NP surface causes a very strong pinning to the magnetic moments of surface Co^{+2} ions and it leads to a strong surface anisotropy which in turn enhances the coercivity of the functionalized system with reference to native NPs. Moreover, the covalent bonding of ligand leads to quenching of surface magnetic moments of Co^{+2} ions because of ligand to metal charge transfer which causes a significant reduction of magnetization of modified NPs with respect to the bare one. Indeed, upon attachment with different type of surfactants, the distinct changes in coercivity and magnetization of native NPs occur due to different degree of splitting of d -orbital energy levels of surface Co^{+2} ions. According to the ligand field theory, it is well known that π -acceptor ligand results in larger crystal field splitting energy (CFSE) of d -orbital energy levels of transition metal ions than π -donor ligand. Therefore, enhanced ligand-metal interaction in case of π -acceptor ligand favours the quenching of orbital magnetic moments of 3d-transition metal ions more^{18,19} and subsequently reduces its spin-orbit coupling. Hence, larger the CFSE of d -orbital energy levels of Co^{+2} ions due to ligand coordination reduces spin-orbit coupling more. Further, as stated in Stoner-Wohlfarth theory, the magnetocrystalline anisotropy energy E_A of a single-domain particle can be approximated as

$$E_A = KV \sin^2 \theta \quad (3.1)$$

where K is the magnetocrystalline anisotropy constant, V is the volume of a NP, and θ is the angle between magnetization direction and easy axis of NP. Since K is determined by the strength of spin-orbit coupling, reduced spin-orbit coupling results in a decrease in magnetocrystalline anisotropy of the NP system. Hence, the surface Co^{+2} ions with higher CFSE of d -orbital energy levels due to ligand interaction should have smaller coercivity.

Not only magnetocrystalline anisotropy but also magnetoelastic, magnetostatic, and shape anisotropy contribute significantly to the coercivity of a magnetic system. The adverse break down of local symmetry at the NP surface enhances the surface anisotropy which has a notable value in case of nano-sized

object. For a spherical particle with diameter D , the anisotropy energy constant (K_{eff}) is described by the relation

$$K_{eff} = K_b + \frac{6}{D}K_s \quad (3.2)$$

where K_b and K_s are the bulk and surface anisotropy energy constants, respectively. Further, Bødker et al.²⁰ have reported that K_{eff} enhances more when the surface is modified with foreign molecules. Hence, the presence of surfactant molecule also enhances the anisotropy, rather coercivity of NP system. Herein, functionalization has been carried out with four ligands, among them, TTAB and CTAB contain π -acceptor tri-methyl amine head group [$N^+(CH_3)_3$], whereas SDS and AOT contain π -donor sulfate head group [SO_4^-]. Due to higher CFSE of Co^{+2} ions in presence of π -acceptor ligand, TTAB and CTAB functionalized $CoFe_2O_4$ NPs show lower coercivity enhancement than SDS and AOT functionalized $CoFe_2O_4$ NPs.

In recent past, Giri et al.²¹ have reported that although Mn_3O_4 NPs being paramagnetic at room temperature become ferromagnetic in nature upon coordination with π -donor ligand. Further, from Table 3.1, it is observed that the coercivity of modified $CoFe_2O_4$ NPs is increased with increasing chain-length of the surfactant, for example, NPs modified with TTAB (higher chain-length) shows higher coercivity than those modified with CTAB (shorter chain-length) though they have the same π -acceptor head group. Similar property is also observed in case of NPs modified with π -donor ligands (AOT/SDS). In general, the ionic surfactants are found to be adsorbed on the NPs' surface due to a number of possible interactions such as covalent bonding, electrostatic forces, Vander Waals force, hydrogen bonding, etc, depending on the system condition.²¹ Therefore, the adsorption of ionic surfactants on $CoFe_2O_4$ NPs' surface is due to Vander Waals force aside from electrostatic interaction. Due to the additive nature of Vander Waals force, the interaction of surfactant with the NPs' surface is expected to be enhanced with increasing number of branching and/or chain-length of the surfactant. Because the attachment of surfactant molecules on NP surface causes a very strong pinning to the magnetic moments of surface Co^{+2} ions,²² it leads to a very strong surface

anisotropy which in turn enhances the coercivity of the functionalized system. Therefore, the influence of both head as well as tail group of surfactant on native CoFe_2O_4 NPs has been individually identified through a prudential analysis of data obtained through magnetic measurement.

The observed decrease in saturation magnetization in modified CoFe_2O_4 NPs with respect to bare one is due to ligand to metal charge transfer effect which enables to quench the unpaired d-electrons of surface Co^{+2} ions and subsequently the net magnetization of the system reduces. Further, larger splitting of *d*-orbital energy levels of transition metal ions in presence of ligand results in greater reduction of magnetization because enhanced ligand-metal interaction helps to quench unpaired d-electrons of Co^{+2} ions more. Hence, TTAB/CTAB modified CoFe_2O_4 NPs result in lower magnetization than SDS/AOT modified NPs. Thus, we can tailor the magnetic properties of the functionalized CoFe_2O_4 NPs by varying both the nature of head and chain-length of surfactant judiciously for its application in specific operation. It is an important encouraging result from fundamental perspective because the enhancement of a specific property of magnetic NPs has increased its effectiveness in the application fields such as biosensing, hyperthermia, drug delivery, and magnetic resonance imaging.

3.4. Conclusion

In conclusion, rational surface modifications of CoFe_2O_4 NPs have been performed in order to investigate the effect of nature of surface coordinated ligand on magnetic response of modified CoFe_2O_4 NPs. A sequence of surface modifications has been implemented with π -acceptor (TTAB, CTAB) and π -donor (SDS, AOT) ligands associated with different chain-length on monodispersed nanocrystalline CoFe_2O_4 . It has been observed that coercivity of native NPs increases as well as magnetization decreases upon coordination with surfactants. Furthermore, we have defined a correlation between the nature of the surface binding ligand and the magnetic behaviour of functionalized CoFe_2O_4 NPs in terms of ligand field theory. The extent of changes in magnetic properties of modified CoFe_2O_4 NPs is strongly

correlated with the efficacy of ligand to induce splitting of *d*-orbital energy levels of Co^{+2} ions. The ligand that induces largest splitting of *d*-orbital energy levels of surface Co^{+2} ions results in nethermost enhancement of coercivity and upmost decrement of saturation magnetization. Moreover, the magnetic response of functionalized CoFe_2O_4 NPs accompanying with same head group, coercivity increases with increasing chain-length of the surface binding ligand. This relationship has been demonstrated employing the additive nature of the Vander Waal's interaction. We believe that these findings would pave a path for further research developments in the field of rational design of surfactant coordinated NPs to enhance its potency in diverse application fields.

Bibliography

- [1] Liu, C.; Zou, B.; Rondinone, A. J.; Zhang, Z. J., Chemical control of superparamagnetic properties of magnesium and cobalt spinel ferrite nanoparticles through atomic level magnetic couplings. *Journal of the American Chemical Society* 2000, **122**, 6263.
- [2] Chikazumi, S., *Physics of Magnetism* (Wiley, New York, 1969).
- [3] Mohaideen, K. K.; Joy, P. A., High magnetostriction and coupling coefficient for sintered cobalt ferrite derived from superparamagnetic nanoparticles. *Applied Physics Letters* 2012, **101**, 072405.
- [4] Kryder, M. H., Ultrahigh-density recording technologies. *MRS Bulletin* 1996, **21**, 17.
- [5] Shiju, N. R.; Guliyants, V. V., Recent developments in catalysis using nanostructured materials. *Applied Catalysis A* 2009, **356**, 1.
- [6] Hafeli, U.; Schutt, W.; Teller, J.; Zborowski, M., *Scientific and Clinical Applications of Magnetic Carriers* (Plenum Press, New York, 1997).
- [7] Gao, J.; Gu, H.; Xu, B., Multifunctional magnetic nanoparticles: design, synthesis, and biomedical applications. *Accounts of Chemical Research* 2009, **42**, 1097.
- [8] Lee, N.; Hyeon, T., Designed synthesis of uniformly sized iron oxide nanoparticles for efficient magnetic resonance imaging contrast agents. *Chemical Society Review* 2012, **41**, 2575.
- [9] Mitchell, D. G., MR imaging contrast agents – what's in a name?. *Journal of Magnetic Resonance Imaging* 1997, **7**, 1.
- [10] Chakraverty, S.; Mitra, S.; Mandal, K.; Nambissan, P. M. G.; Chattopadhyay, S., Positron annihilation studies of some anomalous features of NiFe₂O₄ nanocrystals grown in SiO₂. *Physical Review B* 2005, **71**, 024115.
- [11] Street, R., Properties of Magnetic Materials. *Nature* 1956, **178**, 1023.
- [12] Liu, B. H.; Ding, J.; Dong, Z. L.; Bothroyd, C. B.; Yin, J. H.; Yi, J. B., Microstructural evolution and its influence on the magnetic properties of CoFe₂O₄ powders during mechanical milling. *Physical Review B* 2006, **74**, 184427.
- [13] Pillai, V.; Shah, D. O., Synthesis of high-coercivity cobalt ferrite particles using water-in-oil microemulsions. *Journal of Magnetism and Magnetic Materials* 1996, **163**, 243.
- [14] Pal, D.; Mandal, M.; Chaudhuri, A.; Das, B.; Sarkar, D., Micelles induced high coercivity in single domain cobalt-ferrite nanoparticles. *Journal of Applied Physics* 2010, **108**, 124317.
- [15] Limaye, M. V.; Singh, S. B.; Date, S. K.; Kothari, D.; Reddy, V. R.; Gupta, A.; Sathe, V.; Choudhary, R. J.; Kulkarni, S. K., High coercivity of oleic acid capped CoFe₂O₄ nanoparticles at room temperature. *Journal of Physical Chemistry B* 2009, **113**, 9070.
- [16] Mitra, S.; Das, S.; Mandal, K.; Chaudhuri, S., Synthesis of a α -Fe₂O₃ nanocrystal in its different morphological attributes: growth mechanism, optical and magnetic properties. *Nanotechnology* 2007, **18**, 275608.
- [17] Liu, C.; Rondinone, A. J.; Zhang, Z. J., Synthesis of magnetic spinel ferrite CoFe₂O₄ nanoparticles from ferric salt and characterization of the size-dependent superparamagnetic properties. *Pure Applied Chemistry* 2000, **72**, 37.
- [18] Leeuwen, D. A. van; Ruitenbeek, J. M. van; L. Jongh, J. De, Quenching of magnetic moments by ligand metal interactions in nano-sized magnetic metal clusters. *Physical Review Letters* 1994, **73**, 1432.
- [19] Figgis, B. N.; Hitchman, M. A., *Ligand field theory and its applications* (Wiley-VCH, New York, 2000).
- [20] Bødker, F.; Mørup, S.; Linderoth, S., Surface effects in metallic iron nanoparticles. *Physical Review Letters* 1994, **72**, 282.
- [21] Giri, A.; Goswami, N.; Pal, M.; Myint, M. T. Z.; Al-Harhi, S.; Singha, A.; Ghosh, B.; Dutta, J.; Pal, S. K., Rational surface modification of Mn₃O₄ nanoparticles to induce multiple

photoluminescence and room temperature ferromagnetism. *Journal of Material Chemistry C* 2013, **1**, 1885.

[22] Zhang, R.; Somasundaran, P., Advances in adsorption of surfactants and their mixtures at solid/solution interfaces. *Advances in Colloid and Interface Science* 2006, **123**, 213.

Chapter 4

Synthesis of Non-ionic Surfactant Coordinated CoFe₂O₄ Nanoparticles For Magnetic Characterization

This chapter demonstrates the effect of nature and the number of donor head group as well as chain-length of tail group of surfactant on the magnetic response of surfactant coordinated CoFe₂O₄ NPs.

4. Tuning of Magnetic Response of CoFe_2O_4 Nanoparticles Through Non-ionic Surfactants

4.1. Preamble

The conservation of innate ferromagnetic character of magnetic nanomaterials (NMs) with reduced size is of great importance for developing portable technological devices such as high-density magnetic recording, magnetic tunnel junction, magnetostrictive sensor, and magneto-optic devices.² Among different 3d transition metal oxide based magnetic nanoparticles (NPs), extensive studies on CoFe_2O_4 NPs have been performed due to their high coercivity, moderate saturation magnetization, large magnetocrystalline anisotropy, low cost, remarkable chemical and mechanical stability.¹ However, gradual decrease in size of CoFe_2O_4 NPs towards superparamagnetic size limit results in zero coercivity due to ambient thermal energy which can easily randomize its direction of magnetization. Recent advancement of surface science suggests that surface modification of bare CoFe_2O_4 NPs using surfactants can significantly enhance its magnetic properties and in an attempt to tune that enhanced magnetic properties by varying the nature of head and chain-length of tail group of the surfactant has been presented in *Chapter 3*. Upon getting knowledge about the fact that donor head group of surfactants can enhance the magnetic property of functionalized CoFe_2O_4 NPs more than the acceptor head group of surfactants due to weak ligand-metal interaction, it is our fundamental research interest to investigate the effect of nature and number of donor head group of the surfactant on the magnetic property of functionalized CoFe_2O_4 NPs.

In this chapter, we have reported the tuning of enhanced coercivity and reduced magnetization of functionalized CoFe_2O_4 NPs by varying the number of same donor head and tail group of the surface binding ligand and also investigated the effect of nature of the donor head group of the surfactant on the magnetic properties of functionalized CoFe_2O_4 NPs. For the sake of understanding the role of donor head groups, we have chosen the ligands of Tween and TritonX groups where

Tween group of ligands have larger number of σ -donor head groups than TritonX group of ligands along with a single π -donor head group. To distinguish the effect of chain-length, we have varied the chain-length of ligands within individual groups, such as TritonX-100 has larger chain-length than TritonX-114 and Tween-80 has longer chain than Tween-20. We have demonstrated the correlation between the surface binding ligand and magnetic properties of functionalized NPs in terms of charge transfer effect and Vander Waal's interaction.

4.2. Experimental Section

4.2.1. Material Used

The precursor salts, Cobalt Chloride ($\text{CoCl}_2, 6\text{H}_2\text{O}$), Ferric Chloride ($\text{FeCl}_3, 6\text{H}_2\text{O}$), and a series of surfactants namely, (1) TritonX-114 (TX-114) ($\text{C}_{14}\text{H}_{22}\text{O}(\text{C}_2\text{H}_4\text{O})_n$, [$n = 7-8$]), (2) TritonX-100 (TX-100) ($\text{C}_{14}\text{H}_{22}\text{O}(\text{C}_2\text{H}_4\text{O})_n$, [$n=9-10$]), (3) Tween-20 (T-20) ($\text{C}_{58}\text{H}_{114}\text{O}_{26}$), (4) Tween-80 (T-80) ($\text{C}_{64}\text{H}_{124}\text{O}_{26}$) are obtained from Sigma-Aldrich. Sodium hydroxide (NaOH) is purchased from Merck. All the reagents are of analytical grade and used without further purification. Double distilled, de-ionized water is used as a solvent.

4.2.2. Synthesis of Surfactant Coordinated CoFe_2O_4 Nanoparticles

We have synthesized CoFe_2O_4 NPs by surfactant-assisted wet chemical route (as described in *Chapter 2* in detail) with controllable size distribution by using four different surfactants, namely, (1) TX-114, (2) TX-100, (3) T-20, and (4) T-80 as shown in Figure 4.1. The TritonX group of surfactants contain C-O-C and -OH as σ -donor head groups and Tween group of surfactants have the same groups in addition to an extra C=O, π -donor head group. Moreover, increasing number of σ -donor head groups (TX-114<TX-100, T-20<T-80) for a given group of surfactant helps to identify the magnetic responses solely evoked by the donor head group of the surfactant.

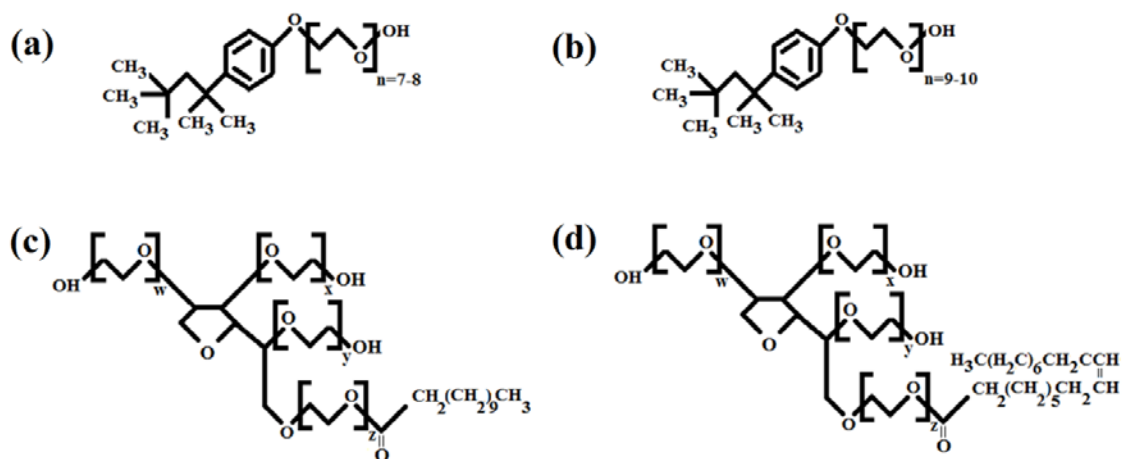


Figure 4.1. Schematic diagram of surfactants (a) TX-114, (b) TX-100, (c) T-20, and (d) T-80 used in the synthesis of CoFe_2O_4 NPs. The TritonX group of surfactants are smaller in size with C–O–C and –OH as σ -donor head groups whereas the Tween group of surfactants are larger in size with same groups in addition to an extra C=O, π -donor head group.

Initially, we have prepared the aqueous solutions of 0.2M $\text{CoCl}_2 \cdot 6\text{H}_2\text{O}$, 0.4M $\text{FeCl}_3 \cdot 6\text{H}_2\text{O}$, 4M NaOH, and a series of surfactants individually. The mixture of salt solutions along with different micelle is stirred constantly for 15 min and heated to a constant temperature of 45 $^\circ\text{C}$ in a thermostat. It is then added drop by drop to the pre-heated sodium hydroxide solution at 80 $^\circ\text{C}$, taken in three-neck flask, keeping the flow rate, stirring speed, temperature constant. Initially, the mixture is turned into reddish brown and after 1 h of constant stirring at 80 $^\circ\text{C}$, a black solution is obtained. Finally, the precipitation is collected by centrifugation, washed several times by water, and dried at room temperature. Since reaction temperature, pressure, reagent concentration, stirring speed, and reactant addition rate influence the size of the particle, they are maintained in a similar manner for all the cases. Thorough control of these reaction parameters allows us to narrow down the size distribution in the range 70–90 nm.

4.3. Result and Discussions

We have synthesized surfactant coordinated CoFe_2O_4 NPs following a wet chemical method (as described in *Chapter 2* in detail). TEM study was performed to characterize the size and morphology of the as-prepared and functionalized NPs as shown in Figure 4.2 (a) and (b) respectively. They reveal that all the particles were

spherical in shape and fairly monodispersed with particle diameter in the range of 70–90 nm. The size distribution graphs, as shown in Figure 4.2 (d) and (e) demonstrate that the average size of the particles was of the order of 80 nm for both the cases. The XRD patterns of all the samples as shown in Figure 4.2 (c) confirm their single phase inverse spinel face centred cubic structure (JCPDS Card No. 22-1086).

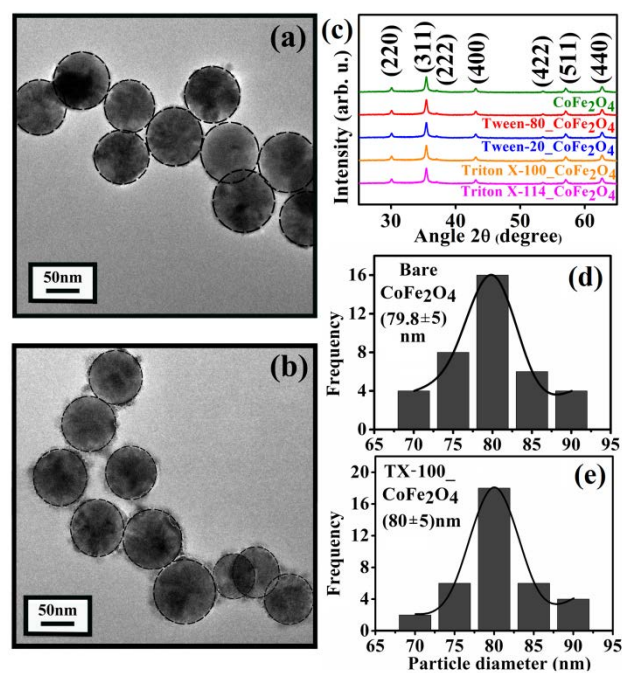


Figure 4.2. TEM images of (a) bare, and (b) TX-100 functionalized CoFe₂O₄ NPs. (c) Powder X-ray diffractograms of bare and functionalized CoFe₂O₄ NPs. All diffraction peaks in the figure are perfectly indexed in the literature to the face centred cubic inverse spinel structure of CoFe₂O₄ NPs. Size distribution graph of (d) bare, and (e) TX-100 functionalized CoFe₂O₄ NPs.

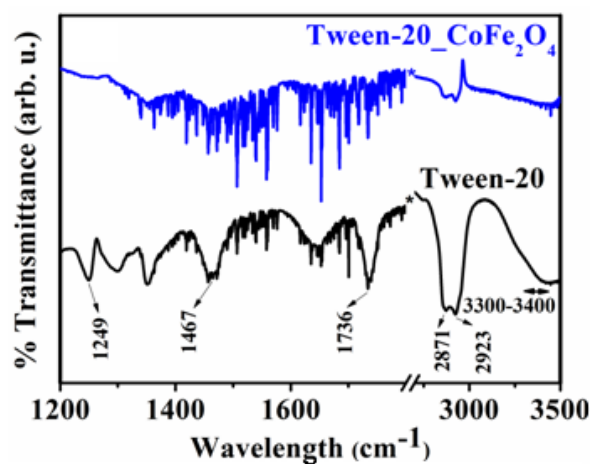


Figure 4.3. FTIR spectra of Tween-20 functionalized CoFe₂O₄ NPs with Tween-20 alone.

To investigate the interaction of ligand with the NP surface, a comparative FTIR spectroscopic study has been performed on both the ligand and surfactant coordinated CoFe_2O_4 NPs as shown in Figure 4.3. The ligand T-20 shows five characteristic bands (in the range of $1200\text{--}3000\text{cm}^{-1}$) at 1249 , 1467 , 1736 , 2871 , and 2923cm^{-1} which are associated with the stretching of ester C-O, bending of CH_2 , stretching of ester C=O, and symmetric and antisymmetric stretching of alkyl C-H bonds respectively and a characteristic band in the range of $3300\text{--}3400\text{cm}^{-1}$ belongs to the stretching of -OH bond. However, in case of surfactant modified NP, all these bands of bare ligand are broadened and/or suppressed which imply that a potent surface modification of the NP has occurred upon functionalization.

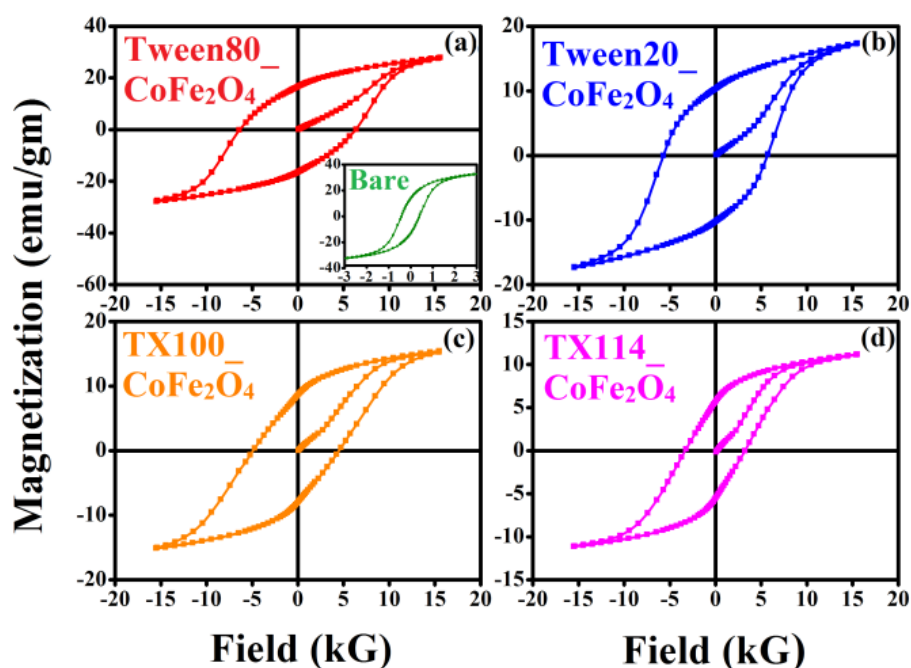


Figure 4.4. Room temperature field dependent magnetization study of (a) Tween-80, (b) Tween-20, (c) Triton X-100, and (d) Triton X-114 capped CoFe_2O_4 NPs. The inset of (a) represents the hysteresis loop of bare CoFe_2O_4 NPs.

Table 4.1. List of average particle diameter, coercivity (H_c), magnetization (M_s), anisotropy energy (E_A), and percentage change in H_c and M_s of surfactant coordinated CoFe_2O_4 NPs with respect to bare.

Name	H_c (kOe)	M_s (emu/g)	E_A (J/kg)	% H_c increase	% M_s decrease
Bare CoFe_2O_4	0.391	40.13	4.45		
TX-114_ CoFe_2O_4	3.32	11.12	8.4	88.22	72.29
TX-100_ CoFe_2O_4	4.91	15.23	19.97	92.03	62.05
T-20_ CoFe_2O_4	5.73	17.36	26.17	93.18	56.74
T-80_ CoFe_2O_4	6.4	27.86	48.7	93.89	30.57

Figure 4.4 shows the magnetic hysteresis loops of bare and surfactant coordinated CoFe_2O_4 NPs and Table 4.1 lists their corresponding magnitude of coercivity, saturation magnetization, and anisotropy energy. Due to the positive surface charges of $\text{Co}^{+2}/\text{Fe}^{+3}$ ions, the CoFe_2O_4 molecule induces a dipole moment to the approaching surfactant which in turn causes a large crystal field splitting of d -orbital energy levels of those surface $\text{Co}^{+2}/\text{Fe}^{+3}$ ions.⁶⁻⁸ The ligand field theory (LFT) suggests that the degree of crystal field splitting depends on the nature as well as the number of functional head group of those ligands.

The crystal field splitting energy (CFSE) of d -orbital energy levels of transition metal ions increases with greater interaction of donor functional groups of the ligand with them.⁹ Functional groups of smaller ligands can interact with surface ions of the NP more efficiently than their larger counterpart. Thus, smaller ligand favours enhanced electrostatic ligand-metal interaction which results in larger CFSE. The TritonX group of surfactants are smaller in size with C-O-C and -OH as σ -donor head groups whereas the Tween group of surfactants are larger in size with same groups in addition to an extra C=O, π -donor head group (as mentioned in Figure 4.1). Therefore, the enhanced ligand-metal interaction in case of TritonX modified CoFe_2O_4 NPs helps to quench the unpaired orbital magnetic moments of surface $\text{Co}^{+2}/\text{Fe}^{+3}$ ions more efficiently than the Tween group modified one through the process of ligand to metal charge transfer (LMCT) and results more diminution of its saturation magnetization than that of the Tween group modified NPs. Since only the unpaired number of electrons of Co^{+2} ions are responsible for the net magnetization of CoFe_2O_4 NP system, from now on, we consider the effect of ligand on Co^{+2} ions only.

Due to LMCT, the odd electrons of surface Co^{+2} ions get paired up with the electrons coming from ligand and therefore, the spin-orbit coupling of the functionalized NP system is going to decrease significantly. Stoner-Wohlfarth theory suggests that magnetocrystalline anisotropy energy of magnetic NPs extensively depends on its spin-orbit coupling. Therefore, the maximally reduced spin-orbit coupling of TritonX modified CoFe_2O_4 NPs results in huge decrease (~ 1 kG) of its

magnetocrystalline anisotropy or rather the coercivity than that of the Tween group modified NPs. Moreover, it is also well known that σ -donor ligands result in larger CFSE than π -donors.⁹ Therefore, the presence of a single π -donor functional group (C=O) in the Tween group of surfactants helps to enhance the ferrimagnetic character of Tween modified CoFe₂O₄ NP system more than the TritonX modified one as smaller CFSE results in reduced ligand metal interaction.

Table 4.1 indicates that the coercivity for a particular group of functionalized CoFe₂O₄ NPs increases with increasing chain-length of the surfactant, say, for example, within the TritonX group, TX-100 (higher chain-length) coated NPs show higher coercivity than those modified with TX-114 (shorter chain-length). In general, the non-ionic surfactants are found to be adsorbed on the NPs' surface and it is governed by a number of interactions such as covalent bonding, electrostatic forces, Vander Waals force, hydrogen bonding, etc, depending on the system condition.¹⁰ Therefore, in our case, the adsorption of non-ionic surfactants on CoFe₂O₄ NPs' surface is due to Vander Waals force aside from induced electrostatic interaction. Due to the additive nature of Vander Waals force, the interaction of surfactant with the NPs' surface is expected to be enhanced with increasing number of branching and/or chain-length of the surfactant. Because the attachment of surfactant molecules on NP surface causes a very strong pinning to the magnetic moments of surface Co⁺² ions,¹¹ it leads to a very strong surface anisotropy which in turn enhances the coercivity of the functionalized system. Thus, we can infer that surface modification has an extensive impact on the magnetic properties of transition metal oxide based magnetic nanostructures and more importantly, its magnetic properties can be well regulated by judiciously varying donor head and tail group of the surface binding ligand.

4.4. Conclusion

In conclusion, we have synthesized CoFe₂O₄ NPs with four non-ionic surfactants in order to investigate the effects of nature of donor head group as well as increasing number of donor head and tail groups of the surfactant on its magnetic

properties. We have found that the ligand that induces smallest CFSE results in strongest ferromagnetic activation of the functionalized NPs. Moreover, the coercivity is found to increase with increasing chain-length of the surface binding ligand. We believe that apart from the fundamental scientific interest, our work would put a step forward in the development of rational designing of surfactant coordinated NPs to enhance its potency in diverse application fields.

Bibliography

- [1] Bozorth, R. M., Ferromagnetism (D. Van Nostrand Company, New York, 1961).
- [2] Dorsey, P. C.; Lubitz, P.; Chrisey, D. B.; Horwitz, J. S., CoFe₂O₄ thin films grown on (100) MgO substrates using pulsed laser deposition. *Journal of Applied Physics* 1996, **79**, 6338.
- [3] Liu, B. H.; Ding, J.; Dong, Z. L.; Bothroyd, C. B.; Yin, J. H.; Yi, J. B., Microstructural evolution and its influence on the magnetic properties of CoFe₂O₄ powders during mechanical milling. *Physical Review B* 2006, **74**, 184427.
- [4] Limaye, M. V.; Singh, S. B.; Date, S. K.; Kothari, D.; Reddy, V. R.; Gupta, A., High coercivity of oleic acid capped CoFe₂O₄ nanoparticles at room temperature. *Journal of Physical Chemistry B* 2009, **113**, 9070.
- [5] Rakshit, R.; Mandal, M.; Pal, M.; Mandal, K., Tuning of magnetic properties of CoFe₂O₄ nanoparticles through charge transfer effect. *Applied Physics Letters* 2014, **104**, 092412.
- [6] Pal, M.; Singh, A. K.; Rakshit, R.; Mandal, K., Surface chemistry modulated introduction of multifunctionality within Co₃O₄ nanocubes. *RSC Advances* 2015, **5**, 16311.
- [7] Pal, M.; Rakshit, R.; Mandal, K., Facile functionalization of Fe₂O₃ nanoparticles to induce inherent photoluminescence and excellent photocatalytic activity. *Applied Physics Letters* 2014, **104**, 233110.
- [8] Pal, M.; Rakshit, R.; Mandal, K., Surface modification of MnFe₂O₄ nanoparticles to impart intrinsic multiple fluorescence and novel photocatalytic properties. *ACS Applied Materials and Interfaces* 2014, **6**, 4903.
- [9] Figgis, B. N.; Hitchman, M. A., Ligand field theory and its applications (Wiley-VCH, New York, 2000).
- [10] Zhang, R.; Somasundaran, P., Advances in adsorption of surfactants and their mixtures at solid/solution interfaces. *Advances in Colloid and Interface Science* 2006, **123**, 213.
- [11] Bødker, F.; Mørup, S.; Linderoth, S., Surface effects in metallic iron nanoparticles. *Physical Review Letters* 1994, **72**, 282.

Chapter 5

Morphology & Size Dependent Magnetic Responses of MFe_2O_4 ($M= Fe, Co, \& Mn$) & SiO_2 Coated MFe_2O_4 Nanostructures

This chapter demonstrates detailed morphology, size, and nonmagnetic SiO_2 coating effect on the magnetic responses of as-synthesized different MFe_2O_4 ($M= Fe, Co, \text{ and } Mn$) nanostructures.

5. Morphology and Size Dependent Magnetic Response of MFe_2O_4 (M=Fe, Co, and Mn) and SiO_2 Coated MFe_2O_4 Nanomaterials

5.1. Preamble

Fabrication of magnetic nanomaterials (NMs) and design them to achieve desired morphology has become a topic of great interest to the researchers during last few decades. Morphology of the NMs plays an important role in tuning their magnetic as well as electronic transport properties. It has been found that materials having building blocks with same composition but different morphology can have different properties.^{1,2} During last few years, the researchers have developed various procedures to synthesize different nanostructures (NSs) such as sphere, rod, wire, chain, disc, tiles, etc., and they have found different properties for different morphologies. Among all other NSs, researchers are very much interested in fabricating nano hollow spheres (NHSs) because of their special morphology and peculiar characteristics. The hollow structure has several applications such as in catalysis, controlled drug delivery, light fillers, low dielectric constant materials, radar absorbing materials, photonic crystals, high density magnetic storage, spintronics device etc.^{3,4} Large void space of hollow sphere can be used to encapsulate drugs, cosmetics, and DNA and also for their controlled release. These materials have low density due to their hollow interior and large effective surface area which can help to absorb the electromagnetic (EM) radiation more efficiently as well as expand the array of imaging markers that are very suitable for revelation of cancer at an early stage.

Most of the applications of magnetic NSs require a coating with a nonmagnetic and biocompatible ligand since they possess an immense tendency to get agglomerated very easily and SiO_2 coated magnetic nanoparticles (NPs) are found to get more easily dispersed in liquid media by screening the magnetic dipolar attraction among the magnetic NPs. The silica coating also protects the NPs

from leaching in an acidic environment. The existence of abundant silanol groups on the silica layer of magnetic NSs helps to attach various functional groups and most importantly, it can provide a chemically inert surface for magnetic NPs in biological systems^{5,6} which can be very useful in biomedical applications such as cell labeling⁷ and cell separation,⁸ targeted drug delivery,^{9,10} and magnetic ferrofluids hyperthermia.^{11,12} Moreover, SiO₂ coating of magnetic NPs provides immense importance in the applications of electromagnetic shielding due to its high dielectric property as well as diamagnetism.

In this chapter, we have reported the facile template free solvothermal synthesis of MFe₂O₄ (M= Co, Fe, and Mn) NPs and a series of NHSs of increasing diameter followed by SiO₂ coating over their surface through Stöber process and finally carried out thorough investigation of their magnetic response depending on their morphology, size, and the presence of nonmagnetic layer over the surface. Detailed study reveals that enhanced surface/bulk atomic ratio of nano hollow structures affects its magnetic properties significantly in contrast to NP configuration. Moreover, SiO₂ coating over the surface of the magnetic NSs is found to introduce huge surface anisotropy and ligand to metal charge transfer which in turn changes the magnetic property of bare NSs incomparably.

5.2. Experimental Section

5.2.1. Material Used

The precursor salts, Cobalt Chloride (CoCl₂, 6H₂O), Ferric Chloride (FeCl₃, 6H₂O), Manganese Chloride (MnCl₂, 6H₂O), Ethylene Glycol, Urea, Oleylamine, and Tetraethyl Orthosilicate are obtained from Sigma-Aldrich. Ethyl Alcohol and Ammonium Hydroxide are purchased from Merck. All the reagents are of analytical grade and used without further purification. Double distilled, de-ionized water is used during the synthesis.

5.2.2. Synthesis of MFe_2O_4 (M= Fe, Co, and Mn) Nanoparticles and Nano hollow spheres

MFe_2O_4 (M= Fe, Co, and Mn) NP and a series of NHSs of different diameter were synthesized by a facile template free solvothermal method (as described in Chapter 2 in detail) based on novel mechanism, Ostwald ripening (as described in Chapter 1 in detail).¹³⁻¹⁵ In a typical synthesis of MFe_2O_4 NHSs, the metal ion salts (only $FeCl_3, 6H_2O$ in case of Fe_3O_4 and addition of $CoCl_2, 6H_2O/MnCl_2, 6H_2O$ in case of $CoFe_2O_4$, and $MnFe_2O_4$ NHSs respectively in 2:1 ratio), and a base, urea were dissolved in a mixture of ethylene glycol and ethanol which are also taken in 2:1 ratio. A capping agent, oleylamine was added to the solution mixture and finally a homogeneous clear solution was transferred into a teflon lined stainless steel autoclave and heated to 200 °C for 12 h in case of Fe_3O_4 , 180 °C for 12 h in case of $CoFe_2O_4$, and 200 °C for 24 h in case of $MnFe_2O_4$ NHSs. Finally, the as-prepared black product is collected by centrifugation, washed several times by alcohol, and dried at room temperature. We have been able to synthesize MFe_2O_4 NHSs of increasing diameter only by modulating the amount of capping agent, oleylamine. More specifically, increasing amount of capping agent reduces the size of the NHSs since capping agent restricts the growth of the nanocrystals. Additionally, the synthesis of MFe_2O_4 NPs has been carried out following the same procedure as the NHS but with reduced reaction time. Detailed amount of precursor salts, solvents, base, capping agent, and reaction time for the synthesis of MFe_2O_4 (M= Co, Fe, and Mn) NPs and NHSs are presented in Table 5.1, Table 5.2, and Table 5.3 respectively.

Table 5.1. List of amount of precursor salts, solvents, base, capping agent, and reaction time for the synthesis of $CoFe_2O_4$ NPs and NHSs.

$CoFe_2O_4$	$CoCl_2, 6H_2O$ (g)	$FeCl_3, 6H_2O$ (g)	Ethylene Glycol (ml)	Ethanol (ml)	Urea (g)	Oleylamine (ml)	Reaction time (h)
NP-100	0.36	0.891	20	10	0.53	3	9
NHS-100	0.36	0.891	20	10	0.53	3	12
NHS-160	0.36	0.891	20	10	0.53	2.5	12
NHS-250	0.36	0.891	20	10	0.53	2	12
NHS-350	0.36	0.891	20	10	0.53	1.5	12

Table 5.2. List of amount of precursor salts, solvents, base, capping agent, and reaction time for the synthesis of Fe₃O₄ NPs and NHSs.

Fe ₃ O ₄	FeCl ₃ ·6H ₂ O (g)	Ethylene Glycol (ml)	Ethanol (ml)	Urea (g)	Oleylamine (ml)	Reaction time (h)
NP-100	1.56	20	10	0.53	3	9
NHS-100	1.56	20	10	0.53	3	12
NHS-160	1.56	20	10	0.53	2.5	12
NHS-250	1.56	20	10	0.53	2	12
NHS-350	1.56	20	10	0.53	1.5	12
NHS-725	1.56	20	10	0.53	1	12

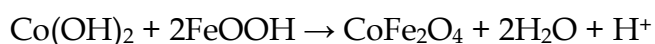
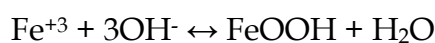
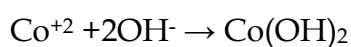
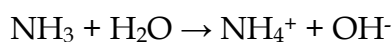
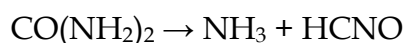
Table 5.3. List of amount of precursor salts, solvents, base, capping agent, and reaction time for the synthesis of MnFe₂O₄ NPs and NHSs.

MnFe ₂ O ₄	MnCl ₂ ·6H ₂ O (g)	FeCl ₃ ·6H ₂ O (g)	Ethylene Glycol (ml)	Ethanol (ml)	Urea (g)	Oleylamine (ml)	Reaction time (h)
NP-160	0.3	0.891	20	10	0.53	3	20
NHS-160	0.3	0.891	20	10	0.53	3	24
NHS-310	0.3	0.891	20	10	0.53	2.5	24
NHS-410	0.3	0.891	20	10	0.53	2	24
NHS-480	0.3	0.891	20	10	0.53	1.5	24

To the best of our survey, one-step self-templated method based on novel mechanism, Ostwald ripening for the controlled synthesis of MFe₂O₄ nano hollow structures along with wide range of size variation is absent in the extant literatures. Till date, a general strategy for the convenient high yield synthesis of MFe₂O₄ NHSs is hard template mediated approach¹⁶ which involves a coating over template (core) by controlled surface precipitation followed by the core removal through thermal or chemical means. It has several intrinsic disadvantages, which range from the inherent difficulty of achieving high product yields from the multistep synthetic process to the lack of structural robustness of the shells upon template removal which in general attracts a lot of attention for the fabrication of NHSs through template free methods.

In order to evaluate the process of core excavation of MFe₂O₄ NHSs, we have conducted time dependent synthesis study of CoFe₂O₄ NHS-350 at various reaction time of 3, 6, 9, and 12 h. A series of TEM images of the resulting products as shown in Figure 5.1. (a)-(d) indicates the distinct changes in the surface and interior of the nano-spheres with time. Initially, after reaction of 3 h, a nano-leaf like structure is observed (Figure 5.1. (a)) and these small nano-crystallites are found to aggregate all

together to form a solid sphere with rough surface (Figure 5.1. (b)) during 3-6 h interval. With a longer reaction time of 9 h, a hollowing effect is noticed (Figure 5.1. (c)) and the solid sphere starts to form porous spheres of smooth surface. After 12 h of reaction time, the distinct contrast between the margin and the interior of the spheres (Figure 5.1. (d)) confirms the formation of NHSs with smooth surface. The possible chemical reactions for the synthesis of hollow CoFe_2O_4 nano-spheres are proposed as follows:¹⁷



During the reaction, urea has helped to precipitate Co^{+2} and Fe^{+3} ions of the precursor salts to their corresponding hydroxides and after the heat treatment, CoFe_2O_4 phase is developed. The underlying mechanism for the synthesis of NHSs is Ostwald ripening which involves a gradual outward migration of crystallites through a recrystallization process. The reaction mechanism for the synthesis of $\text{MnFe}_2\text{O}_4/\text{Fe}_3\text{O}_4$ NSs follows the same way as CoFe_2O_4 NSs, however it involves the salt of $\text{Mn}^{+2}/\text{Fe}^{+2}$ ions instead of Co^{+2} ion only.

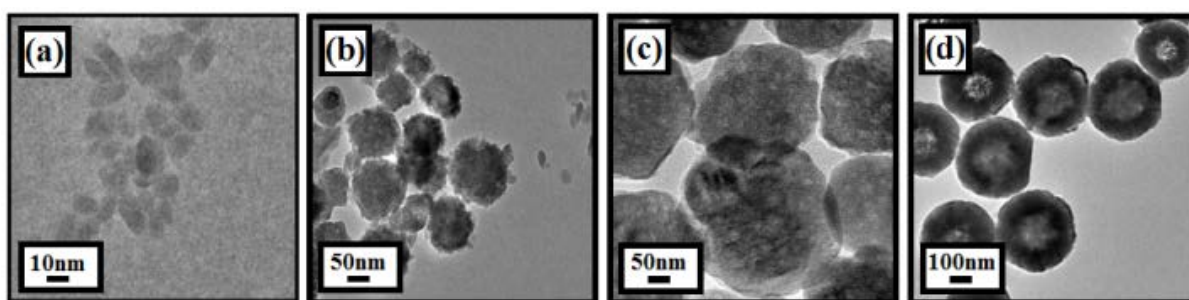


Figure 5.1. Formation mechanism of CoFe_2O_4 NHS-350 and its representative TEM images in four intermediate steps: (a) 3 h, (b) 6 h, (c) 9 h, (d) 12 h.

5.2.3. Synthesis of SiO₂ Coated MFe₂O₄ (M= Fe, Co, and Mn) Nanoparticles and Nano hollow spheres

The surface coating of MFe₂O₄ (M= Fe, Co, and Mn) NSs with SiO₂ has been carried out through Stöber process (as described in *Chapter 5*). In a typical synthesis, 0.04 gm of as-prepared MFe₂O₄ NPs or NHSs were added to the mixture of 70 ml ethanol, 7 ml of de-ionized water, and 2 ml NH₄OH (30 wt%) solution and stirred for 1 h with high speed to get a well dispersed solution of MFe₂O₄ NSs. Thereafter, 1 ml of tetraethyl orthosilicate (TEOS) was added to the above solution, drop by drop and kept it for another 15 h at room temperature under continuous vigorous stirring so that SiO₂ would be coated on the surface of MFe₂O₄ NMs through hydrolysis followed by condensation of TEOS.¹⁸ Finally, silica coated MFe₂O₄ (SiO₂@MFe₂O₄) NSs were collected via magnetic extraction and washed for a couple of time with absolute ethanol to remove all residual SiO₂. Finally, the resulting sample was separated through centrifugation and dried at room temperature. Since sample concentration, stirring speed, and reaction time influence the shell thickness of SiO₂ over the NPs surface, they are maintained in a similar manner for all the cases. Thorough control of these reaction parameters allows us to generate a uniform layer of SiO₂ over the surface of the magnetic NSs with shell thickness in the range 21-37 nm in case of MFe₂O₄ (M= Co, Fe, and Mn) NHS-350. With decrease in size of the NHS, the shell thickness of SiO₂ over the NS's surface is found to decrease due to enhanced magnitude of their surface to volume ratio.

5.3. Result and Discussions

We have synthesized MFe₂O₄ NPs and a series of NHSs of increasing diameter following a template free solvothermal method (as described in *Chapter 2* in details). TEM study was performed to characterize the size and morphology of the as-prepared MFe₂O₄ (M= Co, Fe, and Mn) NSs as shown in Figures 5.2, 5.3, and 5.4 (a) respectively. The difference in contrast between the margin and the interior of the sphere confirms the hollow nature of NHSs. The high resolution TEM (HRTEM) images as shown in Figures 5.2, 5.3, and 5.4 (b) clearly resolve their atomic lattice

fringes and the calculated inter-planar distances between the lattice fringes are found to be nearly 0.24, 0.251, and 0.254 nm, which corresponds to the distance between (311) planes of the MFe_2O_4 ($M=Fe, Co, Mn$) crystal lattice respectively. Small area electron diffraction (SAED) patterns of the NHS as shown in Figures 5.2, 5.3, and 5.4 (c) show bright diffractive dots that represent their single crystalline nature.

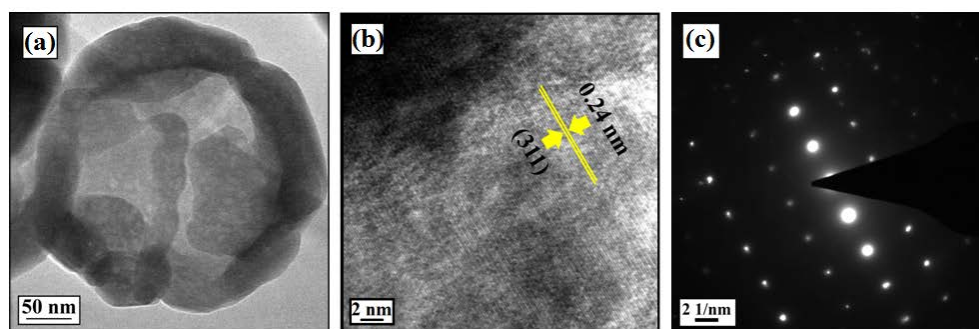


Figure 5.2. (a) TEM image, (b) HRTEM image, and (c) SAED pattern of Fe_3O_4 NHS.

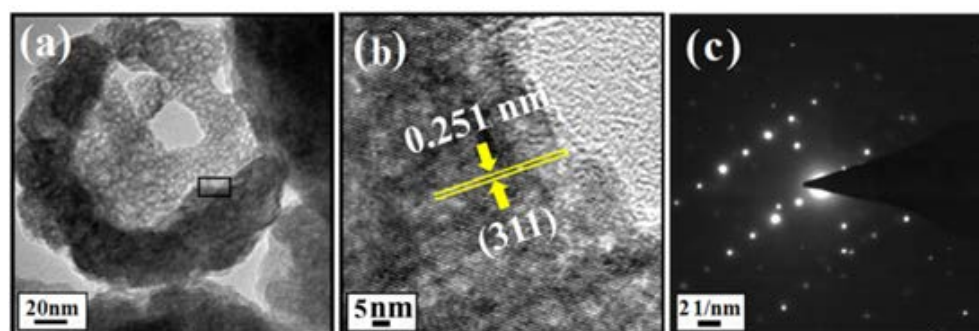


Figure 5.3. (a) TEM image, (b) HRTEM image, and (c) SAED pattern of $CoFe_2O_4$ NHS.

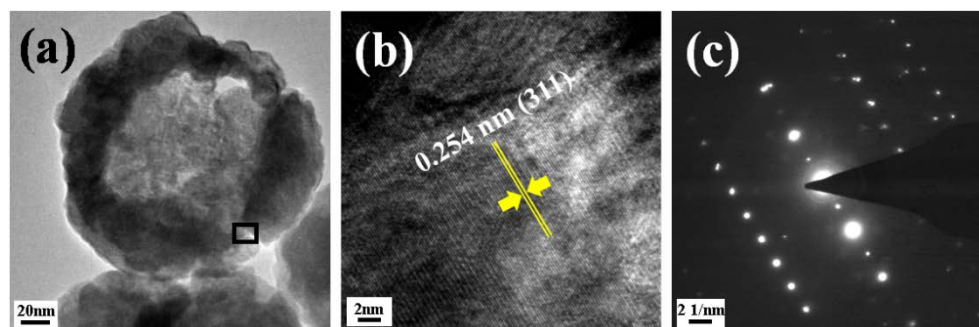


Figure 5.4. (a) TEM image, (b) HRTEM image, and (c) SAED pattern of $MnFe_2O_4$ NHS.

All XRD patterns of MFe_2O_4 NPs and NHSs as shown in Figures 5.5, 5.6, and 5.7 confirm their single phase, spinel face centered cubic structure and from broadening of their Bragg reflection peaks, the average crystallite size of the NHSs is found to increase with increasing average diameter of the NHSs using Scherrer's equation as listed in Table 5.4, 5.5, 5.6. The XRD patterns of $SiO_2@MFe_2O_4$ samples

(inset of Figures 5.5, 5.6, and 5.7) clearly indicate the amorphous SiO_2 profile with broad peaks at low angles and the typical sharp peaks of MFe_2O_4 crystalline phase.

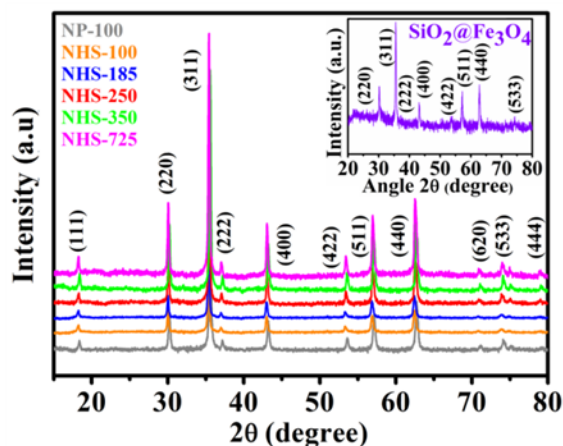


Figure 5.5. XRD patterns of all Fe_3O_4 NP and NHSs. Inset shows the XRD pattern of $\text{SiO}_2@Fe_3O_4$ NHS.

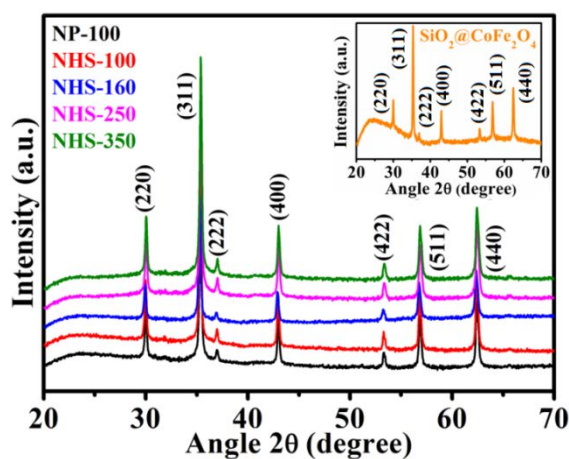


Figure 5.6. XRD patterns of all CoFe_2O_4 NP and NHSs. Inset shows the XRD pattern of $\text{SiO}_2@CoFe_2O_4$ NHS.

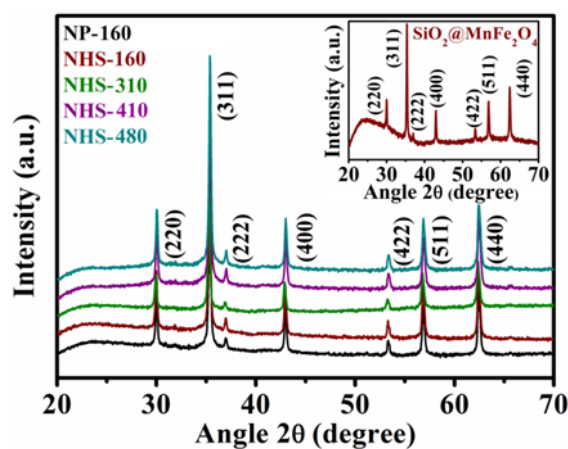


Figure 5.7. XRD patterns of all MnFe_2O_4 NP and NHSs. Inset shows the XRD pattern of $\text{SiO}_2@MnFe_2O_4$ NHS.

Figures 5.8 (a)-(f) and 5.9 (a)-(e) show the field emission scanning electron microscope (FESEM) images of all as-synthesized Fe_3O_4 and CoFe_2O_4 NPs and NHSs of increasing diameter respectively whereas Figures 5.10 (a)-(e) show the TEM images of MnFe_2O_4 NPs and NHSs of increasing diameter.

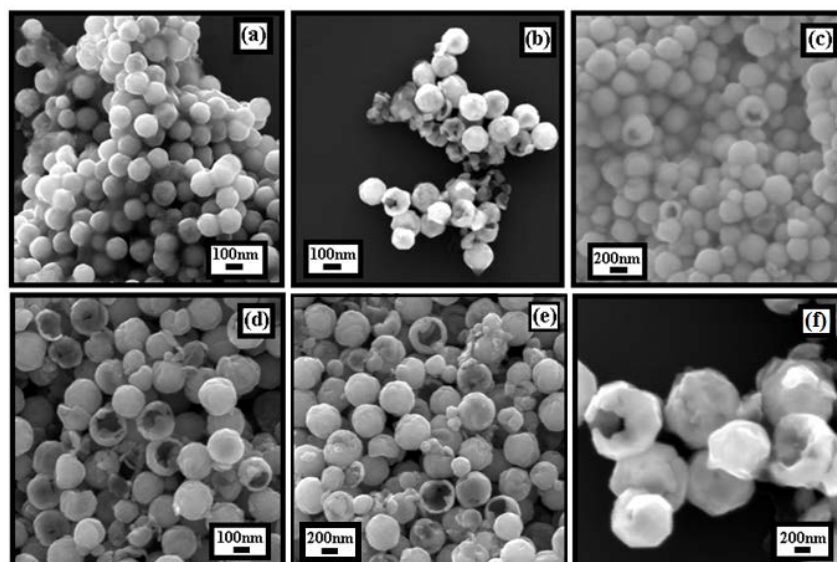


Figure 5.8. SEM images of Fe_3O_4 NP-(a) 100, NHS-(b) 100, (c) 160, (d) 250, (e) 350, and (f) 725.

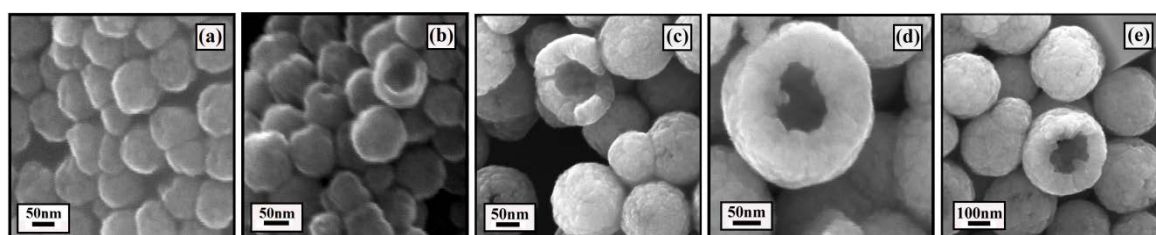


Figure 5.9. SEM images of CoFe_2O_4 NP-(a) 100, NHS-(b) 100, (c) 160, (d) 250, and (e) 350.

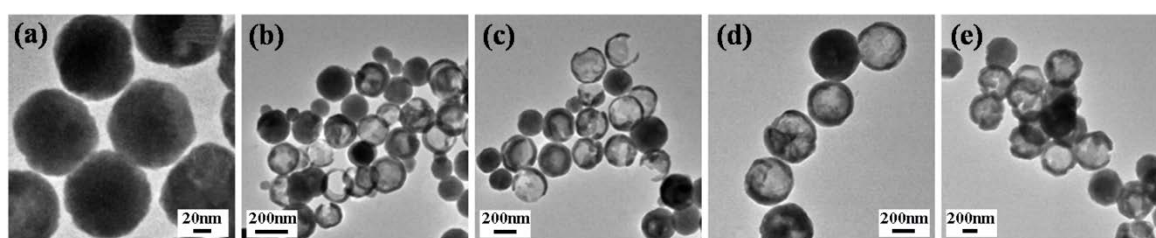


Figure 5.10. TEM images of MnFe_2O_4 NP-(a) 160, NHS-(b) 160, (c) 310, (d) 410, (e) 480.

The TEM images of $\text{SiO}_2@\text{MFe}_2\text{O}_4$ ($\text{M}=\text{Fe}, \text{Co}, \text{Mn}$) NPs and NHSs of increasing diameter are represented in Figures 5.11 (a)-(f), 5.12 (a)-(e), and 5.13 (a)-(e) respectively.

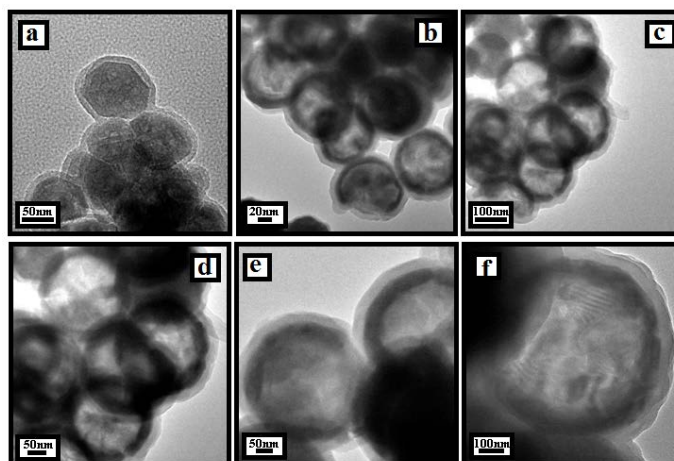


Figure 5.11. TEM images of $\text{SiO}_2@Fe_3O_4$ NP-(a) 100, NHS-(b) 100, (c) 185, (d) 250, (e) 350, and (f) 725.

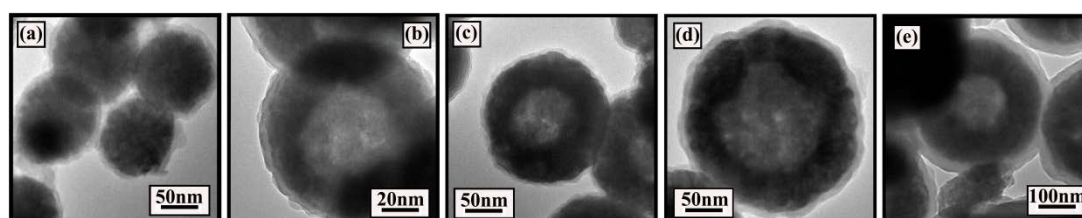


Figure 5.12. TEM images of $\text{SiO}_2@CoFe_2O_4$ NP-(a) 100, NHS-(b) 100, (c) 160, (d) 250, and (e) 350.

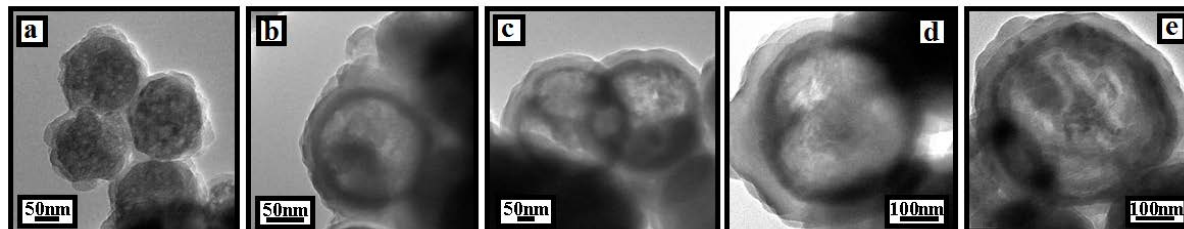


Figure 5.13. TEM images of $\text{SiO}_2@MnFe_2O_4$ NP-(a) 160, NHS-(b) 160, (c) 310, (d) 410, (e) 480.

Figure 5.14 (a) exhibits the scanning transmission electron micrograph (STEM) of $\text{SiO}_2@CoFe_2O_4$ NHS-250. A line scanned energy dispersive X-ray (EDX) spectrometry was performed across its radius, specified by an orange line. Figures 5.14 (b)-(d) show the EDX line scanning profile of Si, Co, and Fe, respectively, where Co and Fe profiles show lower intensity at the centre and edge, whereas Si shows higher intensity at the outer edge of the spectrum profile, confirming the synthesis of $\text{SiO}_2@CoFe_2O_4$ nanomaterials. The overall EDX spectrum as shown in Figure 5.14 (e) determines the magnitude of elemental composition as listed in inset.

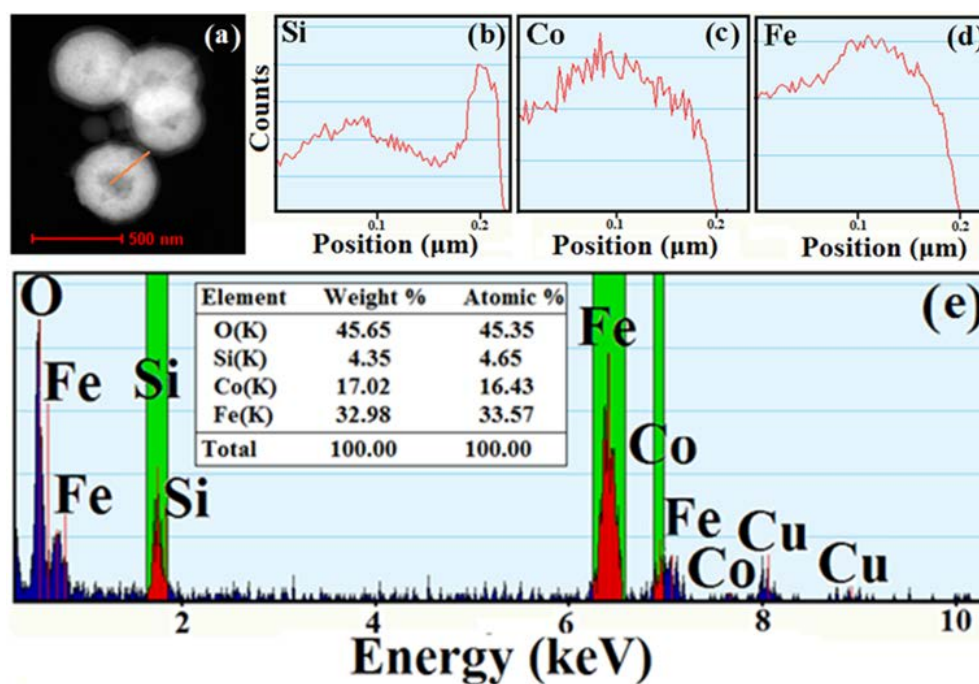


Figure 5.14. (a) STEM image of single $\text{SiO}_2@\text{CoFe}_2\text{O}_4$ NHS-250. (b)-(d) EDX line scanning of Si, Co, and Fe, respectively, across the orange line of $\text{SiO}_2@\text{CoFe}_2\text{O}_4$ NHS-250 indicated in (a). (e) Overall EDX of $\text{SiO}_2@\text{CoFe}_2\text{O}_4$ nanostructure.

Table 5.4: List of average diameter, average crystallite size, and average shell thickness of all as synthesized Fe_3O_4 NP and NHSs.

Sample name	Average diameter (D) nm	Average crystallite size (D) nm	Average shell thickness (t) nm
NP-100	100(±3)	16.69	0
NHS-100	100(±5)	29.89	30
NHS-185	185(±10)	35.09	35
NHS-250	250(±9)	36.65	50
NHS-350	350(±15)	38.56	65
NHS-725	725(±17)	39.5	150

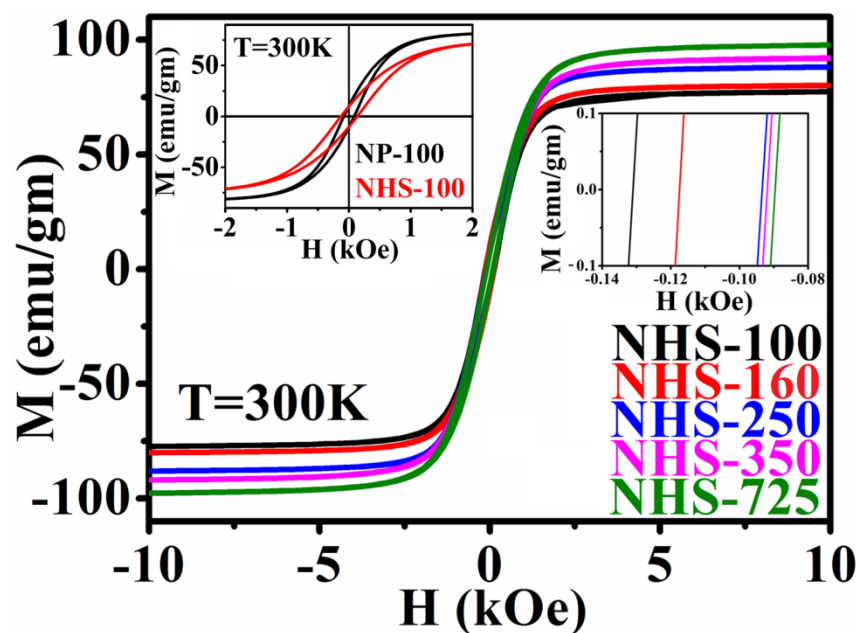
Table 5.5. List of average particle diameter, crystallite size, and shell thickness of all as synthesized CoFe_2O_4 NP and NHSs.

Sample name	Average diameter (D) nm	Average crystallite size (D) nm	Average shell thickness (t) nm
NP-100	100±5	39.15±5	0
NHS-100	100±4	40.32±4	18
NHS-160	160±5	42.57±6	38
NHS-250	250±7	44.19±8	43
NHS-350	350±3	48.17±7	110

Table 5.6. List of average particle diameter, crystallite size, and shell thickness of all as-synthesised MnFe₂O₄ NP and NHSs.

Sample name	Average diameter (D) nm	Average crystallite size (D) nm	Average shell thickness (t) nm
NP-160	160(±5)	18.02	0
NHS-160	160(±7)	21.41	31
NHS-310	310(±10)	35.12	47
NHS-410	410(±8)	37.01	51
NHS-480	480(±7)	38.72	110

The room temperature field dependent magnetization measurements of all MFe₂O₄ (M=Fe, Co, and Mn) NSs are shown in Figures 5.15, 5.16, and 5.17 respectively. The list of H_c and M_s of MFe₂O₄ (M=Fe, Co, and Mn) NSs is presented in Table 5.7, 5.8, and 5.9 respectively. The CoFe₂O₄ NSs are found to exhibit more coercivity in contrast to Fe₃O₄ and MnFe₂O₄ NSs.

**Figure 5.15.** Field dependent magnetization study of Fe₃O₄ NHSs of different diameter at 300 K. Left inset shows the comparative M-H loop of Fe₃O₄ NP and NHS of diameter 100 nm. Right inset shows the zoomed image of H_c for the NHSs of increasing diameter.**Table 5.7.** List of H_c and M_s of all as-synthesized Fe₃O₄ NSs at room temperature.

Magnetic Property	NP-100	NHS-100	NHS-160	NHS-250	NHS-350	NHS-725
H _c (kOe)	0.08	0.13	0.117	0.094	0.092	0.089
M _s (emu/gm)	85.48	76.78	80.96	87.66	91.84	97.70

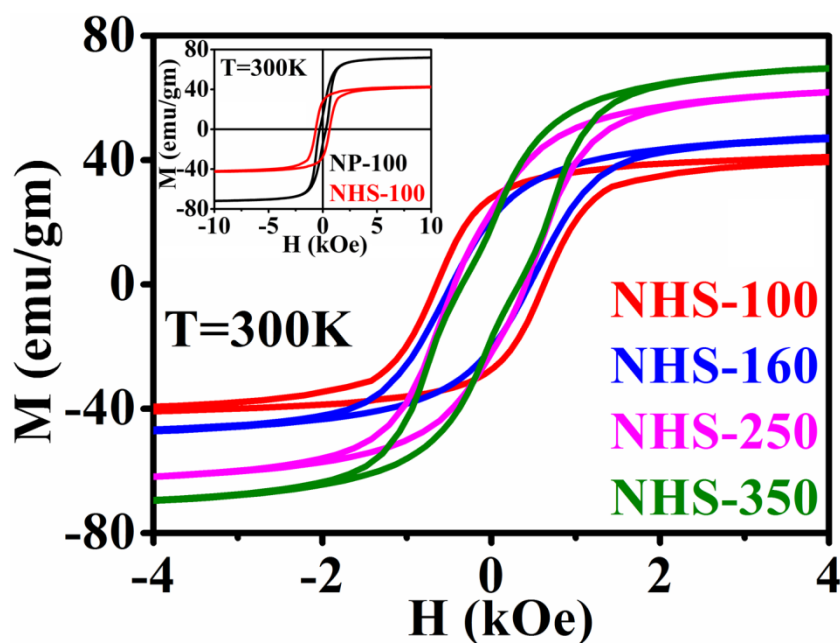


Figure 5.16. Field dependent magnetization study of CoFe_2O_4 NHSs of different diameter at 300 K. Inset shows the comparative M-H loop of CoFe_2O_4 NP and NHS of diameter 100 nm.

Table 5.8. List of H_c and M_s of all as-synthesized CoFe_2O_4 NSs at room temperature.

Magnetic Property	NP-100	NHS-100	NHS-160	NHS-250	NHS-350
H_c (kOe)	0.30	0.64	0.46	0.44	0.34
M_s (emu/gm)	71.95	40.32	47.17	62.24	69.77

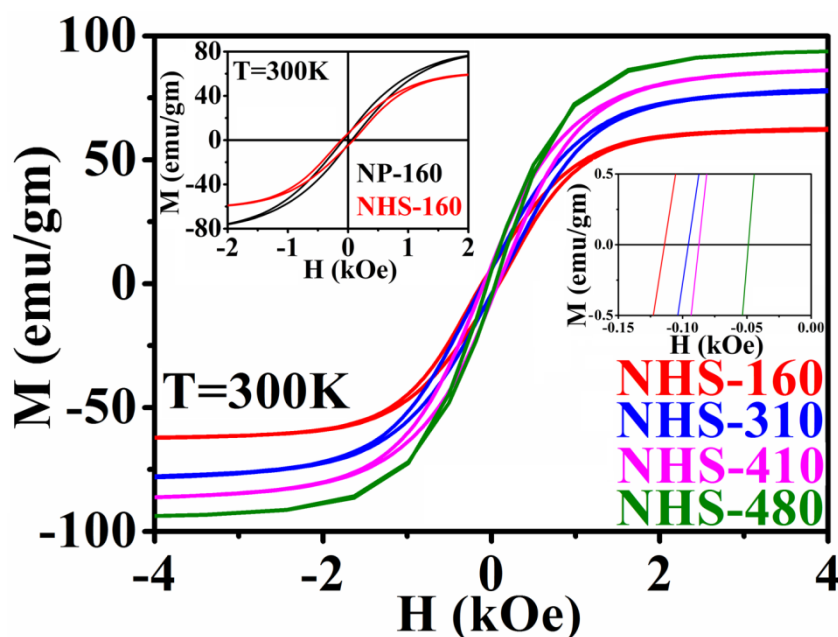


Figure 5.17. Field dependent magnetization study of MnFe_2O_4 NHSs of different diameter at 300 K. Left inset shows the comparative M-H loop of MnFe_2O_4 NP and NHS of diameter 160 nm. Right inset shows the zoomed image of H_c for the NHSs of increasing diameter.

Table 5.9. List of H_c and M_s of all as-synthesized MnFe_2O_4 NSs at room temperature.

Magnetic Property	NP-160	NHS-160	NHS-310	NHS-410	NHS-480
H_c (kOe)	0.076	0.114	0.095	0.089	0.05
M_s (emu/gm)	79.99	62.31	78.28	85.89	93.50

The drastic differences in the obtained results for NHSs in contrast to its solid counterpart of same diameter indicate that the presence of additional inner surface of the hollow morphology induces significant surface effect in its magnetic property. The outer surface spin disorder in addition to the inner surface spin disorder of NHS configuration causes a noticeable enhancement of surface anisotropy along with a huge suppression of net M_s which leads to a simultaneous increase in H_c and decrease in M_s in contrast to NPs. The H_c is found to increase from 0.08 to 0.13 kOe in case of Fe_3O_4 , 0.3 to 0.64 kOe for CoFe_2O_4 , and 0.076 to 0.114 kOe in case of MnFe_2O_4 whereas the M_s found to decrease from 85.48 to 76.78 emu/gm in case of Fe_3O_4 , 71.95 to 40.32 emu/gm for CoFe_2O_4 , and 79.99 to 62.31 emu/gm in case of MnFe_2O_4 with the change in configuration from NP to NHS. In case of NHSs of different diameter, the value of H_c is found to decrease whereas M_s is found to increase with increasing diameter at room temperature. For example, in case of Fe_3O_4 NHSs, the H_c is found to decrease from 0.13 to 0.089 kOe and M_s is found to

increase from 76.78 to 97.70 emu/gm with increasing size of the NHS from 100 to 725 nm. Furthermore, the H_c is found to decrease from 0.64 to 0.34 kOe and M_s is found to increase from 40.32 to 69.77 emu/gm with increasing size of the NHS from 100 to 350 nm in case of CoFe_2O_4 NHSs. For MnFe_2O_4 NHSs, the H_c is found to decrease from 0.114 to 0.05 kOe and M_s is found to increase from 62.31 to 93.50 emu/gm with increasing size of the NHS from 160 to 480 nm in case of MnFe_2O_4 NHSs. Basically, increase in size of MFe_2O_4 NHSs results in an decreased surface spin disorder due to a lower fraction of superficial $\text{Fe}^{2+}/\text{Co}^{2+}/\text{Mn}^{2+}$ ions with incomplete coordination environments which attributes to a increase in M_s along with a decrease in a surface anisotropy.

The room temperature M-H measurements of all $\text{SiO}_2@\text{MFe}_2\text{O}_4$ (M=Fe, Co, Mn) NSs are shown in Figure 5.18, 5.19, and 5.20 respectively. The list of change in H_c and M_s of $\text{SiO}_2@\text{MFe}_2\text{O}_4$ (M=Fe, Co, and Mn) NSs is presented in Table 5.10, 5.11, and 5.12 respectively.

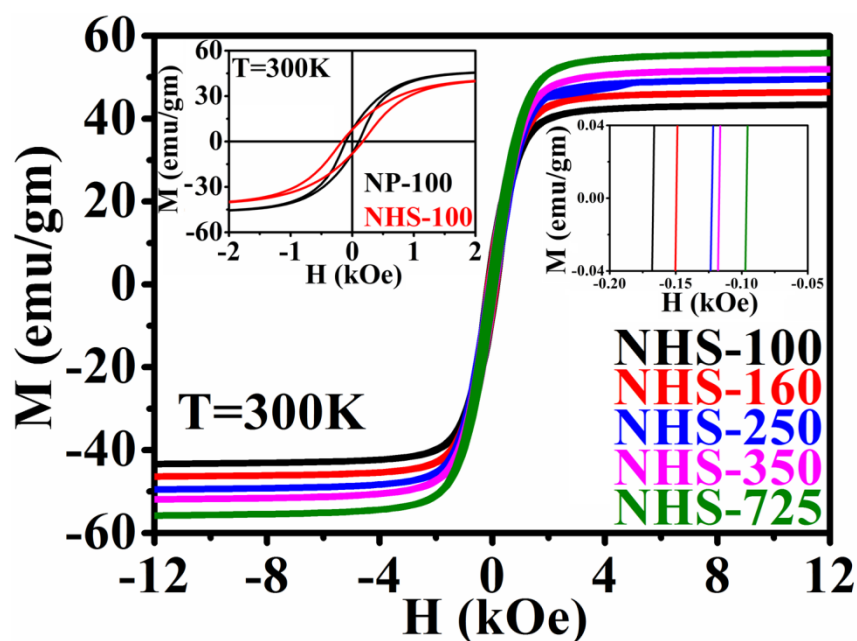
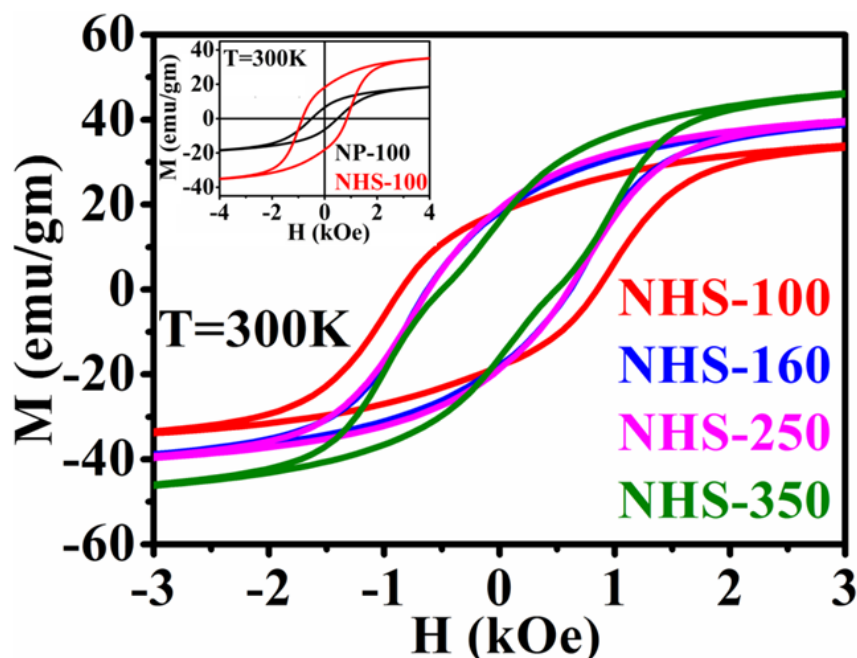


Figure 5.18. Field dependent magnetization study of $\text{SiO}_2@\text{Fe}_3\text{O}_4$ NHSs of different diameter at 300 K. Left inset shows the comparative M-H loop of $\text{SiO}_2@\text{Fe}_3\text{O}_4$ NP and NHS of diameter 100 nm. Right inset shows the zoomed image of H_c for the NHSs of increasing diameter.

Table 5.10. List of H_c and M_s of all as-synthesized $\text{SiO}_2@Fe_3O_4$ NSs at room temperature.

Magnetic Property	NP-100	NHS-100	NHS-160	NHS-250	NHS-350	NHS-725
H_c (kOe)	0.108	0.168	0.149	0.123	0.117	0.096
M_s (emu/gm)	48.16	43.50	46.47	49.57	51.97	55.92

**Figure 5.19.** Field dependent magnetization study of $\text{SiO}_2@CoFe_2O_4$ NHSs of different diameter at 300 K. Inset shows the comparative M-H loop of $\text{SiO}_2@CoFe_2O_4$ NP and NHS of diameter 100 nm.**Table 5.11.** List of H_c and M_s of all as-synthesized $\text{SiO}_2@CoFe_2O_4$ NSs at room temperature.

Magnetic Property	NP-100	NHS-100	NHS-160	NHS-250	NHS-350
H_c (kOe)	0.48	0.86	0.62	0.6	0.49
M_s (emu/gm)	19.11	35.94	38.33	45.07	51.07

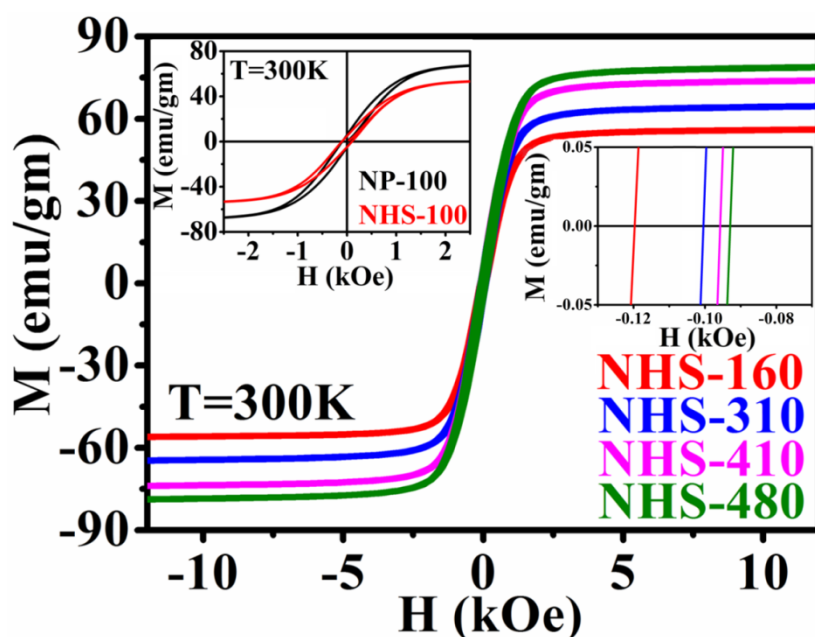


Figure 5.20. Field dependent magnetization study of $\text{SiO}_2\text{@MnFe}_2\text{O}_4$ NHSs of different diameter at 300 K. Left inset shows the comparative M-H loop of $\text{SiO}_2\text{@MnFe}_2\text{O}_4$ NP and NHS of diameter 160 nm. Right inset shows the zoomed image of H_c for the NHSs of increasing diameter.

Table 5.12. List of H_c and M_s of all as-synthesized $\text{SiO}_2\text{@MnFe}_2\text{O}_4$ NSs at room temperature.

Magnetic Property	NP-160	NHS-160	NHS-310	NHS-410	NHS-480
H_c (kOe)	0.0956	0.12	0.1	0.0957	0.0928
M_s (emu/gm)	67.82	53.22	64.13	73.72	79.02

It is found that the surface modification of bare MFe_2O_4 ($\text{M}=\text{Fe}, \text{Co}, \text{Mn}$) NSs with SiO_2 has a notable impact on their magnetic properties at room temperature. The co-ordination of SiO_2 molecules to the NS's surface causes a very strong pinning to the magnetic moments of surface $\text{Fe}^{2+}/\text{Co}^{2+}/\text{Mn}^{2+}$ ions and leads to a strong surface anisotropy which in turn enhances the H_c of the $\text{SiO}_2\text{@MFe}_2\text{O}_4$ system with reference to bare MFe_2O_4 .¹⁹ Further, the significant reduction of M_s in case of modified NSs is due to ligand (SiO_2) to metal charge transfer effect²⁰ (as described in *Chapter 1*, *Chapter 3*, and *Chapter 4*) which enables to quench the unpaired d electrons of $\text{Co}^{2+}/\text{Mn}^{2+}/\text{Fe}^{2+}$ ions and subsequently reduces the net magnetization of the system.

To get the knowledge about magnetic dynamic behaviour, AC susceptibility measurements have been carried out for MnFe_2O_4 and Fe_3O_4 NPs and NHSs. Figures

5.21 (a) and (b) show the plots of imaginary component of AC susceptibility (χ'') as a function of temperature ranging from 5 K to 300 K for MnFe_2O_4 NPs and NHSs of diameter 160 nm respectively as a powder. It is investigated for four different frequencies of 83, 253, 503, and 757 Hz. The plot in case of NP-160 displays that χ'' increases rapidly with temperature, attains a maxima and then starts to decrease again whereas two pronounced maxima are found for NHS-160.

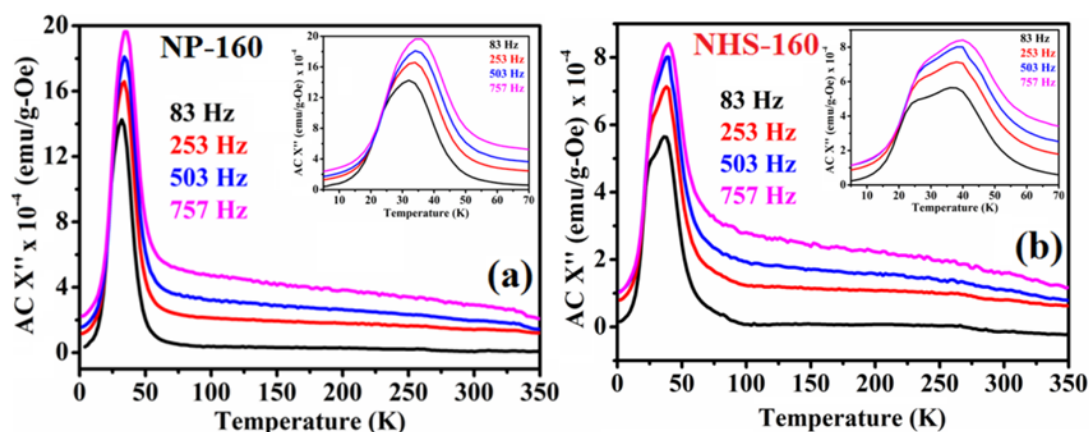


Figure 5.21. Imaginary part of AC susceptibility as a function of temperature in case of MnFe_2O_4 (a) NP-160, (b) NHS-160 for different frequencies. Insets show their zoomed images in the temperature range of 5-350 K.

We have carried out Mössbauer spectroscopy analysis for both the MnFe_2O_4 NP and NHS-160 at room temperature in order to investigate the origin of extra peak of MnFe_2O_4 NHS-160. It indicates that both the NMs are magnetically ordered as shown in Figures 5.22 (a) and (b). The local environment around Fe atoms of MnFe_2O_4 NP and NHS-160 are checked by ^{57}Fe Mössbauer spectroscopy. The hyperfine parameters obtained after fitting the spectra are tabulated in Table 5.13. Each spectrum has been fitted with two sextets. The sextet S1 with lower isomer shift indicates the tetrahedral Fe^{+3} site whereas the sextets S2 with higher isomer shift denotes the octahedral Fe^{+3} site. Similar hyperfine parameters of sextet S1 and S2 in case of MnFe_2O_4 NP and NHS of diameter 160 nm confirm that the chemical environment of Fe^{3+} ions in tetrahedral and octahedral sites is same for both the cases. Therefore, the peak at low temperature is due to the spin glass behaviour of the NSs as proposed by Kodama and his research group.^{21,22} They found that the canted spins in ferrite NPs freeze into a spin glass-like phase at temperatures below 50 K.²³ The main origin of spin glass-like behaviour in ferrite NPs can also be due to

strong inter-particle interactions within individual particles.²⁴⁻²⁶ The spin glass temperature (T_g) is found to exhibit a slight dependence on the measurement frequency as listed in Table 5.14. It follows a very narrow shift from 31.96 K to 35 K with increasing frequency from 83 Hz to 757 Hz in case of NP configuration due to interparticle interactions, for example dipole-dipole or interparticle exchange interactions exist within the powdered MnFe_2O_4 sample.

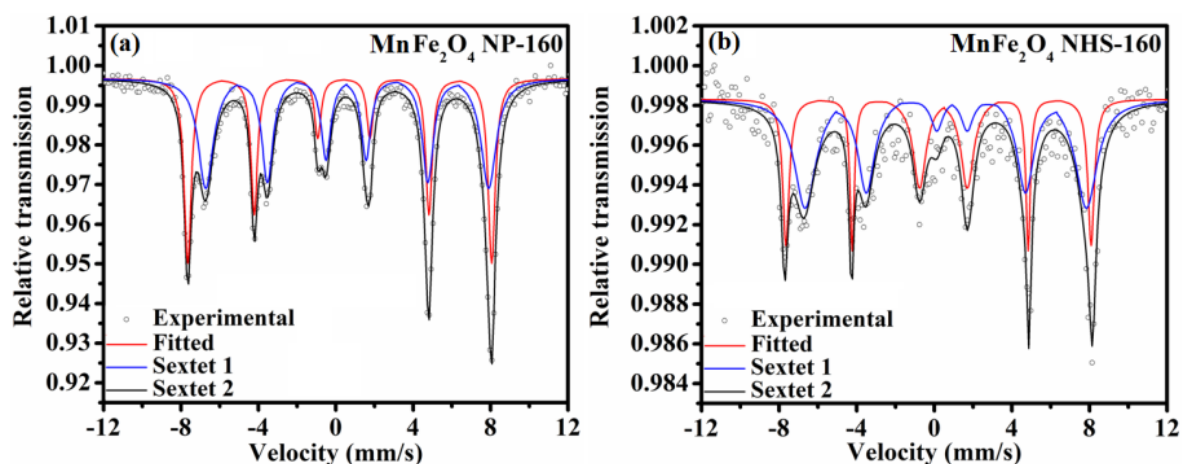


Figure 5.22. Mössbauer spectra of MnFe_2O_4 (a) NP, and (b) NHS of diameter 160 nm. Empty circles and black lines denote experimental and fitted spectra respectively.

Table 5.13. Mössbauer parameters of MnFe_2O_4 NP and NHS of diameter 160 nm.

Sample Name	Site	Isomer shift (mm/s) (± 0.01 mm/s)	Quadrupole splitting (mm/s) (± 0.01 mm/s)	Internal Hyperfine field (kOe) (± 2 kOe)
MnFe_2O_4 NP-160	S1	0.31	0.10	488
	S2	0.58	0.03	454
MnFe_2O_4 NHS-160	S1	0.33	0.08	487
	S2	0.70	0.01	450

Table 5.14. List of T_g obtained from χ'' vs T graph for different frequencies in case of MnFe_2O_4 NP and NHS of diameter 160 nm.

Frequency (Hz)	T_B for NP-160	T_B for NHS-160	
83	31.96	35.98	23.86
253	33.95	38.04	24.74
503	33.95	39.09	25.96
757	35.00	40.00	27.91

The two pronounced maxima in case of NHS-160 may be due to the presence of double surfaces of NHS configuration, implying that T_g of the nano hollow structures carries sensitively the unique signature of its structural properties.

Recently, Khurshid et al.²⁷ presented spin-glass like freezing of inner and outer surface layers in hollow γ -Fe₂O₃ NPs. They explicated that the magnetic behaviour of γ -Fe₂O₃ NHSs at the inner and outer surfaces is not identical. They found that the spins at the outer surface layer exhibits a higher degree of frustration than the spins at the inner layer of the 15 nm γ -Fe₂O₃ hollow particles. Therefore, the peak developed at lower temperature is due to the higher surface anisotropy of outer spin layer of MnFe₂O₄ NHSs. Similar property has been found for the Fe₃O₄ NP and NHSs configuration of 100 nm diameter as shown in Figure 5.23. The T_g obtained from χ'' vs T graph of Fe₃O₄ NP-100 and NHS-100 for different frequencies are listed in Table 5.15.

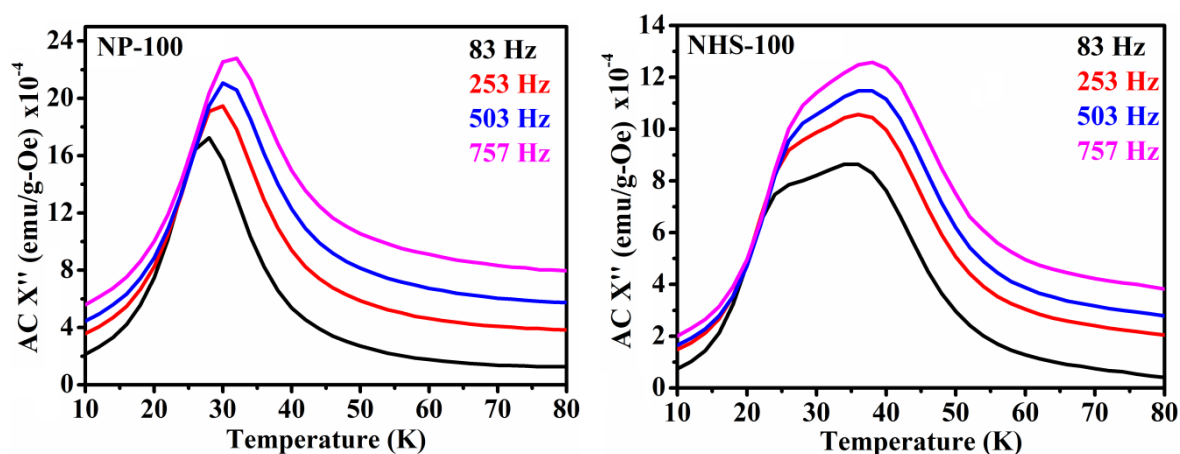


Figure 5.23. Imaginary part of AC susceptibility as a function of temperature in case of Fe₃O₄ (a) NP-100, (b) NHS-100 for different frequencies. Insets show their zoomed images in the temperature range of 10-80 K.

Table 5.15. List of T_g obtained from χ'' vs T graph for different frequencies in case of Fe₃O₄ NP and NHS of diameter 100 nm.

Frequency (Hz)	T _g for NP-100	T _g for NHS-100	
83	27.91	23.97	35.13
253	29.75	25.88	36.92
503	30.16	25.87	37.96
757	32.1	27.97	39.6

In order to investigate the possible domain structure of Fe₃O₄ NHSs of different diameters, we have carried out AFM and MFM analysis as described in Chapter 1 in detail. The AFM and MFM images of Fe₃O₄ NHS-100, 250 and 725 are shown in Figure 5.24 (a-f). The typical sample topography and uniform size distribution of all sets of hollow spheres can be observed from their AFM images. In

addition to the spherical aggregates, micrometer sized wavy back-ground can also be seen which is due to the multi-layer formation of spheres, thus creating the valleys and hilly areas. By comparing with the AFM images one can find the topographical features (distinct grains and grain boundaries) in the corresponding MFM images in addition to the alternate dark/bright contrast. The presence of topography in all these MFM images of hollow spheres is mainly because of the fact that magnetic dipoles are centered at the magnetic particles and the magnetic signal decays very fast in the absence of them. Since the MFM contrast mainly depends on the strength of magnetic stray field as generated by the macroscopic domain configuration, therefore from this magnetic contrast the possible domain structure of the magnetite hollow spheres can be predicted. In the corresponding image, light colored regions correspond to the repulsion of the MFM tip from sample and dark color represents attraction of the tip. Areas having poor contrast represent the magnetic regions having magnetization direction perpendicular to that of tip.

MFM micrograph of NHS-100 (as shown in Figure 5.24 (b)) shows the individual round spots of either contrast (dark when the particle magnetization is parallel or bright when anti-parallel to the tip magnetization) or dipole type behaviour (when the particle magnetization makes an oblique angle to the surface) where the magnetic signal consists of two spots of opposite contrast localized at the extremities with no other magnetic structure in between them. This type of magnetic response is due to the single domain (SD) characteristics where each particle has an individual magnetic dipole moment which is locked at a particular direction. NHS-185 also shows similar SD characteristics.

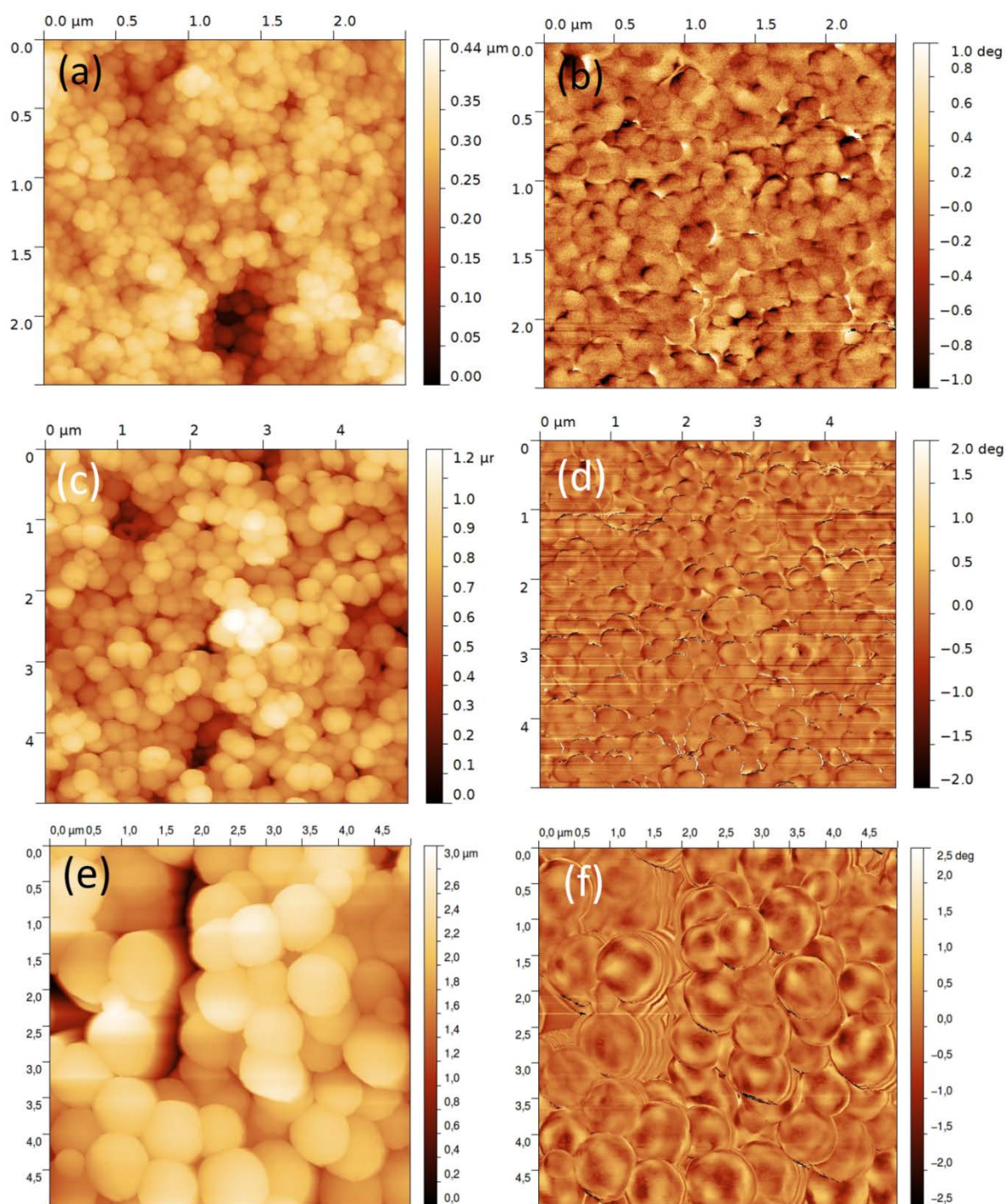


Figure. 5.24. AFM images of (a), (c), and (e) NHS-100, NHS-250, and NHS-725 respectively; and corresponding MFM images of (b), (d) and (f) NHS-100, NHS-250, and NHS-725 respectively.

For hollow spheres of NHS-250 (as shown in Figure 5.24 (d)), the phase contrast is poor though the magnetic response of each sphere is distinct; i.e. each sphere behaves as a single magnetic region having uniform magnetization. This type of magnetic response is significantly different from that of (SD) characteristics

explained above. Therefore, the domain configuration of NHS-250 can be classified as pseudo single domain (PSD) type, though very few of them show some extent of single domain characteristics having dipole type magnetic contrast. NHS-350 also shows similar PSD characteristics. For NHS-725 samples, it can be observed that each sphere consists of several alternate regions with bright and dark contrasts which indicate the presence of magnetic domains having different magnetization directions; i.e. multi domain (MD) magnetic configuration.

5.4. Conclusion

In conclusion, we have been able to find out the size and morphology dependence as well as the effect of SiO₂ coating on the magnetic response of bare MFe₂O₄ (M=Fe, Co, and Mn) NSs. Detailed study reveals that NHS configuration exhibits higher H_c and lesser M_s in contrast to its solid configuration due to their high effective surface area. Moreover, it is found that the magnetic responses of MFe₂O₄ NHSs can be tailored by varying their nano-size as well as by coating their surface with diamagnetic SiO₂ molecules. The attachment of foreign molecule to the surface of NMs causes an enhancement of surface anisotropy which in turn causes an increase in H_c of SiO₂@MFe₂O₄ NSs. Since SiO₂ is kind of donor ligand, the reduced M_s is due to ligand (SiO₂) to metal (M⁺²) charge transfer effect.

Bibliography

- [1] Sun, S., Recent advances in chemical synthesis, self-assembly, and applications of FePt nanoparticles. *Advance Materials* 2006, **18**, 393.
- [2] Duan, X.; Huang, Y.; Cui, Y.; Wang, J.; Lieber, C. M., Indium phosphide nanowires as building blocks for nanoscale electronic and optoelectronic devices. *Nature (London)* 2001, **409**, 66.
- [3] Hyeon, T.; Lee, S. S.; Park, J.; Chung, Y.; Na, H. B., Synthesis of highly crystalline and monodisperse maghemite nanocrystallites without a size-selection process. *Journal of American Chemical Society* 2001, **123**, 12798.
- [4] Woo, K.; Lee, H. J.; Ahn, J.; Park, Y. S., Sol-gel mediated synthesis of Fe₂O₃ nanorods. *Advance Materials* 2003, **15**, 1761.
- [5] Deng, Y.-H.; Wang, C.-C.; Hu, J.-H.; Yang, W.-L.; Fu, S.-K., Investigation of formation of silica-coated magnetite nanoparticles via sol-gel approach. *Colloids and Surfaces A* 2005, **262**, 87.
- [6] Mazaleyrat, F.; Ammar, M.; LoBue, M.; Bonnet, J.-P.; Audebert, P.; Wang, G.-Y.; Champion, Y.; Hytch, M.; Snoeck, E., Silica coated nanoparticles: synthesis, magnetic properties and spin structure. *Journal of Alloys and Compounds* 2009, **483**, 473.
- [7] Farrell, E.; Wielopolski, P.; Pavljasevic, P.; Kops, N.; Weinans, H.; Bernsen, M. R.; Osch, G. J. V. M. van, Cell labelling with superparamagnetic iron oxide has no effect on chondrocyte behaviour. *Osteoarthritis and Cartilage* 2009, **17**, 961.
- [8] Ahn, J.; Chung, W.-J.; Pinnau, I.; Guiver, M. D., Polysulfone/silica nanoparticle mixed-matrix membranes for gas separation. *Journal of Membrane Science* 2008, **314**, 123.
- [9] Emerich, D. F.; Thanos, C. G., The pinpoint promise of nanoparticle-based drug delivery and molecular diagnosis. *Biomolecular Engineering* 2006, **23**, 171.
- [10] Kearney, A. S., Prodrugs and targeted drug delivery. *Advanced Drug Delivery Reviews* 1996, **19**, 225.
- [11] Hergt, R.; Dutz, S., Magnetic particle hyperthermia - biophysical limitations of a visionary tumour therapy. *Journal of Magnetism and Magnetic Materials* 2007, **311**, 187.
- [12] Hergt, R.; Hiergeist, R.; Hilger, I.; Kaiser, W. A.; Lapatnikov, Y.; Margel, S.; and Richter, U., Maghemite nanoparticles with very high AC-losses for application in RF-magnetic hyperthermia. *Journal of Magnetism and Magnetic Materials* 2004, **270**, 345.
- [13] Wang, X.; Yuan, F. L.; Hu, P.; Yu, L. J.; Bai, L., Self-assembled growth of hollow spheres with octahedron-like Co nanocrystals via one-pot solution fabrication. *Journal of Physical Chemistry C* 2008, **112**, 8773.
- [14] Hu, P.; Yu, L. J.; Zuo, A. H.; Guo, C. Y.; Yuan, F. L., Fabrication of monodisperse magnetite hollow spheres. *Journal of Physical Chemistry C* 2009, **113**, 900.
- [15] Zeng, H. C., Ostwald Ripening: A synthetic approach for hollow nanomaterials. *Current Nanoscience* 2007, **3**, 177-181.
- [16] Meng, Y.; Chen, D.; Jiao, X., Synthesis and characterization of CoFe₂O₄ hollow spheres. *European Journal of Inorganic Chemistry* 2008, **2008**, 4019-4023.
- [17] Schaber, P. M.; Colson, J.; Higgins, S.; Thielen, D.; Anspach, B.; Brauer, J., Thermal decomposition (pyrolysis) of urea in an open reaction vessel. *Thermochimica Acta* 2004, **424**, 131.
- [18] Chaudhuri, A.; Mandal, M.; Mandal, K., Preparation and study of NiFe₂O₄/SiO₂ core-shell nanocomposites. *Journal of Alloys and Compounds* 2009, 487, 698.
- [19] Rakshit, R.; Mandal, M.; Pal, M.; Mandal, K., Tuning of magnetic properties of CoFe₂O₄ nanoparticles through charge transfer effect. *Applied Physics Letters* 2014, **104**, 092412.

-
- [20] Pal, M.; Kundu, A. ; Rakshit, R.; Mandal, K., Ligand-induced evolution of intrinsic fluorescence and catalytic activity from cobalt ferrite nanoparticles. *ChemPhysChem* 2015, **16**, 1627.
- [21] Mørup, S.; Brok, E.; Frandsen, C., Spin Structures in magnetic nanoparticles. *Journal of Nanomaterials* 2013, **2013**, 720629.
- [22] Kodama, R.; Berkowitz, A., Atomic-scale magnetic modeling of oxide nanoparticles. *Physical Review B* 1999, **59**, 6321.
- [23] Kodama, R. H.; Berkowitz, A. E.; McNiff, E. J.; Foner, S., Surface spin disorder in ferrite nanoparticles. *Journal of Applied Physics* 1997, **81**, 5552.
- [24] Mamiya, H.; Nakatani, I.; Furubayashi, T., Blocking and freezing of magnetic moments for iron nitride fine particle systems. *Physical Review Letters* 1998, **80**, 177.
- [25] Mørup, S., Superparamagnetism and spin glass ordering in magnetic nanocomposites. *European Letters* 1994, **28**, 671.
- [26] Mørup, S.; Bodker, F.; Hendriksen, P. V.; Linderøth, S., Spin-glass-like ordering of the magnetic moments of interacting nanosized maghemite particles. *Physical Review B* 1995, **52**, 287.
- [27] Khurshid, H.; Lampen-Kelley, P.; Iglesias, Ò.; Alonso, J.; Phan, M. H.; Sun, C. J.; Saboungi, M. L.; Srikanth, H., Spin-glass-like freezing of inner and outer surface layers in hollow γ -Fe₂O₃ nanoparticles. *Scientific Reports* 2015, **5**, 15054.

Chapter 6

High Frequency Electromagnetic Responses of MFe₂O₄ (M= Fe and Co) Nanostructures in Terahertz Region

This chapter demonstrates the morphology, size dependent electromagnetic responses of as-synthesized different MFe₂O₄ (M= Fe and Co) nanostructures in the terahertz frequency limit in detail and also develop a model confirming polaronic transport property of those semi-metallic materials.

6. Morphology and Size Dependent Electromagnetic Response of MFe_2O_4 (M=Fe and Co) Nanostructures in Terahertz Region

6.1. Preamble

In condensed matter physics, many elementary and collective low energy excitations occur in the terahertz (THz) frequency range, such as phonons, magnons, plasmons, energy band gap transition of superconductors, excitonic transition of semiconductor etc. Moreover, majority of dynamical phenomena in solids such as scattering, tunnelling, and recombination occur on characteristic times scales of picoseconds, i.e., in the THz frequency range.¹ Therefore, the study of THz dynamics of the materials is important from the view point of exploring basic physics as well as from the perspective of their future innovative applications. Moreover, THz-time domain spectroscopy (THz-TDS), an ultrafast non-contact technique allows us to measure the THz conductivity of nanomaterials (NMs) over picosecond time scales.²⁻⁷ In recent past, a wide class of NMs, such as metal,⁸ semiconductors,⁹ and oxides¹⁰⁻¹² with various morphology and sizes has been extensively studied utilizing THz-TDS. Mostly, the THz conductivity of many metal and semiconductor NMs in which electrons or holes are the charge carriers for electrical transportation is found to follow Drude-Smith,¹³ exciton polarizability,¹⁴ plasmon resonance¹⁵ model, as in case of photo-excited TiO_2 nanoparticles (NPs),¹⁶ InP NPs,¹⁷ semiconducting polymer molecules,^{18,19} graphene,²⁰ and carbon nanotubes.^{21,22} The deviation from typical Drude²³ behaviour in case of nano-systems is due to their high surface to volume ratio, quantum confinement, and percolative transport property which results in faster carrier decay. In addition to back-scattering of the charge carrier and their trapping at the surface states, the plasmon resonances in metal or the formation of excitons in semiconductor²⁴ NMs also plays important role in controlling their transport property. However, an understanding of the carrier dynamics of transition metal oxide based semi-metallic magnetic nanostructures (NSs) where the charge

transportation is basically through polaronic hopping is still absent in the extant literature.

In today's life, due to rapid enhancement of wireless communication, digital systems, and fast processors, a considerable attention has been focused on the fabrication of materials that possess a broad absorption frequency, high absorption capacity, low weight, good thermal stability, and antioxidant property. A long term research reveals that the ferrite NSs are the best material for absorbing radio frequency and microwave radiation due to their high saturation magnetization, large anisotropy field, low conductivity, and high surface to volume ratio. The hollow NSs of these ferrite materials are found to absorb electromagnetic (EM) radiation more efficiently due to large surface area and multiple internal reflections within the cavity. Therefore, the study of their EM responses with various morphologies and sizes in the THz frequency region may rise opportunities in the space, stealth technology, electromagnetism based electronic devices such as sensors, switches, and so on.

In this section, we have primarily investigated the ultrafast carrier dynamics of Fe_3O_4 and CoFe_2O_4 NPs and a series of nano hollow spheres (NHSs) of increasing diameter as a representative semi-metallic sample and proposed a model to explain their complex conductivity in the THz frequency range. The experimental results of complex THz conductivity have been explained in the framework of Polaron model by incorporating the concept of polaronic hopping, scattering as well as their tunnelling from one crystallite to another. Our work confirms that the thermally activated polaron is the fundamental carrier for electrical transportation in semi-metallic Fe_3O_4 and CoFe_2O_4 NSs and their hopping is the main mechanism for conduction.

6.2. Experimental Section

6.2.1. Material Used

The precursor salts, Cobalt Chloride ($\text{CoCl}_2, 6\text{H}_2\text{O}$), Ferric Chloride ($\text{FeCl}_3, 6\text{H}_2\text{O}$), Ethylene Glycol, Urea, and Oleylamine are obtained from Sigma-Aldrich. Ethyl Alcohol is purchased from Merck. All the reagents are of analytical grade and used without further purification.

6.2.2. Synthesis of MFe_2O_4 (M= Fe and Co) Nanoparticles and Nano hollow spheres

The synthesis of Fe_3O_4 NPs of diameter 100 nm and NHSs of diameter 100, 185, 250, 350, 725 nm and CoFe_2O_4 NPs of diameter 100 nm and NHSs of diameter 100, 160, 250, 350 nm is already presented in *Chapter 5*.

6.3. Result and Discussions

The XRD patterns of all as-synthesized samples as shown in Figure 6.1 confirm their single phase, spinel face centered cubic structure (JCPDS card no. 22-1086) and from broadening of their Bragg reflection peaks, the average crystallite size of Fe_3O_4 NHSs is found to increase with increasing average diameter of the NHSs (as listed in Table 6.1) using Scherrer's equation. Energy-dispersive X-ray (EDX) spectroscopic analysis of Fe_3O_4 NHS-250 (Inset of Figure 6.1) confirms the absence of elemental composition of the capping agent, oleylamine which may play significant role in THz absorption. Both the TEM images of NHS-250 and NP-100 (as shown in Figures 6.2 (a) and (b)) confirm the synthesis of uniform shaped Fe_3O_4 nanostructured materials. The inset of the TEM images indicates their nearly homogeneous size distribution. The intensive contrast between the black margin and the bright centre of the particles (Figure 6.2 (a)) implies the hollow nature of the as-obtained spheres. The list of average diameter (D), average shell thickness (t) of all as-synthesized NSs, as mentioned in Table 6.1, are calculated from the TEM micrographs. Meticulous analysis of Table 6.1 points out that the difference between

the average crystallite size and the average shell thickness in case of NHS-100 and NHS-185 are comparable whereas NHSs of larger average diameter show a huge difference in their magnitude. It reflects the fact that NHS-100 and NHS-185 are single crystalline in nature, while NHSs of larger average diameter are polycrystalline.

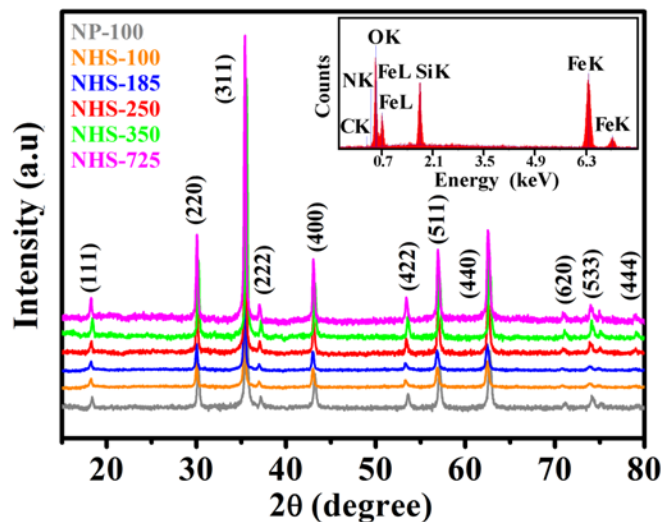


Figure 6.1. X-ray diffraction images of all as-synthesized Fe_3O_4 NP and NHSs of different average diameters. Inset shows the EDX spectrum of the Fe_3O_4 NHS-250 indicating the presence of the elemental composition of only Fe and O of Fe_3O_4 .

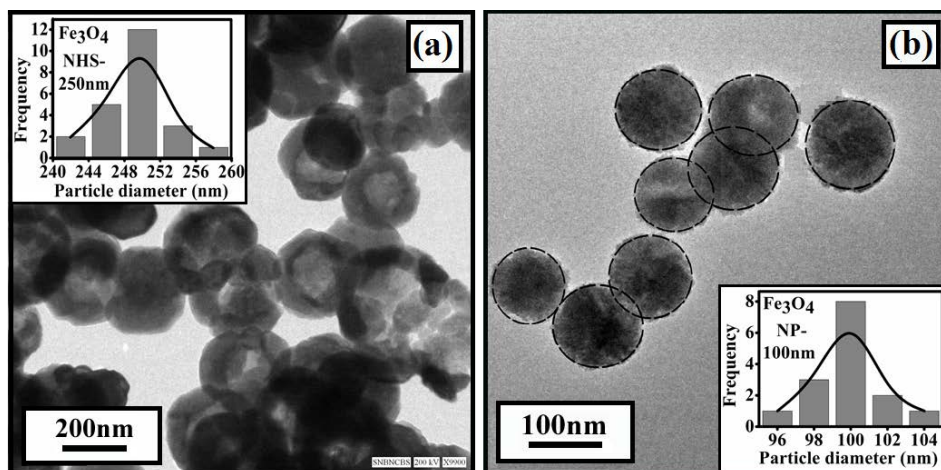


Figure 6.2. TEM images of Fe_3O_4 (a) NHSs of average diameter 250 nm, and (b) NPs of average diameter 100 nm. Inset of the TEM images shows their corresponding size distribution.

Table 6.1: List of average diameter, average crystallite size, and average shell thickness of all as synthesized NP and NHSs.

Sample name	Average diameter (D) nm	Average crystallite size (D) nm	Average shell thickness (t) nm
NP-100	100(±3)	16.69	0
NHS-100	100(±5)	29.89	30
NHS-185	185(±10)	35.09	35
NHS-250	250(±9)	36.65	50
NHS-350	350(±15)	38.56	65
NHS-725	725(±17)	39.5	150

The X-ray diffraction (XRD) patterns of all CoFe_2O_4 NSs, as shown in Figure 6.3 (a) confirm face centred cubic inverse spinel structure (JCPDS card no. 22-1086) of CoFe_2O_4 . Energy-dispersive X-ray (EDX) spectroscopic analysis (inset of Figure 6.3 (a)) confirms the absence of elemental composition of the capping agent, oleylamine which may play significant role in THz absorption. The SEM image of NP-100 (Figure 6.3 (b)) indicates that the NPs have a nearly homogeneous size distribution (90–110 nm), with an average size of 100 nm, as shown in Figure 6.3 (f). Figure 6.3 (c) shows the TEM images of CoFe_2O_4 NHS-350, confirming their uniform size and hollow configuration. Figure 6.3 (g) shows its size distribution graph where the size of as-synthesized NHSs varies from 340–360 nm with an average size of 350 nm. The high resolution TEM (HRTEM) image (Figure 6.3 (d)) of NHS-350 confirms its crystallinity and the calculated inter-planar distance between consecutive lattice fringes is about 0.251 nm, which corresponds to the distance between (311) planes of CoFe_2O_4 crystal lattice. Figure 6.3 (e) shows the selected area electron diffraction (SAED) pattern of NHS-350, indicating single crystalline nature of as-synthesized NHSs.

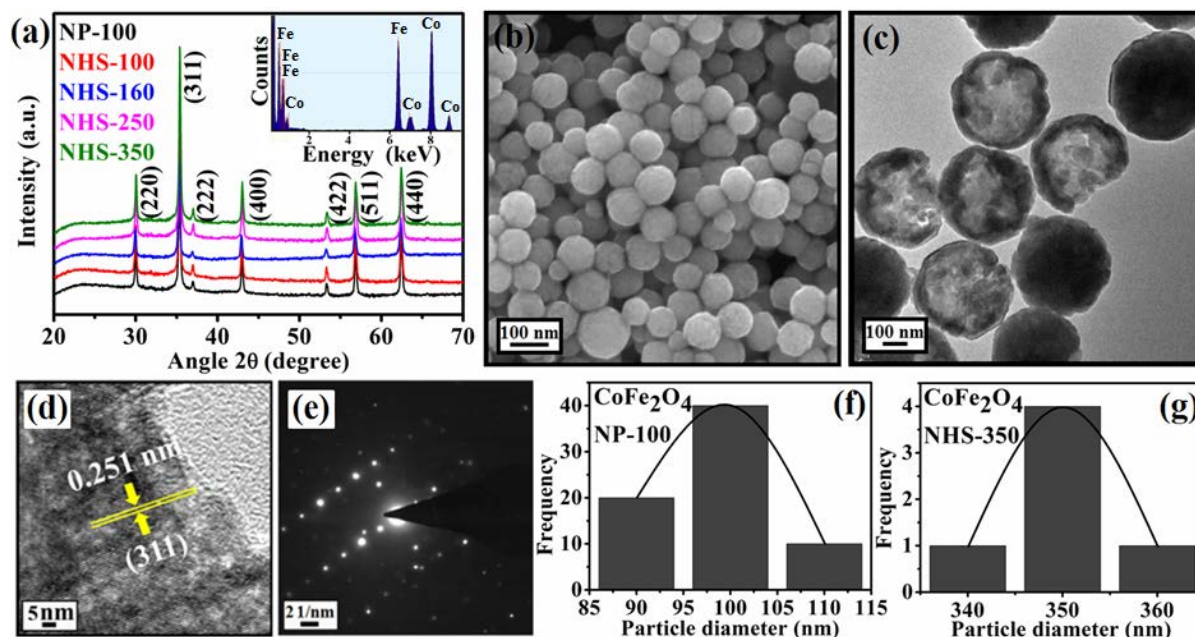


Figure 6.3. (a) XRD patterns of all CoFe_2O_4 NMs. Inset shows the EDX spectrum of CoFe_2O_4 NHS-350, indicating the presence of the elemental composition of only Co, Fe and O. (b) SEM image CoFe_2O_4 NP-100, (c) TEM image, (d) HRTEM image, (e) SAED pattern of CoFe_2O_4 NHS-350. The size distribution graphs of CoFe_2O_4 (f) NP-100, and (g) NHS-350.

Table 6.2. List of average particle diameter, crystallite size, and shell thickness of CoFe_2O_4 NMs.

Sample name	Average diameter (D) nm	Average crystallite size (D) nm	Average shell thickness (t) nm
NP-100	100±5	39.15±5	0
NHS-100	100±4	40.32±4	18
NHS-160	160±5	42.57±6	38
NHS-250	250±7	44.19±8	43
NHS-350	350±3	48.17±7	110

The THz transmission spectra of all the samples were measured using THz-TDS (as discussed in *Chapter 2* in detail) in which THz pulses are sent through the sample and the time-dependent transmitted pulses are recorded and transformed into frequency-dependent values. In order to quantify the effect of THz radiation on the proposed ferrite NSs, the relevant material parameters, such as the absorptivity, permittivity, permeability and conductivity are deduced from the detailed features of transmitted pulses, using an iterative algorithm of multi-pass transmission through the sample.

Figure 6.4 shows the absorption spectra for each of the six samples of Fe_3O_4 NSs in the frequency range 0.4 to 2.0 THz whereas Figures 6.5 display the same for

CoFe₂O₄ NPs where the frequency range of analysis for NP-100, NHS-100, 160, 250, 350 is found to vary from 0.1 to 0.9, 0.5, 0.4, 0.3, and 0.7 THz respectively. As shown in Figure 6.4, the total absorption of Fe₃O₄ NP is approximately zero with its peaks at 0.57, 0.81, 1.05, 1.29, 1.54 and 1.76 THz which appear to be at a regular energy level spacing of ~ 0.24 THz (~ 0.9 meV). Similarly, the total absorption spectrum of CoFe₂O₄ NP configuration is also found to exhibit equi-spaced peaks at 0.17, 0.31, 0.44, 0.59, 0.73, and 0.82 THz with an energy level spacing of ~ 0.13 THz (~ 0.53 meV) as shown in Figure 6.5. However, the absorption spectrum of CoFe₂O₄ NP is found to increase with frequency of the THz radiation in contrast to Fe₃O₄ NP. These equi-spaced peaks are developed due to lower-order acoustic phonon modes in a simple harmonic oscillator potential as experimentally observed by Samuelsen et al.²⁵ and also indicates the fact that a single photon absorption ($h\nu$) is involved in the process of the extraction of vibration energy from the THz radiation field by the dipoles which are developed due to vibration of the transition metal oxide molecule upon THz excitation.

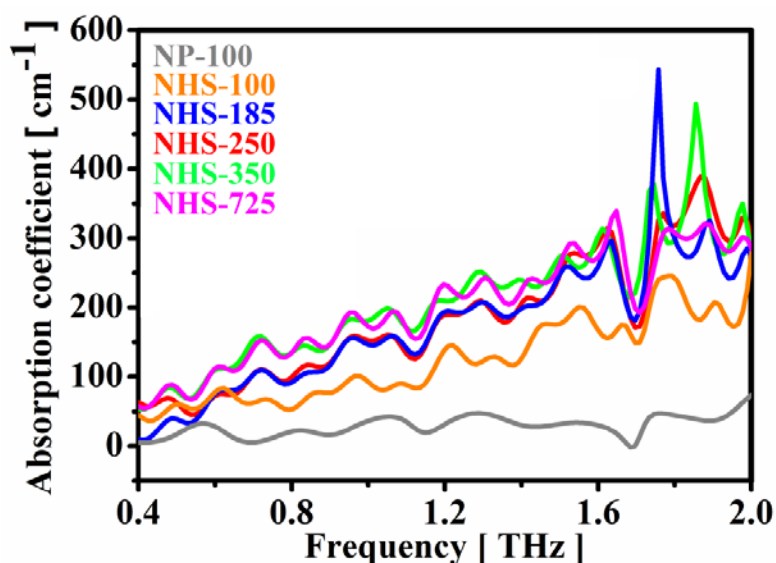


Figure 6.4. Absorption spectra of all as-synthesized Fe₃O₄ NP and NHSs of different average diameters in the frequency range 0.4 to 2.0 THz.

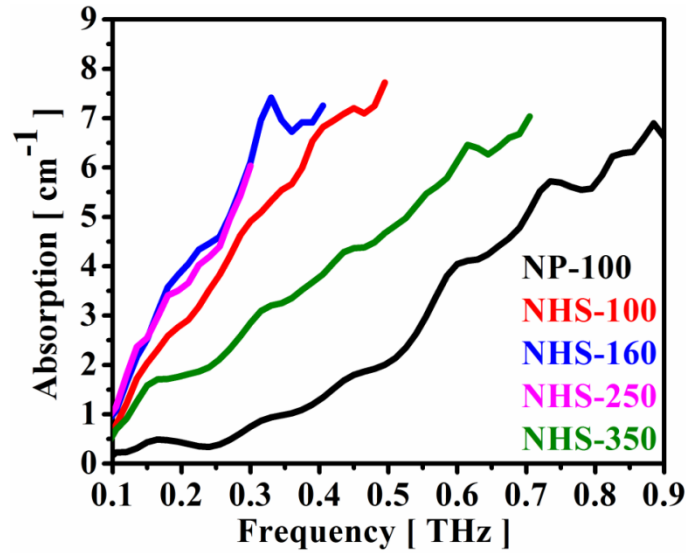


Figure 6.5. Absorption spectra of all as-synthesized CoFe_2O_4 NMs in the frequency range 0.1 to 0.9 THz.

Absorption mainly depends on the thickness and the nature of the material and also on the wavelength of incident radiation. According to the absorption theory of EM radiation²⁶, if dI is the amount of beam irradiance absorbed from the incident THz pulse propagating in the z direction through an infinitesimal distance dz within the material, then

$$dI = \alpha_{abs}(\omega)I dz \quad (6.1)$$

$$\alpha_{abs}(\omega) = \frac{2\omega k(\omega)}{c} \quad (6.2)$$

where I , the beam irradiance at z , α_{abs} , the absorption co-efficient, ω , the frequency of the incident THz radiation, c , the velocity of light in free space and $k(\omega)$, the imaginary part of the complex refractive index. It simply suggests that longer the distance covered by the incident radiation, greater is the absorption. In case of NHSs, its hollow configuration helps to confine the THz electromagnetic radiation and the multiple internal reflections offered by each interfaces of its nano-shell structure compel the ray to travel a longer distance than the NP of average diameter equivalent to NHS-100 which therefore, result in enhanced THz absorption with respect to NP as well as with increasing average shell thickness of the NHSs upto 350 nm. Apart from thickness of the material, the absorption of EM radiation also depends on its dielectric and magnetic loss. Upon THz excitation, the relatively large

specific surface area and double interfaces of the nano-shell structure greatly help to produce enormous interfacial polarization (electric or magnetic dipoles) which significantly enhances the EM wave attenuation in contrast to NPs as well as with increasing NHS's average diameter. However, it is noteworthy that above NHS-350 (in case of Fe_3O_4) and NHS-160 (in case of CoFe_2O_4), the total THz absorption is found to decrease in spite of large specific surface area and nano-shell thickness. The deviation from increasing trend with size is due to the fact that apart from shell thickness, absorption of EM radiation also depends on dielectric as well as magnetic loss of the material. Moreover, the monotonically increasing nature of frequency dependent THz absorption for all NSs is due to higher energy of incident radiation, leading to higher absorption, as expressed in Equation 6.2.

To investigate the possible mechanism for THz absorption whether it is due to dielectric or magnetic loss, the complex permittivity is measured using THz-TDS for both the Fe_3O_4 and CoFe_2O_4 NSs. The permittivity essentially originates from the electronic, ionic and intrinsic electric dipole polarization²⁷ of the material on which the crystal structure, size and geometrical morphology have an extensive impact. Because of the double interfaces of NHS, it produces a large number of charge multipoles at each interface upon interaction with THz radiation in comparison to the NP and thus results in larger real permittivity (ϵ') than NPs (as shown in Figure 6.6(a) and Figure 6.7 (a)). The size dependency of ϵ' for the Fe_3O_4 NHSs reveals that ϵ' increases with specific surface area upto NHS-350 and thereafter, it decreases significantly as in the case of NHS-725 with average shell thickness 150 nm. It may be due to the same reason as why the NP with an average diameter of 100 nm shows low ϵ' . However, Fe_3O_4 NHS-725 exhibits greater ϵ' than NP-100 due to the nano-excavation which helps to confine the electric field within the sample and thus results in a large number of electric dipoles in comparison to NP-100. The size dependency of ϵ'' for the CoFe_2O_4 NHSs reveals that the dielectric loss is found to increase with specific surface area upto NHS-160 and thereafter, it decreases as in the case of NHS-250 and NHS-350 with average shell thickness of 43 and 110 nm respectively, indicating that shell thickness of the NHSs plays an key role in controlling the THz absorption of the NMs. CoFe_2O_4 NHS-350 exhibits considerably

low ϵ'' in contrast to NHS-250 since its shell thickness is almost comparable to the average diameter of NP-100. However, NHS-350 exhibit greater ϵ'' than NP-100 due to its hollow configuration which helps to confine the electric field within the material and thus results in a higher dielectric loss compared to NP-100.

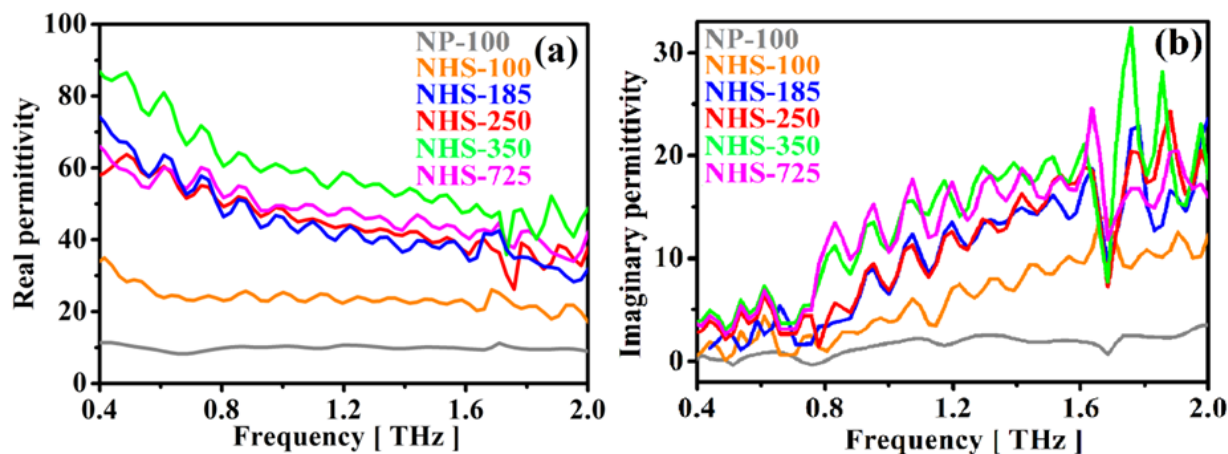


Figure 6.6. (a) Real, (b) imaginary part of the complex permittivity of all as-synthesized Fe_3O_4 NPs and NHSs in the frequency range of 0.4–2.0 THz.

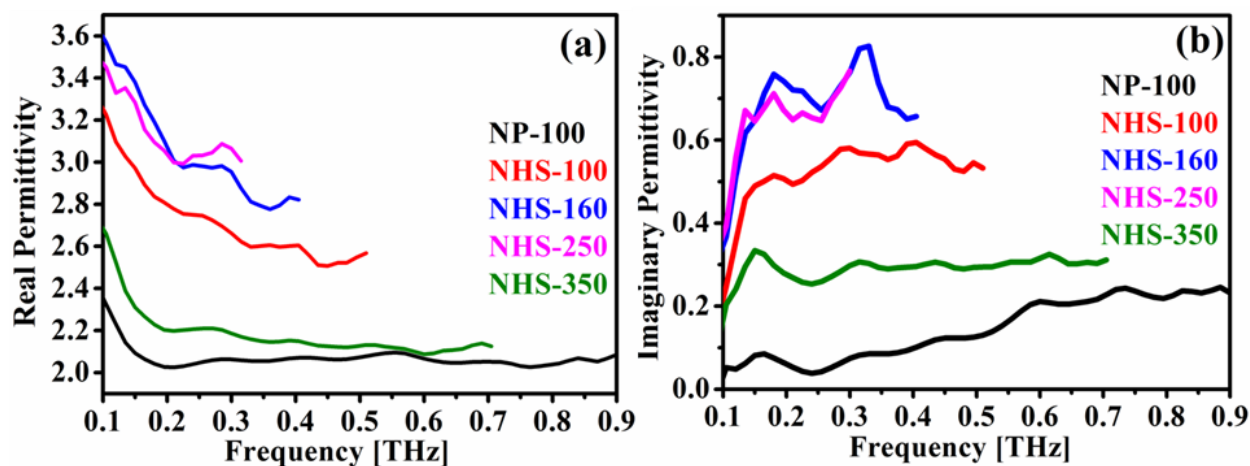


Figure 6.7. (a) Real, (b) Imaginary permittivity of all as-synthesized CoFe_2O_4 NMs in the frequency range 0.1–0.9 THz.

In order to study the influence of enhanced THz absorption on the electrical transport property of transition metal oxide based magnetic NSs, we performed a frequency dependent conductivity measurement as shown in figures 6.8 (a) and (b) for Fe_3O_4 NSs and 6.9 (a) and (b) for CoFe_2O_4 NSs. The room temperature size dependent THz conductivity study demonstrates that the real part of THz conductivity (σ') is positive and increasing with increasing frequency, while the imaginary component (σ'') is negative and decreasing with increasing frequency which indicates its strong deviation from classical Drude model. The morphology

and size dependent study reveal the influence of THz absorption on the electrical transport property of ferrite NPs. It is found that the nano hollow configuration exhibits greater THz conduction in contrast to NP configuration having same diameter of 100 nm and the magnitude of THz conductivity of NHSs increases with size upto a critical diameter, and then it starts to decrease, following Tinkham equation²⁸, a relation between the field transmission, $T(\omega)$ and the sample's complex conductivity,

$$\tilde{\sigma}(\omega) = \frac{n+1}{Zd} \left(\frac{1}{T(\omega)} - 1 \right) \quad (6.3)$$

where, n is the sample's terahertz index of refraction, Z is the impedance of free space and d is the sample thickness.

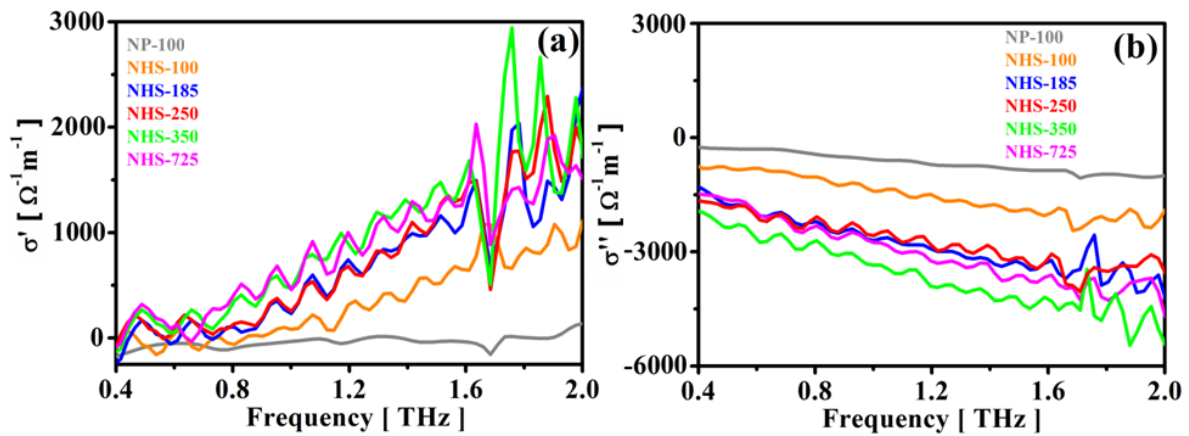


Figure 6.8. (a) Real, (b) imaginary part of complex conductivity of all as-synthesized Fe_3O_4 NPs and NHSs in the frequency range (0.4–2.0) THz.

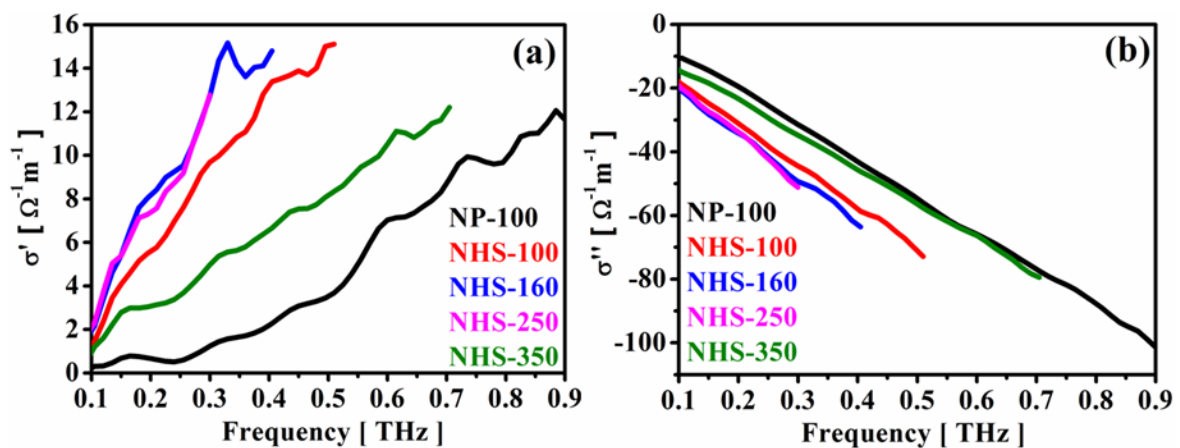


Figure 6.9. (a) Real, (b) Imaginary parts of complex conductivity of all CoFe_2O_4 NMs in the frequency range (0.1–0.9) THz.

Upon interaction with ferrite NMs, the THz energy is initially distributed among the electrons by electron-electron scattering and eventually it is damped to lattice by electron-phonon scattering within a few picoseconds. After thermalization, the time-domain response of ferrite NSs is found to be dominated by low energy acoustic phonon vibration which is associated with the acoustic mode quantization in a simple harmonic potential well and causes to generate electric dipoles. When an electron moves through this dielectric crystal of ferrite then, the phonon cloud effectively screens the charge of the moving electron and therefore enhances its mobility along with decrease in its effective mass and thus, results in polaron which plays significant role in determining electrical transport property of magnetite. It is well known that magnetite is a spin-polarized, mixed-valence (Fe^{2+} - Fe^{3+}) metal with a room temperature DC conductivity of only about 0.1% to that of Cu metal which occurs due to the thermally activated polaronic hopping of its extra electron between the Fe^{2+} and Fe^{3+} ions on the octahedral sites of magnetite. CoFe_2O_4 is also a spin polarized²⁹, mixed valance system in which the hopping of an extra electron between $\text{Fe}^{2+}/\text{Fe}^{3+}$ ions, present at both octahedral and tetrahedral site and hole hopping between $\text{Co}^{3+}/\text{Co}^{2+}$ ions, present at tetrahedral site are responsible for electrical conduction. Therefore, it is our fundamental research interest to present a theoretical background of THz induced ultrafast carrier dynamics of semi-metallic CoFe_2O_4 NMs.

6.4. Theoretical Model

As soon as a carrier encounters a nanocrystalline boundary within its mean free path, it can either leave the grain if its energy is sufficiently high to overcome the energy barrier simply by hopping, or it can scatter from the grain boundary or tunnel through the grain when its energy is low. The back-scattering of a carrier from the grain boundary in general causes carrier localization and makes the system bound. Moreover, thermally activated polaronic hopping which plays key role in determining the conductivity of semi-metallic NMs is also a bound state of electron due to strong electron-phonon coupling. Therefore, it is expected that a series

sequence of two contributions, i.e., the conductivities of bound carriers and tunnelling carriers dominates the THz conductivity of semi-metallic ferrite NMs.

The frequency dependence of the complex conductivity $\sigma_b^*(\omega)$ for bound carriers (as discussed in *Chapter 1*) at an angular frequency (ω) of THz excitation is given by the Equation 6.4,³⁰

$$\sigma_b^*(\omega) = \frac{\sigma_b(0)}{1 - i\omega\tau_D \left(1 - \frac{\omega_0^2}{\omega^2}\right)} \quad (6.4)$$

where $\sigma_b(0) = \frac{e^2 n_b \tau_D}{m}$ is the Lorentz's dc conductivity with number of bound carrier n_b , and ω_0 , the resonant frequency of ferrite NMs.

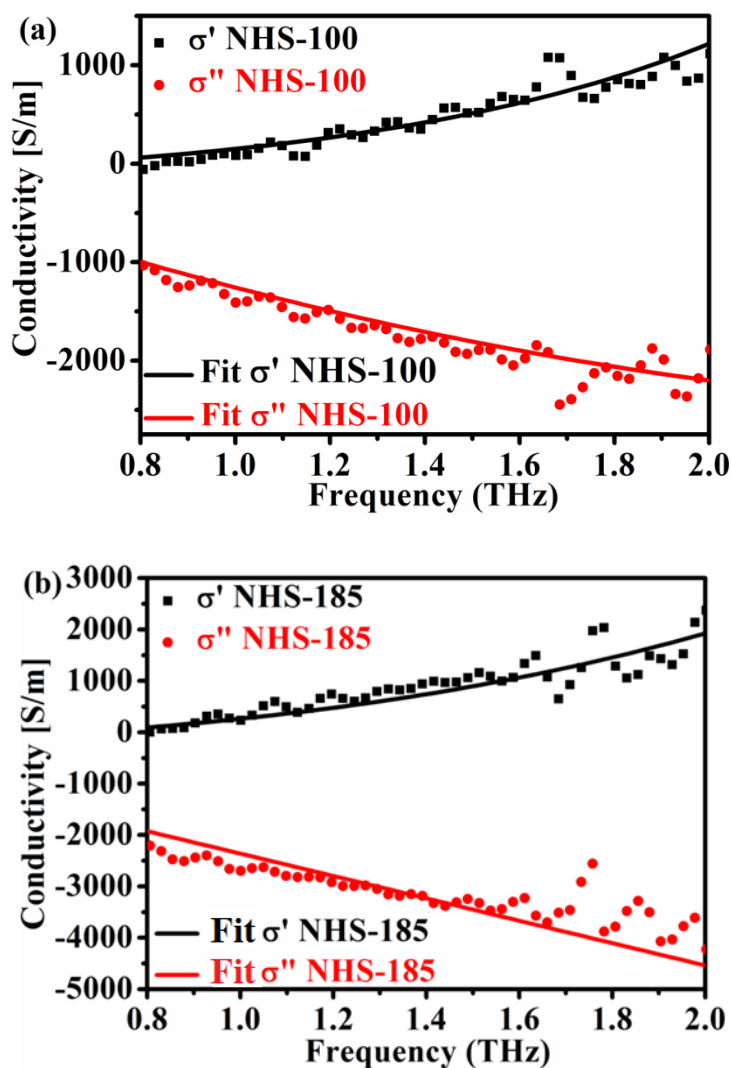
In case of hopping model, the conductivity of electrons tunnelling between the states in a randomly localized space (as discussed in *Chapter 1*) is presented by the Dyre expression 6.5,³¹

$$\sigma_t^*(\omega) = \sigma_t(0) \frac{i\omega\tau_t}{\ln(1 + i\omega\tau_t)} \quad (6.5)$$

where $\sigma_t(0) = \frac{n_t (er)^2}{2kT\tau_t}$ is the dc tunnelling conductivity with τ_t , the tunnelling time, r , the tunnelling distance i.e. distance between two consecutive grains, n_t , the number of tunnelling carriers, k , the Boltzmann constant, and T , the temperature. Since hopping and tunnelling conductivity through localized states occur in a random manner, they are similar to the band transport along a percolative path. Therefore, a percolation argument can help in formulating the ac conductivity in three dimensional CoFe_2O_4 NMs. According to the percolation path method, the complex conductivity due to a series sequence of bound and tunnelling carries is given by,³²

$$\frac{1}{\sigma^*(\omega)} = \frac{f}{\sigma_b^*(\omega)} + \frac{1-f}{\sigma_t^*(\omega)} \quad (6.6)$$

where f is the volume fraction of grains. Excellent fits to the present model in Equation 6.6 are obtained simultaneously for both σ' and σ'' of all Fe_3O_4 and CoFe_2O_4 NSs, as shown in Figures 6.10 (a)-(e), and 6.11 (a)-(e), for a given set of fitting parameters τ_D , τ_t , ω_0 , and m^* as summarized in Table 6.3 and 6.4 respectively. Detailed calculation of theoretical model, volume fraction (f), carrier density, tunnelling distance for Fe_3O_4 and CoFe_2O_4 NSs is presented in the Appendix. The magnitude of effective mass in Table 6.3 and 6.4 confirms the existence of polaron which exhibits microscopic polaron hopping along with significant interface scattering within the nanocrystals, as well as percolative transport between the consecutive nanocrystals in semi-metal.



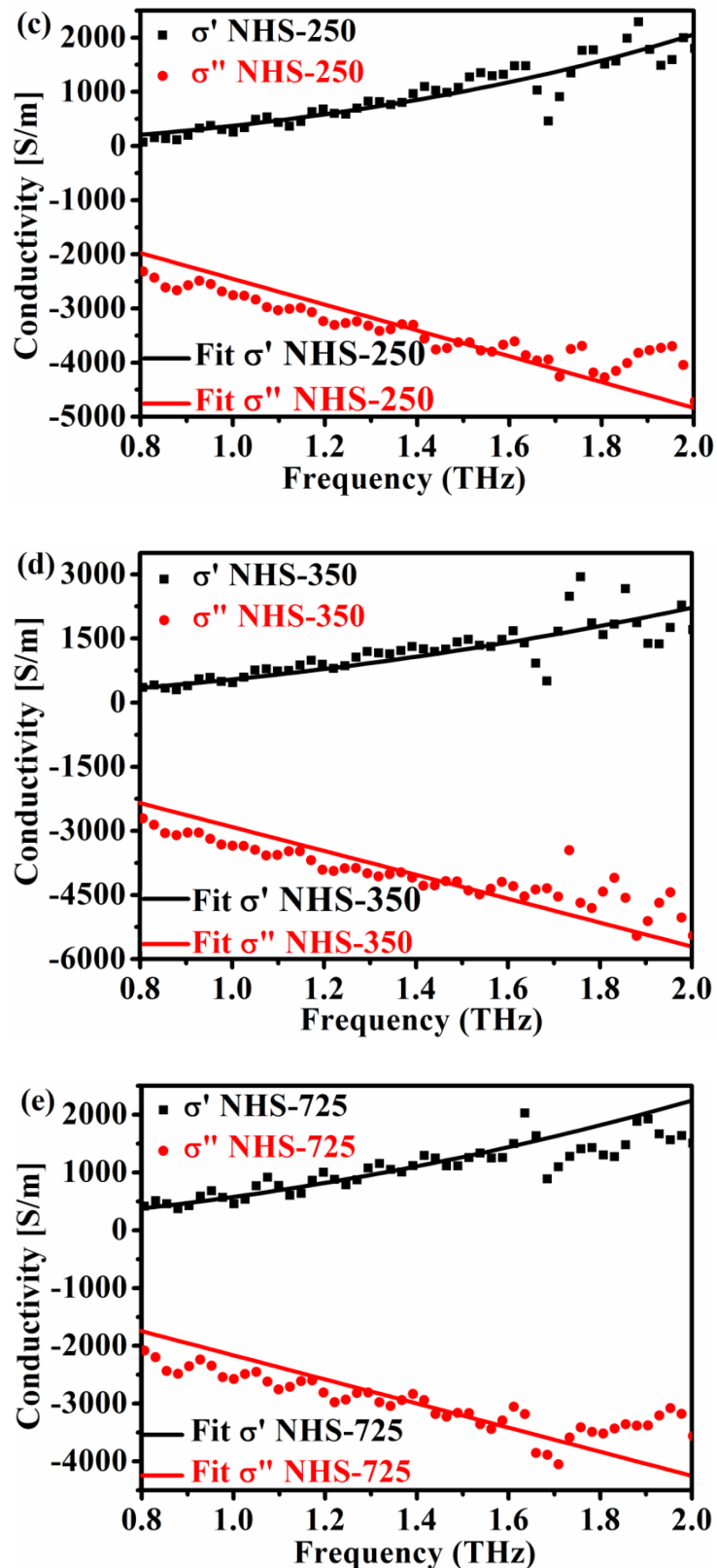
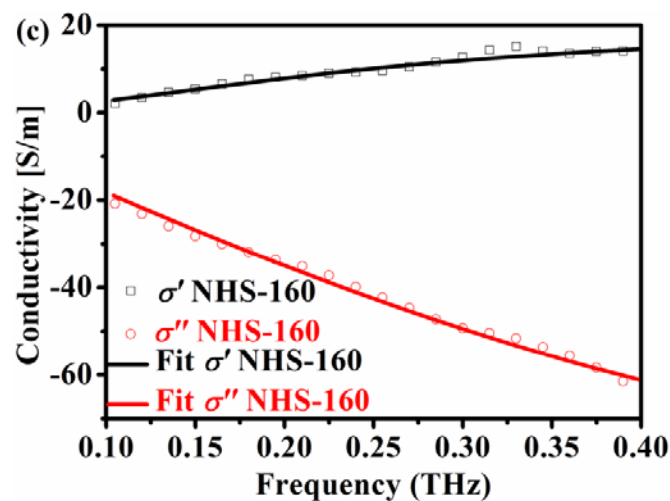
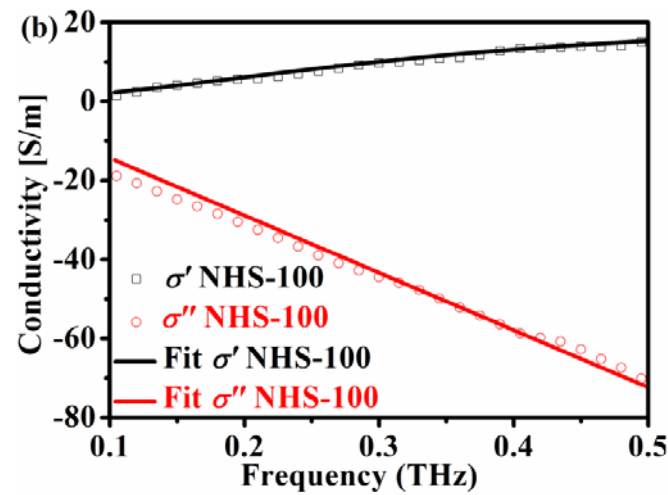
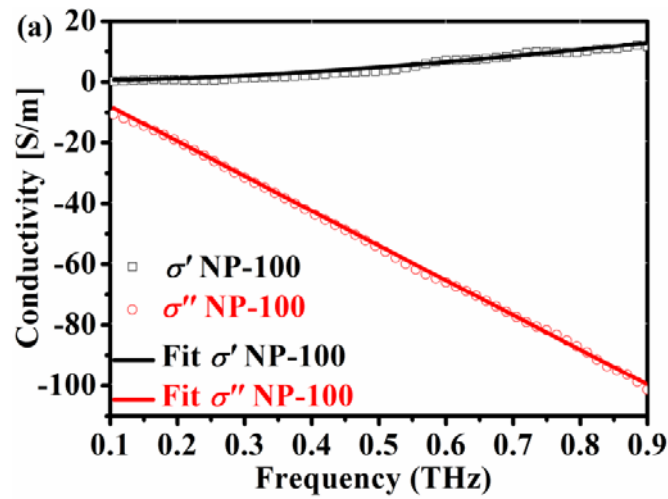


Figure 6.10. Real and imaginary parts of complex conductivity of Fe_3O_4 (a) NHS-100, (b) NHS-185, (c) NHS-250, (d) NHS-350, (e) NHS-725 in the frequency range (0.8-2.0) THz. Symbol represents experimental data whereas the line indicates the fitted graph.

Table 6.3. List of fitting parameters for Polaron Model in case of $\text{Fe}_3\text{O}_4\text{NHSs}$.

Name	$n_b (10^{26})$ (m^{-3})	$n_t (10^{28})$ (m^{-3})	τ_D (10^{-12})(s)	τ_t (10^{-12})(s)	$\omega_0 (10^{13})$ (Hz)	r (nm)	f	$m^* (10^{-31})$ (kg)
NHS-100	6.2	1.3	2	2.3	5.7	1.7	0.46	25.05
NHS-185	3.1	1.3	0.99	1.09	3.7	1.8	0.39	16.35
NHS-250	3.03	1.21	0.99	1.1	3.8	1.7	0.4	16.06
NHS-350	3.5	1.3	0.99	0.1	2.4	1.7	0.38	13.3
NHS-725	3.37	1.38	0.09	0.075	2.5	1.68	0.45	13.79



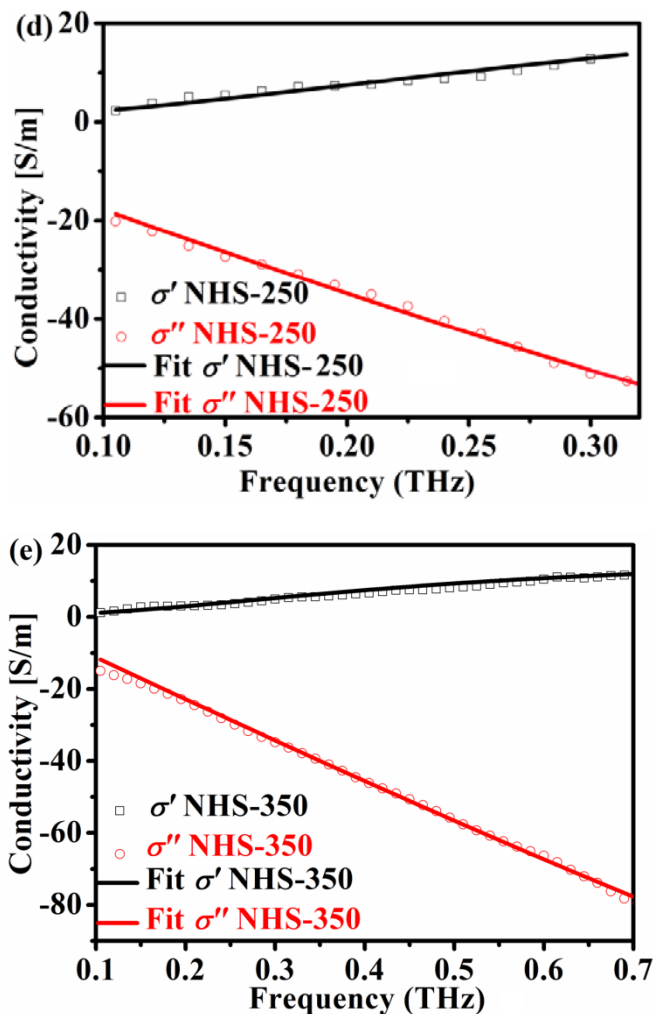


Figure 6.11. Real and imaginary parts of complex conductivity of CoFe_2O_4 (a) NP-100, (b) NHS-100, (c) NHS-160, (d) NHS-250, (e) NHS-350 in the frequency range (0.1-0.9) THz. Symbol represents experimental data whereas the line indicates the fitted graph.

Table 2. List of fitting parameters for Polaron Model in case of CoFe_2O_4 NHSs.

Name	$n_b (10^{27})$ (m^{-3})	$n_i (10^{28})$ (m^{-3})	τ_D (10^{-19})(s)	τ_t (10^{-18})(s)	$\omega_0 (10^{14})$ (Hz)	r (nm)	f	$m^* (10^{-31})$ (kg)
NP-100	2.2	2.5	20.9	3.6	9.76	1.7	0.51	32.06
NHS-100	2.1	2.5	4.04	2.5	9.1	1.7	0.33	30.37
NHS-160	2.2	2.5	3.7	1.2	8.3	1.7	0.42	25.14
NHS-250	2.1	2.5	6.3	2.0	7.5	1.7	0.37	29.57
NHS-350	2.0	2.5	5.32	3.0	9.4	1.7	0.5	31.94

Polaron physics plays an important role in describing magneto-resistive perovskites,³³ high temperature superconductors,³⁴ molecular semiconductors,³⁵ fullerenes,³⁶ polar semiconductors³⁷ etc. However, there exist only theoretical results concerning the spectral property, optical conductivity of polaronic systems at different electron-phonon interaction strength. Recently, THz-TDS, combined with ultrafast optical excitation opens up the opportunity to investigate the polaron

transport in nanocrystalline semi-metals which is a subject of notable technological and fundamental attention. From the technological standpoint, it is crucial for many important applications in magneto-polaron optics,³⁸ thermoelectronics and spintronics,³⁹ photodetectors,⁴⁰ and EM interference shielding devices for stealth and space^{41,42} technology. The theoretical studies by Tannhauser,⁴³ Mott,^{44,45} and Austin and Mott⁴⁶ describes the low temperature phase of transition metal oxide as a Wigner crystallization of polaron and points out the fact that whether it is small or intermediate, it in any case should be heavier than the free electron's mass. At low temperature, the effective mass of polaron in Fe₃O₄ is theoretically found to be approximately 10 times greater than the free electron's mass,³⁸ leading to no thermally activated polaronic hopping. Therefore, it is obvious that the absence of freezing of phonon at room temperature enhances its interaction with acoustic phonon which can lead to high carrier mobility along with reduction in its effective mass in comparison to the effective mass at low temperature and it is found to be consistent with our obtained results as listed in Table 6.3 and 6.4. Moreover, the electron-phonon interaction is found to enhance with increasing THz absorption, leading to reduction in the effective mass of polaron. Therefore, the enhanced magnitude of THz conduction in case of NHS configuration is due to its greater THz absorption capability which causes to generate more number of thermally activated polarons in comparison to NP as well as enhance the electron-phonon interaction. It is also valid for the study of size dependent conduction of NHSs. Due to interdependency, σ'' performs exactly opposite to σ' . It is a promising result from the view point of basic physics as well as from the perspective of future innovative application because the enhancement of THz absorption and conduction properties of light weight, anti-oxidant magnetic ferrite NHSs can increase its effectiveness in numerous application fields such as EMI shielding in THz frequency range, stealth technology, and space technology. These kind NMs are slightly different from recently developed new class of material, termed as "Metamaterials" in which extra properties are developed due to the artificially-designed repetitive structures. However, in our case of solvothermally synthesized NHSs, the properties are

dramatically improved in comparison to its solid counterparts only because of its nano-excavation.

6.5. Conclusion

In summary, we have presented a theoretical perspective of strong non-Drude THz conductivity of semi-metallic NMs such as Fe_3O_4 and CoFe_2O_4 NSs in terms of Polaron model. The agreement of experimental result with the proposed theoretical model confirms that the carrier dynamics follows microscopic polaron hopping with significant interface scattering within the nanocrystals, as well as percolative transport between the consecutive nanocrystals. Moreover, the morphology and size dependent conductivity study of a series of NHSs of increasing diameter and its solid counterpart reveals that the hollow structure exhibits greater THz conduction than its solid counterparts due to the enhancement of local electric field within the nano-hole and the magnitude of THz conductivity increases with THz absorptivity of the NMs, following Tinkham Equation. We believe that the exceptional THz conductivity of Fe_3O_4 and CoFe_2O_4 NHSs in contrast to its NP configuration would open up enormous new encouraging and beneficial applications toward diverse fields; for example, electronic devices for commerce, industry, and military affairs.

Bibliography

- [1] Tonouchi, M., Cutting-edge terahertz technology. *Nature Photonics* 2007, **1**, 97.
- [2] Schmuttenmaer, C. A., Exploring dynamics in the far-infrared with terahertz spectroscopy. *Chemical Review* 2004, **104**, 1759.
- [3] Jepsen, P. U.; Schairer, W.; Libon, I. H.; Lemmer, U.; Hecker, N. E.; Birkholz, M.; Lips, K.; Schall, M., Ultrafast carrier trapping in microcrystalline silicon observed in optical pump-terahertz probe measurements. *Applied Physics Letters* 2001, **79**, 1291.
- [4] Cooke, D. G.; Hegmann, F. A.; Mazur, Y. I.; Ma, W. Q.; Wang, X.; Wang, Z. M.; Salamo, G. J.; Xiao, M.; Mishima, T. D.; Johnson, M. B., Anisotropic photoconductivity of InGaAs quantum dot chains measured by terahertz pulse spectroscopy. *Applied Physics Letters* 2004, **85**, 3839.
- [5] Ostroverkhova, O.; Cooke, D. G.; Shcherbyna, S.; Egerton, R. F.; Hegmann, F. A.; Tykewski, R. R.; Anthony, J. E., Band like transport in pentacene and functionalized pentacene thin films revealed by sub picosecond transient photoconductivity measurements. *Physical Review B* 2005, **71**, 035204.
- [6] Rakshit, R.; Sarkar, D.; Pal, M.; Serita, K.; Tonouchi, M.; Mandal, K., Acoustic vibration induced high electromagnetic responses of Fe₃O₄ nano-hollow spheres in the THz regime. *Journal of Physics D: Applied Physics* 2015, **48**, 245301.
- [7] Frenzel, A. J.; Lui, C. H.; Fang, W.; Nair, N. L.; Herring, P. K.; Jarillo-Herrero, P.; Kong, J.; Gedik, N., Observation of suppressed terahertz absorption in photoexcited graphene. *Applied Physics Letters* 2013, **102**, 113111.
- [8] Thoman, A.; Kern, A.; Helm, H.; Walther, M., Nanostructured gold films as broadband terahertz anti reflection coatings. *Physical Review B* 2008, **77**, 195405.
- [9] Cooke, D. G.; MacDonald, A. N.; Hryciw, A.; Meldrum, Al.; Wang, J.; Frank, Q. L.; Hegmann, F. A., Ultrafast terahertz conductivity of photoexcited nanocrystalline silicon. *Journal of Materials Science: Materials in Electronics* 2007, **18**, S447.
- [10] Coker, T. L.; Titova, L. V.; Foumaux, S.; Bandulet, H. C.; Brassard, D.; Kieffer, J. C.; Khakani, M. A. El.; Hegmann, F. A., Terahertz conductivity of the metal-insulator transition in a nano granular VO₂ film. *Applied Physics Letters* 2010, **97**, 221905.
- [11] Han, J.; Woo, B. K.; Chen, W.; Sang, M.; Lu, X.; Zhang, W., Terahertz dielectric properties of MgO nanocrystals. *Journal of Physical Chemistry C* 2008, **112**, 17512.
- [12] Zou, X.; Luo, J.; Lee, D.; Cheng, C.; Springer, D.; Nair, S. K.; Cheong, S. A.; Fan, H. J.; Chia, E. E. M., Temperature-dependent terahertz conductivity of tin oxide nanowire films. *Journal of Physics D: Applied Physics* 2012, **45**, 465101.
- [13] Smith, N. V., Classical generalization of the Drude formula for the optical conductivity. *Physical Review B* 2001, **64**, 155106.
- [14] Wang, F.; Shan, J.; Islam, M. A.; Herman, I. P.; Bonn, M.; Heinz, T. F., Exciton polarizability in semiconductor nanocrystals. *Nature Materials* 2006, **5**, 861.
- [15] Nienhuys, H. K.; Sundström, V., Influence of plasmons on terahertz conductivity measurements. *Applied Physics Letters* 2005, **87**, 012101.
- [16] Turner, G. M.; Beard, M. C.; Schmuttenmaer, C. A., Carrier localization and cooling in dye-sensitized nanocrystalline titanium dioxide. *Journal of Physical Chemistry B* 2002, **106**, 11716.
- [17] Beard, M. C.; Turner, G. M.; Murphy, J. E.; Micic, O. I.; Hanna, M. C.; Nozik, A. J.; Schmuttenmaer, C. A., Electronic coupling in InP nanoparticle arrays. *Nano Letters* 2003, **3**, 1695.
- [18] Hendry, E.; Schins, J. M.; Candeias, L. P.; Siebbeles, L. D. A.; Bonn, M., Efficiency of exciton and charge carrier photogeneration in a semiconducting polymer. *Physical Review Letters* 2004, **92**, 196601.

- [19] Hendry, E.; Koeberg, M.; Schins, J. M.; Nienhuys, H. K.; Sundström, V.; Siebbeles, L. D. A.; Bonn, M., Interchain effects in the ultrafast photophysics of a semiconducting polymer: THz time-domain spectroscopy of thin films and isolated chains in solution. *Physical Review B* 2005, **71**, 125201.
- [20] Zou, X.; Shang, J.; Leaw, J.; Luo, Z.; Luo, L.; La-o-vorakiat, C.; Cheng, L.; Cheong, S. A.; Su, H.; Zhu, J. X.; Liu, Y.; Loh, K. P.; Neto, A. H. C.; Yu, T.; Chia, E. E. M., Terahertz conductivity of twisted bilayer graphene. *Physical Review Letters* 2013, **110**, 067401.
- [21] Jeon, T. I.; Kim, K. J.; Kang, C.; Maeng, I. H.; Son, J. H.; An, K. H.; Lee, J. Y.; Lee, Y. H., Optical and electrical properties of preferentially anisotropic single-walled carbon-nanotube films in terahertz region. *Journal of Applied Physics* 2004, **95**, 5736.
- [22] Altan, H.; Huang, F.; Federici, J. F.; Lan, A. D.; Grebel, H., Optical and electronic characteristics of single walled carbon nanotubes and silicon nanoclusters by terahertz spectroscopy. *Journal of Applied Physics* 2004, **96**, 6685.
- [23] Dressel, M.; Grüner, G., *Electrodynamics of solids: Optical properties of electrons in matter* (Cambridge, Cambridge University Press, 2002).
- [24] Ugawa, A.; Rinzler, A. G.; Tanner, D. B., Far-infrared gaps in single-wall carbon nanotubes. *Physical Review B* 1999, **60**, R11305.
- [25] Samuelsen, E. J.; Steinsvoll, O., Low-energy phonons in magnetite. *Physica Status Solidi (b)* 1974, **61**, 615.
- [26] Bohren, C. F., Huffman, D. R., *Absorption and scattering of light by small particles* (Wiley-VCH, German, 2007).
- [27] Zhuo, R. F.; Feng, H. T.; Chen, J. T.; Yan, D.; Feng, J. J.; Li, H. J.; Geng, B. S.; Cheng, S.; Xu, X. Y.; Yan, P. X., Multistep synthesis, growth mechanism, optical, and microwave absorption properties of ZnO dendritic nanostructures. *Journal of Physical Chemistry C* 2008, **112**, 11767.
- [28] Nuss, M. C.; Orenstein, J., *Millimeter and submillimeter wave spectroscopy of solids* (Springer-Verlag, Berlin Heidelberg, 1998).
- [29] Kakade, S. G.; Ma, Y. R.; Devan, R. S.; Kolekar, Y. D.; Ramana, C. V., Dielectric, complex impedance, and electrical transport properties of erbium (Er³⁺) ion-substituted nanocrystalline, cobalt-rich ferrite (Co_{1.1}Fe_{1.9-x}Er_xO₄) *Journal of Physical Chemistry C* 2016, **120**, 5682.
- [30] Fox, A. M., *Optical properties of solids* (Oxford University, New York, 2001).
- [31] Dyre, J. C.; Schroder, T. B., Universality of ac conduction in disordered solids *Reviews of Modern Physics* 2000, **72**, 873.
- [32] Kasap, S., *Principles of electronic materials and devices* (McGraw Hill, Boston, 2006).
- [33] Millis, A. J., Lattice effects in magnetoresistive manganese perovskites. *Nature* 1998, **392**, 147.
- [34] Shen, K. M.; Ronning, F.; Lu, D. H.; Lee, W. S.; Ingle, N. J. C.; Meevasana, W.; Baumberger, F.; Damascelli, A.; Armitage, N. P.; Miller, L. L.; Kohsaka, Y.; Azuma, M.; Takano, M.; Takagi, H.; Shen, Z. X., Missing quasiparticles and the chemical potential puzzle in the doping evolution of the cuprate superconductors. *Physical Review Letters* 2014, **93**, 267002.
- [35] Troisi, A., Prediction of the absolute charge mobility of molecular semiconductors: the case of rubrene. *Advance Materials* 2007, **19**, 2000.
- [36] Han, J. E.; Gunnarsson, O.; Crespi, V. H., Strong superconductivity with local Jahn-Teller phonons in C₆₀ solids. *Physical Review Letters* 2003, **90**, 167006.
- [37] Devreese, J. T., Polarons in semiconductors, *Encyclopedia of modern optics* (Academic Press, New York, 2004).
- [38] Haken, H.; Wagner, M., *Cooperative phenomena* (Springer, New York, 1973).
- [39] Bubnova, O.; Khan, Z. U.; Wang, H.; Braun, S.; Evans, D. R.; Fabretto, M.; Talemi, P. H.; Dagnelund, D.; Arlin, J. B.; Geerts, Y. H.; Desbief, S.; Breiby, D. W.; Andreasen, J. W.;

- Lazzaroni, R.; Chen, W. M.; Zozoulenko, I.; Fahlman, M.; Murphy, P. J.; Berggren, M.; Crispin, X.; Semi-metallic polymers. *Nature Materials* 2014, **13**, 190.
- [40] Wang, Y.; Mansour, N.; Salem, A.; Brennan, K. F.; Ruden, P. P.; Theoretical study of a potential low-noise semimetal-based avalanche photodetector. *IEEE Journal of Quantum Electronics* 1992, **28**, 507.
- [41] Hatakeyama, K. R.; Inui, T., Electromagnetic wave absorber using ferrite absorbing material dispersed with short metal fibre. *IEEE Transactions on Magnetism* 1984, **20**, 1261.
- [42] Draine, B. T.; Lazarian, A., Magnetic Dipole Microwave Emission from Dust Grains. *Journal of Astrophysics* 1999, **512**, 740.
- [43] Tannhauser, D. S., Conductivity in iron oxides. *Journal of Physics and Chemistry of Solids* 1962, **23**, 25.
- [44] Mott, N. J., Conduction in non-crystalline materials.III. Localized states in a pseudogap and near extremities of conduction and valence bands. *Philosophical Magazine* 1969, **20**, 1.
- [45] Mott, N. J., Electrons in disordered structures. *Advances in Physics* 1967, **16**, 49.
- [46] Austin, I. G.; Mott, N. J., Polarons in crystalline and non-crystalline materials *Advances in Physics* 1969, **18**, 41.

Appendix

I. Detail Calculation of Polaron Model

The frequency dependence of the complex conductivity $\sigma_b^*(\omega)$ for bound carriers at an angular frequency (ω) of THz excitation is given by the Equation 1

$$\sigma_f^*(\omega) = \frac{\tau_D e^2 n_b / m}{1 - i\omega\tau_D \left(1 - \frac{\omega_0^2}{\omega^2}\right)} = A \frac{1}{1 - i\omega\tau_D \left(1 - \frac{\omega_0^2}{\omega^2}\right)} \quad (1)$$

where, $A = \tau_D e^2 n_b / m$

In case of hopping model, the conductivity of electrons tunnelling between the states in a randomly localized space is presented by the Dyre expression (2)

$$\sigma_t^*(\omega) = \sigma_t(0) \frac{i\omega\tau_t}{\ln(1 + i\omega\tau_t)} = \frac{n_t (er_t)^2}{2kT\tau_t} \frac{i\omega\tau_t}{\ln(1 + i\omega\tau_t)} = B \frac{i\omega\tau_t}{\ln(1 + i\omega\tau_t)} \quad (2)$$

where, $B = \frac{n_t (er_t)^2}{2kT\tau_t}$

If $\ln(1 + i\omega\tau_t) = \left(\frac{\omega^2\tau_t^2}{2} + i\omega\tau_t\right)$, then

$$\sigma_t^*(\omega) = B \frac{i\omega\tau_t}{\left(\frac{\omega^2\tau_t^2}{2} + i\omega\tau_t\right)} = B \frac{1}{\left(1 - \frac{i\omega\tau_t}{2}\right)} \quad (3)$$

According to the percolation path method, the complex conductivity due to a series sequence of bound and tunnelling carriers is given by,

$$\frac{1}{\sigma^*(\omega)} = \frac{f}{\sigma_f^*(\omega)} + \frac{1-f}{\sigma_t^*(\omega)} \quad (4)$$

$$\begin{aligned} \Rightarrow \frac{1}{\sigma^*(\omega)} &= \frac{f\sigma_t^*(\omega) + (1-f)\sigma_f^*(\omega)}{\sigma_f^*(\omega)\sigma_t^*(\omega)} \\ \Rightarrow \sigma^*(\omega) &= \frac{\sigma_f^*(\omega)\sigma_t^*(\omega)}{f\sigma_t^*(\omega) + (1-f)\sigma_f^*(\omega)} \end{aligned} \quad (5)$$

Now,

$$\begin{aligned} \sigma_f^*(\omega)\sigma_t^*(\omega) &= A \frac{1}{1 - i\omega\tau_D \left(1 - \frac{\omega_0^2}{\omega^2}\right)} B \frac{1}{\left(1 - \frac{i\omega\tau_t}{2}\right)} \\ \Rightarrow \sigma_f^*(\omega)\sigma_t^*(\omega) &= AB \frac{\left[1 + i\omega\tau_D \left(1 - \frac{\omega_0^2}{\omega^2}\right)\right] \left(1 + \frac{i\omega\tau_t}{2}\right)}{\left[1 + \omega^2\tau_D^2 \left(1 - \frac{\omega_0^2}{\omega^2}\right)^2\right] \left(1 + \frac{\omega^2\tau_t^2}{4}\right)} \\ \Rightarrow \sigma_f^*(\omega)\sigma_t^*(\omega) &= C \left[1 + i\omega\tau_D \left(1 - \frac{\omega_0^2}{\omega^2}\right)\right] \left(1 + \frac{i\omega\tau_t}{2}\right) \end{aligned}$$

where, $C = AB \frac{1}{\left[1 + \omega^2\tau_D^2 \left(1 - \frac{\omega_0^2}{\omega^2}\right)^2\right] \left(1 + \frac{\omega^2\tau_t^2}{4}\right)}$

$$\Rightarrow \sigma_f^*(\omega)\sigma_t^*(\omega) = C \left[1 + i\omega\tau_D \left(1 - \frac{\omega_0^2}{\omega^2}\right) + \frac{i\omega\tau_t}{2} - \frac{\omega^2\tau_D\tau_t}{2} \left(1 - \frac{\omega_0^2}{\omega^2}\right)\right]$$

$$\Rightarrow \sigma_f^*(\omega)\sigma_t^*(\omega) = C \left\{ \left[1 - \frac{\omega^2\tau_D\tau_t}{2} \left(1 - \frac{\omega_0^2}{\omega^2}\right)\right] + i \left[\frac{\omega\tau_t}{2} + \omega\tau_D \left(1 - \frac{\omega_0^2}{\omega^2}\right)\right] \right\} = C(D + iE)$$

where, $D = \left[1 - \frac{\omega^2\tau_D\tau_t}{2} \left(1 - \frac{\omega_0^2}{\omega^2}\right)\right]$ and $E = \left[\frac{\omega\tau_t}{2} + \omega\tau_D \left(1 - \frac{\omega_0^2}{\omega^2}\right)\right]$

And,

$$\begin{aligned} \frac{1}{f\sigma_t^*(\omega) + (1-f)\sigma_f^*(\omega)} &= \frac{1}{fB \frac{1}{\left(1 - \frac{i\omega\tau_t}{2}\right)} + (1-f)A \frac{1}{1 - i\omega\tau_D \left(1 - \frac{\omega_0^2}{\omega^2}\right)}} \\ \Rightarrow \frac{1}{f\sigma_t^*(\omega) + (1-f)\sigma_f^*(\omega)} &= \frac{1}{fB \frac{\left(1 + \frac{i\omega\tau_t}{2}\right)}{\left(1 + \frac{\omega^2\tau_t^2}{4}\right)} + (1-f)A \frac{\left[1 + i\omega\tau_D \left(1 - \frac{\omega_0^2}{\omega^2}\right)\right]}{\left[1 + \omega^2\tau_D^2 \left(1 - \frac{\omega_0^2}{\omega^2}\right)^2\right]}} \\ \Rightarrow \frac{1}{f\sigma_t^*(\omega) + (1-f)\sigma_f^*(\omega)} &= \frac{\left(1 + \frac{\omega^2\tau_t^2}{4}\right) \left[1 + \omega^2\tau_D^2 \left(1 - \frac{\omega_0^2}{\omega^2}\right)^2\right]}{fB \left(1 + \frac{i\omega\tau_t}{2}\right) \left[1 + \omega^2\tau_D^2 \left(1 - \frac{\omega_0^2}{\omega^2}\right)^2\right] + (1-f)A \left[1 + i\omega\tau_D \left(1 - \frac{\omega_0^2}{\omega^2}\right)\right] \left(1 + \frac{\omega^2\tau_t^2}{4}\right)} \\ \Rightarrow \frac{1}{f\sigma_t^*(\omega) + (1-f)\sigma_f^*(\omega)} &= \frac{FG}{fBG \left(1 + \frac{i\omega\tau_t}{2}\right) + (1-f)AF \left[1 + i\omega\tau_D \left(1 - \frac{\omega_0^2}{\omega^2}\right)\right]} \end{aligned}$$

where, $F = \left(1 + \frac{\omega^2\tau_t^2}{4}\right)$ and $G = \left[1 + \omega^2\tau_D^2 \left(1 - \frac{\omega_0^2}{\omega^2}\right)^2\right]$

$$\Rightarrow \frac{1}{f\sigma_t^*(\omega) + (1-f)\sigma_f^*(\omega)} = \frac{H}{I \left(1 + \frac{i\omega\tau_t}{2}\right) + K \left[1 + i\omega\tau_D \left(1 - \frac{\omega_0^2}{\omega^2}\right)\right]}$$

where, $H=FG$, $I=fBG$, and $K=(1-f)AF$

$$\Rightarrow \frac{1}{f\sigma_t^*(\omega) + (1-f)\sigma_f^*(\omega)} = \frac{H}{(I+K) + i \left[\frac{I\omega\tau_t}{2} + K\omega\tau_D \left(1 - \frac{\omega_0^2}{\omega^2}\right) \right]}$$

$$\Rightarrow \frac{1}{f\sigma_t^*(\omega) + (1-f)\sigma_f^*(\omega)} = \frac{H}{L + iM}$$

where, $L=I+K$ and $M = \left[\frac{I\omega\tau_t}{2} + K\omega\tau_D \left(1 - \frac{\omega_0^2}{\omega^2} \right) \right]$

Therefore, Equation 5 becomes

$$\sigma^*(\omega) = \frac{\sigma_f^*(\omega)\sigma_t^*(\omega)}{f\sigma_t^*(\omega) + (1-f)\sigma_f^*(\omega)} = \frac{C(D+iE)H}{(L+iM)}$$

$$\sigma^*(\omega) = \frac{C(D+iE)H(L-iM)}{L^2 + M^2}$$

$$\sigma^*(\omega) = \frac{CH[(DL+EM) + i(EL-DM)]}{L^2 + M^2} \quad (6)$$

$$\sigma^R(\omega) = \frac{CH(DL+EM)}{L^2 + M^2} \quad (7)$$

and

$$\sigma^I(\omega) = \frac{CH(EL-DM)}{L^2 + M^2} \quad (8)$$

Equations 7 and 8 represent the real and imaginary conductivity of Polaron model.

II. Detail Program Code of Polaron Model

Terminal type set to 'wxt'

gnuplot> e=1.6e-19

gnuplot> k=1.38e-23

gnuplot> T=300

gnuplot> a(x)=td*e**2*nb/m

gnuplot> b(x)=nt*e**2*r**2/(2*k*T*tt)

gnuplot> c(x)=a(x)*b(x)/((1+(x*1e12)**2*td**2*(1-x0**2/(x*1e12)**2)**2)*(1+(x*1e12)**2*tt**2/4))

gnuplot> d(x)=(1-(x*1e12)**2*td*tt*(1-x0**2/(x*1e12)**2)/2)

gnuplot> e(x)=((x*1e12)*td*(1-x0**2/(x*1e12)**2)+(x*1e12)*tt/2)

gnuplot> f(x)=(1+(x*1e12)**2*tt**2/4)

gnuplot> g(x)=(1+(x*1e12)**2*td**2*(1-x0**2/(x*1e12)**2)**2)

gnuplot> h(x)=f(x)*g(x)

gnuplot> i(x)=f*b(x)*g(x)

gnuplot> k(x)=(1-f)*a(x)*f(x)

gnuplot> l(x)=i(x)+k(x)

gnuplot> m(x)=i(x)*(x*1e12)*tt/2+k(x)*(x*1e12)*td*(1-x0**2/(x*1e12)**2)

gnuplot> n(x)=c(x)*h(x)*(d(x)*l(x)+e(x)*m(x))/(l(x)**2+m(x)**2)

gnuplot> td=2e-12; nb=1e27; nt=1.6e28; tt=2e-12; x0=4e14; r=3e-9; f=0.418; m=20e-31

gnuplot> fit n(x) 'Real Fe3O4 NHS-100.txt' via td,N,n,tt,x0,r,f,m

gnuplot> plot n(x), "Real Fe3O4 NHS-100.txt"

III. Detail Calculation of Total Concentration of Charge Carrier (n):

A. The concentration of charge carrier for Fe_3O_4 NMs is given by,

$$n = \frac{N_A \rho_m n_{\text{Fe,Co}}}{M} = \frac{6.023 \times 10^{23} \times 5.17 \times 1}{231.533} = 1.34 \times 10^{22} \text{ cm}^{-3} = 1.34 \times 10^{28} \text{ m}^{-3}$$

where, N_A is the Avogadro number, ρ_m is the density, M is the molecular weight, and n_{Fe} is the number of type of atoms.

B. The concentration of charge carrier for CoFe_2O_4 NMs is given by,

$$n = \frac{N_A \rho_m n_{\text{Fe,Co}}}{M} = \frac{6.023 \times 10^{23} \times 5.29 \times 2}{234.62} = 2.72 \times 10^{22} \text{ cm}^{-3} = 2.72 \times 10^{28} \text{ m}^{-3}$$

where, N_A is the Avogadro number, ρ_m is the density, M is the molecular weight, and $n_{\text{Fe,Co}}$ is the number of type of atoms.

IV. The Calculation of Tunnelling Distance (r):

A minimum grain boundary can be formed involving two unit cells of two grains connected with each other.

A. Tunnelling Distance (r) for Fe_3O_4 Nanostructures:

Since the lattice parameter of Fe_3O_4 is 0.839 nm, then the distance between two consecutive grains is $(0.839+0.839) \text{ nm} = 1.678 \text{ nm} \approx 1.7 \text{ nm}$

B. Tunnelling Distance (r) for CoFe_2O_4 Nanostructures:

Since the lattice parameter of CoFe_2O_4 is 0.838 nm, then the distance between two consecutive grains is $(0.838+0.838) \text{ nm} = 1.676 \text{ nm} \approx 1.7 \text{ nm}$

V. The Calculation of Volume Fraction of Crystalline Phase (f):

A. The calculation of volume fraction of crystalline phase (f) for Fe_3O_4 nanostructures:

1. The Calculation of Volume Fraction of Crystalline Phase (f) of Fe_3O_4 NHS-100:

The volume of the scoop is $(500 \times 500 \times 40) \mu\text{m}^3 = 10^{16} \text{ nm}^3$.

For the NHS of 100 nm,

$$\text{The number of NHSs along the length of the scoop} = \frac{500 \times 10^3}{100} = 5 \times 10^3$$

$$\text{The number of NHSs along the breadth of the scoop} = \frac{500 \times 10^3}{100} = 5 \times 10^3$$

$$\text{The number of NHSs along the height of the scoop} = \frac{40 \times 10^3}{100} = 0.4 \times 10^3$$

$$\text{The volume of the crystalline phase of each NHS-100} = \frac{4}{3} \pi [50^3 - 20^3] = 0.49 \times 10^6 \text{ nm}^3$$

Therefore, the volume of crystalline phase of the NHSs within the scoop =

$$(0.49 \times 10^6 \times 5 \times 10^3 \times 5 \times 10^3 \times 0.4 \times 10^3) = 4.9 \times 10^{15}$$

$$\text{Therefore, the volume fraction of crystalline phase} = \frac{3.49 \times 10^{15}}{10^{16}} = 0.49$$

2. The Calculation of Volume Fraction of Crystalline Phase (f) of Fe₃O₄ NHS-185:

The volume of the scoop is (500x500x40) μm³=10¹⁶ nm³.

For the NHS of 185 nm,

$$\text{The number of NHSs along the length of the scoop} = \frac{500 \times 10^3}{185} = 2.7 \times 10^3$$

$$\text{The number of NHSs along the breadth of the scoop} = \frac{500 \times 10^3}{185} = 2.7 \times 10^3$$

$$\text{The number of NHSs along the height of the scoop} = \frac{40 \times 10^3}{185} = 0.216 \times 10^3$$

$$\text{The volume of the crystalline phase of each NHS-100} = \frac{4}{3} \pi [92.5^3 - 57.5^3] = 2.5189 \times 10^6 \text{ nm}^3$$

Therefore, the volume of crystalline phase of the NHSs within the scoop =

$$(2.5189 \times 10^6 \times 2.7 \times 10^3 \times 2.7 \times 10^3 \times 0.216 \times 10^3) = 3.96636 \times 10^{15}$$

$$\text{Therefore, the volume fraction of crystalline phase} = \frac{3.96636 \times 10^{15}}{10^{16}} = 0.3966$$

3. The Calculation of Volume Fraction of Crystalline Phase (f) of Fe₃O₄ NHS-250:

The volume of the scoop is (500x500x40) μm³=10¹⁶ nm³.

For the NHS of 250 nm,

The number of NHSs along the length of the scoop = $\frac{500 \times 10^3}{250} = 2.0 \times 10^3$

The number of NHSs along the breadth of the scoop = $\frac{500 \times 10^3}{250} = 2.0 \times 10^3$

The number of NHSs along the height of the scoop = $\frac{40 \times 10^3}{250} = 0.16 \times 10^3$

The volume of the crystalline phase of each NHS-250 = $\frac{4}{3} \pi [125^3 - 75^3] = 6.414 \times 10^6 \text{ nm}^3$

Therefore, the volume of crystalline phase of the NHSs within the scoop =

$$(6.414 \times 10^6 \times 2.0 \times 10^3 \times 2.0 \times 10^3 \times 0.16 \times 10^3) = 4.10496 \times 10^{15}$$

Therefore, the volume fraction of crystalline phase = $\frac{4.10496 \times 10^{15}}{10^{16}} = 0.41$

4. The Calculation of Volume Fraction of Crystalline Phase (f) of Fe₃O₄ NHS-350:

The volume of the scoop is $(500 \times 500 \times 40) \mu\text{m}^3 = 10^{16} \text{ nm}^3$.

For the NHS of 350 nm,

The number of NHSs along the length of the scoop = $\frac{500 \times 10^3}{350} = 1.42857 \times 10^3$

The number of NHSs along the breadth of the scoop = $\frac{500 \times 10^3}{350} = 1.42857 \times 10^3$

The number of NHSs along the height of the scoop = $\frac{40 \times 10^3}{350} = 0.1142857 \times 10^3$

The volume of the crystalline phase of each NHS-250 = $\frac{4}{3} \pi [175^3 - 110^3] = 16.874 \times 10^6 \text{ nm}^3$

Therefore, the volume of crystalline phase of the NHSs within the scoop =

$$(16.874 \times 10^6 \times 1.42857 \times 10^3 \times 1.42857 \times 10^3 \times 0.1142857 \times 10^3) = 3.9356 \times 10^{15}$$

Therefore, the volume fraction of crystalline phase = $\frac{3.9356 \times 10^{15}}{10^{16}} = 0.39$

5. The Calculation of Volume Fraction of Crystalline Phase (f) of Fe₃O₄ NHS-725:

The volume of the scoop is $(500 \times 500 \times 40) \mu\text{m}^3 = 10^{16} \text{ nm}^3$.

For the NHS of 725 nm,

The number of NHSs along the length of the scoop = $\frac{500 \times 10^3}{725} = 0.689655 \times 10^3$

The number of NHSs along the breadth of the scoop = $\frac{500 \times 10^3}{725} = 0.689655 \times 10^3$

The number of NHSs along the height of the scoop = $\frac{40 \times 10^3}{725} = 0.05517 \times 10^3$

The volume of the crystalline phase of each NHS-725 =

$$\frac{4}{3} \pi [362.5^3 - 212.5^3] = 159.3376 \times 10^6 \text{ nm}^3$$

Therefore, the volume of crystalline phase of the NHSs within the scoop =

$$(159.3376 \times 10^6 \times 0.689655 \times 10^3 \times 0.05517 \times 10^3) = 4.1810 \times 10^{15}$$

Therefore, the volume fraction of crystalline phase = $\frac{4.18 \times 10^{15}}{10^{16}} = 0.418$

B. The Calculation of Volume Fraction of Crystalline Phase (f) for CoFe_2O_4 Nanostructures:

1. The Calculation of Volume Fraction of Crystalline Phase (f) of CoFe_2O_4 NP-100:

The volume of the scoop is $(500 \times 500 \times 40) \mu\text{m}^3 = 10^6 \text{ nm}^3$.

For the NP of 100 nm,

The number of NPs along the length of the scoop = $\frac{500 \times 10^3}{100} = 5 \times 10^3$

The number of NPs along the breadth of the scoop = $\frac{500 \times 10^3}{100} = 5 \times 10^3$

The number of NPs along the height of the scoop = $\frac{40 \times 10^3}{100} = 0.4 \times 10^3$

The volume of the crystalline phase of each NP-100 = $\frac{4}{3} \pi [50^3] = 0.523 \times 10^6 \text{ nm}^3$

Therefore, the volume of crystalline phase of the NHSs within the scoop =

$$(0.523 \times 10^6 \times 5 \times 10^3 \times 5 \times 10^3 \times 0.4 \times 10^3) = 5.23 \times 10^{15}$$

Therefore, the volume fraction of crystalline phase = $\frac{5.23 \times 10^{15}}{10^{16}} = 0.523$

2. The Calculation of Volume Fraction of Crystalline Phase (f) of CoFe_2O_4 NHS-100:

The volume of the scoop is $(500 \times 500 \times 40) \mu\text{m}^3 = 10^{16} \text{ nm}^3$.

For the NHS of 100 nm,

The number of NHSs along the length of the scoop = $\frac{500 \times 10^3}{100} = 5 \times 10^3$

The number of NHSs along the breadth of the scoop = $\frac{500 \times 10^3}{100} = 5 \times 10^3$

The number of NHSs along the height of the scoop = $\frac{40 \times 10^3}{100} = 0.4 \times 10^3$

The volume of the crystalline phase of each NHS-100 = $\frac{4}{3} \pi [50^3 - 32^3] = 0.386 \times 10^6 \text{ nm}^3$

Therefore, the volume of crystalline phase of the NHSs within the scoop =

$$(0.386 \times 10^6 \times 5 \times 10^3 \times 5 \times 10^3 \times 0.4 \times 10^3) = 3.86 \times 10^{15}$$

Therefore, the volume fraction of crystalline phase = $\frac{3.86 \times 10^{15}}{10^{16}} = 0.386$

3. The Calculation of Volume Fraction of Crystalline Phase (f) of CoFe₂O₄ NHS-160:

The volume of the scoop is $(500 \times 500 \times 40) \mu\text{m}^3 = 10^6 \text{ nm}^3$.

For the NHS of 160 nm,

The number of NHSs along the length of the scoop = $\frac{500 \times 10^3}{160} = 3.1 \times 10^3$

The number of NHSs along the breadth of the scoop = $\frac{500 \times 10^3}{160} = 3.1 \times 10^3$

The number of NHSs along the height of the scoop = $\frac{40 \times 10^3}{160} = 0.25 \times 10^3$

The volume of the crystalline phase of each NHS-160 = $\frac{4}{3} \pi [80^3 - 42^3] = 1.8 \times 10^6 \text{ nm}^3$

Therefore, the volume of crystalline phase of the NHSs within the scoop =

$$(1.8 \times 10^6 \times 3.1 \times 10^3 \times 3.1 \times 10^3 \times 0.25 \times 10^3) = 4.3 \times 10^{15}$$

Therefore, the volume fraction of crystalline phase = $\frac{4.3 \times 10^{15}}{10^{16}} = 0.43$

4. The Calculation of Volume Fraction of Crystalline Phase (f) of CoFe₂O₄ NHS-250:

The volume of the scoop is $(500 \times 500 \times 40) \mu\text{m}^3 = 10^6 \text{ nm}^3$.

For the NHS of 250 nm,

$$\text{The number of NHSs along the length of the scoop} = \frac{500 \times 10^3}{250} = 2 \times 10^3$$

$$\text{The number of NHSs along the breadth of the scoop} = \frac{500 \times 10^3}{250} = 2 \times 10^3$$

$$\text{The number of NHSs along the height of the scoop} = \frac{40 \times 10^3}{250} = 0.16 \times 10^3$$

$$\text{The volume of the crystalline phase of each NHS-250} = \frac{4}{3} \pi [125^3 - 82^3] = 5.8 \times 10^6 \text{ nm}^3$$

$$\text{Therefore, the volume of crystalline phase of the NHSs within the scoop} = (5.8 \times 10^6 \times 2 \times 10^3 \times 2 \times 10^3 \times 0.16 \times 10^3) = 3.712 \times 10^{15}$$

$$\text{Therefore, the volume fraction of crystalline phase} = \frac{3.712 \times 10^{15}}{10^{16}} = 0.3712$$

5. The Calculation of Volume Fraction of Crystalline Phase (f) of CoFe_2O_4 NHS-350:

$$\text{The volume of the scoop is } (500 \times 500 \times 40) \mu\text{m}^3 = 10^6 \text{ nm}^3.$$

For the NHS of 350 nm,

$$\text{The number of NHSs along the length of the scoop} = \frac{500 \times 10^3}{350} = 1.428 \times 10^3$$

$$\text{The number of NHSs along the breadth of the scoop} = \frac{500 \times 10^3}{350} = 1.428 \times 10^3$$

$$\text{The number of NHSs along the height of the scoop} = \frac{40 \times 10^3}{350} = 0.114 \times 10^3$$

$$\text{The volume of the crystalline phase of each NHS-250} = \frac{4}{3} \pi [175^3 - 65^3] = 21.29 \times 10^6$$

nm^3

$$\text{Therefore, the volume of crystalline phase of the NHSs within the scoop} = (21.29 \times 10^6 \times 1.428 \times 10^3 \times 1.428 \times 10^3 \times 0.114 \times 10^3) = 4.949 \times 10^{15}$$

$$\text{Therefore, the volume fraction of crystalline phase} = \frac{4.949 \times 10^{15}}{10^{16}} = 0.49$$

Chapter 7

Biomedical Application of CoFe₂O₄ and SiO₂ Coated CoFe₂O₄ Nano hollow spheres Through Bilirubin Adsorption

This chapter demonstrates an unprecedented bilirubin adsorption efficiency of CoFe₂O₄ and SiO₂@CoFe₂O₄ nanostructures, specifically nanoparticles and nano-hollow spheres in contrast to the commercially available activated carbon and resin which are generally used for hemoperfusion and hemodialysis.

7. Excellent Bilirubin Adsorption of CoFe_2O_4 and SiO_2 Coated CoFe_2O_4 Nanoparticles and Nano hollow spheres

7.1. Preamble

In the last three decades, hollow magnetic nanostructured materials have attracted tremendous attention of the researchers owing to their low density, high porosity, high surface area, large pore volume, and surface permeability which give rise to wide variety of applications in the field of catalyst,¹ energy storage device,² chemical sensors,^{3,4} and photonic crystals.⁵ All these features along with non-toxicity, biodegradability, and controlled transport property of 3d transition metal oxide based magnetic nanomaterials (NMs), specifically ferrites facilitate their application in biomedicine, as for instance in drug delivery systems,⁶ biolabeling,⁷ magnetic hyperthermia,^{8,9} and magnetic resonance imaging contrast enhancers.^{10,11} Recently, CoFe_2O_4 (CFO) NMs, a mixed-valence oxide of transition metals with a inverse spinel structure have been investigated extensively as targeted imaging agents,¹² and a platform for hyperthermia application in cancer treatment¹³ due to their high saturation magnetization, large magnetocrystalline anisotropy, high coercivity, simple preparation technique, low cost, remarkable chemical and mechanical stability, and biocompatibility.¹⁴ Among diversified morphologies such as thin films,¹⁵ nanoflakes,¹⁶ and microporous particles,¹⁷ CFO nano hollow spheres (NHSs) are the potential candidates for their application in hyperthermia treatment, drug delivery due to their high coercivity¹⁸ and hollow interior which can be utilized for the removal of toxic materials from waste materials as well as for encapsulation-release of drug molecules.^{19,20}

It is well known that bilirubin (BR) is the yellow-orange breakdown product of the heme group in aged red blood cells²¹ and excreted in the bile after conjugation with glucuronic acid. However, when its conjugation with glucuronic acid is inhibited, as in neonatal jaundice and in hereditary forms of congenital jaundice, excess BR deposits to various tissues, giving rise to severe hyperbilirubinemia and

neurotoxicity. Now-a-days, conventional treatments for severe hyperbilirubinemia include phototherapy,²² hemoperfusion,²³ hemodialysis,²⁴ and exchange blood transfusion²⁵ methodology. To date, phototherapy is the most effective treatment for severe jaundice.²⁶ However, it involves long exposure of UV ray for 10-12 h per day and its efficacy may diminish with age due to increased skin thickness and decreased surface/mass ratio.²⁷ Other techniques consist of passage of patient's blood through a column with absorptive materials such as resin²⁸ and activated carbon²⁹ aiming to suppress the BR level. Therefore, a long term research has been carried out to accelerate the process of BR adsorption either by using new materials or by varying their size or morphology. Till now, Duan et. al.³⁰ reported that BR adsorption in perfusion is at the highest speed from 15 to 45 min with resin and 1.5 to 3 h with activated charcoal column.

Herein, we utilize as-synthesized CFO NHSs (as described in *Chapter 5* in detail) of desirable diameter and nanoparticles (NPs) for efficient BR removal from its aqueous solution. A comparative study of CFO and SiO₂ coated CFO (SiO@CFO) nanostructures (NSs) reveals that the electrostatic interaction between -NH₂ group of oleylamine (OLA) which is used during the synthesis of CFO NSs and -OH group of BR leads to an exceptional adsorption activity. A total 98% adsorption of BR is found to take place only within 8 min by using CFO NHSs of diameter 350 nm. The remarkable efficiency of the developed magnetic NSs towards the suppression of BR level combined with biocompatibility³¹ indicates their promise in therapeutic applications against hyperbilirubinemia.

7.2. Experimental Section

7.2.1. Synthesis of CoFe₂O₄ and SiO₂ Coated CoFe₂O₄ Nanoparticles and Nano hollow spheres

CFO NPs of diameter 100 nm and a series of NHSs of diameter 100, 160, 250, and 350 nm were prepared through a facile template free solvothermal technique

and further SiO₂ coating of these NSs have been carried out by employing Stöber method as described in *Chapter 1* and *Chapter 5* in detail.

7.2.2. Adsorption Study

Adsorption experiments were carried out by adding a fixed amount of adsorbent (0.01 g) to a 10 ml of beaker filled with 4 ml diluted BR solutions with varying concentration (0.01–0.03 mg/ml) at pH ~7. The beaker was then placed in a magnetic stirrer with the speed set at 120 rpm. At the end of each adsorption batch runs, the final concentration of dye in the solution was measured using UV-Vis spectrophotometer until steady state has been reached. The amount of dye on CFO adsorbent was calculated from the following equation:

$$q_t = \frac{(C_0 - C_t)V}{m} \quad (7.1)$$

where q_t (mg/g) is the amount of dye adsorbed at time t , C_0 and C_t (mg/ml) are the dye concentrations at initial and any time respectively. V (ml) is the volume of the dye solution, and m (g) is the mass of the adsorbent.

7.3. Result and Discussions

Considering recent significant progress in biomedical application through rational engineering and manipulation of magnetic NMs, we aimed to utilize our developed CFO and SiO@CFO NSs in the degradation of BR, the pigment responsible for the yellow coloration of the skin in jaundice. Figures 7.1 (a) and (b) show the comparative decay of BR over time through UV-Vis spectroscopy in presence of CFO and SiO@CFO NSs of diameter 350 nm at pH ~7. The absence of peaks at 245 and 319 cm⁻¹, corresponding to the decomposition products of BR³² indicates that the reaction follows the adsorption pathway instead of any chemical degradation. It is found that CFO and SiO@CFO NHS-350 adsorb a total 98% and 61% of BR respectively within only 8 min and a total 90% adsorption of BR occurs with 20 min in case of SiO@CFO NHS-350. Recently, Shinke et. al.³³ has reported the adsorption of BR (~90%) in presence of carbon NMs within 60 min which ensures

that our developed CFO NHSs can replace activated carbon, resin used in extracorporeal adsorption treatments.

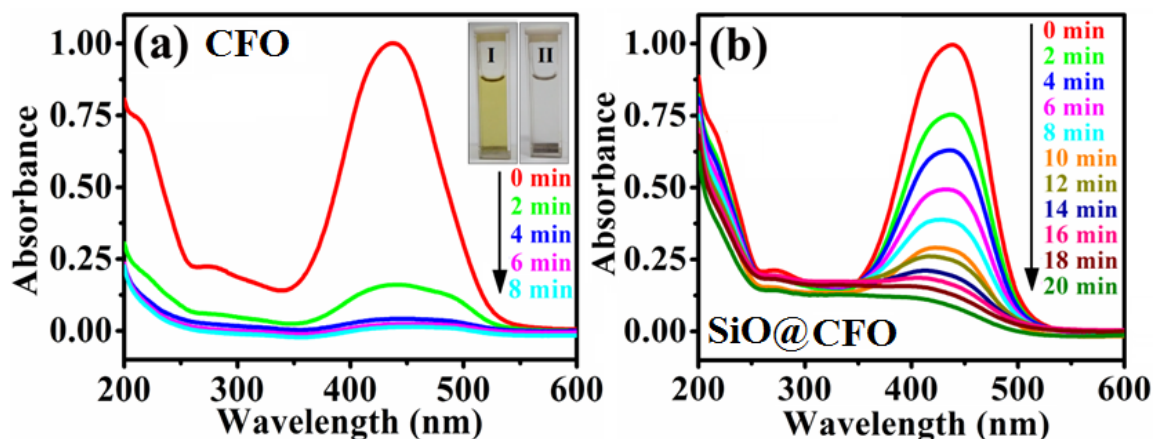


Figure 7.1. UV-Vis spectral changes of aqueous solution of BR with time in presence of (a) CFO NHS-350, and (b) SiO@CFO NHS-350. I and II in the inset (a) show the photographs of BR solution before and after the degradation with CFO NHS-350 under no external light respectively.

In order to examine the controlling mechanism of adsorption such as mass transfer, physisorption, and chemisorption; different kinetic models such as intraparticle diffusion (mass transfer) model, pseudo 1st order (physisorption), and pseudo 2nd order (chemisorption) model were applied to test the obtained experimental data for different absorbent concentration as described in *Chapter 1*.

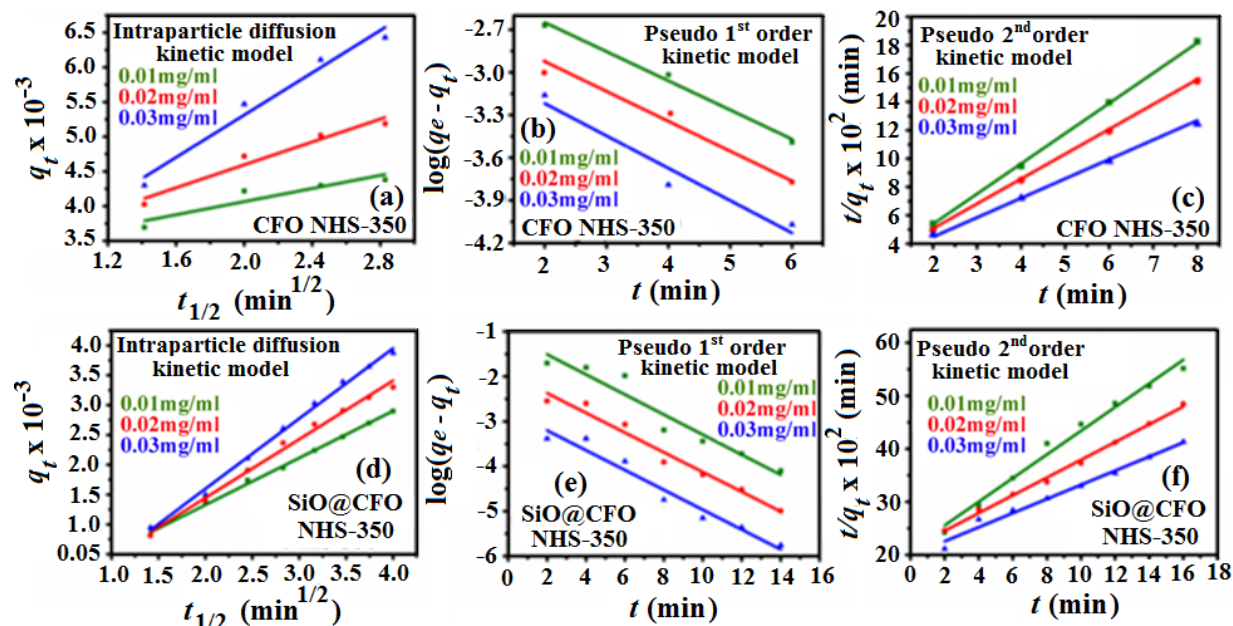


Figure 7.2. Adsorption kinetics of BR on (a)-(c) CFO and (d)-(f) SiO@CFO NHS-350 with intraparticle diffusion, pseudo 1st order, and pseudo 2nd order model respectively.

Table 7.1. Intraparticle diffusion, pseudo 1st order, and pseudo 2nd order kinetic model parameters for different initial BR concentrations at room temperature.

Name of adsorbate	Amount of adsorbate (gm)	C_0 (mg/ml)	$q_{e,exp}$ (mg/g)	Intraparticle diffusion kinetic model			Pseudo first order kinetic model			Pseudo second order kinetic model		
				q_{ei} (mg/g)	k_i (mg/g min ^{1/2})	R^2	q_{e1} (mg/g)	k_1 (min ⁻¹)	R^2	q_{e2} (mg/g)	k_2 (g/mg min)	R^2
CFO NHS-350	0.01	0.01	4.29	4.45	0.47	0.80	6.31	0.52	0.98	4.38	0.82	0.99
		0.02	5.19	5.29	0.82	0.93	8.2	0.48	0.95	5.72	0.45	0.99
		0.03	6.43	6.57	1.52	0.95	10.6	0.47	0.90	7.61	0.21	0.99
SiO@CFO NHS-350	0.01	0.01	2.78	2.92	0.84	0.99	3.46	0.51	0.92	4.69	0.02	0.97
		0.02	3.31	3.40	0.98	0.99	6.05	0.50	0.96	5.97	0.01	0.98
		0.03	3.86	3.96	1.18	0.99	8.02	0.50	0.95	8.18	0.01	0.98

The plots of intraparticle diffusion, pseudo 1st, and pseudo 2nd order kinetic models for both CFO and SiO@CFO NHS-350 are shown in Figures 7.2 (a)-(f). The values of rate constant (k), amount of adsorbed BR on per unit mass of adsorbate at equilibrium (q_e), and the correlation coefficients (R^2) are calculated from these plots and presented in Table 7.1. In case of CFO NHS-350, the value of R^2 for the pseudo 2nd order model is 0.99, and the calculated value of q_e is nearly equal to the experimental value, which suggests that the adsorption follows pseudo 2nd order model and it predicts that the overall rate of adsorption is dominated by chemisorptions which involves a valency force through sharing or exchange of electrons between -OH group of BR and -NH₂ group of OLA, present on the adsorbent's surface. The presence of OLA on NHS surface has been confirmed by performing differential thermal analysis (DTA) (as shown in Figure 7.3) in which the peak indicates the transition between two phases i.e. NHS with and without OLA. In case of SiO@CFO NHS-350, the intraparticle diffusion kinetic model is found to fit closely with the experimental data with $R^2 \sim 0.99$ which implies that herein, the intraparticle diffusion is the rate controlling steps of adsorption instead of chemisorption. It may be due to the presence of porous SiO₂ coating on CFO NSs which lead to a significant diminution of attractive coulomb interaction between adsorbate and adsorbent. Therefore, the comparative BR adsorption study of CFO and SiO@CFO NSs confirms that the presence of OLA plays a significant role in the process of adsorption.

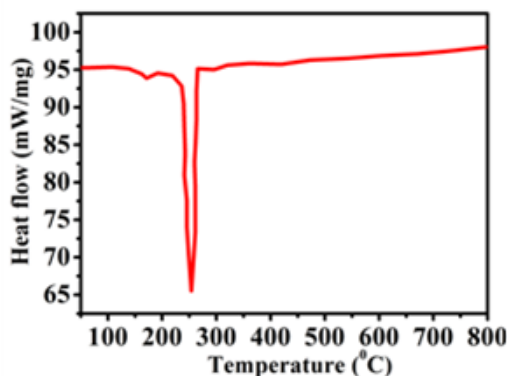


Figure 7.3. DTA curve of CFO NHS-350 confirming the attachment of oleylamine on the surface of the NHSs.

Figures 7.4 (a) and (b) show the effects of initial dye concentrations on the adsorption kinetics of BR on CFO and SiO@CFO NHS-350 respectively. The amount of BR adsorbed at the equilibrium reflects the maximum adsorption of the adsorbent under the operating conditions applied. It is found that an increase in the initial dye concentrations leads to an enhancement of the adsorption capacity of the BR on the adsorbent which is due to the increase in driving force with the concentration gradient. The maximum monolayer adsorption capacity at equilibrium, $q_e = \frac{(C_0 - C_e)V}{m}$ where, C_0 and C_e are the initial and final concentration of BR solution in mg/ml, V is the volume of BR solution in ml and m is the mass of adsorbent in mg, is found to increase from 4.38 to 6.4 mg/g for CFO NHS-350 and 2.92 to 3.9 mg/g for SiO@CFO NHS-350 respectively with an increase in the initial dye concentrations from 0.01 to 0.04 mg/ml.

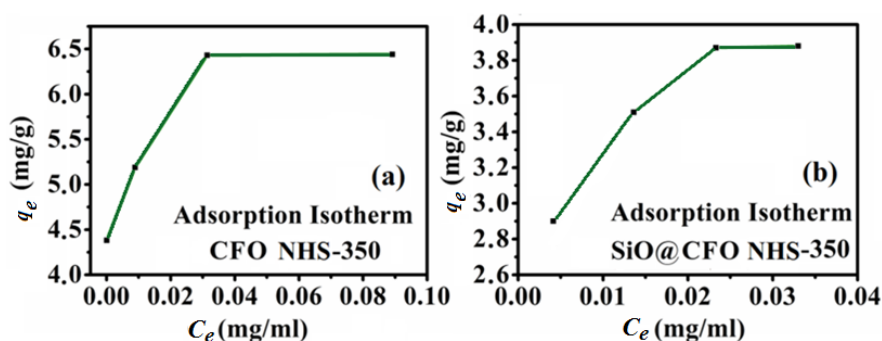


Figure 7.4. Adsorption isotherms of (a) CFO, and (b) SiO@CFO NHS-350.

The plot of pseudo 2nd order kinetic model for all CFO and intraparticle diffusion model for all SiO@CFO NSs are shown in Figures 7.5 (a) and (b). The morphology and size dependent study reveal that hollow NSs helps in achieving a

high BR adsorption in contrast to their NP configuration having same diameter and q_e is found to increase with increasing size of the NHSs. Table 7.2 lists q_e and rate constant of BR adsorption for all CFO and SiO@CFO NSs which indicates that the presence of SiO₂ hinders the adsorption process due to decrease in electrostatic affinity between anionic BR and cationic OLA present on the surface of CFO.

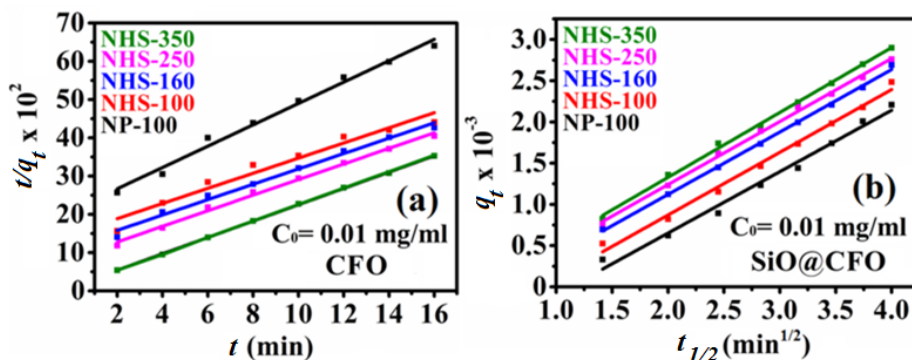


Figure 7.5. (a) Pseudo 2nd order and (b) intraparticle diffusion kinetic models for the adsorption of BR on different CFO and SiO@CFO NSs respectively.

Table 7.2. Equilibrium values of adsorption capacity (q_e) in case of CFO and SiO@CFO NSs for a given amount of adsorbate and BR concentration at room temperature.

Amount of adsorbate (gm)	C_0 (mg/ml)	Name of the adsorbate	q_e (mg/g)	Chemisorption rate (k_2) (g/mg min)	Name of the adsorbate	q_e (mg/g)	Intraparticle diffusion rate (k_i) (mg/g min ^{1/2})
0.01	0.01	CFO NP-100	2.42	1.93	SiO@CFO NP-100	2.14	0.74
		CFO NHS-100	3.43	1.43	SiO@CFO NHS-100	2.41	0.76
		CFO NHS-160	3.64	1.36	SiO@CFO NHS-160	2.61	0.78
		CFO NHS-250	3.95	1.27	SiO@CFO NHS-250	2.77	0.80
		CFO NHS-350	4.65	0.82	SiO@CFO NHS-350	2.92	0.84

The analysis of equilibrium sorption data by fitting them to different isotherm models is an important step for the description of how adsorbate will interact with an adsorbent. The equilibrium sorption data of BR on CFO and SiO@CFO NHS-350 were found to excellently fit to Langmuir adsorption isotherm model (as shown in Figures 7.6 (a) and (b)) which suggests that adsorption takes place homogeneously and is expressed by the following equation: $\frac{C_e}{q_e} = \frac{1}{k_L q_m} + \frac{C_e}{q_m}$, where C_e is the concentration (mg/ml) of BR at equilibrium condition, k_L is a constant and is related to the energy of adsorption (ml/mg), and q_m is the Langmuir monolayer adsorption

capacity. From the graph, the value of maximum BR adsorption capacity (q_m) by both the CFO and SiO@CFO NHS-350 is calculated and presented in Table 7.3. It has been found that these values are very close to the obtained maximum adsorption capacity of BR, calculated from the plot of q_e (mg/g) against C_e (mg/ml) as shown in Figures 7.4 (a) and (b).

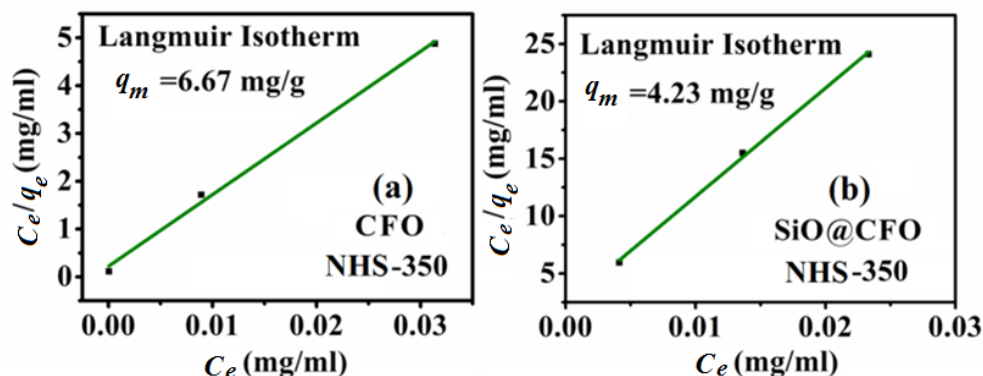


Figure 7.6. Langmuir isotherm plot of BR using (a) CFO and (b) SiO@CFO NHS-350.

Table 7.3. Langmuir adsorption parameters of BR adsorption on (a) CFO, and (b) SiO@CFO NHS-350.

Name of Adsorbent	$q_{e,exp}$ (mg/g)	q_m (mg/g)	k_L (ml/mg)	R^2
CFO NHS-350	6.4	6.67	0.68	0.997
SiO@CFO NHS-350	3.9	4.23	1.04	0.998

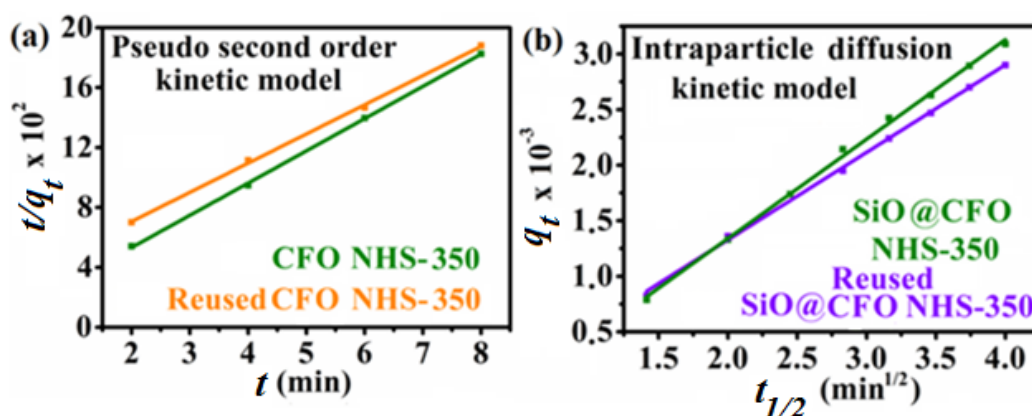


Figure 7.7. Adsorption kinetics of (a) CFO, and (b) SiO@CFO NHS-350 in the degradation of BR with pseudo 2nd order and intraparticle diffusion kinetic model respectively.

To ensure their reusability without any significant loss of their activity, we have carried out the recyclability test through rigorous shaking of those used NSs in presence of chloroform. Figures 7.7 (a) and (b) show the plots of adsorption kinetics of BR affirming the reusability of CFO and SiO@CFO NHSs of diameter 350 nm with almost consistent adsorption rate and equilibrium adsorption capacity. Table 7.4 lists

the amount of adsorbed BR on per unit mass of adsorbate at equilibrium and rate constant for used and reused CFO and SiO@CFO NHS-350. In case of reused CFO NHS-350, the rate constant and the amount of BR adsorbed at equilibrium are found to be approximately 0.45 min^{-1} and 4.89 mg/g respectively whereas in case of reused SiO@CFO NHS-350, they are found to be approximately 0.81 min^{-1} and 2.93 mg/g respectively.

Table 7.4. List of the amount of BR adsorbed per unit mass of adsorbate at equilibrium and rate constant for used and reused CFO and SiO@CFO NHS-350.

CFO NHS-350	q_e (mg/g)	k_2 (g/mg min)
Cycle Number: 1	4.38	0.82
Cycle Number: 2	4.89	0.45
SiO@CFO NHS-350	q_e (mg/g)	k_i (mg/g min ^{1/2})
Cycle Number: 1	2.92	0.84
Cycle Number: 2	2.93	0.81

The adsorbent substances most commonly used in extracorporeal adsorption treatments are resins and activated carbon. However, the application of these adsorbents for *in vitro* diagnostics is limited due to their acute poisoning caused by the low molecular weight substances. Therefore, the development of new adsorptive biocompatible NMs (CFO and SiO@CFO) having direct biomedical significance and excellent efficiency of BR suppression can open up direct therapeutic applications such as hemoperfusion and hemodialysis against hyperbilirubinemia.

7.4. Conclusion

In conclusion, we have demonstrated CFO and SiO@CFO NSs as a biocompatible novel *in vivo* biological probe, having simultaneously innate ferrimagnetism, towards the suppression of BR level in order to avert the harmful effect of phototherapy and hemoperfusion. The size and morphology dependent study suggests that NHS-350 performs as a best BR adsorbent among NP-100 and NHS-*i* (*i*=100, 160, and 250). The comparative BR adsorption study of CFO and SiO@CFO NSs indicates that the electrostatic affinity between anionic carboxyl group of BR and cationic amine group of OLA plays a significant role in adsorbing BR. We believe that the excellent adsorptive efficiency combined with

biocompatibility and recyclability of CFO and SiO@CFO NSs for the degradation of BR, a biologically harmful pigment, reveals their possible therapeutic applications such as hemoperfusion and hemodialysis in case of severe hyperbilirubinemia.

Bibliography

- [1] Kondo, Y.; Yoshikawa, H.; Awaga, K.; Murayama, M.; Mori, T.; Sunada, K.; Bandow, S.; Iijima, S., Preparation, photocatalytic activities, and dye-sensitized solar-cell performance of submicronscale TiO₂ hollow spheres. *Langmuir* 2008, **24**, 547.
- [2] Lou, X. W.; Archer, L. A.; Yang, Z. C., Hollow micro-/nanostructures: Synthesis and applications. *Advanced Materials* 2008, **20**, 3987.
- [3] Wu, Z. L.; Yu, K.; Zhang, S. D.; Xie, Y., Hematite hollow spheres with a mesoporous shell: Controlled synthesis and applications in gas sensor and lithium ion batteries. *Journal of Physical Chemistry C* 2008, **112**, 11307.
- [4] Chang, Y. E.; Youn, D. Y.; Ankonina, G.; Yang, D. J.; Kim, H. G.; Rothschild, A.; Kim, I. D., Fabrication and gas sensing properties of hollow SnO₂ hemispheres. *Chemical Communications* 2009, **27**, 4019.
- [5] Liu, Z. F.; Ding, T.; Zhang, G.; Song, K.; Clays, K.; Tung, C. H., Ternary inverse opal system for convenient and reversible photonic bandgap tuning. *Langmuir* 2008, **24**, 10519.
- [6] Islam, T.; Josephson, L., Current state and future applications of active targeting in malignancies using superparamagnetic iron oxide nanoparticles. *Cancer Biomarkers* 2009, **5**, 99.
- [7] Mazzucchelli, S.; Colombo, M.; Palma, C. D.; Salvade, A.; Verderio, P.; Coghi, M. D.; Clementi, E.; Tortora, P.; Corsi, F.; Prospero, D., Single domain protein A -engineered magnetic nanoparticles: Toward a universal strategy to site-specific labeling of antibodies for targeted detection of tumor cells. *ACS Nano* 2010, **4**, 5693.
- [8] Rachakatla, R. S.; Balivada, S.; Seo, G. M.; Myers, C. B.; Wang, H.; Samarakoon, T. N.; Dani, R.; Pyle, M.; Kroh, F. O.; Walker, B.; Leaym, X.; Koper, O. B.; Chikan, V.; Bossmann, S. H.; Tamura, M.; Troyer, D. L., Attenuation of mouse melanoma by A/C magnetic field after delivery of bi-magnetic nanoparticles by neural progenitor cells. *ACS Nano* 2010, **4**, 7093.
- [9] Minelli, C.; Lowe, S. B.; Stevens, M. M., Engineering nanocomposite materials for cancer therapy. *Small* 2010, **6**, 2336.
- [10] Casula, M. F.; Floris, P.; Innocenti, C.; Lascialfari, A.; Marinone, M.; Corti, M.; Sperling, R. A.; Parak, W. J.; Sangregorio, C., Magnetic resonance imaging contrast agents based on iron oxide superparamagnetic ferrofluids. *Chemistry of Materials* 2010, **22**, 1739.
- [11] Mahmoudi, M.; Sahraian, M. A.; Shokrgozar, M. A.; Laurent, S., Superparamagnetic iron oxide nanoparticles: Promises for diagnosis and treatment of multiple sclerosis. *ACS Chemical Neuroscience* 2011, **2**, 118.
- [12] Joshi, H. M.; Lin, Y. P.; Aslam, M.; Prasad, P. V.; Sikma, E. A. S.; Edelman, R.; Meade, T.; Dravid, V. P., Effects of shape and size of cobalt ferrite nanostructures on their MRI contrast and thermal activation. *Journal of Physical Chemistry C* 2009, **113**, 17761.
- [13] Fantechi, E.; Innocenti, C.; Zanardelli, M.; Fittipaldi, M.; Falvo, E.; Carbo, M.; Shullani, V.; Mannelli, L. D. C.; Ghelardini, C.; Ferretti, A. M.; Ponti, A.; Sangregorio, C.; Ceci, P., A smart platform for hyperthermia application in cancer treatment: Cobalt-doped ferrite nanoparticles mineralized in human ferritin cages. *ACS Nano* 2014, **8**, 4705.
- [14] Bozorth, R. M., *Ferromagnetism* (D. Van Nostrand Company, New York, 1961).
15. Hassan, R. S.; Viart, N.; Bouillet, C. U.; Loison, J. L.; Versini, G.; Vola, J. P.; Crégut, O.; Pourroy, G.; Muller, D.; Chateigner, D., Structural properties of cobalt ferrite thin films deposited by pulsed laser deposition: Effect of the reactive atmosphere. *Thin Solid Films* 2007, **515**, 2943.
- [16] Kumbhar, V. S.; Jagadale, A. D.; Shinde, N. M.; Lokhande, C. D., Chemical synthesis of spinel cobalt ferrite (CoFe₂O₄) nano-flakes for supercapacitor application. *Applied Surface Science* 2012, **259**, 39.

- [17] Silva, J. B.; Brito, W. D.; Mohallem, N. D. S., Influence of heat treatment on cobalt ferrite ceramic powders. *Materials Science and Engineering B* 2004, **112**, 182.
- [18] Srivastava, A. K.; Madhavi, S.; White, T. J.; Ramanujan, R. V., The processing and characterization of magnetic nanobowls. *Thin Solid Films* 2006, **505**, 93.
- [19] An, K.; Hyeon, T., Synthesis and biomedical applications of hollow nanostructures. *Nano Today* 2009, **4**, 359.
- [20] Cheng, K.; Peng, S.; Xu, C. J.; Sun, S. H., Porous hollow Fe₃O₄ nanoparticles for targeted delivery and controlled release of cisplatin. *Journal of the American Chemical Society* 2009, **131**, 10637.
- [21] Kapitulnik, J., Bilirubin: an endogenous product of heme degradation with both cytotoxic and cytoprotective properties. *Molecular Pharmacology* 2004, **66**, 773.
- [22] Veere, C. N. Van Der; Sinaasappel, M.; McDonagh, A. F.; Rosenthal, P.; Labrune, P.; Odi'evre, M.; Fevery, J.; Otte, J.; McClean, P.; Bürk, G.; Masakowski, V.; Sperl, W.; Mowat, A. P.; Vergani, G. M.; Heller, K.; Wilson, J. P.; Shepherd, R.; Jansen, P. L., Current therapy for Crigler-Najjar syndrome type 1: report of a world registry. *Hepatology* 1996, **24**, 311.
- [23] Sideman, S.; Mor, L.; Mihich, M.; Lupovich, S.; Brandes, J. M.; Zetzer, M., Resin hemoperfusion for unconjugated bilirubin removal. *Contributions to Nephrology* 1982, **29**, 90.
- [24] Abel, J. J.; Rountree, L. G.; Turner, B. B., The removal of diffusible substances from the circulating blood by means of dialysis. *Transfusion Science* 1913, **28**, 51.
- [25] Murki, S.; Kumar, P., Blood exchange transfusion for infants with severe neonatal hyperbilirubinemia. *Seminars in Perinatology* 2011, **35**, 175.
- [26] Lamola, A. A.; Blumberg, W. E.; McClead, R.; Fanaroff, A., Photoisomerized bilirubin in blood from infants receiving phototherapy. *Proceedings of the National Academy of Sciences U.S.A.* 1981, **78**, 1882.
- [27] Toietta, G.; Mane, V. P.; Norona, W. S.; Finegold, M. J.; Ng, P.; McDonagh, A. F.; Beaudet, A. L.; Lee, B., Lifelong elimination of hyperbilirubinemia in the Gunn rat with a single injection of helper-dependent adenoviral vector. *Proceedings of the National Academy of Sciences U. S. A.* 2005, **102**, 3930.
- [28] Juneja, D.; Singh, O.; Bhasin, A.; Gupta, M.; Saxena, S.; Chaturvedi, A., Severe suicidal digoxin toxicity managed with resin hemoperfusion: A case report. *Indian Journal of Critical Care Medicine* 2012, **16**, 231.
- [29] Rahman, M. H.; Haqqie, S. S.; McGoldrick, M. D., Acute hemolysis with acute renal failure in a patient with valproic acid poisoning treated with charcoal hemoperfusion. *International Symposium on Home Hemodialysis* 2006, **10**, 256.
- [30] Duan, Z. J.; Li, L. L.; Ju, Jia, Z. H.; Gao, He, G. H., Treatment of hyperbilirubinemia with blood purification in China. *World Journal of Gastroenterology* 2006, **12**, 7467.
- [31] Amiri, S.; Shokrollahi, H.; The role of cobalt ferrite magnetic nanoparticles in medical science. *Materials Science and Engineering C* 2013, **33**, 1-8.
- [32] Kurtin, W. E., Spectroscopy and photochemistry of bilirubin photoproducts. *Photochemistry and Photobiology* 1978, **27**, 503.
- [33] Shinke, K.; Ando, K.; Koyama, T.; Takai, T.; Nakaji, S.; Ogino, T., Properties of various carbon nanomaterial surfaces in bilirubin adsorption. *Colloids and Surfaces B: Biointerfaces* 2010, **77**, 18.

Chapter 8

Environmental Application of CoFe₂O₄ Nano hollow spheres Through Dye Adsorption

This chapter demonstrates an unprecedented dye adsorption capability of CoFe₂O₄ nano hollow spheres and the influence of different functional group of dye on their adsorption rate. In addition, size dependent adsorption capability of a series of CoFe₂O₄ nano hollow spheres of increasing diameter has also been investigated.

8. Effect of Functional Group of Dye on Adsorption Property of CoFe_2O_4 Nano hollow spheres

8.1. Preamble

The rapid growth of industry makes people aware of the need to clean up the water effluents. A long term research has been carried out in finding new innovative methods for reducing the environmental pollution caused by water effluents. There are several types of waste materials that do not readily lend themselves to standard method of water treatments. Dye,¹ a stable, recalcitrant, colorant which has been extensively used in textile, paper, leather, and cosmetic industry is one of them since they are very stable to light and oxidizing agents. Dispose of the dye effluents into the water cause severe problems in nature. It increases the biological oxygen demand (BOD), chemical oxygen demand (COD) which are very dangerous to aquatic plants and animals. Moreover, it interrupts photosynthesis, degrades soil quality, and affects the growth of plants. Due to carcinogenic and toxic nature of dye, their release into environment poses serious aesthetical, and health problems to human being. Thus, industrial dye effluents need to be effectively treated before being discharged into the environment.

There are a large number of physical methods such as oxidation,² coagulation and flocculation,³ ultra chemical filtration,⁴ membrane separation,⁵ chemical treatments,⁶ and adsorption⁷ for the removal of dye from its aqueous solution. Among these, adsorption is one of the most investigated techniques for dye removal mainly due to its simplicity and high level of effectiveness.⁸ Due to large specific surface area, nanomaterials (NMs) have attracted tremendous attention of the current researchers in this regard. Magnetic nanostructures are best for waste water treatment due to their fast magnetic separation after dye adsorption in addition to their high surface area and chemical stability. Zhou et al.⁹ have reported effective adsorption of different dyes on carboxylic hyperbranched polyglycerol functionalized iron oxide-silica magnetic nanoparticles (NPs). Among all the other

nanostructures, in last few years, people are very much interested in fabricating nano hollow spheres (NHSs) because of its hollow interior which enhances its effective surface area. Moreover, the large pore volume of NHSs helps to encapsulate the toxic material more efficiently than NP configuration. Therefore, the development of new adsorptive magnetic NHSs having high selective adsorption capability is advantageous.

In this article, we have highlighted the effect of different functional groups of dye on the adsorption behaviour of CoFe_2O_4 (CFO) NHSs, synthesized by using a simple solvothermal method as mentioned in *Chapter 5* in detail. For this purpose, we have chosen dyes named, fluorescein (FLU), bromophenol blue (BPB), and bromocresol green (BCG) in which FLU contains the carboxyl ($-\text{COOH}$) group and BPB, BCG contain the sulfonyl ($-\text{SO}_3\text{H}$) group in addition to the hydroxyl ($-\text{OH}$) group. Moreover, the difference in steric hindrance for the dyes (as in case of BPB and BCG) having same functional group helps to identify their adsorption behaviour solely evoked by its structure. We have demonstrated an elucidative correlation between the nature of dye and adsorption properties of CFO NHSs in terms of electronic density and complexity of the dyes.

8.2. Experimental Section

8.2.1. Synthesis of CoFe_2O_4 Nano hollow spheres

A series of CFO NHSs of diameter 100, 160, and 250 nm were prepared through a facile template free solvothermal technique as described in *Chapter 5* in detail.

8.2.2. Adsorption Study

Adsorption experiments were carried out by adding a fixed amount of adsorbent (0.01 g) to a 10 ml of beaker filled with 4 ml diluted dye solutions with varying concentration (0.03–0.2 mg/ml) at pH \sim 7. The beaker was then placed in a magnetic stirrer with the speed set at 120 rpm. At the end of each adsorption batch

runs, the final concentration of dye in the solution was measured using UV-Vis spectrophotometer until steady state has been reached. The amount of dye on CFO adsorbent was calculated from the following equation:

$$q_t = \frac{(C_0 - C_t)V}{m} \quad (8.1)$$

where q_t (mg/g) is the amount of dye adsorbed at time t , C_0 and C_t (mg/ml) are the dye concentrations at initial and any time respectively. V (ml) is the volume of the dye solution, and m (g) is the mass of the adsorbent.

8.3. Result and Discussions

Considering the significant progress in waste water treatment through rational engineering and manipulation of magnetic NMs, we aimed to utilize our developed CFO NHSs in the degradation of dyes, FLU, BPB, and BCG. The molecular structures of these dyes as shown in the inset of Figures 8.1 (a)-(c) indicate that the dye FLU contains $-\text{COOH}$ whereas BPB, BCG contain $-\text{SO}_3\text{H}$ in addition to $-\text{OH}$. Figures 8.1 (a)-(c) show the comparative decay study of these dyes over time through UV-Vis spectroscopy in the presence of as-prepared CFO NHSs of diameter 250 nm at pH ~ 7 with initial dye concentration 0.03 mg/ml. The absence of peaks corresponding to the decomposition products of these dyes in the UV-Vis absorption spectrographs indicates that the reaction follows the adsorption pathway instead of any chemical degradation. It is found that CFO nanostructures exhibit an unprecedented efficiency in the removal of these dyes at pH ~ 7 under no external irradiation. It adsorbs a total 95% of FLU, 32% of BPB, and 15% of BCG dyes within only 2 min which ensure that the developed CFO NHSs are the potential candidate for its application in waste water purification.

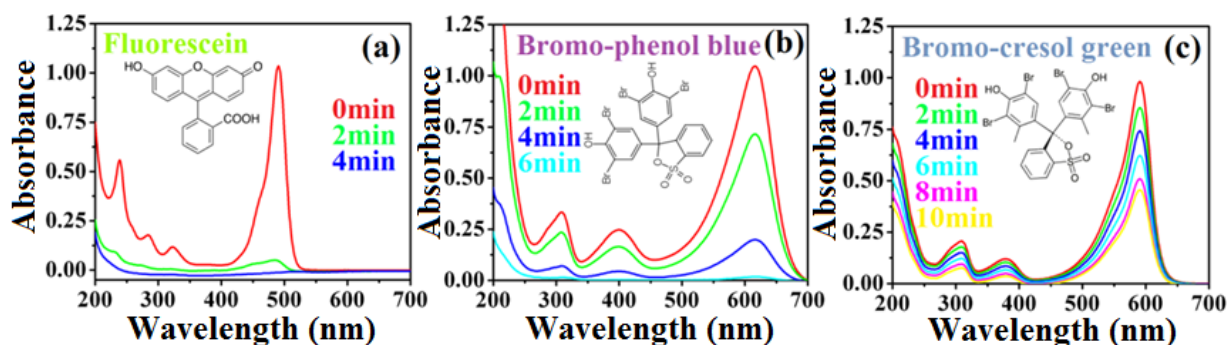


Figure 8.1. UV-Vis spectral changes of aqueous solution of (a) fluorescein, (b) bromophenol blue, and (c) bromocresol green with time in presence of CFO NHS-250 under no external light respectively.

In order to examine the controlling mechanism of adsorption such as mass transfer, physisorption, and chemisorption; different kinetic models such as intraparticle diffusion (mass transfer) model, pseudo 1st order (physisorption), and pseudo 2nd order (chemisorption) model were applied to test the obtained experimental data for different absorbent concentration as described in detail in Chapter 1.

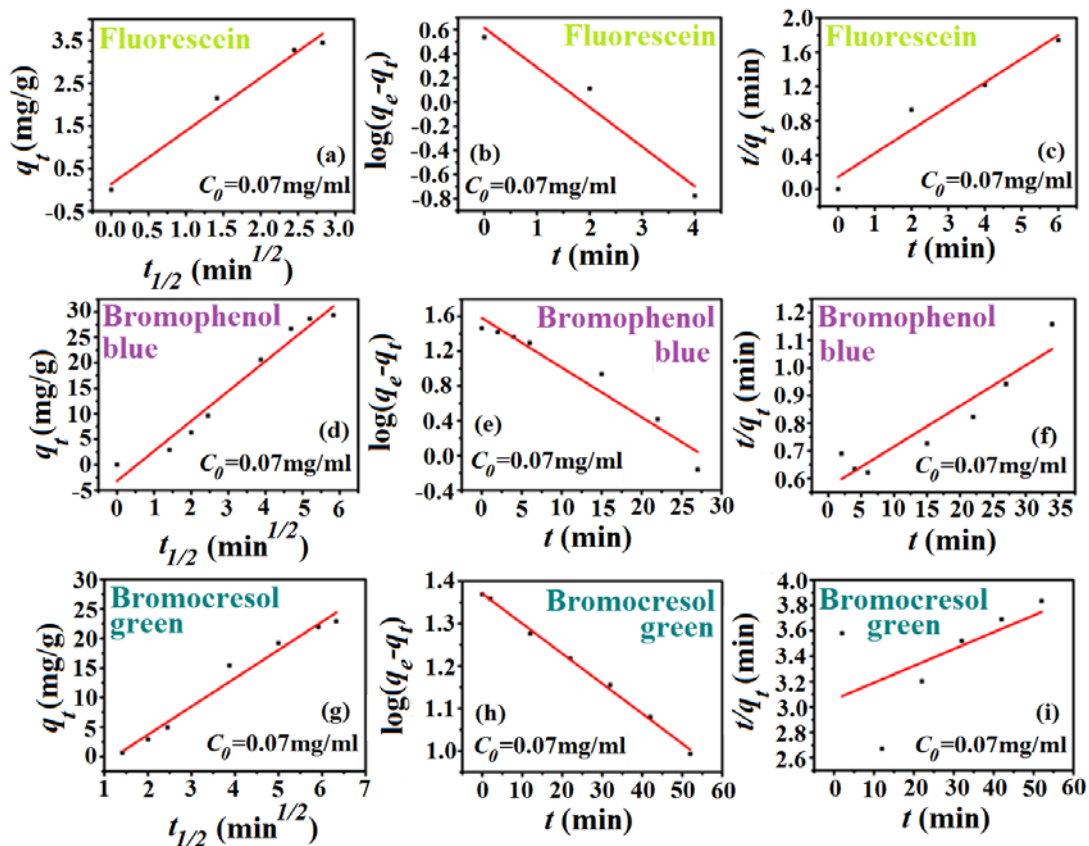


Figure 8.2. Intraparticle diffusion, pseudo 1st order, and pseudo 2nd order kinetic model parameters for fluorescein, bromophenol blue, and bromocresol green at room temperature.

Table 8.1. Intraparticle diffusion, pseudo 1st order, and pseudo 2nd order kinetic model parameters for different initial BR concentrations at room temperature.

Size of CFO	Amount of CFO (g)	Dye	Amount of dye (mg/ml)	$q_{e,exp}$ (mg/g)	Intraparticle diffusion model			Pseudo 1 st order model			Pseudo 2 nd order model		
					q_{ei} (mg/g)	k_i (mg/g min ^{1/2})	R ²	q_{e1} (mg/g)	k_1 (min ⁻¹)	R ²	q_{e2} (mg/g)	k_2 (g/mg min)	R ²
NHS-250	0.01	FLU	0.07	3.45	3.19	1.25	0.99	4.12	0.76	0.98	3.7	0.52	0.97
		BPB		29.34	31.1	5.87	0.98	38.3	0.13	0.98	71.4	3x10 ⁻⁴	0.94
		BCG		24.55	23.0	4.78	0.99	27.5	0.09	0.99	-134	3x10 ⁻⁵	0.17

The plots of the linearized form of intraparticle diffusion, pseudo 1st and pseudo 2nd order kinetic models for CFO NHSs of diameter 250 nm in presence of all the dyes with dye concentration 0.07 mg/ml are shown in Figures 8.2 (a)-(i). The values of rate constant (k), amount of dye adsorbed on adsorbate at equilibrium (q_e), and correlation coefficients (R^2) are calculated from these plots and presented in Table 8.1. It is found that the values of R^2 for the intraparticle diffusion and pseudo 1st order model are of the order of 0.99, and the calculated q_e , values are nearly equal to the experimental values, which suggest that the adsorption process basically follows the intraparticle diffusion and pseudo 1st order model. It predicts that the overall rate of all the dye adsorption is dominated by mainly mass transfer and physisorption which may involve an electrostatic attraction between the anionic group of dye and the cationic amine group of oleylamine, present on the adsorbent's surface. Moreover, the dyes containing -OH group can easily form the hydrogen/electrostatic bonding with the surface hydroxyl group of CFO NHSs,¹³ which may lead to the excellent dye adsorption efficiency of CFO NHSs.

Table 8.1 indicates a higher rate of physisorption in case of FLU containing -COO⁻ group, as compared to the dyes (BPB and BCG) having -SO₃⁻ group which is also verified from the comparative UV-Vis spectroscopy of all the dyes (as shown in Figure 8.3). It may be due to greater electron density of -COO⁻ group than -SO₃⁻ group in addition to -OH bond which accelerates the formation of hydrogen bonding and thus results in greater physisorption in case of FLU than BPB and BCG. Moreover, BPB is found to exhibit higher rate of adsorption than BCG in spite of both having same functional groups (-OH⁻ and -SO₃⁻) due to more sterically hindered configuration of BCG in contrast to BPB.

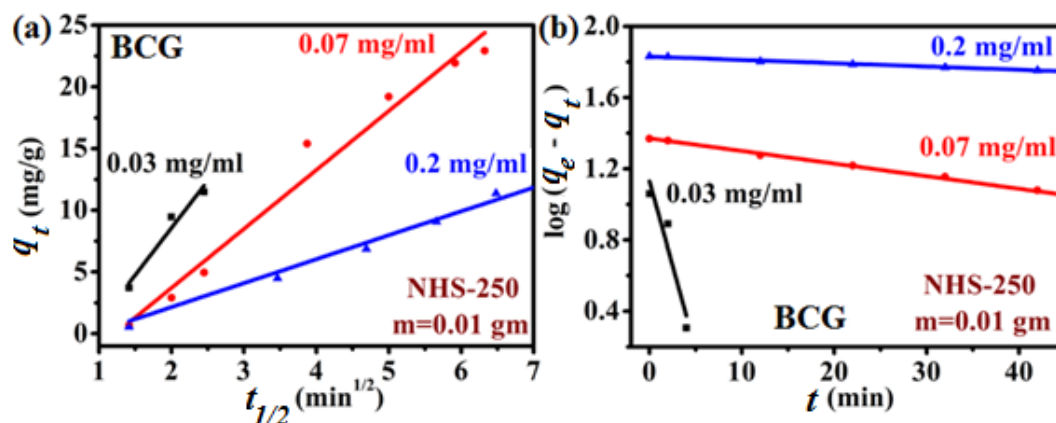


Figure 8.3. Adsorption kinetics of BCG on CFO NHS-250 with (a) intraparticle diffusion, (b) pseudo 1st order with different initial dye concentration.

Table 8.2. Intraparticle diffusion, pseudo 1st order, and pseudo 2nd order kinetic model parameters for different initial BCG concentrations on CFO NHS-250 at room temperature.

Name of adsorbate	Amount of adsorbate (g)	C_0 (mg/ml)	$q_{e,exp}$ (mg/g)	Intraparticle diffusion kinetic model			Pseudo 1 st order kinetic model		
				q_{ei} (mg/g)	k_i (mg/g min ^{1/2})	R^2	q_{e1} (mg/g)	k_1 (min ⁻¹)	R^2
CFO NHS-250	0.01	0.03	11.49	12.00	7.63	0.98	13.48	0.43	0.96
		0.07	24.55	23.05	4.78	0.99	27.48	0.09	0.99
		0.2	68.02	68.22	1.94	0.99	67.59	0.004	0.99

The plots of the linearized form of intraparticle diffusion and pseudo 1st order kinetic models for CFO NHSs of diameter 250 nm in presence of BCG with different dye concentration from 0.03 to 0.2 mg/ml are shown in Figures 8.3 (a) and (b). The values of rate constant (k), amount of dye adsorbed on adsorbate at equilibrium (q_e), and correlation coefficients (R^2) calculated from these plots are presented in Table 8.2. It indicates that with variation of initial BCG concentration from 0.03 to 0.2 mg/ml, a considerable increase in q_e values occurs and it ranges from 11.49 to 68.22 mg/g for the NHS of diameter 250 nm. It is mainly due to the presence of more adsorbate for a fixed amount of surface area of adsorbent. Moreover, both the intraparticle and pseudo 1st order rate constants are found to decrease with increasing the dye concentration which may be due to the decreasing driving force with increasing dye concentration.

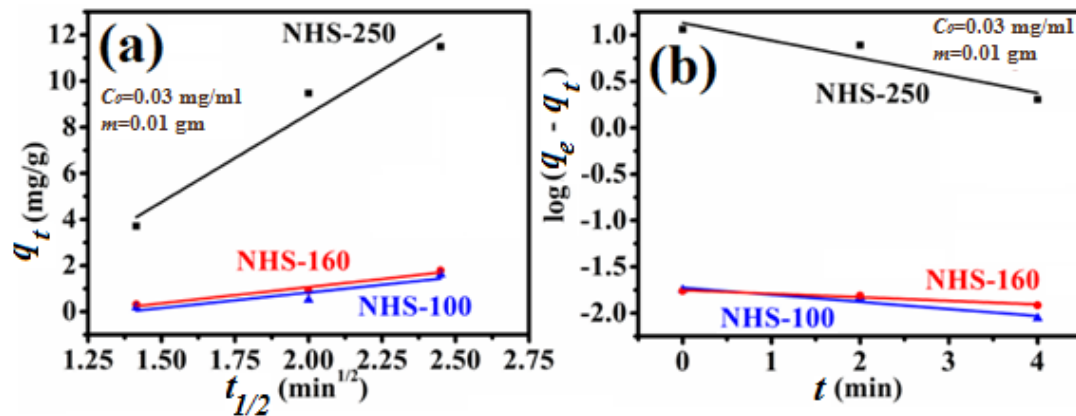


Figure 8.4. (a) Intraparticle diffusion, (b) pseudo 1st order kinetic models for the adsorption of BCG on different CFO nanostructures.

Table 8.3. Adsorption capacity at equilibrium (q_e) of different CFO nanostructures for a given amount of adsorbate and BCG concentration in case of intraparticle diffusion model.

Size of CFO adsorbate	Adsorbate (g)	Initial BG C_0 (mg/ml)	q_{exp} (mg/g)	Intraparticle diffusion model		
				q_{ei} (mg/g)	k_i (mg/g min ^{1/2})	R ²
NHS-250	0.01	0.03	11.49	12.00	7.63	0.98
NHS-160			1.73	1.69	1.4	0.98
NHS-100			1.52	1.43	1.34	0.93

Table 8.4. Adsorption capacity at equilibrium (q_e) of different CFO nanostructures for a given amount of adsorbate and BCG concentration in case of pseudo 1st order model.

Size of CFO adsorbate	Adsorbate (g)	Initial BG C_0 (mg/ml)	q_{exp} (mg/g)	Pseudo 1 st order model		
				q_{e1} (mg/g)	k_1 (min ⁻¹)	R ²
NHS-250	0.01	0.03	12.00	13.48	0.43	0.95
NHS-160	0.01	0.03	0.018	0.018	0.18	0.98
NHS-100	0.01	0.03	0.017	0.017	0.08	0.98

The plot of intraparticle diffusion model and pseudo 1st order kinetic model for all CFO NHSs of different diameters are shown in Figures 8.4 (a) and (b). The size dependent study reveal that the amount of adsorbate absorbed per unit mass of adsorbent is found to increase with increasing size of the NHSs. Table 8.3 and Table 8.4 list the adsorption capacity at equilibrium (q_e) and kinetic rate constant (k) of the adsorption of BCG for all CFO NHSs corresponding to the intraparticle diffusion and pseudo 1st order model respectively. It indicates that the both the mass transfer and physisorption rate constant for CFO NHSs increases with increasing size of the CFO NHSs which signifies that rate of degradation of dye enhances with increasing

size of the adsorbate. Moreover, the amount of dye adsorbed per unit mass of CFO is found to increase with the size of the NHSs.

The analysis of the equilibrium sorption data by fitting them to different isotherm models is another important step for the description of how adsorbate will interact with an adsorbent as described in *Chapter 1*. Herein, we have fitted the sorption data into three models, named Langmuir,¹⁴ Freundlich,¹⁵ and Dubinin Radushkevich¹⁶ (D-R) isotherm as shown in Figures 8.5 (a)-(c) and their corresponding parameters are represented in Table 8.5.

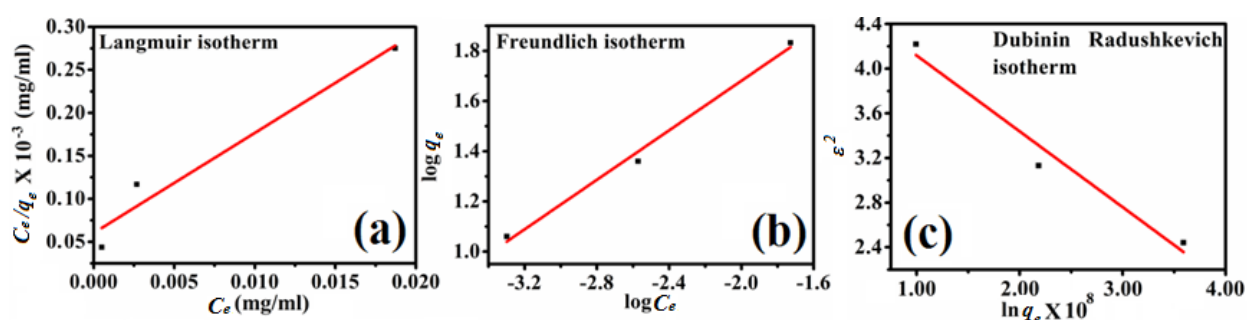


Figure 8.5. (a) Langmuir, (b) Freundlich, (c) Dubinin Radushkevich adsorption isotherm of BCG on CFO NHS-250.

Table 8.5. Adsorption parameters of BCG adsorption on CFO NHS-250.

Name	Langmuir Isotherm			Freundlich Isotherm			D-R Isotherm		
	q_m	K_L	R^2	K_f	$1/n$	R^2	Q_0	K_{DR}	R^2
CFO-250	85.91	193.35	0.98	464.94	0.49	0.99	121.098	6.791	0.98

In our case, the equilibrium sorption data of BCG on the CFO NHS-250 were found to excellently fit to Freundlich adsorption isotherm model as shown in Figure 8.5 (b) which suggests the multilayer adsorption of dye on heterogeneous surface of CFO NHSs, holding the assumption that the adsorption sites are distributed exponentially with respect to the heat of adsorption. The $1/n$ value obtained from Freundlich isotherm indicates that multilayer adsorption of dye on the CFO is favorable which implies that the adsorption of each dye molecule has a different activation energy due to surface roughness, inhomogeneity, and adsorbate-adsorbate interactions.

8.4. Conclusion

In summary, we have demonstrated a comparative adsorption study of CFO NHSs in the removal of dyes, named FLU, BCG, and BPB having different functional groups over a wide range of concentrations at pH ~ 7. Detailed study reveals that the CFO NHSs are the excellent adsorbent in the removal of these dyes due to electrostatic interaction/hydrogen bonding with the surface amine or hydroxyl group of CFO. It is found that CFO NHSs exhibit higher rate of adsorption for FLU than BCG and BPB which may be due to greater electron density of $-\text{COO}^-$ group than $-\text{SO}_3^-$ group. Moreover, steric hindrance offered by the dye molecule is found to play an important role in adsorbing the dye molecule on the CFO surface. The adsorption kinetic of CFO NHS-250 is found to follow intraparticle diffusion and pseudo 1st order model and its maximum adsorption capacity was found to increase from 11.49 to 68.02 mg/g at equilibrium with increasing initial BCG concentrations from 0.03 to 0.2 mg/ml. Moreover, the equilibrium sorption data were found to excellently fit to Freundlich adsorption isotherm model. The excellent adsorptive efficiency of CFO nanostructures in removal of dyes reveals their potential application in waste water treatment.

Bibliography

- [1] Booth, G., *Dyes, General Survey* (Wiley-VCH, New York, 2000).
- [2] Shu, H. Y.; Huang, C. R.; Chang, M. C.; Decolourization of mono-azo dyes in waste water by advanced oxidation process: a case study of acid red and acid yellow. *Chemosphere* 1994, **29**, 2597.
- [3] Parsons, S. A.; Jefferson, B., *Introduction to Potable Water Treatment Processes* (Blackwell Publishing, United Kingdom 2006).
- [4] Allegre, C.; Moulin, P.; Maisseu, M.; Charbit, F.; Treatment and reuse of reactive dyeing effluents. *Journal of Membrane Science* 2006, **269**, 15.
- [5] Gurses, A.; Dogar, C.; Yalcın, M.; Acıkyıldız, M.; Bayrak, R.; Karaca, S., The adsorption kinetics of the cationic dye, methylene blue, onto clay. *Journal of Hazardous Materials* 2006, **131**, 217.
- [6] Pagga, U.; Taeger, K., Development of a method for adsorption of dyestuffs on a activated sludges. *Water Research* 1994, **28**, 1051.
- [7] Santhy, K.; Selvapathy, P., Removal of reactive dyes from wastewater by adsorption on coir pith activated carbon. *Bioresource Technology* 2006, **97**, 1329.
- [8] Han, R.; Ding, D.; Xu, Y.; Zou, W.; Wang, Y.; Li, Y.; Zou, L., Use of rice husk for the adsorption of congo red from aqueous solution in column mode. *Bioresource Technology* 2008, **99**, 2938.
- [9] Zhou, L.; Gao, C.; Xu, W., Magnetic dendritic materials for highly efficient adsorption of dyes and drugs. *ACS Applied Materials and Interfaces* 2010, **2**, 1483.
- [10] Weber, W.J.; Morriss, J. C., Kinetics of adsorption on carbon from solution. *Journal of the Sanitary Engineering Division - Civil Engineering* 1963, **89**, 31.
- [11] Lagergren, S., About the theory of so-called adsorption of soluble substance. *Kungliga Svenska Vetenskapsakademiens Handlingar* 1898, **24**, 1.
- [12] Ho, Y. S.; McKay, G., Sorption of dye from aqueous solution by peat. *Chemical Engineering Journal* 1998, **70**, 115.
- [13] Pirillo, S.; Ferreira, M. L.; Rueda, E. H., The effect of pH in the adsorption of Alizarin and Eriochrome Blue Black R onto iron oxides. *Journal of Hazardous Materials* 2009, **168**, 168.
- [14] Langmuir, I., Adsorption of gases on plain surfaces of glass mica platinum. *Journal of the American Chemical Society* 1918, **40**, 136.
- [15] Freundlich, H. M. F., Uber die adsorption in losungen. *The Journal of Physical Chemistry* 1906, **57**, 385.
- [16] Horsfall, M. J.; Spiff, A. I.; Abia, A. A., Studies on the influence of Mercaptoacetic acid (MAA) Modification of cassava *Manihot culenta* Cran Waste Biomass on the adsorption of Cu^{2+} and Cd^{2+} from aqueous solution. *Bulletin of the Korean Chemical Society* 2004, **25**, 969.

Chapter 9

Conclusion and Scope for Future Work

This chapter gives an overall conclusion of the work described so far and the scopes for further work in this specific field.

9.1. Epilogue

In this thesis, we have mainly focused our work on the synthesis of transition metal oxide (Fe_3O_4 , CoFe_2O_4 , and MnFe_2O_4) based magnetic nanostructures (nanoparticles (NPs) and nano hollow spheres (NHSs)) by different chemical synthesis procedures followed by functionalization and core-shelling in order to enhance their magnetic properties without going to the limit of critical diameter of the nanomaterials (NMs). Very interestingly, the surfactant functionalized CoFe_2O_4 NPs are found to exhibit higher coercivity in contrast to its bare configuration. In addition, morphology and size dependent study reveals that the hollow nanostructures (NSs) exhibit higher coercivity in comparison to its solid configuration of same diameter and it increases with decreasing size of the NSs. Further, the enhanced magnetic properties have been utilized in absorbing electromagnetic (EM) radiation.

In general, the properties which help in absorbing EM radiation are high magnetization, high electric polarization, low conductivity, and high surface area and interestingly, ferrite NSs possess all these properties because of which it is used as a shielding material in microwave as well as radio frequency region. In our study, we have used THz frequency region for analysing the EM absorption properties of ferrite NSs and our investigation reveals that enhanced absorption and complex conductivity of ferrite NHSs in contrast to its NPs configuration is due to their hollow configuration which helps to confine the THz energy through multiple internal reflections offered by double interfaces of NHSs. Moreover, the relatively large specific surface area and double interfaces of the nano-shell structure greatly help to produce enormous interfacial polarization (electric or magnetic dipoles) which significantly enhances the EM wave attenuation in contrast to NPs as well as with increasing NHS's average diameter.

In order to obtain some basic parameters like scattering time, carrier density, a general approach is to fit the conductivity spectra into some models like Drude model or Drude-Smith model. Drude treats the electrons as non-interacting classical

gas which leads to mean free path in nanometer scale range. Therefore, in NMs, it is obvious that the electron gets back scattered from the grain boundary before it could finish its mean free path. Smith incorporates the back scattering parameter into Drude model and till now, most of the researchers utilize this model for many systems. However, it is not correct to use this model in case of bad conductor where there is no free electron. In ferrites, polaron is the fundamental carrier for electrical transportation and their hopping is the main mechanism for conduction.

In an attempt to solve the problem of environmental pollution due to improper management of industrial water, the industrial dye effluents need to be effectively treated before being discharged into the environment. Due to large specific surface area, chemical stability, facile separation, and low cost of synthesis, ferrite NMs have attracted tremendous attention of the current researchers in this regards. Moreover, the biocompatibility of ferrite NSs can be utilized in removing the biologically harmful dye, bilirubin which responsible for jaundice, hyperbilirubinemia, and neurotoxicity. The conventional treatments for severe hyperbilirubinemia include exchange blood transfusion which consists of passage of patient's blood through a column with absorptive materials. Therefore, excellent adsorption activity of ferrite NMs can replace the commercially available activated carbon and resin which are generally used for this purpose.

9.2. Scope for Future Work

Modulation of magnetic properties of functionalized CoFe_2O_4 NPs by judiciously varying both the nature of head and chain-length of surfactant is a very important result for its application in specific operation. The enhancement of a specific property of magnetic NPs has increased its effectiveness in the application fields such as biosensing, hyperthermia, drug delivery, and magnetic resonance imaging.

Due to the rapid enhancement of wireless communication, digital systems, and fast processors, a considerable attention has been focused on the fabrication of materials that possess a broad absorption frequency, high absorption capacity, low

weight, good thermal stability, and antioxidant property and the hollow NSs of these ferrite materials are found to absorb EM radiation more efficiently due to large surface area and multiple internal reflections within the cavity. Therefore, high absorption capability of ferrite hollow NSs in the THz frequency region may rise opportunities in the space, stealth technology, electromagnetism based electronic devices such as sensors, switches, and so on.

The ferrite nano hollow structures having excellent adsorption activity in degradation of biologically harmful pigment, bilirubin can be efficiently used in treatment of hyperbilirubinemia. Moreover, due to the unprecedented adsorption activity of the NSs in degradation of environmentally harmful dye, fluorescein, bromophenol blue, bromocresol green, they can be used in industrial waste water treatment.